



HAL
open science

Réactivation Hydro-Mécanique d'une Faille Rate & State Glissement, Sismicité et Évolution de Perméabilité

Michelle Almakari

► **To cite this version:**

Michelle Almakari. Réactivation Hydro-Mécanique d'une Faille Rate & State Glissement, Sismicité et Évolution de Perméabilité. Géologie appliquée. Université Paris sciences et lettres, 2019. Français. NNT : 2019PSLEM065 . tel-02570431

HAL Id: tel-02570431

<https://pastel.hal.science/tel-02570431>

Submitted on 12 May 2020

HAL is a multi-disciplinary open access archive for the deposit and dissemination of scientific research documents, whether they are published or not. The documents may come from teaching and research institutions in France or abroad, or from public or private research centers.

L'archive ouverte pluridisciplinaire **HAL**, est destinée au dépôt et à la diffusion de documents scientifiques de niveau recherche, publiés ou non, émanant des établissements d'enseignement et de recherche français ou étrangers, des laboratoires publics ou privés.

THÈSE DE DOCTORAT
DE L'UNIVERSITÉ PSL

Préparée à MINES ParisTech

**Réactivation Hydro-Mécanique d'une Faille Rate & State:
Glissement, Sismicité et Évolution de Perméabilité.**

**Hydro-Mechanical Rate & State Fault Reactivation: Slip, Seismicity
and Permeability Enhancement.**

Soutenue par

Michelle ALMAKARI

Le 18 Décembre 2019

École doctorale n°398

**Géosciences Ressources
Naturelle et Environnement**

Spécialité

Géosciences et Géoingénierie

Composition du jury :

Mr. Frédéric CAPP Professeur, Université Nice Sophia Antipolis	<i>Président</i>
Mr. Georg DRESEN Professeur, University of Potsdam	<i>Rapporteur</i>
Mr. Hideo AOCHI Cadre Scientifique des EPIC, BRGM	<i>Rapporteur</i>
Mr. Jean SULEM Professeur, Ecole des Ponts ParisTech	<i>Examineur</i>
Mme. Agnès Helmstetter Chargée de Recherche, Univ. Grenoble Alpes	<i>Examinatrice</i>
Mr. Hervé CHAURIS Professeur, MINES ParisTech	<i>Directeur de thèse</i>
Mr. Pierre DUBLANCHET Chargé de Recherche, MINES ParisTech	<i>Maitre de thèse</i>

“In every end, there is also a beginning.”

A Great and Terrible Beauty
LIBBA BRAY

Acknowledgments

First, I would like to express my deepest appreciation and acknowledgments to my supervisors Pierre DUBLANCHET and Hervé CHAURIS for providing me the opportunity to conduct this thesis. Particularly, I thank Pierre for his guidance, support, constant supervision, as well as for all the long discussions that we had and his very clear explanations. I appreciate a lot the confidence that he had in my work and the freedom he gave me to chose the different directions that I want to explore during my thesis. I also thank him for giving me the opportunity to teach a few sessions of rock mechanics at IPGP, this experience was particularly interesting for me. I would also like to thank Hervé for being constantly involved in my thesis, even in the parts that are not within his area of expertise. I particularly enjoyed working with him to develop and apply the inversion approaches. Even though I had no previous extensive knowledge in this area, his clear explanations and continuous guidance made everything look easy. So I thank him for that. Finally, beyond the scientific discussions, I would also like to thank Pierre and Hervé for their involvement, their advice in every discussion that we had concerning my professional project.

I would also like to thank François Passelègue (EPFL, Lausanne) with whom I had the chance to collaborate. This collaboration allowed me to explore the experimental world, which was new for me, and benefit from his large expertise in this area.

During this thesis, I benefited from a 3 years doctoral contract from MINES ParisTech which allowed me to conduct my research in very good conditions, to which I am entirely grateful. I also had the chance to benefit from additional funding from the Paris Exploration Geophysics Group (GPX), which sponsored my participation to the 3rd international workshop on earthquakes in Cargèse in 2017 and to the EGU General Assembly in Vienna in 2018. I also benefited from the French government program “Investissements d’Avenir” under the grant agreement n ANR-10-IEED-0801 (Project GIS Geodenergie/TEMPERER), which sponsored my participation to the AGU Fall Meeting in Washington, DC in 2018. Finally, I also thank the organisers of the Schatzalp 3rd Induced Seismicity Workshop for giving me the opportunity to participate as a fellowship applicant in this workshop that took place in Davos, Switzerland in 2019.

My sincere thanks go to Harsha BHAT and Frédéric PELLET for taking part in my annual PhD committee. Their comments and recommendations allowed me to improve the quality of my work. I also thank Pierre-François ROUX and Alexandrine GESRET for the many fruitful discussions that we had.

I would also like to thank the members of my jury. It was my great honor that Georg

Acknowledgments

DRESEN and Hideo AOCHI accepted to review my thesis in detail. I thank them in advance for their comments and recommendations. My sincere thanks also go to Jean SULEM, Frédéric CAPPA and Agnès HELMSTETTER for examining my work.

I am so grateful for the Geosciences center, and especially the geophysical team (Mark Noble, Alexandrine Gesret, Hervé Chauris, Pierre Dublanchet, Pierre-François Roux, Nidhal Belayouni and Véronique Lachasse). Thank you for welcoming me, and allowing me to conduct my thesis in very kind, friendly and warm conditions. I particularly thank Véronique Lachasse for always being there for me and for taking care of me when I twisted my ankle. I would also like to thank all my PhD colleagues for their friendship and support over the last three years: Yves Marie Batany, Emmanuel Cocher, Keurfon Lu, Yubing Li, Alexandre Kazantsev, Hao Jiang, Tianyou Zhou, Ahmed Jabrane, Milad Farshad (yes for a long time I was the only girl in the team!). And finally I thank deeply Rita Abou Jaoude for accompanying me during our long journey together. I look forward to being there for you and with you at the day of your PhD defense.

I cannot forget the support of my family. I would not be here if it was not for my parents. Mom and Dad, thank you for your continuous encouragement, unconditional love and for always reminding me how proud you are of my achievements. Thank you for always having the curiosity to understand what I do. This means a lot to me. I also thank my brother and his wife for supporting me, and for constantly visiting me in France whenever they had the chance, the time that we spent together and the memories that we made mean a lot to me.

Last but not least my greatest gratitude goes to my fiancée. You are the reason why I am now at the finishing line of this PhD. Thank you for supporting me throughout my ups and downs. Thank you for believing in me, even when I had doubts in myself. Thank you for always having the time to listen and for being so understanding. I can never forget that you almost memorized my speech of “Ma Thèse en 180 secondes”, you were able to explain the context of my thesis in my place! Finally, thank you for always being there for me, many rough days have passed unnoticed because of you.

Abstract

This PhD thesis is dedicated to the study of injection induced fault reactivation using a coupled hydro-mechanical rate and state model of a fault. Even though the principal mechanisms behind induced fault reactivation are well known, different aspects are not yet fully explored, nor understood. In the first part of this thesis, we explore successively the role of the injection protocol (in particular, injection maximum pressure and injection pressure rate), and the fault frictional parameters on the rate of induced events and their magnitude content, for different heterogeneous 2-D fault configurations. We first point out a temporal correlation between the seismicity rate and the pore pressure rate governing the fault. We then show a dependence of the rate and magnitude content of the seismic events on the injection parameters, as well as the existence of an important trade-off between them, which could not be addressed using the [Dietrich \(1994\)](#)'s seismicity rate model. Concerning the frictional parameters, we show that for the faults tested in this study, the ones having a more stable frictional behavior exhibit a lower induced seismicity rate and seismic moment released. In the last part of this study, the variation of the hydraulic diffusivity during fluid injection with shear slip and effective stress reduction is addressed. For this, we use laboratory injection experiments on an Andesite rock sample, during which the pore pressure was measured at two locations along the fault plane. In an inversion framework, we estimate the best model and the associated uncertainties of an effective diffusivity history that could explain the experimental data. Using this information, we could extend our hydro-mechanical model, which would allow the computation of pore pressure, diffusivity and slip changes along the experimental fault.

Keywords: Fault Reactivation, Fluid Injection, Rate and State Fault Numerical Model, Induced Seismicity, Laboratory Rock Mechanics Experiments, Permeability Enhancement.

Resume

Cette thèse est dédiée à l'étude de la réactivation de faille par injection de fluide, à l'aide d'un modèle hydro-mécanique de faille rate and state. Bien que les principaux mécanismes à l'origine de la réactivation de faille soient bien connus, différents aspects ne sont pas encore complètement explorés, ni compris. Dans la première partie de cette thèse, on explore le rôle du protocole d'injection (en particulier, la pression maximale et le taux de pression d'injection), ainsi que le rôle des paramètres de frottement sur le taux de sismicité et la distribution de magnitude, pour différents types de failles 2-D hétérogènes. On souligne d'abord une corrélation temporelle entre le taux de sismicité et le taux de pression de pore gouvernant la faille. On montre ensuite une dépendance du taux de sismicité ainsi que de la distribution des magnitudes sur les paramètres d'injection. Notamment, une compensation entre ces deux existe pour de grandes valeurs du taux de pression d'injection. Ce comportement ne peut pas être abordé par le taux de sismicité proposé par [Dietrich \(1994\)](#). En outre, on montre que les failles ayant un comportement de frottement plus stable présente un taux de sismicité et un moment sismique libéré plus faibles. Dans la dernière partie de cette étude, la variation de la diffusivité hydraulique au cours de l'injection de fluide avec l'accumulation du déplacement et la réduction de la contrainte normale effective sur la faille est abordée. Pour cela, on utilise des expériences d'injection (réalisées à l'échelle du laboratoire) sur un échantillon d'andésite, où la pression de pore est mesurée à deux endroits le long de la faille. En appliquant des méthodes d'inversion, on estime le meilleur modèle de diffusivité hydraulique et les incertitudes associés, pouvant expliquer les données expérimentales. Avec ces résultats, on peut étendre notre modèle hydro-mécanique, afin de pouvoir calculer la pression de pore, la diffusivité hydraulique et le déplacement accumulé sur la faille expérimentale.

Mots Clés: Réactivation de Faille, Injection de Fluide, Modèle Numérique de Faille Rate and State, Sismicité induite, Expériences de Laboratoire, Évolution de Perméabilité.

Contents

Acknowledgments	iii
Abstract	v
Resume	vii
Chapter 1 Introduction – Fault reactivation due to fluid injection	1
1.1 General Introduction	3
1.2 Industrial Injection Projects and Fault Activation	4
1.2.1 Waste Fluids Disposal (WD)	4
1.2.2 Production of Geothermal Energy (EGS)	4
1.2.3 Hydrofracturing (HF)	5
1.2.4 CO ₂ Injection	5
1.2.5 Secondary recovery of oil and gas or enhanced oil recovery (EOR)	5
1.3 Discrimination between Induced and Natural Seismicity	5
1.4 Observations of Injection Induced Fault Reactivation	7
1.4.1 Observations of Induced Earthquakes	7
1.4.2 Temporal Correlation and Post Shut-in Seismicity	15
1.4.3 Spatial Migration of events	18
1.4.4 Magnitude Content	19
1.4.5 Effect of Injection Parameters	21
1.4.6 Evidence of Induced Aseismic Motion	22
1.5 Managing Induced Seismicity	24
1.6 First Conceptual Models For Fluid Induced Fault Reactivation	27
1.7 Injection Experiments for Better Understanding Fault Reactivation and Induced Seismicity	30
1.7.1 Large Scale In-situ Injection Experiments	30
1.7.2 Decametric Scale Injection Experiments: Seismicity and Aseismic Slip	31
1.7.3 Small Scale Laboratory Injection Experiments	32
1.8 Contributions from different Numerical Modeling Approaches	36
1.8.1 Pressure diffusion based models	36
1.8.2 Injection into rock volumes with Coulomb failure criterion	38
1.8.3 Numerical models based on Fracture Mechanics	38
1.8.4 Models following the seismicity rate model proposed by Dietrich (1994)	39
1.8.5 Burridge-Knopoff based models (Burridge and Knopoff, 1967)	40

1.8.6	Frictional Fault Models	40
1.9	Research Motivation	42
1.10	Thesis and Manuscript Overview	44
Chapter 2 Effect of the injection scenario on the rate and magnitude content of injection-induced seismicity: Case of a heterogeneous fault		49
2.1	Abstract	51
2.2	Introduction	51
2.3	Model	53
2.4	Results	61
2.4.1	Background Seismicity	61
2.4.2	Response to Fluid Injection	61
2.4.3	Sensitivity Analysis	64
2.4.3.1	Choice of Injection Parameters	64
2.4.3.2	Time of Maximum Seismicity Rate and Seismicity Perturbation Duration	65
2.4.3.3	Seismicity Rate Increase	66
2.4.3.4	Magnitude Content	69
2.4.3.5	Seismic Moment Release and number of earthquakes during Phase I, Phase II, and Phase (I-II)	71
2.4.3.6	Change in Diffusive Boundary Conditions	73
2.5	Discussion	75
2.6	Conclusion	79
2.7	Appendix A: Analytical Solution of the Diffusion Equation	80
2.7.1	Injection Phase 1 ($t_i < t < t_r$):	80
2.7.2	Injection Phase 2 ($t_r < t$):	80
2.8	Appendix B: Estimation of the Background Stressing Rate	80
2.9	Appendix C: Analytical Seismicity Rate model following Dietrich (1994)	81
2.9.1	Injection Phase 1 ($t_i < t < t_r$):	82
2.9.2	Injection Phase 2 ($t_r < t$):	82
2.10	Supporting Information	82
Chapter 3 Sensitivity of Induced Seismic Activity to Fault Frictional Parameters		89
3.1	Introduction	91
3.2	Fault Configurations	93
3.3	Results	94
3.3.1	Quick Overview of the Background Seismicity	94
3.3.2	Seismic Response to Fluid Injection	96
3.3.2.1	Phase I	96
3.3.2.2	Phase II	100
3.4	Discussion	101
3.5	Conclusion	103
3.6	Supporting Information	103

Chapter 4 Deterministic and Probabilistic Inversions of Pore Pressure Diffusion: Application to Laboratory Injection Experiments	107
4.1 Introduction	109
4.2 Experimental Data	111
4.2.1 Experimental Setup	111
4.2.2 Experimental Protocol	113
4.2.3 Experimental Results	113
4.3 Methodology	115
4.3.1 Inverse Problem	115
4.3.2 Deterministic inversion	118
4.3.2.1 Adjoint State Method (Gradient method): Theory	118
4.3.2.2 Resolution of the Differential Equations	119
4.3.2.3 Numerical Implementation	120
4.3.3 Metropolis Hastings Algorithm	122
4.3.3.1 Theory and Resolution	122
4.3.3.2 Numerical Implementation	123
4.4 Application to the Experimental Data	125
4.4.1 Estimating the Best Model: Deterministic Approach	125
4.4.2 Estimating the Uncertainties: the MCMC approach	130
4.4.3 Discussion	134
4.5 Diffusivity, Displacement and Effective Stress	135
4.6 Conclusion and Perspectives	140
4.7 Appendix A: Development of the Adjoint State Method	141
 Chapter 5 Conclusions and Perspectives	 145
5.1 General Conclusion	147
5.2 Perspectives	148
5.2.1 Post Shut-in Seismicity	148
5.2.2 Modeling Induced Aseismic Motion and Second Order Triggering of Seismic Failure	149
5.2.3 Hydro-Mechanical Modeling of Laboratory Injection Tests	149
 Bibliography	 153

List of Figures

1.1	Discrimination of natural and induced seismicity, method by Davis and Frohlich (1993)	6
1.2	Induced earthquakes between 2006 and 2017 (Keranen and Weingarten, 2018)	8
1.3	Number of earthquakes per year in the central U.S (Source: USGS)	10
1.4	Temporal correlation (Dorbath <i>et al.</i> , 2009; Kozłowska <i>et al.</i> , 2018)	17
1.5	Migration of induced events away from the well (Shapiro <i>et al.</i> , 1997)	19
1.6	Change in magnitude content (Skoumal <i>et al.</i> , 2014; Schoenball <i>et al.</i> , 2015; Goebel <i>et al.</i> , 2016a; Goebel <i>et al.</i> , 2016b)	20
1.7	Maximum magnitude and injected volume (McGarr, 2014; Van der Elst <i>et al.</i> , 2016)	21
1.8	Effect of injection parameters on features of induced seismicity (Raleigh <i>et al.</i> , 1976; Langenbruch <i>et al.</i> , 2018)	23
1.9	Evidence of aseismic deformation during the Brawly swarm in 2012 (Wei <i>et al.</i> , 2015)	24
1.10	Traffic light systems and earthquake magnitudes (Deichman and Giardini, 2009; Kwiatek <i>et al.</i> , 2019)	26
1.11	Mechanisms for inducing earthquakes (Ellsworth, 2013)	27
1.12	Shear stress as a function of normal stress for a variety of rock types Byerlee (1978)	28
1.13	Conceptual model of induced fault reactivation.	29
1.14	Evidence of aseismic slip from in-situ injection experiments (Guglielmi <i>et al.</i> , 2015b)	32
1.15	Proposed model for injection induced seismicity (De Barros <i>et al.</i> , 2018)	33
1.16	Injection energy plotted against seismic energy (Goodfellow <i>et al.</i> , 2015)	34
1.17	Sketch of fluid injection and fluid flow into a rock medium containing pre-existing fractures.	37
2.1	Fault Model	55
2.2	Pore pressure diffusion	58
2.3	Seismic activity: before and during fluid injection	63
2.4	Time of maximum seismicity rate and seismicity perturbation duration	66
2.5	Dependence of the seismicity rate increase on the injection parameters	68
2.6	Dependence of the moment magnitude distribution on the injection parameters	70
2.7	Evolution of the b -value with the injection parameters	72
2.8	Induced number and rate of earthquakes	74

2.9	Estimation of the background stressing rate	81
2.10	Time series of the moment magnitude M_w for different injection scenarios.	83
2.11	Time series of the cumulative number of earthquakes and the seismic moment for different injection scenarios.	84
2.12	Seismicity rate and injection history for different injection scenario, part 1.	85
2.13	Seismicity rate and injection history for different injection scenario, part 2.	86
2.14	Comparison between different boundary conditions.	87
3.1	Fault configurations: Along strike distribution of the critical slip distance d_c and the ratio of frictional parameters a/b	95
3.2	Dependence of the seismicity rate increase on the injection parameters for different fault configurations.	98
3.3	Variation of the average seismic moment rate with the injection parameters for different fault configurations.	99
3.4	Number of earthquakes and moment magnitude released during Phase II of injection, for the different fault configurations.	101
3.5	Background seismicity for the different fault configurations.	104
3.6	Dependence of the magnitude distribution on the injection parameters, for the different fault configurations.	105
3.7	Spatial distribution of the seismic rupture for fault configuration 5.	106
4.1	Experimental Setup.	112
4.2	Experimental results: pressure and average displacement	114
4.3	Experimental results: Deformation	116
4.4	Flow Chart: Deterministic approach	121
4.5	Flow Chart: Metropolis Hastings Method	124
4.6	Results of the Deterministic Approach for the experiment at $P_c = 30$ MPa.	127
4.8	Results of the Deterministic Approach for the experiment at $P_c = 95$ MPa.	128
4.9	Results of the Deterministic Approach for the experiment at $P_c = 60$ MPa.	129
4.11	Results of the MCMC Method for the experiment at $P_c = 30$ MPa.	131
4.12	Results of the MCMC Method for the experiment at $P_c = 60$ MPa.	132
4.13	Results of the MCMC Method for the experiment at $P_c = 95$ MPa.	133
4.14	Diffusivity and Effective Stress	136
4.15	Relationship between the square of the ratio of the hydraulic diffusivity to the initial diffusivity and the logarithm of the ratio of the mean effective stress to the initial effective stress: at 30 MPa in the range [300 – 700] seconds, 60 MPa in the range [700 – 1400] seconds and 95 MPa in the range [2000 – 4200] seconds. Different colors refer to the different confining pressure values. Diffusivity values are issued from the deterministic method.	138
4.16	Diffusivity and Displacement	139
4.17	Validation of the Gradient Estimation	144
5.1	Numerical hydro-mechanical modeling of the laboratory injection test at 30 MPa of confining pressure.	150

List of Tables

1.1	List of potentially induced earthquakes	16
1.2	List of the main components of some frictional fault models.	41
2.1	Numerical Simulations: List of physical parameters	60
3.1	Characteristics of the different fault configurations.	94
3.2	Background seismicity for the different fault configurations.	96
4.1	Laboratory Injection Experiment: List of geometrical and mechanical parameters.	111
4.2	Laboratory Injection Experiment: List of experimental parameters.	113

Chapter 1

Introduction – Fault reactivation due to fluid injection

Contents

1.1	General Introduction	3
1.2	Industrial Injection Projects and Fault Activation	4
1.2.1	Waste Fluids Disposal (WD)	4
1.2.2	Production of Geothermal Energy (EGS)	4
1.2.3	Hydrofracturing (HF)	5
1.2.4	CO ₂ Injection	5
1.2.5	Secondary recovery of oil and gas or enhanced oil recovery (EOR)	5
1.3	Discrimination between Induced and Natural Seismicity	5
1.4	Observations of Injection Induced Fault Reactivation	7
1.4.1	Observations of Induced Earthquakes	7
1.4.2	Temporal Correlation and Post Shut-in Seismicity	15
1.4.3	Spatial Migration of events	18
1.4.4	Magnitude Content	19
1.4.5	Effect of Injection Parameters	21
1.4.6	Evidence of Induced Aseismic Motion	22
1.5	Managing Induced Seismicity	24
1.6	First Conceptual Models For Fluid Induced Fault Reactivation	27
1.7	Injection Experiments for Better Understanding Fault Reactivation and Induced Seismicity	30
1.7.1	Large Scale In-situ Injection Experiments	30
1.7.2	Decametric Scale Injection Experiments: Seismicity and Aseismic Slip	31
1.7.3	Small Scale Laboratory Injection Experiments	32
1.8	Contributions from different Numerical Modeling Approaches	36
1.8.1	Pressure diffusion based models	36
1.8.2	Injection into rock volumes with Coulomb failure criterion	38
1.8.3	Numerical models based on Fracture Mechanics	38

1.8.4	Models following the seismicity rate model proposed by Dietrich (1994)	39
1.8.5	Burridge-Knopoff based models (Burridge and Knopoff, 1967)	40
1.8.6	Frictional Fault Models	40
1.9	Research Motivation	42
1.10	Thesis and Manuscript Overview	44

Résumé du Chapitre 1 en Français

Certaines activités industrielles peuvent activer des failles pré-existantes et induire du glissement lent (asismique) ou du glissement rapide (sismique) dans le cas des séismes. Parmi ces activités industrielles, on peut citer: les activités minières, le remplissage des grands lacs de barrage ou l'injection de fluide dans le sous-sol associé à des projets d'énergie, comme par exemple la géothermie. Cependant l'injection de fluide présente le plus grand risque sismique, comme elle était la cause de plusieurs grands séismes induits, à titre d'exemple: le séisme de magnitude 5.5 à Denver Colorado en 1967, le séisme de magnitude 5.7 à Prague Oklahoma en 2011 et le séisme de magnitude 5.5 à Pohang City en Corée du Sud. Pour cette raison, on s'intéresse dans cette thèse à l'étude de la réactivation des failles par injection de fluides.

Dans ce chapitre d'introduction, je présente l'état de l'art sur (1) les différentes activités industrielles d'injection de fluide dans le sous-sol qui engendrent une sismicité induite, (2) les méthodes actuelles de discrimination entre sismicité naturelle et induite, (3) les observations de cas réels ainsi que les différentes caractéristiques de la sismicité induite, (4) les méthodes actuelles et les efforts visant à minimiser le risque de la sismicité induite. Ensuite je présente (5) les premiers modèles de la réactivation induite des failles, (6) les différentes études expérimentales d'injection de fluide (à différentes échelles) et les différentes réponses qu'elles ont pu apporter, ainsi que (7) les différents modèles numériques proposés et leur contributions majeures. Finalement, j'expose (8) mes motivations pour ce travail de recherche, ainsi que (9) l'organisation de la thèse et mes contributions majeures.

1.1 General Introduction

We say that a fault is reactivated when slip nucleates along it. If the slip is fast, often called dynamic slip, it can generate seismic waves that can reach the earth's surface. This is what we call a seismic event or earthquake. On the other hand, if the slip is slow, it does not generate any seismic waves, and is called slow slip or aseismic slip.

A seismic event is characterized by the surface of the rupture S and the rupture displacement δ . These parameters allow to estimate the seismic moment of the earthquake $M_0 = \mu S \delta$, where μ represents the rigidity of the rocks (Aki, 1966). The seismic moment is a measure of the energy released by the earthquake. Kanamori (1977) then introduced the earthquake magnitude M_w as a dimensionless characteristic to describe the size of the earthquake as follows: $M_w = 2/3 \log_{10}(M_0) - 6.07$, where M_0 is expressed in Newton meters.

Beyond natural conditions, it has been acknowledged that some human anthropogenic activities can lead to subsurface stress changes, reactivating pre-existing faults and inducing aseismic motion and minor as well as large earthquakes (Ellsworth, 2013; Keranen and Weingarten, 2018).

Induced seismic activity can be caused by mining activities (McGarr *et al.*, 2002; Gibowicz, 2009) like the Belchatow, Poland earthquake in 1980 (Gibowicz, 1984) and the magnitude 5.5 earthquake that stroke Orkney in South Africa in 2014 (Bateman, 2014). Impoundment of deep reservoir lakes in tectonically active regions can also invoke earthquakes that can be damaging (Simpson and Leith, 1988). For instance the deadly 1967 magnitude 6.3 earthquake in Koyna, India was directly related to Koyna dam reservoir (Gupta, 2002). The 1962 magnitude 6.1 earthquake in Hsingfenkiang, China, the 1963 magnitude 5.8 earthquake in Karib, Zimbabwe and the 1966 magnitude 6.3 earthquake in Kremasta, Greece were also linked to lake level changes (Simpson, 1976).

However, nearly the majority of induced earthquakes are linked to energy projects associated with fluid injection. This has become a focus of present research studies and discussions (Ellsworth, 2013), and it is likely to continue as further developments carry on in the industrial, energy related, activities (Keranen and Weingarten, 2018). Injection activities were responsible of some large induced seismic events, like the 1967 M_w 5.5 in Denver Colorado (Healy *et al.*, 1968; Davis and Frohlich, 1993), the 2011 M_w 5.7 earthquake in Prague Oklahoma (Keranen *et al.*, 2013; Van der Elst *et al.*, 2013; McGarr, 2014; Sumy *et al.*, 2014) and the 2017 M_w 5.5 earthquake in Pohang city, South Korea (Kim *et al.*, 2018; Grigoli *et al.*, 2018).

Nonetheless, induced seismic events are not the only seismic outcome from fluid injection, it may sometimes induce some aseismic slip, which was observed during in-situ injection experiments (Guglielmi *et al.*, 2015b; Duboeuf *et al.*, 2017) as well as during real injection activities (Bourouis and Bernard, 2007; Wei *et al.*, 2015; Cornet, 2016). In

this case, induced aseismic slip is suspected to trigger earthquakes as an indirect effect of fluid injection (De Barros *et al.*, 2018).

As injection activities appear to pose the higher risk on seismic hazard, we focus in this thesis on fault reactivation due to fluid injection. The induced fault reactivation is not yet controlled nor fully understood. The aim of this chapter is to present a broad, but not exhaustive, (1) review of different industrial injection activities inducing seismicity, (2) current methods to discriminate between natural and induced seismicity, (3) observations made from real cases, (4) efforts to manage induced seismicity and minimize its risk, (5) the first conceptual models for fluid induced fault reactivation, (6) advances from injection experiments at different scales, and (7) contributions from previous numerical modeling studies. We then (8) expose our motivations for this work, (9) present the thesis organization, and finally (10) point out our major contributions.

1.2 Industrial Injection Projects and Fault Activation

Several industrial injection projects give rise to micro-seismicity as well as to some large seismic events. They do not pose the same risk to seismic hazard though.

1.2.1 Waste Fluids Disposal (WD)

Disposal of waste fluids is widely used in the United States (Ellsworth, 2013), often related to hydraulic fracturing projects. It is suspected to be responsible for the large increase in the seismicity rate in the Central U.S. (Oklahoma, Arkansas, Colorado, Kansas) (Keranen *et al.*, 2014; Rubinstein and Mahani, 2015; Goebel *et al.*, 2016a), as well as for some of the largest induced earthquakes (Keranen *et al.*, 2014; Rubinstein and Mahani, 2015; Yeck *et al.*, 2016). Some authors suggest that among the different injection activities waste fluid disposal poses the highest risk to seismic hazard as it operates for longer times (Ellsworth, 2013), and it injects a large volume of fluids (Horton, 2012; Keranen *et al.*, 2013; Frohlich *et al.*, 2014; Rubinstein *et al.*, 2014).

1.2.2 Production of Geothermal Energy (EGS)

Production of geothermal energy takes part of the sustainable energy plan and is vastly used worldwide. However, geothermal systems were responsible for induced seismic swarms in Krafla (Tang *et al.*, 2008; Evans *et al.*, 2012) and Hengill (Bjornsson, 2004; Axelsson, 2006) in Iceland, in Soutz-sous-Forêt, France with magnitudes up to 2.9 (Majer *et al.*, 2007; Dorbath *et al.*, 2009) and in the Rittershoffen deep geothermal reservoir in Northeast of France (Lengline *et al.*, 2017), as well as large earthquakes, for instance the 1982 magnitude 4.6 earthquake in Geysers, United States (Majer *et al.*, 2007) or the four magnitude 3 earthquakes in 2006 at 3 km depth under the city of Basel in Switzerland (Deichman and Giardini, 2009) that lead to the abandonment of the project, the magnitude 3.5 earthquake in 2013 in St. Gallen, Switzerland (Diehl *et al.*, 2017),

and recently the magnitude 5.4 earthquake in 2017 near Pohang City (Kim *et al.*, 2018; Grigoli *et al.*, 2018).

1.2.3 Hydrofracturing (HF)

Hydraulic fracturing of rocks is used to enhance the permeability of reservoirs (Holland, 2011; Kanamori and Hauksson, 1992). Among many others, it induced a series of earthquakes with a maximum magnitude of 2.3 near Blackpool, United Kingdom (Green *et al.*, 2012), the magnitude 3.8 earthquake in the Horn River Basin of British Columbia that was felt by local population (Farahbod *et al.*, 2015) and the magnitude 4.2 earthquake in Fox Creek Alberta in Western Canada (Atkinson *et al.*, 2016). Shapiro *et al.* (2010) argues that it poses lower probability of inducing large events than in waste fluid disposal and production of geothermal energy as hydraulic fracturing activities operate for a short duration and do not inject large volume of fluids.

1.2.4 CO₂ Injection

CO₂ is injected into deep formations for permanent carbon capture and storage (CCS). Even though it poses non negligible seismic hazard, there exists to few projects (Zobak and Gorelick, 2012). According to Rutqvist *et al.* (2016), no felt seismic event was recorded to date resulting from CO₂ storage projects, even though CO₂ injection in the Cogdell field was suspected to have induced the 2011 magnitude 4.4 earthquake near Snyder, Texas (Gan and Frohlich, 2013).

1.2.5 Secondary recovery of oil and gas or enhanced oil recovery (EOR)

Secondary recovery of oil and gas can also invoke earthquakes (Davis and Pennington, 1989), mainly low magnitude earthquakes too small to be felt (McGarr *et al.*, 2015). It was responsible of a series of small (magnitude lower than 3.5) and shallow earthquakes due to the extraction of natural gas in the Netherlands from shallow deposits (Van Eck *et al.*, 2006).

1.3 Discrimination between Induced and Natural Seismicity

The identification of an induced event may be a complicated job, especially in tectonically active regions (Goebel *et al.*, 2016b), in which many naturally seismic sequences occur. This is particularly the case, if standards seismicity catalogs with high magnitude of completeness are used. Davis and Frohlich (1993) proposed a list of criteria to evaluate the nature of an event, or to assess the seismic hazard of a future project. In the case of a past event, these criteria depend on the background seismicity, the injection practices and the temporal and spatial correlation between the injection activity and the recorded seismicity. The method is presented in Figure 1.1 and consists of a list of “yes” or “no” questions, to which the user answers. A simple count in the end of all the different answers gives an insight on the nature of the seismic event in question. However, in this

method each question is treated equally, regarding its actual importance, without any information about the uncertainties or the evidence. This is why [Verdon et al. \(2019\)](#) extended this method by replacing the “yes” or “no” questions with positive and negative scores, that are modulated with respect to the importance of the question and to the degree of uncertainty. This method allows to estimate an induced assessment ratio that indicates whether the event is induced or not, and an evidence strength ratio that gives an idea about the uncertainty of the result.

Seven Questions Forming a Profile of a Seismic Sequence

Question	Earthquakes Clearly NOT Induced	Earthquakes Clearly Induced	I Denver, Colorado	II Painesville Ohio
<i>Background Seismicity</i>				
1 Are these events the first known earthquakes of this character in the region?	NO	YES	YES	NO
<i>Temporal Correlation</i>				
2 Is there a clear correlation between injection and seismicity	NO	YES	YES	NO
<i>Spatial Correlation</i>				
3a Are epicenters near wells (within 5 km)?	NO	YES	YES	YES?
3b Do some earthquakes occur at or near injection depths?	NO	YES	YES	YES?
3c If not, are there known geologic structures that may channel flow to sites of earthquakes?	NO	YES	NO?	NO?
<i>Injection Practices</i>				
4a Are changes in fluid pressure at well bottoms sufficient to encourage seismicity?	NO	YES	YES	YES
4b Are changes in fluid pressure at hypocentral locations sufficient to encourage seismicity?	NO	YES	YES?	NO?
TOTAL "YES" ANSWERS	0	7	6	3

Figure 1.1 – Discrimination of natural and induced seismicity: Series of seven “yes” or “no” questions to assess whether a certain earthquake was induced by fluid injection activities, from ([Davis and Frohlich, 1993](#)).

Systematic differences in the seismicity rate between natural and induced seismic activities in Oklahoma and Arkansas were reported, typically an increase in background seismicity and a change in the fraction of main shocks ([Llenos and Michael, 2013](#)). In the same spirit, [Goebel et al. \(2016a\)](#) proposed a statistical approach based on the concept

of clustering in time and magnitude, relying on the background seismicity rate and the magnitude content of the seismic events. The latter is generally characterized by the slope, called b-value, of the magnitude frequency distribution: $\log(N(m > M)) = a - bM$, where N is the number of earthquakes per unit of time having a magnitude $m > M$, a is a background seismicity indicator and b represents the ratio between large and small earthquakes and is typically around 1 for natural seismicity (Gutenberg and Richter, 1954). Goebel *et al.* (2016a) argued that an increase in the background seismicity rate and a decrease of the b-value could indicate the fault reactivation through induced seismicity. However, no difference in the magnitude distribution and inter-event times between natural and induced seismicity was observed for the Coso geothermal field in California (Schoenball *et al.*, 2015).

1.4 Observations of Injection Induced Fault Reactivation

1.4.1 Observations of Induced Earthquakes

As mentioned before injection induced seismicity has become an important subject of research and discussion worldwide, as industrial injection activities are inducing micro-seismicity as well as large seismic events all over the globe. In an annual review about induced seismicity, Keranen and Weingarten (2018) presented a map with the location of injection induced earthquakes between 2006 and 2017 in the United States, Canada and Europe (Figure 1.2), pointing out the severity of the situation. In this section, we attempt to briefly review some of the major induced (or potentially induced) seismic events by fluid injection activities, and expose the main reasons of why they were suspected to be induced.

Denver Colorado, United States

One of the first well documented cases of injection induced seismicity was in Rocky Mountain Arsenal in Denver Colorado, where waste contaminated water was injected into a deep well under pressure from 1962 to 1966, with a one year shut in period between 1963 and 1964 (Evans, 1966; Healy *et al.*, 1968). 710 earthquakes with magnitudes in the range $[0.7 - 4.3]$ were recorded during the injection period between 1962 and 1965 within an 8 km radius from the well (Evans, 1966). This seismic sequence was suspected to be injection-induced due to the lack of evidence of similar seismic activity in the area before the waste injection started in 1962 (Healy *et al.*, 1968). Moreover, Evans (1966) found a correlation between the average monthly injection volume and earthquake frequency. Seismic activity did not stop however after injection shut-in in February 1966, earthquakes continued at an average of 4 to 71 earthquakes per month, suggesting a link between the bottom well fluid pressure and the level of seismic activity (Healy *et al.*, 1968). The three largest earthquakes induced were recorded in 1967, 18 months after injection ceased, with a maximum magnitude of 5.5 (Hermann *et al.*, 1981). In an attempt to better understand the relation between the pore pressure and the frequency of induced earthquakes, an in-situ injection experiment was conducted at the Rangely oil field in Denver Colorado in 1969. This will be discussed in section 1.7.1.

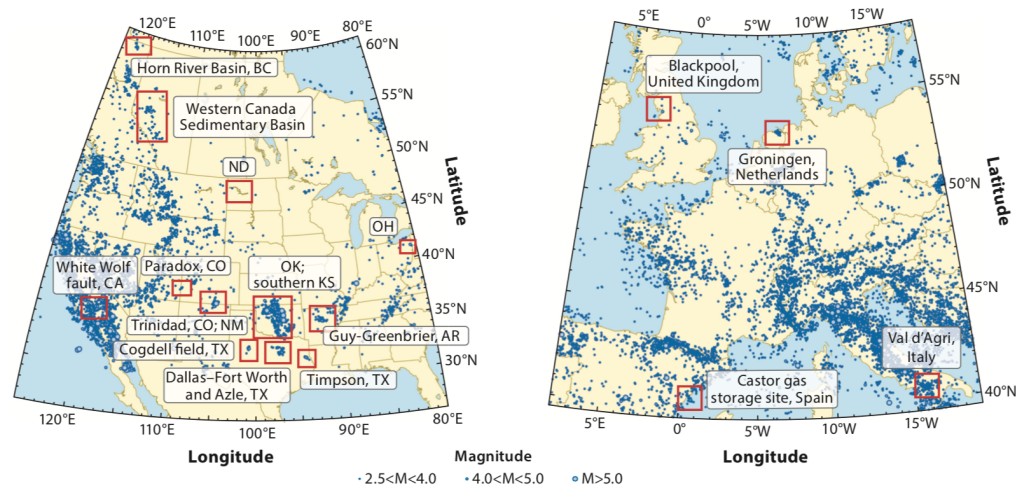


Figure 1.2 – Locations of some induced earthquakes since 2006 and up to 2017 for the United States and Canada (left panel) and Europe (right panel), (Keranen and Weingarten, 2018)

Texas, United States

Injection of fluids for secondary recovery of oil in the Cogdell oil field in West of Texas (between 1957 and 1982) led to a sequence of induced earthquakes that started in 1974 and lasted for about 8 years (Davis and Pennington, 1989). Even though a long time delay, of around 17 years, was observed between the start of injection and the onset of seismic activity, the earthquakes occurred within an array of injection wells, and thus they were suspected to be induced by the injection activities. Davis and Pennington (1989) argued that time is needed for fluid pressure to build up and reach a critical value on a pre-existing fault which could explain the observed time lag. No significant seismic activity was detected in the area after injection stopped in 1982. However, starting in 2004 CO₂ was injected into the Cogdell field, and was suspected to have induced a seismic sequence of 93 earthquakes between 2009 and 2011, with the largest being the 2011 M_w 4.4 earthquake near Snyder. The earthquake epicenters were spread within a 2 km radius area from actively injection wells, and correlated in time with significant increases in CO₂ injection (Gan and Frohlich, 2013).

Hydraulic fracturing operations near the Dallas-Fort Worth Airport in Texas, an area with no previous historical earthquakes, induced a sequence of 10 small earthquakes in 2008 that were felt by the local population. The recorded earthquakes were less than 500 meters away and 200 meters deeper than the injection well (Frohlich *et al.*, 2011). On the other hand, earthquake activity began only 6 weeks after hydraulic fracturing started in Barnett Shale Texas in 2009, within 3.3 km of one or more of the high rate injection wells, while no seismicity was recorded next to other high rate injection wells

(Frohlich, 2012). Analyzing the seismic activity induced in this area between 2009 and 2011, Frohlich (2012) found that increasing injection rate beyond a critical site dependent rate can induce earthquakes if the fluid can reach a suitably oriented fault. Moreover, seismic activity continued in Barnett Shale long after injection stopped in 2009. According to Shapiro and Dinske (2009) post injection seismicity in this case corresponds to a non-linear pressure diffusion throughout the medium surrounding the fault, accompanied by permeability enhancement.

Oklahoma, United States

Oklahoma and the Central U.S. have become one of the major evidence of injection induced seismicity and it caught the attention of several researchers and motivated different observational, theoretical and numerical studies (e.g. Keranen *et al.* (2013), Ellsworth (2013), Keranen *et al.* (2014), Goebel *et al.* (2016a), Langenbruch and Zoback (2016), Yeck *et al.* (2016), Schoenball and Ellsworth (2017), Schoenball *et al.* (2018), Langenbruch *et al.* (2018), Norbeck and Rubinstein (2018) and Johann *et al.* (2018)). Disposal of waste fluids via injection started in 1993 at zero well head pressure and then the latter was increased in steps of around 0.2 MPa in 2001 reaching 3.6 MPa in 2006 (Keranen *et al.*, 2013). Figure 1.3 represents the diagram of the number of earthquakes per year with magnitude three or larger. It shows that the Central U.S. had a low background seismicity rate with an average of 20 – 25 magnitude three or larger earthquakes per year, but then seismic activity experienced a very large increase in 2009 and peaked in 2015, with a total of 3427 ($M \geq 3$) earthquakes between 2009 and 2018. Seismic activity within Oklahoma experienced a 40 fold increase as compared to seismicity between 1976 and 2007 (Keranen *et al.*, 2014). According to McGarr *et al.* (2015), the frequency of earthquakes in Oklahoma with magnitudes greater than 3 ($M_w \geq 3$) exceeded the one in California in 2014, one of the most active seismic regions in the United States (Alden, 2018). This abrupt change in seismicity rate is one of the main arguments to prove that the increase in seismicity in this area is mainly related to waste disposal activities. Seismic activity in Central U.S. started near injection wells and then experienced a broad spatial spread, with events migrating northeast, away from the injection wells, at 0.1 km per day (Keranen *et al.*, 2014). More than 200 earthquakes were recorded 20 km East of Oklahoma City between 2009 and 2011.

Beyond the large increase in seismicity rate, several large earthquakes are potentially induced by the fluid injection activities in Oklahoma, like the M_w 5.7 earthquake sequence in November 2011 near Prague, 5 years after the largest increase in well head pressure, and that was felt in 17 states (Keranen *et al.*, 2013), and more recently the 2016 M_w 5.1 near Fairview, located 12 km from high rate injection wells and that was a part of a two years seismic sequence composed by 63 foreshocks and 89 aftershocks, with moderate magnitudes (Yeck *et al.*, 2016; McGarr and Barbour, 2017) and the 2016 M_w 5.8 earthquake in Pawnee, felt across 7 midwestern states, and that was part of a seismic sequence of small earthquakes (Yeck *et al.*, 2016).

Moreover, a short hydraulic fracturing operation took place in January 2011 in South Central Oklahoma and lasted 7 days. A sequence of 116 earthquakes was detected in the

area. It started 24 hours after the hydraulic fracturing operation began, with magnitudes ranging between 0.6 and 2.9, and presented a strong temporal and spatial correlation with the injection and thus [Holland \(2013\)](#) argues that this sequence is not related to the waste disposal activity but induced by the fracking activity.

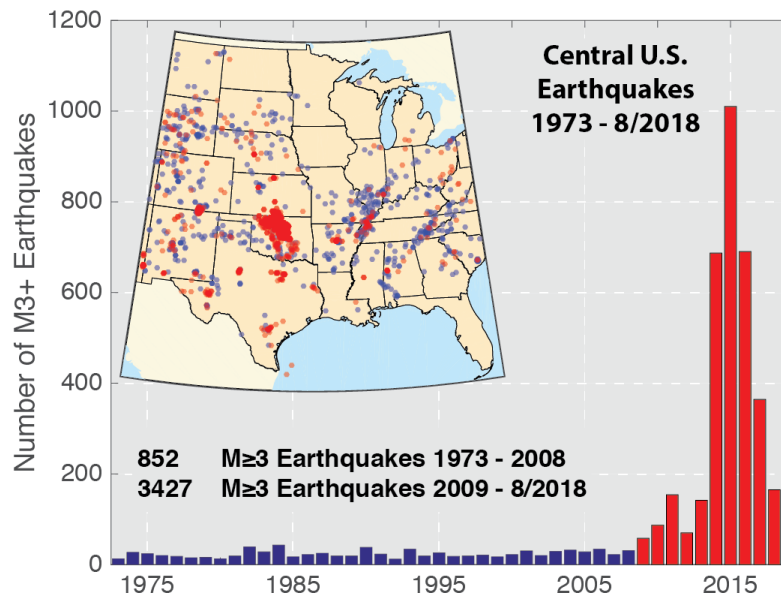


Figure 1.3 – Diagram of the number of earthquakes per year in the central U.S. The area which experienced the largest increase in activity since 2009 is the red cluster at the center of the map. (Source: USGS - <https://earthquake.usgs.gov/research/induced/overview.php>)

Southern Kansas, United States

Disposal of waste fluids in Southern Kansas led the seismic activity to rise dramatically in 2013 with around 1000 earthquakes having magnitudes larger than 2 and 6 with magnitudes exceeding 4, recorded between 2013 and 2016 ([Rubinstein *et al.*, 2018](#)). The 4.9 Milan earthquake was the largest in the sequence ([Choy *et al.*, 2016](#)). Those events were considered as injection induced since no earthquakes of magnitude 4 were ever recorded in the area from 1974 to 2012; moreover the seismic activity exhibited temporal correlation with the injected volume and a spatial correlation with the injection wells ([Rubinstein *et al.*, 2018](#)). Shortly after injection stopped, seismicity subsided near the high rate injection wells, however it remained long after away from the well.

Arkansas, United States

A swarm of hundreds of earthquakes began only a few months after disposal of hydrofracturing waste fluids started in 2009 in Arkansas. The reactivation of the Guy-Greenbrier fault led to 3 large earthquakes (M_w 4, 3.8, 3.9) in 2010 that were widely felt

across the state. A second swarm initiated in February 2011 with the largest earthquake in the sequence being the M_w 4.7 earthquake. The seismicity rate showed a strong correlation with the injected volume (Horton, 2012). This rose the public concern and led to the shut down of the project. Even though earthquakes continued after shut down, the seismicity rate and the magnitude of the events dropped within three months.

Ohio, United States

Wastewater from hydraulic fracturing in the Northeastern U.S were transported and injected near Youngstown Ohio, a region with no known earthquakes in the past, under high pressure up to 17 MPa. This led to a seismic sequence that initiated 13 days after injection started and were composed of 167 induced earthquake during injection in 2011 with magnitudes up to 3.9, that initiated close to the well and then migrated away (Kim, 2013). Frequency of earthquakes was mainly correlated with the daily injection volume and injection pressure and several short period of quiescence were observed following shut-in during the holidays and weekends. Post injection seismicity continued but decreased in rate and magnitudes within month after shut in. The M_w 3.9 earthquake, largest in the sequence, was recorded 24 hours after shut in though (Kim, 2013; Skoumal *et al.*, 2014).

Different sequences of induced seismic activity stroke the eastern part of Ohio between 2013 and 2015, due to hydraulic fracturing in the region. Among them: 1) Poland Township from 4 to 12 March 2014, where events with magnitudes up to M_w 3 nucleated 0.8 km away from the injection well and migrated 600 meters away (Skoumal *et al.*, 2015b), 2) Belmont & Guernsey Counties, an area with no prior documented earthquakes, a seismic swarm with magnitudes up to M_w 2.6 was detected in May 2014, 5 km away from 4 injection wells, and that correlated in time with the hydraulic fracturing operations in the area (Skoumal *et al.*, 2015a), 3) Harrison County where seismic swarms were detected following hydraulic fracturing operations in September 2013 and between August and November 2015 with magnitudes up to M_w 2.6 (Friberg *et al.*, 2014; Skoumal *et al.*, 2016). A very short time lag of around 2 hours was observed in this area between the seismic swarms and the different hydraulic fracturing operations (refer to Figure 1.4.a) (Kozłowska *et al.*, 2018).

California, United States

According to Goebel *et al.* (2016b), it is very hard to detect induced seismicity in regions like California as the tectonic activity in the region is very high. However, he succeeded in correlating the White Wolf fault earthquake swarm in 2005 to wastewater disposal activity, where an abrupt increase in injection rate led to a large increase in seismicity rate, with 3 events recorded with magnitudes larger than 4, with the largest reaching 4.6. The sequence showed strong evidence of event migration away from the injection wells, as well as a change in the magnitude content with an increase in the frequency of large magnitudes: the Gutenberg-Richter b-value decreased from 1 (before injection started) to 0.6 (during injection), this is shown later in the manuscript in Figure 1.6.c. Goebel *et al.* (2016b) argued that this kind of seismic behavior points out the reactivation of the fault due to fluid injection and not tectonic loading.

Canada

Horn River Basin, British Columbia

Hydraulic fracturing operations were conducted in the Horn River Basin of Northeast British Columbia starting in late 2006, for regional shale gas development, which led to a large increase in the seismicity rate in the region, going from 24 event per year before hydraulic fracturing started to around 131 event per year in 2011 (peak period of hydraulic fracturing), with magnitudes increasing from 2.6 in 2006 to 3.6 in 2007 (BCOGC, 2012; Farahbod *et al.*, 2015).

Western Canada Sedimentary Basin

Atkinson *et al.* (2016) correlated the majority of the seismic activity since 2010 in Western Canada sedimentary basin, an area of previously low seismicity, to current hydraulic fracturing operations in the region, due to an observed temporal and spatial correlation between the two. The largest event of the seismic sequence was the 2015 M_w 4.1 earthquake in Fox Alberta, that was induced 8 days after the operations ended. Atkinson *et al.* (2016) also found that the maximum magnitude of induced events from hydraulic fracturing may not be associated to the fluid injected volume, as it was concluded for induced earthquakes from wastewater disposal (McGarr, 2014).

Iceland

Hengill

Two enhanced geothermal systems (EGS) sites were constructed North and South of the Hengill Volcano. Several induced seismic sequences were recorded during different stimulations. Among them: 1) A series of earthquakes were recorded during a stimulation of a 2.8 km deep well in the Hellisheidi field South of the volcano in 2003. The earthquakes were located at 4 to 6 km deep below the well, with magnitudes up to 2.4 (Bjornsson, 2004); 2) In February 2006 a 2 km deep well was stimulated over 3 days with pressures up to 1.8 MPa and several small events with magnitude up to 2 were recorded close to the well (Axelsson, 2006). Following another stimulation of this well that lasted 2.5 days, a seismic sequence of 50 events with magnitudes reaching 2.7 was recorded very close to the well at 2.5 km depth (Evans *et al.*, 2012).

Krafla

Following a geothermal stimulation in an EGS site in this area, an average of 4 events per day with magnitudes reaching 2 were recorded near the injection well (Tang *et al.*, 2008).

Blackpool, United Kingdom

Hydraulic fracturing for shale gas started in 2011 near Blackpool, United Kingdom. A nearby fault was reactivated due to a fluid leak off from the hydraulic fracture (Clarke *et al.*, 2014). The largest event in the sequence was the 2011 magnitude 2.3 earthquake, recorded 1.8 km away from the injection well (Wilson *et al.*, 2015) and it was the first felt

earthquake induced by hydraulic fracturing in Europe. This event was preceded though by a sequence of small magnitudes the day before very close to the injection well (Clarke *et al.*, 2014).

Groningen, Netherlands

Gas production in the Groningen gas field in Northern Netherlands started in 1963. The first recorded induced event was in 1991 with a magnitude of 2.4 (van Thienen-Visser and Breunese, 2015) and seismicity continued for over 10 years with an average of 5 events per year with magnitudes larger than 1.5. However, in 2003 the seismicity rate and the events magnitude started to increase (Muntendam-Bos and Waal, 2013). The largest event occurred in 2012 with a magnitude of 3.6 (van Thienen-Visser and Breunese, 2015), its intensity was high due to its shallow depth so it was widely felt by the population and led to extensive surface damage (TNO, 2013). Bourne *et al.* (2014) found that the compaction of the Groningen field was responsible in the change in seismic activity. Gas production activity was then reduced in the region with the highest compaction in 2014 and increased in other areas with relatively no compaction, which resulted in a slight reduction in seismicity (van Thienen-Visser and Breunese, 2015).

Soultz-sous-Forêt, France

An EGS site with 4 different wells (GPK1 - GPK2 - GPK3 - GPK4) was constructed in Soultz-sous-Forêt France. The site is located in a zone of minor natural earthquake hazard (Majer *et al.*, 2007). Several stimulations of the deep reservoirs were conducted over the years. The first successful one was in September and October 1993 for the well GPK1, during which around 2000 microseismic events were recorded in an area of 400 meter radius around the well, the largest event had a moment magnitude M_w of 1.9 (Cornet *et al.*, 1997). The well GPK2 was stimulated in 2000 for 7 days (Majer *et al.*, 2007), however this stimulation induced more than 700 seismic events with magnitudes exceeding 1 and the majority of the seismic moment released was through medium-size earthquakes (Dorbath *et al.*, 2009). The largest was of magnitude 2.4 and was felt by the population, and it was suspected to be related to sharp changes in injection pressures (Majer *et al.*, 2007). Seismic events continued after shut in but at a slower rate (refer to Figure 1.4.b). The next stimulation took place in 2003 for the well GPK3 and lasted 11 days. It induced only about 250 events with magnitudes larger than 1 (Dorbath *et al.*, 2009), however the maximum magnitude was exceeded with the M_w 2.9 earthquake that was induced 2 days after shut in (Majer *et al.*, 2007), as well the frequency of larger magnitudes increased. Majer *et al.* (2007) showed that a large fault intersects this well, and may be the reason behind the change in magnitude content with respect to the previous stimulation.

Basel, Switzerland

Water was injected under high pressure into permeable basement rocks beneath the city of Basel in Switzerland in the context of an EGS in 2006, which led the seismicity rate to increase from 4 events per year between 1984 and 2006 to around 195 events per year. The induced seismic sequence exhibited an event migration and included 3 consecutive earthquakes of magnitude 2.6, 2.7 and 3.4, that were felt distinctly in the urban area

of Basel. This led to the abandonment of the project. 4 additional earthquakes with magnitudes around 3 were recorded though from January to March 2007 (Deichman and Giardini, 2009). This case study will be further presented and developed in section 1.5 (see also Figure 1.10.b).

Landau, Germany

Landau in Germany which is a region with low seismic activity (Evans *et al.*, 2012) experienced a slight increase in its seismicity rate due to geothermal activity in Rhine Graben that started in 2007. During the early stages of the stimulation, no to little seismic activity was recorded (Baumgartner, 2012), however a sequence of small to moderate earthquakes (magnitudes between 1.5 and 2) were recorded near the well between February 2008 and May 2009 (Evans *et al.*, 2012). The largest event was the magnitude 2.7 earthquake in Landau, located 1.5 to 2 km North of the plant and was felt by the local population (Bonnemann *et al.*, 2010; Gaucher *et al.*, 2015b)

Southern Apennines, Italy

A series of seismic events with magnitudes lower than 2.2 was recorded starting in 2006, 4 days after the onset of waste water disposal operations in the Val d'Agri field, Italy (Valoroso *et al.*, 2009; Stabile *et al.*, 2014). The seismic sequence presented a swarm-type micro-seismicity with a large spatial cluster of 5 km wide and 1 to 5 km depth (Valoroso *et al.*, 2009) and showed a temporal correlation with the injection activity (Stabile *et al.*, 2014).

Helsinki, Finland

An EGS site was constructed near Helsinki, Finland with 6.4 km deep wells. It is the deepest EGS so far. The stimulation lasted 49 days in 2018. Real time seismic activity was well monitored and the injection rate was controlled to try to avoid inducing earthquakes with magnitudes exceeding 2: a low ratio of radiated energy to hydraulic energy input was maintained by reducing injection rate and increasing shut in periods between pumping phases (Kwiatek *et al.*, 2019). 43882 induced microseismic events were recorded over the stimulation period and 1 week after, with moment magnitudes varying between -0.5 and 1.9.

Pohang, South Korea

Hydraulic stimulation in an EGS site near Pohang City in South of Korea started in January 2016 and consisted of 4 different injection phases. Seismic activity was recorded with each phase, with a time lag of only a few days (Kim *et al.*, 2018), and then stopped after injection finished. The magnitudes of induced earthquakes increased with the volume of fluid injected leading to the magnitude 3.1 earthquake that was recorded in April 2017 (Kim *et al.*, 2018), and the magnitude 5.4 mainshock near Pohang City (Kim *et al.*, 2018; Grigoli *et al.*, 2018), suspected to be induced by the geothermal activity. If it is the case it is the largest and most damaging EQ related to an EGS site to date.

Cooper Basin, Australia

A geothermal stimulation took place near Cooper Basin in South Australia in late 2003. More than 2800 induced events were detected in the region (Soma *et al.*, 2004),

with magnitudes exceeding 3. The largest one was the M_w 3.7 recorded in 14 November 2003 (Majer *et al.*, 2007). The seismic activity correlated with the injection schedule, with a higher event rate when the injection rate was highest (Soma *et al.*, 2004).

We conclude this section with a non exhaustive list of potentially induced earthquakes with magnitudes exceeding 3 (Table 1.1).

We have presented so far a review of the major cases of induced seismicity. We will now discuss some common features between the different observations: (1) short or delayed time onset, (2) events spatial migration, (3) magnitude range of induced seismic sequences, (4) observed correlations with injection parameters, (5) and finally we will expose some observations regarding induced aseismic deformation and slip.

1.4.2 Temporal Correlation and Post Shut-in Seismicity

Variable time delays exist between the onset of induced seismicity and injection activity. For instance the seismic sequence near the Val d'Agri field in Italy initiated only 4 days after injection activity started (Valoroso *et al.*, 2009; Stabile *et al.*, 2014) and the one in Youngstown Ohio started 13 days after waste disposal activities started in the region (Kim, 2013). A very short time lag is also observed during hydraulic fracturing: 2 hours time lag in Ohio in 2013 (Kozłowska *et al.*, 2018), as shown in Figure 1.4.a for the induced seismicity in Harrison County, and 24 hours in California (Holland, 2013), or during geothermal operations (e.g. in Soultz-sous-Forêt Majer *et al.* (2007) and Dorbath *et al.* (2009) and Pohang Kim *et al.* (2018)). One reason behind the short time lag may be the high injection pressure. However, Kozłowska *et al.* (2018) argues that the seismicity triggered after 2 hours in Harrison County Ohio is faster than pressure diffusion and may be due to fast poro-elastic changes in pressure. On the other hand, a very long time lag is also observed in some cases, for example in the Codgell oil field in Texas the first event was recorded 18 years after injection activity started (Davis and Pennington, 1989). In this case, the pore pressure diffusion is expected to be very slow, mainly due to the existence of low permeability fluid baffles between the injection well and the neighbouring faults. This may lead the seismicity to occur even years after injection ends (Keranen and Weingarten, 2018).

Moreover, Schoenball *et al.* (2018) reported two temporal behaviors for the seismicity in Oklahoma and Southern Kansas for the different induced seismic sequences: one sequence was governed by a slow process, while another one was governed by a fast process.

Post Shut-in Seismicity

Post shut-in seismicity is vastly observed for fluid injection activity. High seismic activity was recorded for nearly two years after injection stopped in Denver Colorado (Healy *et al.*, 1968). Hsieh and Bredehoeft (1981) argued that pressure diffusion is the principal cause of post shut-in seismicity in this case because the fluid was injected into

M_w	Date	Location	Cause	Reference
5.5	1967	Denver, Colorado	WD	(Healy <i>et al.</i> , 1968; Davis and Frohlich, 1993)
3.7	2003	Cooper Basin, Australia	EGS	(Majer <i>et al.</i> , 2007)
4.6	2005	Central Valley, California	WD	(Goebel <i>et al.</i> , 2016b)
3.4	2007	Basel, Switzerland	EGS	(Deichman and Giardini, 2009)
3.3	2009	Dallas-Fort Worth, Texas	WD	(Frohlich <i>et al.</i> , 2011)
4	2011	Youngstown, Ohio	WD	(Kim, 2013; Skoumal <i>et al.</i> , 2014)
4.7	2011	Central Arkansas (Guy Arkansas)	WD	(Horton, 2012)
4.4	2011	Snyder, Texas	CO ₂ injection	(Gan and Frohlich, 2013)
4.8	2011	Fashioning, Texas	Production of gas	(Frohlich <i>et al.</i> , 2014)
5.7	2011	Prague, Oklahoma	WD	(Keranen <i>et al.</i> , 2013; Sumy <i>et al.</i> , 2014)
5.3	2011	Trinidad Colorado	WD	(Viegas <i>et al.</i> , 2012; Rubinstein <i>et al.</i> , 2012; Barnhart <i>et al.</i> , 2014)
3.8	2011	Horn River Basin, British Columbia	HF	(BCOGC, 2012; Farahbod <i>et al.</i> , 2015)
4.9	2012	East Texas	WD	(Brown and Frohlich, 2013)
3.6	2012	Groningen, Netherlands	Production of gas	(van Thienen-Visser and Breunese, 2015)
3.5	2013	Saint Gallen, Switzerland	EGS	(Edwards <i>et al.</i> , 2015)
4.1	2015	Fox Creek, Alberta, Canada	HF	(Atkinson <i>et al.</i> , 2016)
5.1	2016	Fairview, Oklahoma	WD	(McGarr and Barbour, 2017)
5.8	2016	Pawnee, Oklahoma	WD	(Yeck <i>et al.</i> , 2016)
5.5	2017	Pohang, South Korea	EGS	(Kim <i>et al.</i> , 2018; Grigoli <i>et al.</i> , 2018)

¹[*Note.*] WD = Waste Disposal; EGS = Enhanced Geothermal Systems; HF = Hydraulic Fracturing.

Table 1.1 – List (non exhaustive) of potentially induced large earthquakes ($M_w > 3$) by fluid injection

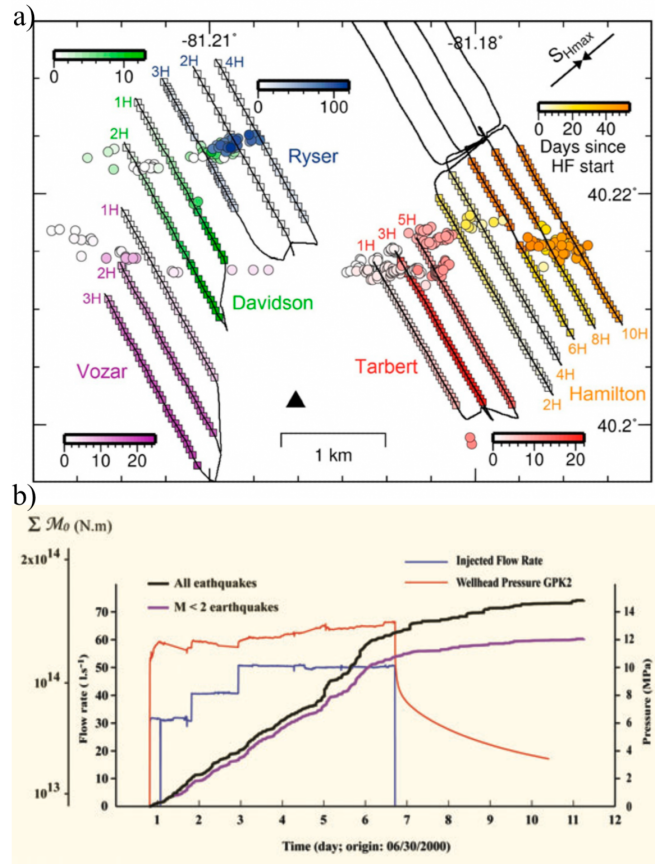


Figure 1.4 – Panel a: Map of hydraulic fracturing operations in Ohio where squares represent stimulation stages and circles represent induced seismicity. The time lag is represented by the color scale and shows how seismic activity starts very shortly following hydraulic operations, from (Kozłowska *et al.*, 2018). Panel b: Time series of the pressure (red), flow rate (blue) and cumulative seismic moment (black for all earthquakes and violet for earthquakes with magnitude less than 2) during the stimulation in Soutz-sous-Forêt in 2000: seismic activity continues for several days after stimulation ends, from (Dorbath *et al.*, 2009)

a fracture zone surrounded by low permeability crystalline basement. In Basel, several hours after the project shut down, a large M_L 3.4 was recorded 3 kilometers under the city (Deichman and Giardini, 2009) and micro-seismicity continued for two more years (Haring *et al.*, 2008; Deichman and Giardini, 2009). Post shut-in seismicity was also recorded for several days at the EGS site in Soutz-sous-Forêt as shown in Figure 1.4.b (Dorbath *et al.*, 2009). Moreover, it was observed that for geothermal projects, the largest magnitudes tend to occur shortly after the end of injection (Langenbruch and Shapiro, 2010).

It is very difficult to assess whether or not seismicity will continue after shut-in, and what between reservoir or injection properties could dominate the post shut-in seismic activity (Majer *et al.*, 2007). For instance,

- During the waste disposal activity in Youngstown Ohio in 2011, quiescence intervals were observed during short periods of no pumping at the wellhead during holidays. The observed quiescence period length decreased as the pressure at the wellhead and the injected volume increased. And after the final shut-in, where the pressure was at its highest (17 MPa), earthquakes continued at a smaller rate after shut-in with respect to during waste disposal activity (Kim, 2013).

This observation would suggest a correlation between shut-in seismicity and the injection pressure and injected volume. On the other hand,

- During hydraulic fracturing operation in the eastern part of Ohio in 2013, seismicity continued after shut-in for the deep seismic sequences, while it stopped for the shallow ones (Kozłowska *et al.*, 2018).
- During waste disposal activity in Arkansas, after injection shut-in in 2016 seismicity stopped in the vicinity of the well, but continued at larger distances 10 km away (Rubinstein *et al.*, 2018).

These observations in turn puts in evidence the effect of the reservoir parameters and permeability of the medium.

Finally, the characteristics of post-injection seismicity differ from one case to another. No systematic common observations were reported. As different parameters appear to influence post shut-in seismicity (injection pressure, volume, reservoir parameters and medium permeability), this issue remains to be further investigated and explored.

1.4.3 Spatial Migration of events

Spatial migration of events is commonly observed during injection induced seismic sequences (Rubinstein and Mahani, 2015). Earthquakes were recorded at least 10 km away from the injection well during the disposal of waste fluids in Denver, Colorado (Healy *et al.*, 1968; Hermann *et al.*, 1981; Hsieh and Bredehoeft, 1981). In Ohio, earthquakes migrated away from the well from the eastern part, close to the injection, of the fault to the western part (Kim, 2013). As for Oklahoma, earthquakes were recorded 20 km away from the well in 2014 (Keranen *et al.*, 2014), and continued to migrate until seismicity spread over an area of 200 by 200 km² (Schoenball and Ellsworth, 2017). Figures 1.5a and 1.5b illustrate the migration of the seismic events away from the well at the Fenton Hill experiment in 1983 and the Soultz-sous-Forêt experiment in 1993, respectively, reported by Shapiro *et al.* (1997, 2002).

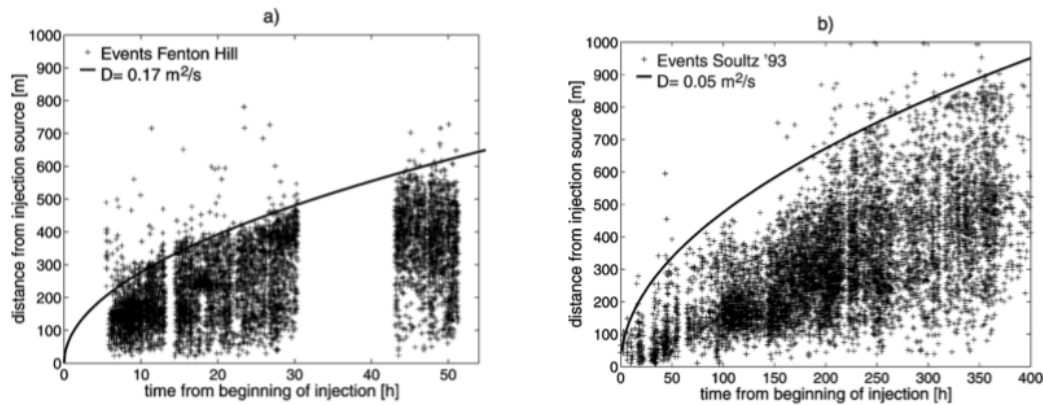


Figure 1.5 – Time series of the distance of recorded events with respect to the injection source for a) the Fenton Hill experiment in 1983 and b) the Soultz-sous-Forêt experiment in 1993, from (Shapiro *et al.*, 1997)

1.4.4 Magnitude Content

The magnitude content of a seismic sequence is often represented through the b-value of the Gutenberg-Richter magnitude distribution (Gutenberg and Richter, 1954), where a decrease of the b-value could be interpreted by an increase in the frequency of large magnitudes and an increase of the b-value indicates an increase in the frequency of lower magnitudes. Low b-values were observed for several cases of injection induced seismicity: (1) a low b-value (< 1) was observed for the entire seismic sequence in Ohio (Skoumal *et al.*, 2014) as shown in Figure 1.6.a; (2) a decrease in the b-value from 1.3 to 1.1 was associated with fault reactivation due to fluid injection in Oklahoma (Goebel *et al.*, 2016a) as shown in Figure 1.6.b; (3) a strong decrease of the b-value from 1 to 0.6 accompanied a strong deviation of the magnitude distribution from typical Gutenberg-Richter behavior during injection for the earthquake swarm in California in 2005 (Goebel *et al.*, 2016b) as shown in Figure 1.6.c; (4) and finally a decrease in the b-value was observed during hydraulic fracturing operations in Ohio in 2013 (Kozłowska *et al.*, 2018). Schoenball *et al.* (2015) argues that no change in the magnitude distribution was observed due to the geothermal activities near the Coso field in California (Figure 1.6.d), however he compared recorded seismicity data near the geothermal field to the data recorded away from the field, both recorded during injection without knowledge of the magnitude distribution prior to injection activities.

The magnitude content can also be characterized by the maximum magnitude of the events. Shapiro *et al.* (2007, 2010, 2011) argued that the size of the stimulated reservoir may control the size of the largest induced earthquake. However, McGarr (2014) proposed an upper bound limit to the seismic moment that depends especially of the total volume of fluid injected and showed that this limit is valid for the majority of injection induced seismicity cases (Figure 1.7.a). However, the recent 5.4 Pohang earthquake does not

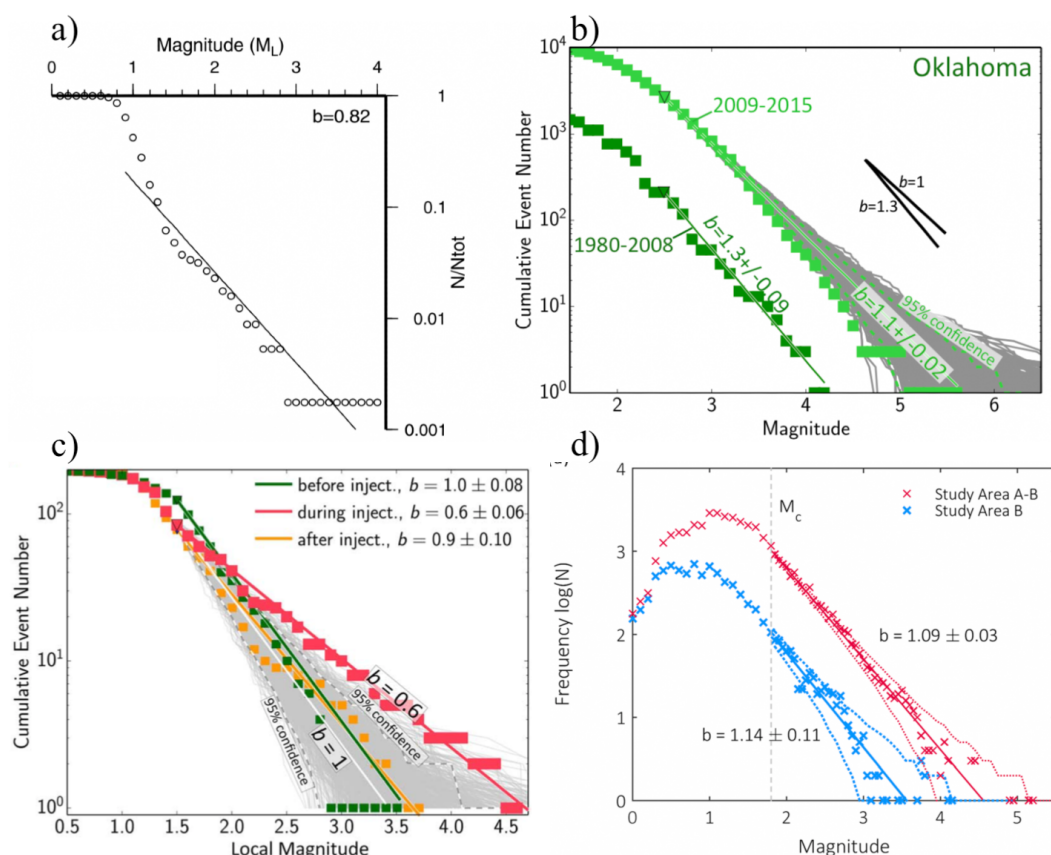


Figure 1.6 – Panel a: Magnitude frequency distribution for induced seismicity in Youngstown Ohio, between 2011 and 2014, from (Skoumal *et al.*, 2014). Panel b: Magnitude frequency distribution for induced seismicity in Oklahoma, between 1980 and 2008 in dark green and between 2009 and 2015 after seismic activity escalated in light green, from (Goebel *et al.*, 2016a). Panel c: Magnitude frequency distribution for induced seismicity in California in 2005, before (green color), during (red color), and after (orange color) peak injection rates, from (Goebel *et al.*, 2016b). Panel d: Magnitude frequency distribution: area B: 5 km radius area around the Coso geothermal field, area A-B: 30 km radius area from the geothermal field without area B, from (Schoenball *et al.*, 2015).

follow this estimation, as its real magnitude exceeds by two orders the estimated one according to the associated injected volume in this case (Grigoli *et al.*, 2018). On the other hand, according to Van der Elst *et al.* (2016), the maximum magnitude is not bounded by the injection volume, and can be as statistically expected. He argued that the injected volume controls the number of induced earthquakes exceeding a certain magnitude, rather than the maximum magnitude of the events as suggested by McGarr (2014) (Figure 1.7.b).

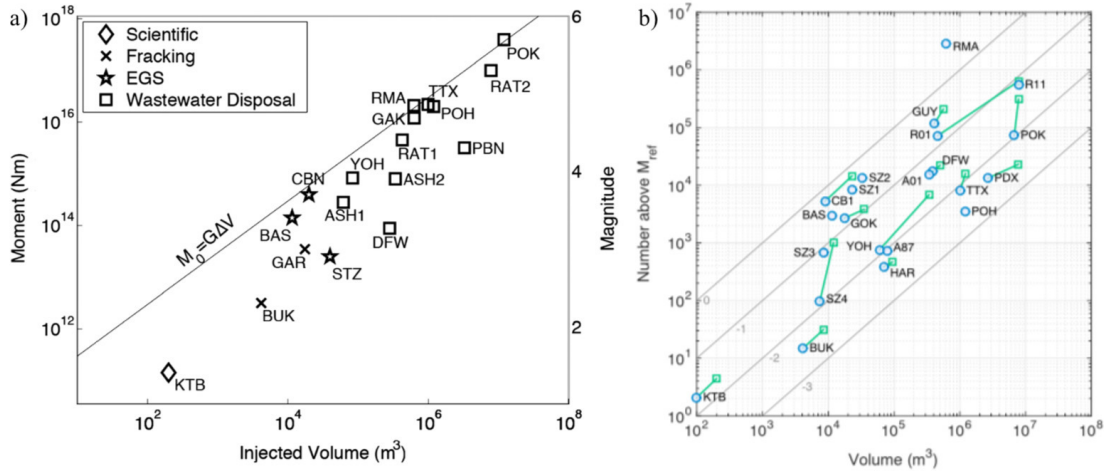


Figure 1.7 – Panel a: Upper bound of the maximum seismic moment and magnitude as functions of total volume of injected fluid, from (McGarr, 2014). Panel b: Number of induced earthquakes versus injected volume, the gray lines refer to the different reference magnitudes M_{ref} from (Van der Elst *et al.*, 2016)

What controls the magnitude content of induced seismic sequences is not yet fully understood and remains an open subject for debate. Nonetheless, the different observations of induced seismicity agree that induced fault reactivation is characterized by a change in the magnitude content with respect to the background seismicity.

1.4.5 Effect of Injection Parameters

Injection parameters, such as well head pressure, injected volume and injection rate have been observed to have an impact on the induced seismic response. However, finding a physical relation between those parameters and the seismic activity can be somehow complicated (Ellsworth, 2013). We review here some of the observational correlations made between injection parameters and induced seismicity.

As mentioned in the previous section, according to Shapiro *et al.* (2007), the probability of inducing a large magnitude earthquake is correlated with the injected volume. In the same spirit, McGarr (2014) found that the maximum magnitude of a seismic sequence is proportional to the injected volume, whereas Van der Elst *et al.* (2016) correlated the injected volume to the number of induced earthquakes (Figure 1.7).

During an injection experiment in the Rangely oil field in Colorado in 1969 (which will be discussed more in details in the section 1.7.1), it was found that the well head pressure controls the number of induced earthquakes, and by managing it one could somehow control the seismic response (Raleigh *et al.*, 1976). Figure 1.8.a shows how the monthly number of earthquakes followed the reservoir pressure during this experiment. The same

behavior was observed in Oklahoma as the seismic moment released escalated during the Jones swarm in 2009 after the increase of the well head pressure (Keranen *et al.*, 2014). Similarly, as injection was interrupted during the holidays in Youngstown Ohio in 2011, the pressure dropped at the well head, and each drop was followed by a quiescence period of around 4 days (Kim, 2013).

On the other hand, Weingarten *et al.* (2015) found that induced seismicity is more closely related to rates of injection, rather than pressure or volume. During the seismic sequence between 1962 and 1970 in Colorado, the frequency of earthquakes correlated with changes in injection rate (Gibbs *et al.*, 1973). However, in Arkansas between 2013 and 2016 and in Oklahoma, a time lag between seismicity rate and injection rate was observed, of around 2 to 6 months in Arkansas (Rubinstein *et al.*, 2018) and 2 to 5 months in Oklahoma (Langenbruch and Zoback, 2016) (Figure 1.8.b). Langenbruch and Zoback (2016) found that for Oklahoma the seismicity rate is rather temporally correlated with the pressure rate, instead of the injection rate (Figure 1.8.b). According to Langenbruch *et al.* (2018), even if pressure continues to increase, the seismicity rate will decrease if the rate of pressure increase is slowing down.

However, the effect of injection parameters on the seismic response can be important near the injection well, and relatively insignificant for distant remote seismicity (Keranen and Weingarten, 2018). This can explain why an injection shut-in can lead sometimes to a rapid decrease in seismic activity in the vicinity of the well, and have no effect at larger distances where seismicity continues (Rubinstein *et al.*, 2018).

To summarize, the effect of injection parameters is not yet fully understood, as in each case a different correlation of seismicity with a certain injection parameter was proposed. Nonetheless, the injection data that researchers receive from the industrialists are often average daily, weekly or even monthly data. More precise data may help further investigate such correlations.

1.4.6 Evidence of Induced Aseismic Motion

Beyond micro-seismic activity and large induced earthquakes, fluid injection can promote aseismic slip. It is however hard to record aseismic motions, as they are usually too slow and can go undetected without proper monitoring networks (Wei *et al.*, 2015; Cornet, 2016). For this reason, indirect approaches were considered to assess the existence of induced aseismic motion. During the 1993 geothermal stimulation in Soultz-sous-Forêt, the maximum slip from the recorded microseismic events was estimated to a few millimetres, whereas the borehole televiewer observations indicated slip motions reaching 4 centimetres. Cornet *et al.* (1997) then interpreted these slip event observations being driven by aseismic motion. Bourouis and Bernard (2007) later found that the same seismic sources have been reactivated, and were driven by the fault creep surrounding them. Another example of indirect evidence of aseismic motion is during the geothermal stimulation in Soultz-sous-Forêt that took place in 2000. (Calo *et al.*, 2011) conducted a

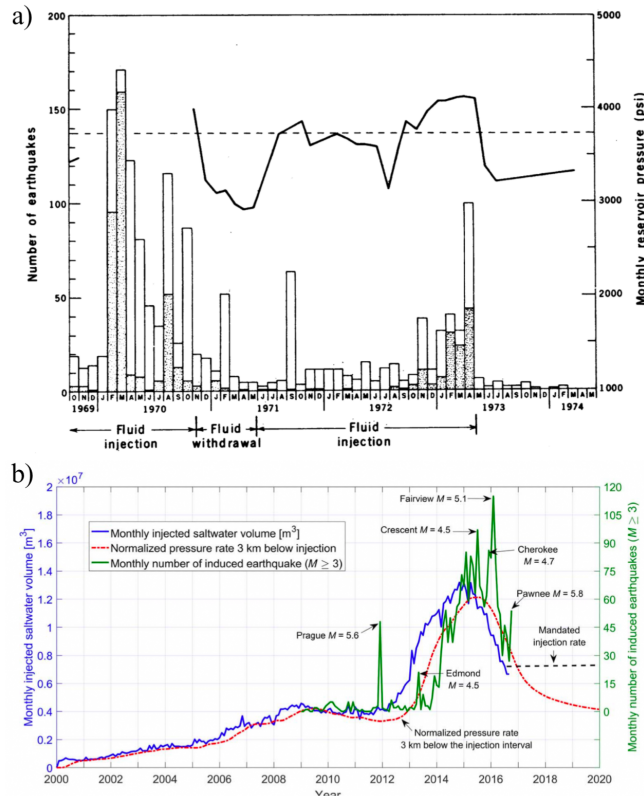


Figure 1.8 – Panel a: Monthly number of earthquakes (represented by the bars) and the monthly reservoir pressure during the injection experiment in the Rangely oil field in 1969, from (Raleigh *et al.*, 1976). Panel b: Monthly injection rate (in blue), monthly earthquake rate (in green), and pore pressure rate at 3 km below injection (in red) for the seismicity in Central and Western Oklahoma, from (Langenbruch and Zoback, 2016)

4-D tomography of P-wave velocities, and argued that the fast changes in P-wave velocities are caused by aseismic motions. For the same stimulation, Schoenball *et al.* (2014) inverted the focal mechanisms of the recorded seismic events and found that the stress regime changed due to the injection from strike-slip faulting to normal faulting. They attributed this change to large-scale aseismic deformation. Again in Soultz-sous-Forêt, during the circulation test conducted in 2010, Lengline *et al.* (2014) reported a large variation in the stress drop for the same asperities, which they then associated to the existence of stable sliding. Furthermore, the hydraulic stimulation of the Rittershoffen deep geothermal reservoir in Northeast of France induced two distinct seismic swarms separated by a quiescence period of 4 days. Lengline *et al.* (2017) argued that the delay between the two seismic swarms was caused by a period of aseismic slip.

A very well documented case of observation of aseismic deformation is the 6 days

seismic swarm of 2012 within the Brawley geothermal field in California. Using InSAR and leveling data, [Wei *et al.* \(2015\)](#) analysed the evolution of aseismic deformation before and during the injection. They found that on the onset of the injection start in 2010, the subsidence rate experienced a rapid increase by a factor of 10, going from an average of 4.8 millimetres per year to around 5 centimetres per year (Figure 1.9). They also argued that the observed aseismic deformation was the triggering mechanism of the seismic swarm.

In addition, direct evidence of induced aseismic slip was observed during in-situ injection experiments ([Guglielmi *et al.*, 2015b](#); [Duboeuf *et al.*, 2017](#); [De Barros *et al.*, 2018](#)). This will be discussed in the section 1.7.2. Nonetheless, whether observed by direct or indirect methods, it appears that slow aseismic deformation takes an important part of the fluid induced fault slip reactivation. It is therefore crucial to be better monitored and further studied ([Wei *et al.*, 2015](#); [Cornet, 2016](#); [Lengline *et al.*, 2017](#)).

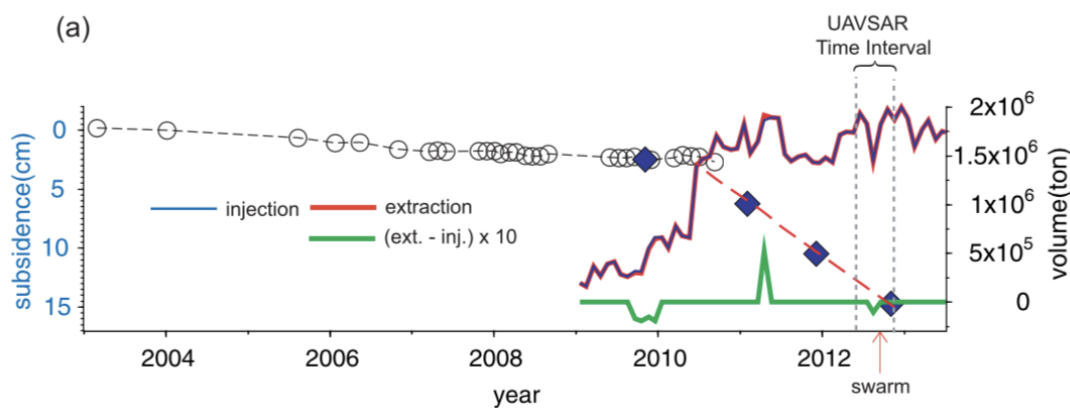


Figure 1.9 – Evidence of aseismic slip in the Brawley swarm in 2012: Time series of the subsidence (black circles are derived from InSAR and blue diamonds from leveling) with the monthly injection and production volume ([Wei *et al.*, 2015](#)).

1.5 Managing Induced Seismicity

The seismic hazard due to industrial fluid injection activities is increasing, especially with the triggering of some large earthquakes (please refer to Table 1.1 for examples). The injection activities are however sometimes necessary, or to the least an important tool towards the development of sustainable energy. This is especially the case of enhanced geothermal systems. In such cases, the local communities and industrials need to find a compromise in order to achieve an “economic” project, with an associated “acceptable” seismic risk. This gave rise to “Traffic Light Systems (TLS)” ([Bommer *et al.*, 2006](#)). The idea is to mitigate the risk of induced seismicity by adjusting the injection protocol (reducing injection rate, well-head pressure or duration of pumping), as

managing injection activities was observed to control the seismic hazard (McGarr *et al.*, 2015). It is basically an “Observation - Action” process, based on the accepted tolerance of the local community. The main parameters considered in the TLS are the earthquakes magnitudes and the peak ground velocity (PGV). When the accepted thresholds are exceeded, actions should be taken. The TLS protocol consists of three different stages: a) green: no threshold has been reached, injection activity continues normally, b) orange is a warning stage where intermediate thresholds may have been exceeded, injection can proceed with caution and at reduced rates, c) red: actual thresholds are exceeded and injection activity is immediately suspended (Grigoli *et al.*, 2017). In some cases, further actions should be taken if large magnitude earthquakes continue after injection shut-in, like bleeding of the well and releasing the pressure (Haring *et al.*, 2008). A Classical TLS requires a large seismic monitoring network and real time monitoring (Gaucher *et al.*, 2015a).

A TLS was installed in Berlin, El Salvador during the hydraulic stimulation that took place in the geothermal field in 2003 (Bommer *et al.*, 2006). The temporal evolution of the cumulative number of induced earthquakes was considered as an additional indicator in this case. The implemented TLS here was a success and always indicated a green light (Bommer *et al.*, 2006). The geothermal stimulation in Helsinki, Finland in 2018 was also monitored through a TLS, where a moment magnitude of 2 was set at the upper limit for earthquake magnitudes. The stimulation was injection-rate controlled and the threshold was never exceeded, the maximum magnitude recorded reached 1.9 (Figure 1.10.a)(Kwiatek *et al.*, 2019).

However, TLS implementation was not always a success. For the case in Basel in Switzerland, citizens phone calls were also considered as a warning indicator (Haring *et al.*, 2008). After the 2.6 magnitude earthquake in December 2006, the orange light was activated and injection rate was reduced and later on injection was stopped (Haring *et al.*, 2008; Deichman and Giardini, 2009). Another 2.7 magnitude earthquake was recorded 4 hours later and a 3.4 magnitude earthquake an hour after that, leading the industrialists to bleed out the well and release the well-head pressure (Haring *et al.*, 2008). Even though all these actions were taken, 3 large earthquakes (magnitude 3) were recorded between January and March in 2007 (Figure 1.10.b) (Deichman and Giardini, 2009). The TLS in this case was not at all efficient and the project has been since then abandoned (Haring *et al.*, 2008). This also happened in Fox Creek in Alberta Canada during hydraulic fracturing operations. The thresholds for limit was set to 4 and was exceeded during the 2016 M_w 4.1 earthquake (Atkinson *et al.*, 2016), and thus the operations were stopped (Schultz *et al.*, 2017).

More recently, a TLS along with the application of cyclic injection scheme were tested against seismic risk mitigation in August 2017 in Pohang, South Korea, where the threshold of magnitude was set to 2. The largest magnitude recorded was 1.9 during and shortly after injection (Hofmann *et al.*, 2019), giving a success of the mitigation protocol.

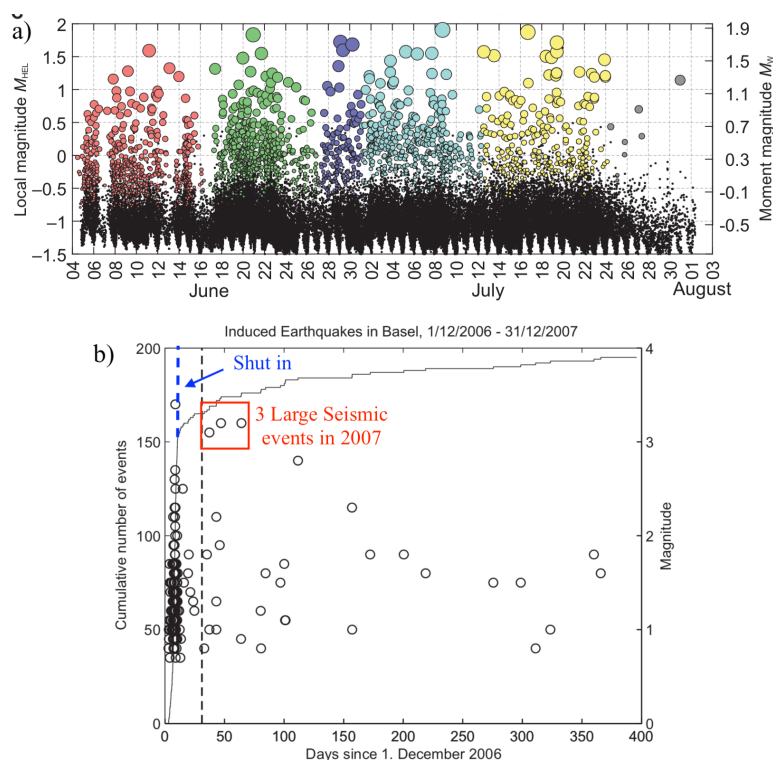


Figure 1.10 – Time series of earthquake magnitude when using a TLS: Panel a: In Helsinki Finland, from (Kwiatek *et al.*, 2019). The different colors refer to the different injection stages; b) Panel b: in Basel Switzerland, modified from (Deichman and Giardini, 2009)

However, the magnitude 5.5 earthquake that was recorded in November 2017 in Pohang is believed to being induced by injection activities (Kim *et al.*, 2018; Grigoli *et al.*, 2018). Thus, whether the mitigation protocol was efficient or not is still questionable.

Baisch *et al.* (2019) argues that the capacity of a TLS to prevent an earthquake has more limitations than typically assumed, as the basic assumptions of a TLS can not be generalized to all injection-induced cases. The theory behind a TLS lies on the fact that all large earthquakes are preceded by a series of precursors, which once detected can allow the industrialists to regulate the injection protocol to prevent the large earthquake Baisch *et al.* (2019). This is not always true, and may be the case of the induced seismicity in Fox Creek Alberta where a direct large earthquake (M_w 4.1) was recorded (Atkinson *et al.*, 2016; Schultz *et al.*, 2017). Another weak point of TLS is the incapacity to mitigate post-injection seismicity as it is beyond operational control (Baisch *et al.*, 2019). Classical TLS are useful to mitigate seismic hazard and risk during early stages of injection (McGarr *et al.*, 2015; Baisch *et al.*, 2019).

A new generation of TLS called “Adaptative Traffic Light System” (ATLS) is now under development and testing phase (Wiemer *et al.*, 2014; Mignan *et al.*, 2017). The idea is to improve pre-defined alarm systems and overcome the limitations of the classical method, by including a study risk and numerical modeling along with the real time data processing. The objective is to model and reproduce seismicity during the injection activity and then forecast seismicity rate and seismic hazard, even after injection shut-in. One should never forget though that these methods are statistical tools to help injection regulators and not a real forecast of future seismicity.

1.6 First Conceptual Models For Fluid Induced Fault Reactivation

All the observations presented in the previous section suggest two different mechanisms for induced fault reactivation: (1) via a direct pore fluid pressure effect where the fluid diffuses into the fault, and (2) due to poro-elasticity and changes in loading conditions on the fault, in this case the fluid does not diffuse into the fault (Ellsworth, 2013) (Figure 1.11).

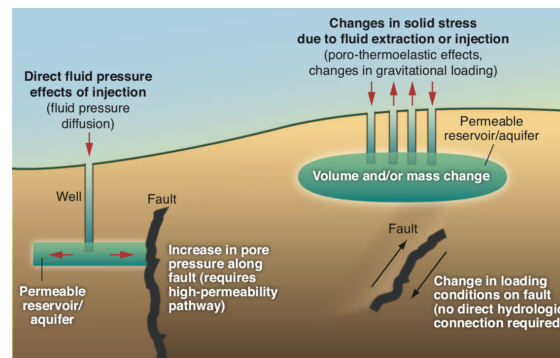


Figure 1.11 – Mechanisms for inducing earthquakes: earthquakes can be induced by increasing the pore pressure acting on a fault (left) or by changing the shear and normal stress acting on the fault (right), (Ellsworth, 2013)

A pre-existing fault is reactivated when the shear stress acting on it exceeds its shear strength. The latter is proportional to the product of the effective normal stress and the friction coefficient μ ranging between 0.6 and 0.85 as shown in Figure 1.12 (Byerlee, 1978).

The effect of direct pore pressure was first introduced by Hubert and Rubey (1959) and later applied by Healy *et al.* (1968) for the seismicity in Denver, Colorado. They argue that the increase in pore pressure along the fault reduces the effective normal stress along the fault’s plane, and thus decreases the frictional resistance $\tau = \tau_0 + \sigma_{\text{eff}}\mu$ where τ_0 is the cohesive strength, σ_{eff} the effective normal stress ($\sigma_{\text{eff}} = \sigma_T - p$), μ is the friction

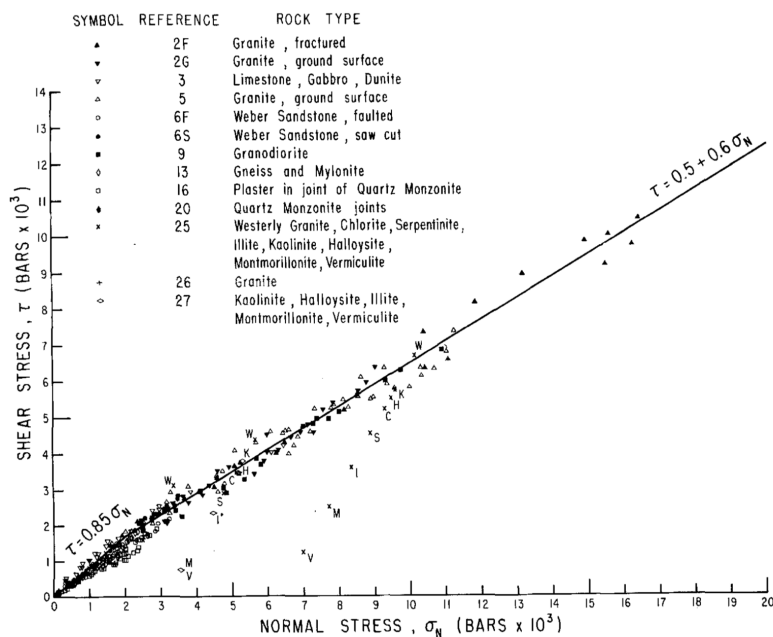


Figure 1.12 – Rock Failure Criterion: Shear stress as a function of normal stress for a variety of rock types, from [Byerlee \(1978\)](#).

coefficient, σ_T the lithostatic normal stress and p the pore pressure ([Byerlee, 1978](#)). This process is illustrated in [Figure 1.13a](#). Fault reactivation is then reached when the stress along the fault exceeds its frictional resistance ([Figure 1.13d](#)). In this case, permeable pathways assure the diffusion of pore pressure from the vicinity of the injection well into the neighbouring fault (refer to the left panel in [Figure 1.11](#)).

Using such a conceptual model, [Hsieh and Bredehoeft \(1981\)](#) found that the migrating seismicity tracks the diffusion of a pore pressure front of 3.2 MPa for Denver Colorado, while [Keranen *et al.* \(2014\)](#) argued that the critical threshold of the pore pressure front is 0.07 MPa for Oklahoma.

On the other hand, [Segall \(1989\)](#) investigated how poro-elastic effects could change the stress state along the fault and move the fault close to failure. This process is illustrated in [Figure 1.13b](#). Induced seismicity due to hydraulic fracturing in Harrison County Ohio started only 2 hours after activity started. [Kozłowska *et al.* \(2018\)](#) argued that induced seismicity onset was faster than the pressure diffusion process, and that it may be caused by fast poro-elastic changes in pressure. Finally [Figure 1.13c](#) illustrates the stress state from direct pore pressure effects and poro-elastic effects.

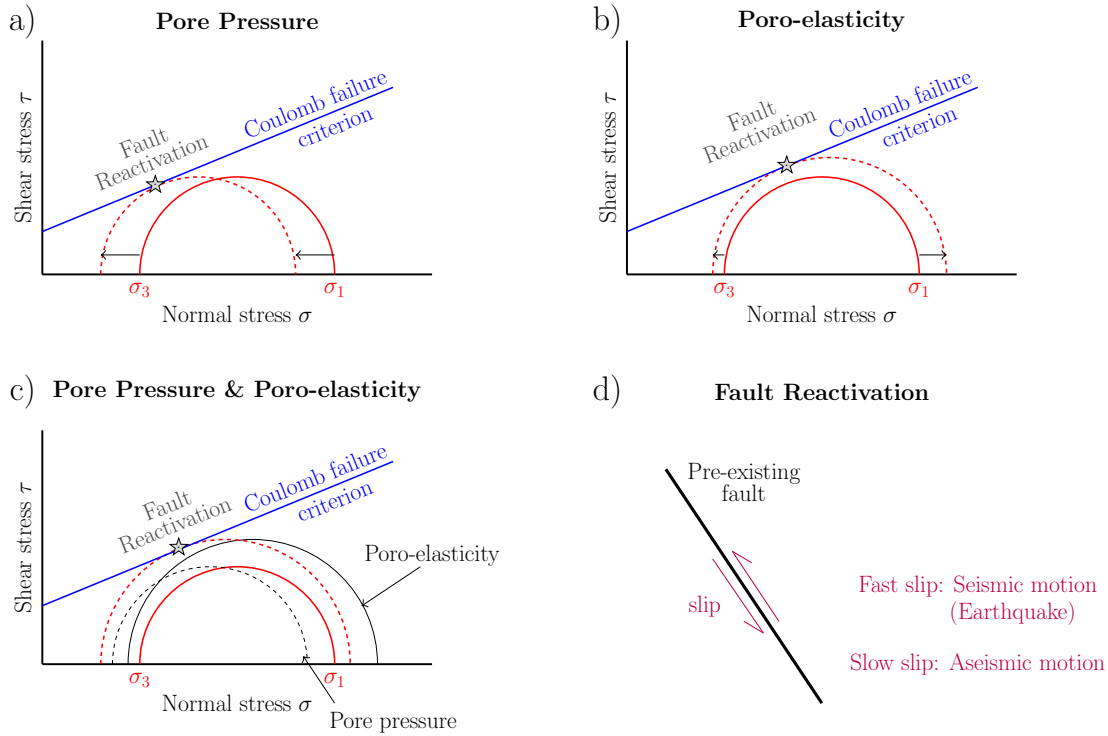


Figure 1.13 – Conceptual model of induced fault reactivation: the effects of direct pore pressure and poro-elastic effects on fault failure: (a) pore pressure, (b) poro-elasticity, (c) pore pressure and poro-elasticity. In these subplots the solid red plot represents the initial stress state while the dashed red plot refers to the final stress state at fault reactivation. (d) Schematic diagram of fault slip reactivation on a pre-existing fault.

Necessity to better understand injection induced seismicity

The conceptual model presented in Figures 1.11 and 1.13 is a very simplified model of fault reactivation, and cannot fully explain all the observations, in particular: aseismic reactivation, time delay, post-injection seismicity, magnitude content and dependence on injection scenario. Thus the need to better understand all the physical processes increases. The rapid rise in induced seismicity has indeed led to a large increase in research (Keränen and Weingarten, 2018) and a rise in the yearly number of published papers on induced seismicity (Grigoli *et al.*, 2017). Injection experiments and numerical modeling studies can help resolve some open questions and shed light into some physical mechanisms of induced seismicity. They will be the subject of the next two sections.

1.7 Injection Experiments for Better Understanding Fault Reactivation and Induced Seismicity

Different scales of injection experiments exist: 1) Large scale in-situ experiments (kilometer scale) with the purpose to investigate how different injection practices can influence the seismic features of resulting induced seismicity, 2) Intermediate decametric scale where injection experiments are conducted on real natural faults, accompanied by a dense monitoring network, to track fault reactivation by seismicity and aseismic slip, 3) Small scale injection experiments that consist of experiments conducted on rock samples in the laboratory (centimeter scale), in order to investigate how a coupled fluid – pre-existing fault can influence fault reactivation. Here we review some injection experiments conducted at the different scales.

1.7.1 Large Scale In-situ Injection Experiments

As mentioned earlier in section 1.4.1, injection-induced seismicity in Denver Colorado revealed a link between the bottom well fluid pressure and seismic activity. To further investigate this relation, an in-situ injection experiment was conducted in the Rangely oil field of Colorado. It started in October 1969 and lasted for around 3 years and a half (Raleigh *et al.*, 1976). The experiment consisted of 2 successive cycles of fluid injection and fluid withdrawal. The bottom-hole pressure was monitored and showed a direct correlation with the number of induced seismic events. The experiment confirmed the theory of Healy *et al.* (1968) that earthquakes are triggered by an increase in pore pressure beyond a critical threshold. It also showed that induced seismicity can be controlled and the fault can be strengthened by adjusting the fluid pressure in a fault zone (Raleigh *et al.*, 1976). We should note though that in this case the time lag between seismicity and injection was less than a day, due to the existence of high permeable fluid conduits allowing the transmission of pressure between injection wells and the fault. This may not be always the case, for low permeability conduits, once could expect longer time lag between injection and seismicity, or a totally different behavior.

Another long term hydraulic experiment was run in the German Continental Deep Drilling Borehole (KTB site) that started in 2002 (Shapiro *et al.*, 2006). It consisted of one year of fluid production phase followed by a one year of fluid injection phase. No induced seismicity was recorded during the first phase and nearly third of the second phase. Induced seismicity started 110 days through phase 2, approximately when the volume of fluid injected in phase 2 exceeded the total volume of fluid extracted during phase 1 (Shapiro *et al.*, 2006). The seismic productivity was lower than previous injection experiments conducted in this site (Shapiro *et al.*, 1997). It was concluded that reducing the pressure before injection can then mitigate the seismic risk in two ways: 1) by delaying the onset of induced seismicity and 2) decreasing the seismic productivity.

1.7.2 Decametric Scale Injection Experiments: Seismicity and Aseismic Slip

Injection experiments in underground laboratories are a bit more controlled than large scale in-situ experiments. In this case, the experiments are accompanied by a dense monitoring network. The main objective is to investigate the seismic/aseismic aspect of induced seismicity.

In the attempt to better understand all the possible mechanisms of injection-induced seismicity, an in-situ experiment was conducted at the low noise underground laboratory (LSBB) in the south of France in 2010, where fluid was directly injected into a 500 meter long natural inactive fault (Guglielmi *et al.*, 2015b), under step increasing injection rates. During the experiment, the fault slip and opening were measured and induced seismicity was detected, and are plotted in Figure 1.14 against pressure and injection rate. This experiment confirmed the evidence of injection-induced aseismic slip, where a slip of around 0.3 millimetres accompanied with a fault opening were recorded before the onset of seismic activity (Guglielmi *et al.*, 2015b). The observed aseismic slip was associated with a 20-fold increase in fault permeability (Guglielmi *et al.*, 2015a,b; Bhattacharya and Viesca, 2019). A hydromechanical modeling of the experiment showed that even though aseismic slip was mainly confined to fluid-pressurized zone (Guglielmi *et al.*, 2015b), the aseismic rupture front, once initiated, accelerates ahead of the fluid-pressurized area (Bhattacharya and Viesca, 2019).

Another set of in-situ experimental fluid injections took place in the same site in 2015, with a denser monitoring network. The experiment consisted of 10 high pressure injection tests, performed at different depths and in different geological contexts. The increase in fluid pressure led to a fault opening and aseismic slip near the injection (Duboeuf *et al.*, 2017). The recorded seismicity was very scattered, and the seismic deformation formed less than 4 % of the total deformation. According to Duboeuf *et al.* (2017), the spatio-temporal distribution of the seismicity could not be mapped by a simple diffusion process, they argued that the seismicity may not be directly induced by the increase in pore pressure, but rather triggered by the induced aseismic slip. Large permeability enhancement associated with creation of new fractures was also observed during this injection experiment (Duboeuf *et al.*, 2017).

In order to test the response of different lithologies, two in-situ fluid injection experiments were conducted also at the decameter-scale, the first in low permeable shale in Tournemire, France in 2014 and the second in highly fractured limestones in Rustrel, France in 2015. In both experiments, the induced deformation was mainly aseismic and formed around 95 % of the total seismic deformation (De Barros *et al.*, 2018). Following the three decameter-scale in-situ injection experiments (Guglielmi *et al.*, 2015b; Duboeuf *et al.*, 2017; De Barros *et al.*, 2018), De Barros *et al.* (2018) argued that beyond the typical mechanism of induced seismicity by decrease of effective stress, first introduced by Healy *et al.* (1968), exists another mechanism where the increase in pore pressure could first lead to aseismic failures, which in turn could trigger seismic failure through stress

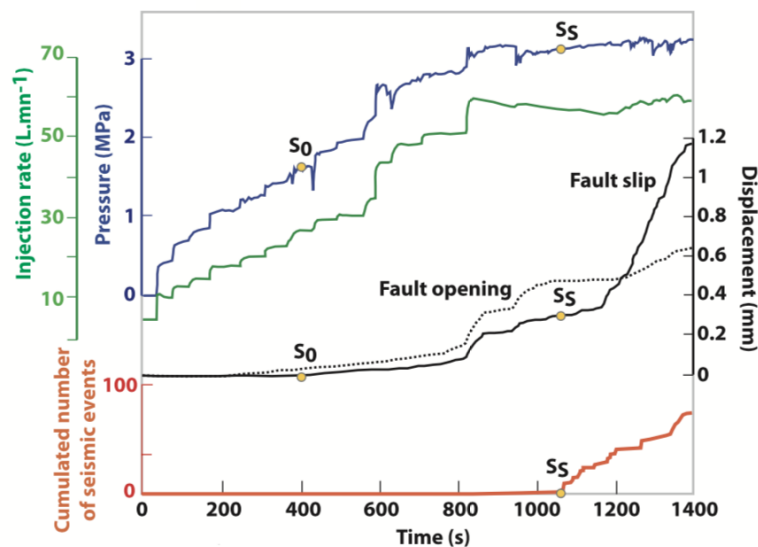


Figure 1.14 – Fault slip, opening and induced seismicity during fluid injection experiment at the LSBB site. Time series of the pressure and injection rate are represented respectively in blue and green. Fault slip and fault opening are represented by black solid and dotted lines, respectively. The cumulative number of seismic events is plotted in red (Guglielmi *et al.*, 2015b).

transfer. The proposed model, containing the two different mechanisms, is presented in Figure 1.15. They also pointed out the role of permeability increase in this mechanism, this will be further discussed in section 1.7.3.

More recently, Kwiatek *et al.* (2018) investigated the pico-seismicity recorded during a subdecimeter hydraulic fracturing experiment at the underground Aspö Hard Rock Laboratory, Sweden in 2015. Six different hydraulic tests were conducted under three different injection schemes with maximum injection pressure reaching 13 MPa. Around 196 seismic events were recorded, having magnitudes in the range $[-4.2 - -3.5]$. Kwiatek *et al.* (2018) argued the existence of a correlation between the hydraulic energy and the total seismic moment released. They showed that in the context of this experiment, the seismic energy released is highly over-estimated by the McGarr (2014)'s relation (refer to Figure 1.7a), and suggested the existence of aseismic deformation accompanying the recorded pico-seismicity that was not detected by the monitoring network.

1.7.3 Small Scale Laboratory Injection Experiments

Small scale laboratory injection experiments are the most controlled ones. They mainly consist of studying how different parameters (fault roughness, stress state, injection rate, fault permeability and porosity, etc.) could influence fault reactivation processes in the

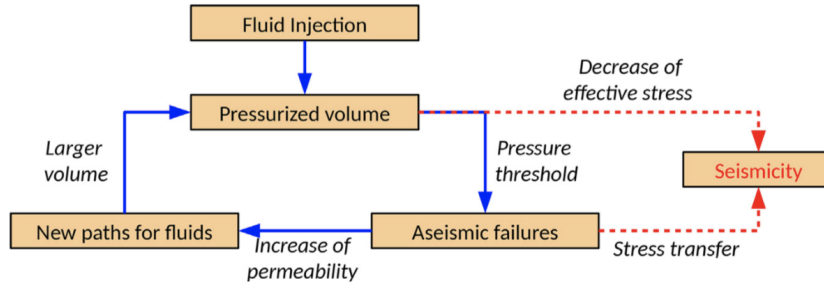


Figure 1.15 – Proposed model for injection induced seismicity: Direct effect of pore pressure (by the decrease of the effective stress) or through stress transfer from aseismic deformation, from in-situ experiments by [De Barros *et al.* \(2018\)](#).

context of a coupled fluid – fault framework.

[Nemoto *et al.* \(2008\)](#) conducted slip experiments on a fractured granite rocks with rough surface to investigate the dynamic responses of existing fractures. They pointed out the importance of incorporating the fault surface geometry in future studies. Here the rough surface led the slip to increase stepwise accompanied by an increase in the fluid flow, caused by sudden drops in pore pressure and shear dilation.

[Goodfellow *et al.* \(2015\)](#) conducted eight hydraulic fracture experiments in the laboratory on Westerly granite cylindrical samples, at different stress states and injection rates. Their goal was to investigate the energy budget of such industrial activities. They recorded the radiated seismic energy and acoustic emissions and found that while the seismic energy presents a very small fraction of the injection energy (Figure 1.16), the deformation energy can go up to 94 % of the injection energy. [Goodfellow *et al.* \(2015\)](#) then argued that aseismic deformation plays a significant part in the energy budget of hydraulic fracturing.

During an experimental fluid induced rock deformation, it was observed that the induced fault slip and slip velocity correlate well with the variation of fluid pressure rather than with the magnitude of fluid pressure ([French *et al.*, 2016](#)).

([Rutter and Hackston, 2017](#)) conducted laboratory experiments on two different rock samples in order to investigate how fault and rock permeability could influence the nature of induced fault slip. They found that for permeable rocks, it is more likely to induce stable sliding, however in impermeable rocks, the fluid overpressure could suddenly access the fault plane and produce seismic slip instabilities.

[Scuderi *et al.* \(2017\)](#) conducted laboratory creep experiments to investigate the fault slip evolution due to fluid injection, especially on faults characterized by stable frictional behavior. They found that the decrease of effective normal stress weakens the fault,

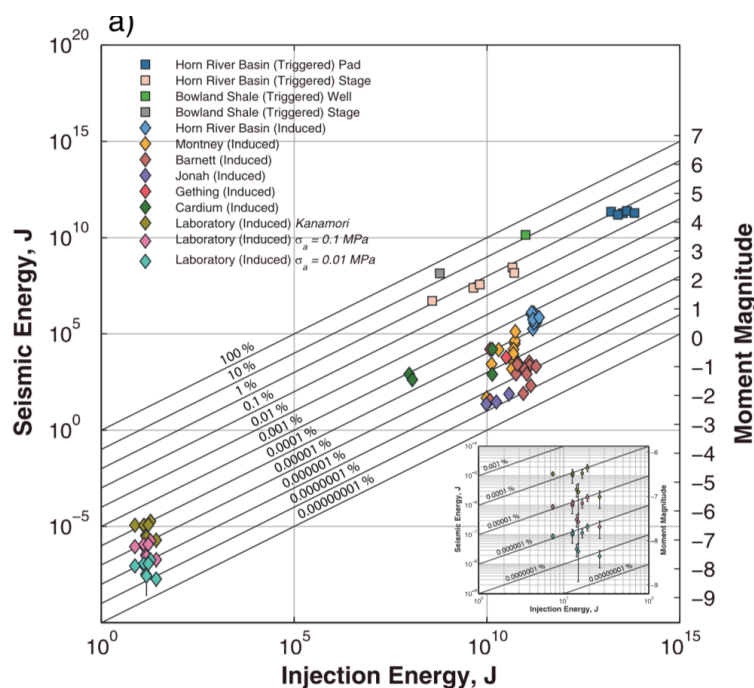


Figure 1.16 – Injection energy plotted against seismic energy, the reference lines correspond to the seismic injection efficiency in percentages, that is the ratio of seismic energy to injection energy, from [Goodfellow *et al.* \(2015\)](#).

makes it frictionally unstable and drive dynamic slip instability. Moreover, they found that the fault slip behavior is very sensitive to the initial stress state and the injection rate.

To further investigate the effect of fault roughness [Ye and Ghassemi \(2018\)](#) conducted injection-induced shear tests on several granite samples having each a different fault surface roughness. At first they showed that the increase in fault pressure can induce significant shear slip, which in turn can result in a large increase of fracture permeability. The permeability enhancement is larger for rougher faults, and can be retainable with decreasing pressure on rough fault surfaces. They also showed that smooth surfaces experienced lower slip velocities and stress drops than rough ones. And finally they showed that the degradation of asperities increases with fault roughness.

[Passelegue *et al.* \(2018\)](#) studied the effect of fluid injection pressure rate on the re-activation of faults during laboratory experiments on a Westerly granite sample. They pointed out how a large injection pressure rate can lead to local over-pressures and large pressure heterogeneities along the fault, that can reactivate faults and lead to seismic failures beyond the fluid pressurized region.

Following the in-situ injection experiment at the LSBB site ([Guglielmi *et al.*, 2015b](#))

(discussed in section 1.7.2), [Cappa *et al.* \(2019\)](#) conducted laboratory experiments on limestone rock samples from the same in-situ fault, under slow injection rate. In the early stages of the experiment, increase in fluid pressure induced aseismic stable slip, that can later accelerate and trigger earthquakes beyond the pressurized zone. The experiment mainly succeeds in reproducing the observations from the original in-situ experiment. [Cappa *et al.* \(2019\)](#) argues that during the experiment, as the response to the increase in pore pressure, the friction along the fault shifts to stable behavior, which in turn would lead to aseismic motion.

Permeability/Hydraulic diffusivity Enhancement

We presented so far laboratory injection experiments that investigate induced fault slip reactivation. We will now discuss some experimental studies that examine permeability enhancement. Indeed, the dynamics of fluid-fault interactions are complex, as both an increase in fluid pressure and fault reactivation could affect the hydromechanical properties of the fault via a permeability enhancement. Beyond laboratory studies focused on explaining certain aspects of induced fault reactivation, several laboratory experiments were conducted in order to assess the change in permeability/diffusivity with respect to changes in effective stress, and slip accumulation.

- **Effective Stress Effect**

Increase in fluid pressure from injection activities decreases the normal effective stress along the fault ([Rutter and Mecklenburgh, 2018](#)). This reduction may cause an enhancement of the permeability along the fault. During laboratory experiments, it was observed that permeability changes, following changes in the differential stress applied on the rock sample ([Zoback and Byerlee, 1975](#)). [Fisher and Zwart \(1996\)](#) conducted in-situ bulk permeability measurements between the North American and Caribbean plates and observed changes in the fault's permeability by several order of magnitude following changes in fluid pressure. Moreover, during laboratory triaxial experimental permeability tests, [Ghabezloo *et al.* \(2009\)](#) found that pore pressure changes have more impact on the fracture permeability than confining pressure.

- **Fault Reactivation Effect**

It was observed that fault's permeability can change following a seismic event and slip accumulation ([Zhang and Tullis, 1998](#); [Baghbanan and Jing, 2008](#)). This is relatively frequent during injection-induced seismicity. Fault zone permeability was observed to vary following fault reactivation and shear displacement during laboratory experiments ([Chen *et al.*, 2000a](#); [Gutierrez *et al.*, 2000](#); [Wu *et al.*, 2017](#); [Im *et al.*, 2018](#)).

We presented in this section contributions from injection experimental studies at three different scales (in-situ scale, decametric scale, and laboratory scale). Another way to study fluid induced fault reactivation is the use of mechanical models. This will be the subject of the next section.

1.8 Contributions from different Numerical Modeling Approaches

Figure 1.17 represents a sketch of a fluid injection into a rock medium containing pre-existing fractures. To model induced fault reactivation, different factors should be taken into consideration: (A) source modeling, (B) fluid flow modeling, (C) rock medium modeling. Figure 1.17 summarizes the major approaches already proposed to model each factor. As it is complicated for a numerical study to consider all the physical processes and mechanisms, due to the complexity of the resulting problem, each study adopts some hypotheses and neglect some physical processes depending on the objective of the investigation. For instance, studies that investigate the dynamics of the seismic rupture, may simplify sometimes the fluid flow modeling, on the contrary to the studies that investigate how the fluid flow affects the induced seismicity. The different approaches presented in Figure 1.17 will be gradually introduced and explained in the following sections.

Here we present a review of some, certainly not all, numerical studies, present their points of similarities and differences, discuss their limitations and finally expose their main contributions. We divide the models into categories based on their hypothesis: (1) pressure diffusion based models, (2) injection into rock volumes, (3) numerical models based on Fracture Mechanics, (4) models following the seismicity rate model proposed by [Dietrich \(1994\)](#), (5) Burridge-Knopoff based models and (6) frictional fault models.

1.8.1 Pressure diffusion based models

Pressure based models do not take into account any mechanical coupling with the frictional properties of the medium or any elastic interactions. They concentrate only on the diffusion process and conservation of mass of the fluid flow, with a simple triggering mechanism based on pressure thresholds, and do not consider seismic events interactions (foreshocks, aftershocks, ...).

Using such model, and based on the assumption that the increase in pore pressure could re-activate faults and trigger earthquakes if the faults are close to failure (Figure 1.11a), [Shapiro *et al.* \(1997\)](#) proposed the following equation for the propagation of the triggering front:

$$r = \sqrt{4\pi Dt}, \quad (1.1)$$

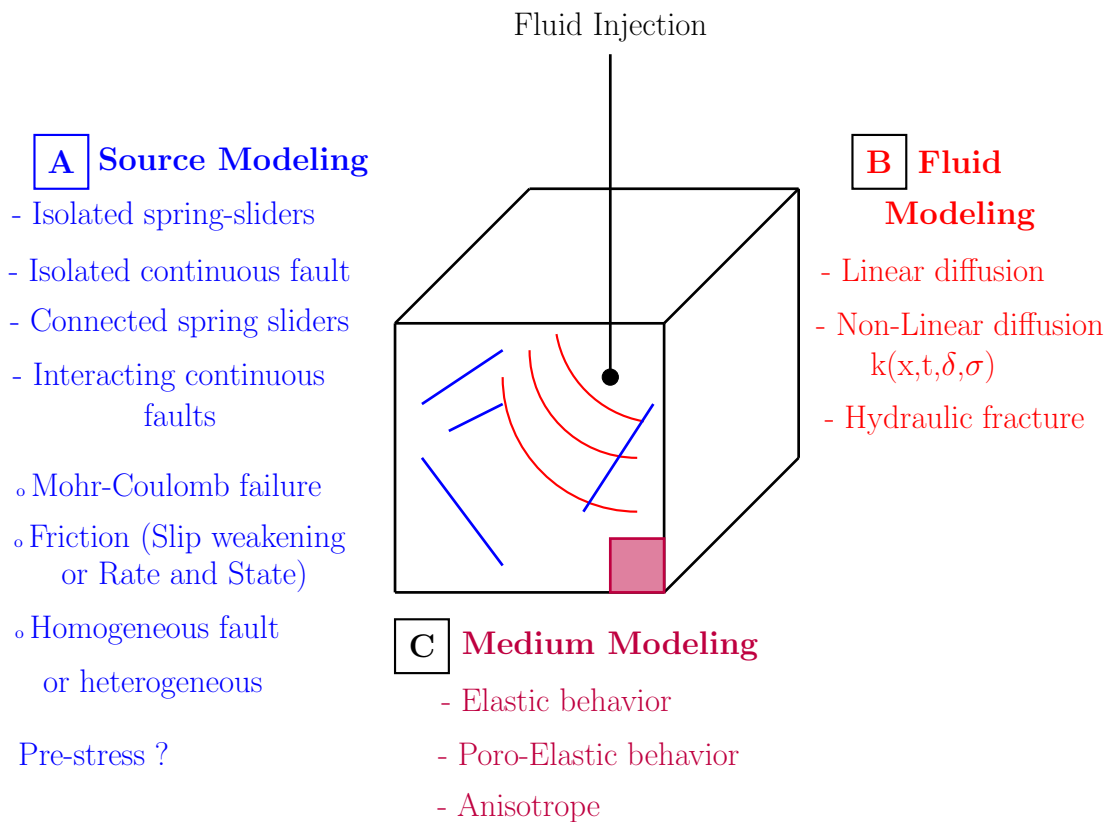


Figure 1.17 – Sketch of fluid injection and fluid flow (red color) into a rock medium (purple color) containing pre-existing fractures (blue color). It presents the major challenges and approaches to model (A) the sources (fractures), (B) the fluid flow (k is the medium permeability, x is the space coordinate, t is the time, δ is the displacement and σ is the effective stress) and (C) the rock medium’s behavior.

where r in the distance between the earthquake and the injection well, D in the hydraulic diffusivity and t is the time. This model was able to explain the spatio-temporal distribution of the induced seismic events following a hydraulic fracturing experiment in the German Continental Deep Drilling Borehole (KTB) in 1994 (Engeser, 1996), as well as in Fenton Hill in 1983 and in Soultz-sous-Forêt in 1993 (Shapiro *et al.*, 2002) (Figure 1.5).

Such model can only reproduce linear diffusion processes. For this reason, Shapiro and Dinske (2009) incorporated a non-linear pressure diffusion process taking into account permeability enhancement, with considering the same reactivation criterion. In addition to triggering from linear pressure, his model allows for triggering from new volume creation and opening in rocks, mainly observed in hydraulic fracturing operations. In this case, the triggering front depends on the diffusivity D_0 and injection source rate Q_0 ,

that in turn are pressure-dependent:

$$r_t \propto (D_0 Q_0^n t^{n(i+1)+1})^{1/(3n+2)}, \quad (1.2)$$

where t is the time, n is the power law exponent of the dependence of the diffusivity on the pressure and i in the power law exponent of the injection rate (i.e. $i = 0$ means constant injection rate). With the use of this model, Shapiro and Dinske (2009) showed that the seismicity in Barnett Shale Texas following hydraulic fracturing operations (Frohlich, 2012) exhibits non-linear pressure characteristics. Hummel and Muller (2009) further extended this model by considering diffusivity anisotropy (resulting from localized hydraulic fracturing), and showed that induced seismicity in Fenton Hill was at first triggered by pressure diffusion, and later by the extension of the fracture domain.

Such models are quite effective in estimating a triggering front and explaining whether the seismicity follow the fluid diffusion or is triggered by a hydraulic fracture propagation. However, they fail to explain induced seismic sequences where event clustering (Schoenball and Ellsworth, 2017) may be observed. They also cannot investigate events magnitude distribution. As well, in such models the time delay is only related to fluid flow (instantaneous triggering).

1.8.2 Injection into rock volumes with Coulomb failure criterion

Induced seismicity can be simulated by a point source injection into an elastic rock medium, and where failure obeys the Coulomb failure criterion. Such approach was adopted in different studies. In particular, Langenbruch and Shapiro (2010) divided the rock medium into similar cells (simulating pre-existing fractures), in which each cell could only be reactivated once, whereas Schoenball *et al.* (2010) proposed to divide the rock volume into cells with different sizes, having a finer mesh near the injection source. Nonetheless, the use of such models does not allow to model seismic multiplets, as well as the characterization of the magnitude content of the induced events.

1.8.3 Numerical models based on Fracture Mechanics

Several numerical studies are based on fracture mechanics. Typically their objective is to investigate the aspects of the induced seismic rupture: initiation, arrest, directivity, etc. In general, such studies consider only one seismic rupture, and do not explore the seismicity rate. We present here some of these models.

Dempsey and Suckale (2016) coupled a semi-analytical solution of a crack propagation with fluid diffusion in order to investigate the directivity of the induced seismic rupture. With the same model, Dempsey *et al.* (2016) then explored the rupture arrest. Similarly, Galis *et al.* (2017) coupled the Griffith crack equilibrium criterion with fluid diffusion, and investigated the rupture length with respect to the pressurized area. In another

approach, [Garagash and Germanovish \(2012\)](#) studied the direct effect of fluid diffusion on the onset of dynamic slip. On the other hand, [Azad *et al.* \(2017\)](#) investigated the effect of fault opening on the onset and growth of dynamic slip where no fluid diffusion is considered.

Although these models differ in concept and methodology, they all agree on the importance of the initial stress along the fault on the aspects of dynamic rupture, which may dominate the pressure perturbation. The latter mainly control the onset of the seismic rupture.

1.8.4 Models following the seismicity rate model proposed by [Dietrich \(1994\)](#)

[Dietrich \(1994\)](#) proposed a 0-D model able to estimate the seismicity rate following a stressing rate perturbation. In this approach, the fault is modelled via a population of non-interacting nucleation sources, in which each can rupture independently. The nucleation sources are governed by rate and state friction behavior ([Dietrich, 1972](#); [Rice and Ruina, 1983](#)), with a state variable that depends on slip and normal stress ([Linker and Dietrich, 1992](#)). In this context, the seismicity rate writes:

$$R = \frac{r}{\gamma \dot{\tau}_r}, \quad (1.3)$$

where r is the background seismicity rate at the reference shear stressing rate $\dot{\tau}_r$, and γ is a state variable that evolves with time and stressing history as follows

$$d\gamma = \frac{1}{a\sigma} \left(dt - \gamma d\tau + \gamma \left(\frac{\tau}{\sigma} - \alpha \right) d\sigma \right), \quad (1.4)$$

where a in the rate and state frictional parameter, σ is the effective stress, t is time, τ is the shear stress and α is a non-dimensional constant ([Linker and Dietrich, 1992](#)). Several studies use this approach to investigate injection induced seismicity.

In particular, [Segall and Lu \(2015\)](#) coupled this model with poro-elasticity in the context of a constant rate fluid injection into a homogeneous full space. They showed that poro-elastic effects dominate over pressure diffusion at large distances. [Chang and Segall \(2016\)](#) extended this model by considering a layered geometry with basement faults, to explore the effect of the fault properties and geometry. The same model was later used by [Chang *et al.* \(2018\)](#) to investigate the key parameters controlling post-injection seismicity, as medium permeability and history of injection rates. Beyond poro-elastic effects, [Barbour *et al.* \(2017\)](#) used this model to investigate the effect of varying the injection rate on induced seismicity, on which the seismicity rate turned out to be largely dependent.

More recently, this seismicity rate model was coupled with the injection history for Oklahoma and Kansas and was used to investigate the observed seismicity. In particular,

Norbeck and Rubinstein (2018) investigated the observed time lag between injection rate and seismicity rate; whereas Dempsey and Riffault (2019) assessed the effectivity of the volume reduction plan proposed to reduce the induced seismicity rate in Western Oklahoma.

The use of such model in the context of injection induced seismicity can be very advantageous, as it is very easy to couple it with pressure and stress perturbations. The use of rate and state friction introduces possible time delays in the seismic response. Such model can be quite effective to forecast real cases seismicity rates if calibrating data is available. However, it does not allow the investigation of the magnitudes of induced seismic events, nor their location with respect to the injection source, and it ignores static triggering.

1.8.5 Burridge-Knopoff based models (Burridge and Knopoff, 1967)

The Burridge and Knopoff model (Burridge and Knopoff, 1967) consists of a 1-D series of spring-slider systems, where each mass slider contacts a frictional surface from one side, and is subjected to tectonic loading on the other side. The spring-slider systems can slip independently. Several studies use this approach to model the seismicity along a fault, for instance Baisch *et al.* (2010) coupled it with fluid diffusion considering a slip-dependent permeability and where the seismic rupture obeys the Coulomb criterion. Turuntaev and Riga (2017) then extended the multiple spring slider system model by incorporating rate and state friction.

Such model generates seismic events with magnitude characterization. In particular, Baisch *et al.* (2010) argued that large magnitude events observed after shut in may be driven by a geometric effect of the reservoir associated with the pressure diffusion; whereas Turuntaev and Riga (2017) showed the existence of a tradeoff between the number of induced seismic events and their magnitude content. However, such model oversimplifies the stress interactions between the different asperities along the fault.

1.8.6 Frictional Fault Models

In such models, the fault is modeled as a linear segment (1-D fault embedded into a 2-D medium), or a planar fault (2-D fault plane embedded in a 3-D medium), in which the sliding behavior along the fault is governed by friction. The latter can be considered constant (Coulomb static friction), can follow a slip weakening law (friction decreases with slip), or can be governed by rate and state friction (friction does not depend only on slip, but on an additional state variable as well). The advantage of such models is the possibility to build synthetic seismicity catalogs with events location, nucleation time and magnitude. In general such models take into consideration mechanical stress interactions between the different elements along the fault. We present here some attempts to couple

these models with fluid flow or injection, and the resulting contributions. To simplify the presentation of the different models, we list in Table 1.2 the fault model, the friction and the fluid flow used in each study.

Study	Fault Model	Friction	Fluid Flow
McClure and Horne (2011)	2-D model	Rate and State	Non-linear diffusion
Cappa and Rutqvist (2011b)	2-D model	Static friction	Non-linear diffusion
Cappa and Rutqvist (2011a, 2012)	2-D model	Slip weakening	Non-linear diffusion
Aochi <i>et al.</i> (2014)	3-D model	Coulomb friction	Non-linear diffusion (porosity & fault width evolution)
Dietrich <i>et al.</i> (2015)	3-D model	Rate and State	Linear diffusion
Kroll <i>et al.</i> (2017)	3-D model	Rate and State	Linear diffusion
Cappa <i>et al.</i> (2018)	2-D model	Rate and State	Non-linear diffusion
Dublanchet (2019)	2-D model	Rate and State	Linear diffusion

²[Note.] 2-D model: 1-D fault embedded in a 2-D medium; 3-D model: 2-D fault embedded in a 3-D medium.

Table 1.2 – List of the main components (fault model, friction law and fluid flow) of some frictional fault models.

In particular, McClure and Horne (2011) investigated post-injection seismicity which they found to be controlled by the diffusion of pressure. Their model also predicted that production of fluid from the well may help reduce shut-in seismic activity. Dietrich *et al.* (2015) also investigated the rate of post-injection seismicity and found that it obeys an Omori law decay (Omori, 1894).

Cappa and Rutqvist (2011b) explored shear induced permeability enhancement and showed how it can promote fault instability. On the other hand, Aochi *et al.* (2014) considered the healing process and found that when the permeability of the fault decreases following a slip event, the fluid can get trapped inside the fault.

Cappa and Rutqvist (2012) investigated the expansion of the dynamic slip with respect to the pressurized zone in the context of a CO₂ injection, whereas Cappa *et al.* (2018) investigated the influence of the fault hydromechanical properties on the growth of injection-induced aseismic slip.

Finally, Cappa and Rutqvist (2011a) explored the effect of the stress anisotropy. Kroll *et al.* (2017) investigated the effect of initial stress and frictional properties of the fault on

induced seismicity while [Dublanche et al. \(2019\)](#) explored their effect of the induced aseismic crack expansion.

1.9 Research Motivation

We have presented so far a broad review of numerous observations about fluid induced fault reactivation. Then, we have discussed contributions from various injection experiments (at different scales) as well as the main recent numerical studies dedicated to hydro-mechanical fault reactivation. As showed, the response of a pre-existing fault to fluid injection activities can be highly variable. We observe:

- seismic and aseismic induced response,
- event clustering or event migration away from the injection source,
- short and long time delay to induced response, and post-injection seismicity,
- change in magnitude content.

A lot of mechanical parameters seem to influence slip reactivation:

- initial stress conditions,
- fault frictional properties,
- fault hydro-mechanical properties (permeability, porosity, roughness, etc),
- rock medium hydro-mechanical properties,
- localization of the fault or pre-existing fracture with respect to the injection source,
- injection operations properties (injection pressure, injection rate, injected volume).

Even though the dense monitoring and extensive studies of real case observations can give a lot of information and shed the light into the effect of the different parameters, there is still a lot of aspects that are not fully explored nor understood. We aim in this thesis to further investigate certain aspects of induced fault reactivation using numerical modeling. We investigate three main aspects:

(1) Explore the effect of injection parameters (in particular the pressure and pressure rate) on the magnitude and rate of induced events

Various correlations have been proposed between earthquake frequency and injection pressure ([Raleigh et al., 1976](#); [Keranen et al., 2014](#)) or injection rate ([Gibbs et al., 1973](#); [Weingarten et al., 2015](#)). More recently, the seismicity rate in Oklahoma was observed to follow the pressure rate variation along the fault ([Langenbruch and Zoback, 2016](#)). Several observations correlated the injected volume either to the maximum magnitude of

induced earthquakes (Shapiro *et al.*, 2007; McGarr, 2014) or to the number of seismic events (Van der Elst *et al.*, 2016). On the other hand, according to numerous numerical studies the extent of dynamic rupture length is weakly sensitive to injection perturbation and rather dependent on the initial stress state of the fracture (Garagash and Germanovich, 2012; Galis *et al.*, 2017; Azad *et al.*, 2017).

Numerous models have been proposed to investigate the effect of varying injection rate, pressure, etc., on the seismicity and magnitude content (e.g. McClure and Horne (2011), Barbour *et al.* (2017) and Dempsey and Riffault (2019)). However, they either considered simplified stress interactions, or considered homogeneous frictional parameters.

Here we propose to explore how the injection protocol could affect the seismicity rate and the magnitude distribution in the context of a fully heterogeneous fault governed by rate and state friction. Moreover, we discuss how the behavior of such a heterogeneous fault could differ from (1) typical homogenous ones, and (2) simplified seismicity rate models following Dietrich (1994).

(2) Explore the effect of the frictional behavior of the fault in the response to fluid injection

Several observations suggest a dependence between the frictional properties of the fault and its response to fluid injection. In particular, Dorbath *et al.* (2009) observed different characteristics for induced seismicity for two hydraulic fracturing operations in Soultz-sous-Forêt, only 450 m apart. Moreover, fault frictional properties are suspected to have affected the induced seismic response during the hydraulic stimulations in Soultz-sous-Forêt, Basel and Cooper Basin (McClure and Horne, 2014), while weak geological structures were correlated with the locations of induced seismic events in Oklahoma (Shunping *et al.*, 2018).

Several studies emphasized on the effect of the frictional behavior of a fault (e.g. Kroll *et al.* (2017), Galis *et al.* (2017) and Dublanquet (2019)). However, none of these studies consider frictional heterogeneity along the fault plane. Nonetheless, evidence of heterogeneous fault material was reported by Fagereng and Sibson (2010). As well, the observation of seismic repeaters along existing faults (Nadeau and Johnson, 1998; Lengline and Marsan, 2009) suggests the existence of relatively stable and unstable patches along the faults. For this reason, we are particularly interested to model heterogeneous faults. *Here we investigate how different frictional parameters distribution along the fault plane could influence its response to fluid injection.*

(3) Investigate hydraulic diffusivity enhancement during laboratory injection induced fault reactivation experiments

While investigating the effect of the injection parameters and the fault frictional properties, we assume in our numerical approach a time-independent diffusivity. However,

permeability enhancement, associated with effective stress reduction and fault reactivation process, has been widely observed during fluid injection activities, in the context of laboratory experiments (e.g. [Zoback and Byerlee \(1975\)](#), [Baghbanan and Jing \(2008\)](#), [Ghabezloo *et al.* \(2009\)](#) and [Rutter and Mecklenburgh \(2018\)](#)), as well as in-situ injection tests ([Guglielmi *et al.* \(2015b\)](#), [Duboeuf *et al.* \(2017\)](#) and [Bhattacharya and Viesca \(2019\)](#)).

To better understand how these two processes (reduction of effective normal stress and slip activation) combined can affect the evolution of the permeability or hydraulic diffusivity throughout an injection test, *we conducted laboratory injection tests in collaboration with François Passelègue from EPFL, Lausanne, during which we measured the pressure history at two different locations along the experimental fault plane. We then developed and applied deterministic ([Plessix, 2006](#)) and probabilistic ([Metropolis *et al.*, 1953](#); [Hastings, 1970](#)) inversion to the experimental pressure measurements, in order to estimate the time history of the hydraulic diffusivity throughout the injection test.* This allowed us to analyse the diffusivity variation with respect to the reduction of the mean effective stress and average shear slip along the fault plane.

The ultimate objective is to use such information in order to build a fully coupled hydro-mechanical model, which would allow us to compute pressure and shear displacements taking into consideration hydraulic diffusivity evolution. We can compare the results of such simulations with the experimental strain data, to further understand the relation between the fluid and the slip front.

1.10 Thesis and Manuscript Overview

The rest of this manuscript is organized as follows:

- Chapter 2

This chapter is dedicated to studying how some injection parameters could influence the characteristics of induced seismic activity, in the context of a punctual simplified injection protocol in a heterogeneous 1-D fault embedded in a 2-D medium, able to produce complex and irregular rupture sequences.

For this, *we develop and couple a linear injection and diffusion model with an earthquake simulator* previously developed by [Dublanche \(2018\)](#), considering a Dietrich-Ruina heterogeneous fault ([Dietrich, 1972](#); [Rice and Ruina, 1983](#); [Linker and Dietrich, 1992](#)). This allows us to build a synthetic seismicity catalog evaluating events time, location, magnitude.

We first use this model to show how the seismicity and the magnitude histories are highly sensitive to the changes of pressure and pressure rate along the fault. Then, we explore the variability of the seismic response with respect to the imposed injection parameters.

This chapter is published in the Journal of Geophysical Research, Solid Earth (Almakari *et al.*, 2019). The content (text, figures) of this article was not modified.

- Chapter 3

This chapter is dedicated to explore the effect of the fault frictional parameters on the injection induced seismic response. In order to test different stability conditions along the fault, we generate four additional heterogeneous fault configurations, and we use the same numerical model presented in chapter 2. *First we show that the general dependence of induced seismicity on the injection parameters that we observed in the previous chapter remains valid for the different fault configurations tested here. And then we show that faults having a more stable frictional behavior can resist more to fluid injection as they exhibit a lower induced seismicity rate and generate a lower seismic moment.*

- Chapter 4

In this chapter, *we use laboratory injection experiments conducted on a saw-cut fault in an Andesite rock sample, under triaxial loading.* During the injection tests, we measure the pressure history at two different locations along the fault plane. We then apply numerical inversion to the experimental data, which allows us to characterize the hydraulic diffusivity history along the fault throughout the injection test. For this, *we developed and implemented: (1) a gradient-based deterministic approach (Plessix, 2006), (2) and a probabilistic one based on the Markov Chain Monte Carlo algorithm (Metropolis et al., 1953; Hastings, 1970); to the 2-D pressure diffusion process along the fault plane.* We then applied this method to the experimental data and showed to what extent we can be confident with the inverted results using such algorithms. *We finally investigate the observed diffusivity temporal variations throughout the injection tests with respect to the reduction in effective stress and shear slip accumulation.*

The numerical method and the results presented in this chapter are submitted for publication in *Geophysical Journal International*.

- Chapter 5

In this final chapter, we summarize and discuss the main conclusions of this thesis, and expose the principal perspectives and work in progress.

Contributions

In my thesis, I developed a linear pressure diffusion code in 1-D using a finite difference method, taking into consideration different boundary conditions. I then coupled it with

an existing rate and state earthquake simulator (Dublanche, 2018), which I use in Chapter 2 and 3. The code is written in Fortran 90 and parallelized using MPI library (Pacheco, 1997). With this code, I constructed a large database (event time, location, and magnitude) of synthetic induced earthquakes (on five different 2-D heterogeneous fault configurations). The main challenge was in generating a continuous heterogeneous 2-D fault, in which each asperity can nucleate a seismic rupture, independently of the others (Rubin and Ampuero, 2005), and that is able to generate a complex pattern of seismic ruptures, with magnitudes obeying Gutenberg-Richter distribution (details in Chapter 2). I also applied the 0-D seismicity rate model proposed by Dietrich (1994) to my coupled fault – fluid diffusion model, and compared and discussed the results and limitations of such approach with respect to the continuous fault that we propose. Moreover, I extended the diffusion code to a 2-D elliptical fault configuration, considering Neuman boundary conditions, using a finite volume method. I make use of this code to solve the diffusion process in the experimental injection tests in Chapter 4. Finally, I implemented and developed the deterministic and probabilistic inversions, that I use in Chapter 4 as well. The main challenges for the deterministic approach were the gradient estimation and the manipulation of the initial and boundary conditions for such an elliptical fault. Whereas, for the probabilistic approach, it was the adjustment of the different parameters in order to achieve a good acceptance rate (details in Chapter 4).

Concerning the real data experiments presented in Chapter 4, the experimental work is a collaboration with François Passelègue, from EPFL, Lausanne, during which I participated in the laboratory experiments.

Finally, parts of my thesis work have been presented during international workshops and conferences:

- M. Almakari, P. Dublanche, H. Chauris, (2017). Injection - Induced Seismicity in a "Rate-and-State" Asperity Model. International workshop: Earthquakes: Nucleation, triggering, rupture and relationship with aseismic processes, Cargèse, Corsica (*Poster presentation*).
- M. Almakari, P. Dublanche, H. Chauris (2018). Injection-induced seismicity controlled by the pore pressure rate. EGU General Assembly, Vienna (*Oral presentation*).
- M. Almakari, P. Dublanche, H. Chauris (2018). Dependence of Injection-Induced Seismicity on the Injection Scenario. AGU Fall Meeting, Washington D.C. (*Poster presentation*).
- M. Almakari, F. Passelègue, P. Dublanche (2019). Shear induced fluid flow and permeability enhancement during fluid injection laboratory experiment. Schatzalp 3rd Induced Seismicity Workshop, Davos, Switzerland (**Fellowship applicant** – *Poster presentation*).

As well, part of the results is published / submitted, in review:

- M. Almakari, P. Dublanchet, H. Chauris, F. Pellet (2019). Effect of the Injection Scenario on the Rate and Magnitude Content of Injection-Induced Seismicity: Case of a Heterogeneous Fault. *Journal of Geophysical Research: Solid Earth*, 124. <https://doi.org/10.1029/2019JB017898>.
- M. Almakari, H. Chauris, F. Passelègue, P. Dublanchet, A. Gesret. Fault's Hydraulic Diffusivity Enhancement During Injection Induced Fault Reactivation: Application of Pore Pressure Diffusion Inversions to Laboratory Injection Experiments. *Submitted, in review to Geophysical Journal International*.

Following the requirements of MINES ParisTech, since this manuscript is written in English, we include at the beginning of each chapter a small summary in French.

Chapter 2

Effect of the injection scenario on the rate and magnitude content of injection-induced seismicity: Case of a heterogeneous fault

Contents

2.1	Abstract	51
2.2	Introduction	51
2.3	Model	53
2.4	Results	61
2.4.1	Background Seismicity	61
2.4.2	Response to Fluid Injection	61
2.4.3	Sensitivity Analysis	64
2.5	Discussion	75
2.6	Conclusion	79
2.7	Appendix A: Analytical Solution of the Diffusion Equation	80
2.7.1	Injection Phase 1 ($t_i < t < t_r$):	80
2.7.2	Injection Phase 2 ($t_r < t$):	80
2.8	Appendix B: Estimation of the Background Stressing Rate	80
2.9	Appendix C: Analytical Seismicity Rate model following Dietrich (1994)	81
2.9.1	Injection Phase 1 ($t_i < t < t_r$):	82
2.9.2	Injection Phase 2 ($t_r < t$):	82
2.10	Supporting Information	82

In this chapter, the model and the results are presented as a journal article, that had undergone full peer review and was published on the 22 of July 2019, in the scientific journal: Journal of Geophysical Research: Solid Earth (doi: 10.1029/2019JB017898).

Résumé du Chapitre 2 en Français

Comme évoqué précédemment, l'injection de fluides dans des formations souterraines peut réactiver les failles pré-existantes et modifier le risque sismique. Actuellement, différents aspects de la sismicité induite restent mal compris, notamment l'effet des différents paramètres d'injections. Ce chapitre est alors dédié à étudier l'effet de la pression d'injection et du taux de pression sur le taux de sismicité induite et la distribution de magnitude des événements. Afin de modéliser la sismicité déclenchée par un fluide circulant à l'intérieur d'une faille, on couple un modèle de faille rate and state 2D hétérogène, avec un modèle d'injection ponctuelle au centre de la faille et de diffusion linéaire 1D le long de la faille. La faille hétérogène étudiée peut générer des séquences d'événements irrégulières, avec des magnitudes qui suivent la distribution Gutenberg Richter.

En premier lieu, on montre qu'une telle injection de fluide conduit à une forte augmentation du taux de sismicité. On observe une corrélation temporelle entre le taux de sismicité et le taux de pression de pore qui gouverne la faille. La perturbation de sismicité s'arrête lorsque la pression de pore atteint un régime stationnaire sur la faille.

Dans la deuxième partie de ce chapitre on montre que le taux de sismicité dépend fortement de la pression d'injection: l'amplification de la sismicité est plus importante pour des pressions plus grandes. De même, l'amplitude de la perturbation de sismicité augmente avec les valeurs du taux de pression d'injection, tant qu'un certain seuil de taux de pression n'est pas dépassé. Au-delà de ce seuil, l'augmentation du taux d'injection produit des événements de grandes magnitudes plus fréquemment. Dans ce cas, la comparaison de notre modèle avec le taux de sismicité proposé par [Dietrich \(1994\)](#) met en relief la relation qui existe entre le taux de sismicité et la variation de la distribution de magnitude.

2.1 Abstract

Injection of fluids into underground formations reactivates preexisting faults and modifies the seismic hazard, as demonstrated by the 2011 M_w 5.7 and the 2016 M_w 5.8 earthquakes in Oklahoma. Currently, the effect of injection remains poorly understood. We model the seismicity triggered by a fluid flowing inside a Dietrich-Ruina heterogeneous 2-D fault, which can generate irregular sequences of events with magnitudes obeying Gutenberg Richter distribution. We consider a punctual injection scenario where injection pressure increases at a constant rate until a maximum pressure is reached and kept constant. We show that such a fluid injection leads to a sharp increase in the seismicity rate, which correlates with the time series of the pore pressure rate, for a wide range of injection pressure. Increasing the final pressure leads to an increase in the amplitude and the duration of the seismicity rate perturbation but also to a decrease in the frequency of large magnitude events. The maximum seismicity rate during the sequence also increases with the injection pressure rate, as long as a pressure-rate threshold is not exceeded. Beyond it, the effect of increasing the injection rate is to make large magnitude earthquakes more frequent. While the total number of induced earthquakes is essentially controlled by the maximum pressure, the total seismic moment liberated increases with both the maximum pressure and the pressure rate. The comparison of our model to Dietrich's [1994] model shows the important trade-off existing between seismicity rate perturbations and magnitude content variations of fluid induced seismicity.

2.2 Introduction

It has been acknowledged, since the 1960s, that injection of fluids into underground formations alters the stresses on the Earth's crust, inducing micro earthquakes and modifying the seismic hazard (Simpson, 1986). Fluid injection could be related to different human activities, such as wastewater disposal (Healy *et al.*, 1968; Horton, 2012; Ellsworth, 2013), hydrofracturing (Kanamori and Hauksson, 1992; Holland, 2011) and production of geothermal energy (Majer *et al.*, 2007; Deichman and Giardini, 2009; Bachmann *et al.*, 2011). Wastewater disposal seems to represent the highest risk, as it operates for longer duration and injects much more fluid (Ellsworth, 2013).

Beyond microseismic activities, many significant earthquakes were suspected to be injection-induced events, with moment magnitudes exceeding 3: the M_w 4.85 in Rocky mountain arsenal (Healy *et al.*, 1968; Hermann *et al.*, 1981), the 1967 M_w 5.5 in Denver Colorado (Healy *et al.*, 1968; Davis and Frohlich, 1993), the four M_w 3 in Basel, Switzerland, between 2006 and 2007 (Deichman and Giardini, 2009), the 2011 M_w 4.7 in Guy, Arkansas (Horton, 2012), the 2011 M_w 5.3 in Trinidad, Colorado (Viegas *et al.*, 2012; Rubinstein *et al.*, 2012), the 2011 M_w 3.9 in Youngstown, Ohio (Kim, 2013; Skoumal *et al.*, 2014), the M_w 5.7 in Prague Oklahoma in 2011 (Keranen *et al.*, 2013; Van der Elst *et al.*, 2013; McGarr, 2014; Sumy *et al.*, 2014), the 2011 and 2012 M_w 4.8 in Texas (Froh-

lich *et al.*, 2014), and the 2016 M_w 5.8 earthquake in Pawnee, Oklahoma (Yeck *et al.*, 2016).

According to Healy *et al.* (1968) and Raleigh *et al.* (1976), injection-induced earthquakes correspond to fault reactivation, triggered by an increase of the fluid pore pressure. In fact, the failure along the fault is reached when the stress on the fault exceeds its frictional strength τ . The latter is proportional to the effective normal stress (Byerlee, 1978), following:

$$\tau = \tau_0 + \sigma_{\text{eff}}\mu, \quad (2.1)$$

where τ_0 is the cohesive strength, σ_{eff} the effective normal stress ($\sigma_{\text{eff}} = \sigma_T - p$), μ is the friction coefficient, σ_T the lithostatic normal stress, and p the pore pressure. Thus, an increase of pore pressure can decrease the effective normal stress, and consequently decrease the frictional strength on a fault close to failure. Some authors argue that earthquakes are triggered if the pore pressure exceeds a critical pressure threshold (Hubert and Rubey, 1959; Healy *et al.*, 1968; Raleigh *et al.*, 1976), while Frohlich (2012) considers that a seismic event can be induced when the injection rate reaches a critical rate and the permeability of the medium allows the fluids to reach a suitably oriented fault.

Even though it has been acknowledged that injection-induced earthquakes are caused by either direct pore pressure effects or poroelastic stress changes, currently, the main controlling parameters of injection-induced seismicity remain poorly understood. With the increasing number of induced earthquakes, it is crucial to identify the key parameters governing this phenomenon. The injection scenario, in terms of injection pressure or injection rate, was observed to be an essential parameter controlling the induced seismicity. For instance Frohlich (2012) observed that fluid injection can induce seismicity only if the injection pressure and injection rate are large enough, in the presence of a favorably oriented fault. It was also observed that the seismicity in Oklahoma rose 20 years after injection started, however only 5 years after an abrupt increase in the wellhead pressure (Keranen *et al.*, 2013). On the other hand, Langenbruch and Zoback (2016) proposed a diffusion model for the seismicity in Oklahoma that can explain the previous induced seismic sequences, and found that by decreasing the injection rate, the pore pressure rate at 3 km depth can decrease and can lead to a drop in the seismicity rate. Dempsey and Riffault (2019) proposed a numerical model for the seismicity rate in Oklahoma and also showed that a reduction in injection rate may lead to a decrease in the seismicity rate, while the characteristic time to reach the background seismicity level depends on the magnitude of the injection rate reduction.

Many numerical models have been proposed to study the reactivation of fault slip and the triggering of seismic activity, such as spring slider systems (Baisch *et al.*, 2010) or a homogeneous planar fault (Aochi *et al.*, 2014), both governed by Coulomb friction. In the latter case, the friction μ is considered to be constant, and thus time-dependent characteristics of fault friction (healing for instance) are not taken into account. Alternatively, rate- and state-dependent friction law (Dietrich, 1979; Ruina, 1983) considers the effects of both sliding speed and the history of the sliding surface and allows for healing

and multiple successive reactivations. It is therefore better suited to explain features of the earthquake cycle. Various models based on the rate- and state-dependent friction have been developed, like a multidegree of freedom spring-slider system by [Turuntaev and Riga \(2017\)](#), a homogeneous rate-weakening fault by [McClure and Horne \(2011\)](#) and [Kroll *et al.* \(2017\)](#), or based on the seismicity rate model proposed by [Dietrich \(1994\)](#) as [Segall and Lu \(2015\)](#), [Barbour *et al.* \(2017\)](#) and [Chang *et al.* \(2018\)](#). But these models either have not fully explored the role of injection history or considered simplified stress interactions. The alternative modelling approach by [Garagash and Germanovish \(2012\)](#) and [Azad *et al.* \(2017\)](#) is to study the effect of hydrofracturing on the onset of dynamic slip, but in their model the seismic cycle was not modeled: It is not possible to determine the magnitudes or the rate of the induced seismicity. Some of these latter models studied the effect of changing the flow rate on the induced seismicity. In particular [Barbour *et al.* \(2017\)](#) showed that for an equivalent injected volume, a variable injection rate may lead to a larger seismicity rate increase compared to the one under constant injection rate, while [Chang *et al.* \(2018\)](#) showed that a gradual decrease in injection rate can reduce postinjection seismicity rate. However, none of these two models take into consideration the magnitude content of the induced seismic events. On the other hand, [Rutqvist *et al.* \(2013\)](#) investigated the effect of variable injection rate on the magnitude of the seismic rupture in the context of hydraulic fracturing of shale gas reservoirs; however, this study only focused of the first hydraulic rupture. More extensive work is needed to fully understand the role of the different injection parameters on the different features of seismic activity.

Here we systematically study the effect of the fluid injection scenario on the features of induced seismic activity along a planar heterogeneous fault with rate- and state-dependent friction ([Dietrich, 1979](#); [Ruina, 1983](#)), and effective normal stress dependent state variable ([Linker and Dietrich, 1992](#)). Our model considers fault frictional heterogeneous behavior, so as to produce a realistic seismic activity in terms of seismicity rate and magnitude distribution. We couple a 2-D rate- and state-dependent asperity model ([Dublanche, 2018](#)), with a 1-D fluid diffusion model along the fault segment. We test over 196 different injection scenarios by changing the injection rate, the maximum pressure at the well head, and the diffusive boundary conditions. We aim to define the principal parameters controlling the rate and the magnitudes of induced events.

2.3 Model

We consider a linear planar heterogeneous fault sheared between two 2-D elastic half-spaces (Figure 2.1a). The fault slips in mode III. Outside a finite segment of size L_0 (in this study $L_0 = 1,754.5$ m, see Table 2.1), we assume a constant slip rate V_0 ($V_0 = 10^{-9}$ m/s), while inside the finite segment, slip is resisted by heterogeneous rate-

and state- dependent friction, defined as

$$\tau = \sigma_{\text{eff}}\mu = \sigma_{\text{eff}} \left[\mu_0 + a(x) \ln \left(\frac{V}{V_0} \right) + b(x) \ln \left(\frac{V_0\theta}{d_c(x)} \right) \right], \quad (2.2)$$

where $\tau = \tau(x, t)$ is the frictional strength depending on time t and along strike distance x , $\sigma_{\text{eff}} = \sigma_{\text{eff}}(x, t)$ is the effective normal stress ($\sigma_{\text{eff}}(x, t) = \sigma_{\text{T}} - p(x, t)$, where σ_{T} is a constant lithostatic normal stress and $p(x, t)$ in the pore pressure), $\mu = \mu(x, t)$ is the friction, μ_0 is the reference friction coefficient, $a(x)$ and $b(x)$ are the constitutive parameteres, $V = V(x, t)$ is the sliding velocity, $\theta = \theta(x, t)$ is the state variable, and $d_c(x)$ is the characteristic distance. [Dietrich \(1979\)](#) and [Ruina \(1983\)](#) interpreted the state variable as a characteristic contact lifetime and proposed an evolution law, called “aging law”:

$$\frac{d\theta}{dt} = 1 - \frac{V\theta}{d_c}, \quad (2.3)$$

where state and thus friction evolve even with stationary contact. According to [Rice and Ruina \(1983\)](#), the state evolution law may also depend on prior normal stress. Following a step increase or decrease in normal stress, the state variable (and consequently shear strength) experiences a sudden increase, or decrease, respectively ([Linker and Dietrich, 1992](#)). This effect could be formulated as:

$$\frac{d\theta}{d\sigma} = -\frac{\alpha\theta}{b\sigma}, \quad (2.4)$$

where α is a nondimensional constant varying between 0.2 and 0.6. In our modeling approach, we couple equation (2.3) with equation (2.4) to take into consideration the reduction of the effective stress effect resulting from the increase of pore pressure after fluid injection:

$$\dot{\theta} = 1 - \frac{V\theta}{d_c(x)} - \frac{\alpha\theta}{b(x)\sigma_{\text{eff}}}\dot{\sigma}_{\text{eff}} = 1 - \frac{V\theta}{d_c(x)} + \frac{\alpha\theta}{b(x)(\sigma_{\text{T}} - p)}\dot{p}. \quad (2.5)$$

We define a linear fault with a heterogeneous distribution of the rate and state constitutive parameters a and b . We propose a combination of velocity-weakening and velocity-strengthening patches along the fault, noted in the following as VW and VS, respectively. Each patch is characterized by a particular set (a, b, d_c) of rate and state parameters. The friction coefficient on the fault is governed by the the ratio $r(x) = a(x)/b(x)$. The fault exhibits a velocity weakening or velocity strengthening behavior, for r smaller or bigger than 1, respectively. While the VW patches (called “asperities”) are more likely to break under seismic loading, the VS ones (called “creeping areas” or “barriers”) slide aseismically most of the time. Although the effect of injection on the aseismic slip is not the purpose of this study, we considered VS as a way to increase seismic complexity. On the VW patches, $a = a_w = 3.10^{-4}$ and $b = b_w = 7.10^{-4}$, giving $r \approx 0.43$, while on the VS patches, $a = a_s = 7.2.10^{-3}$ and $b = b_s = 5.9.10^{-3}$, giving $r = 1.2$ (values from [Table 2.1](#)). Moreover, we consider a heterogeneous distribution of the different patch sizes. We sample 58 different patches, where the half length of the different patches is distributed

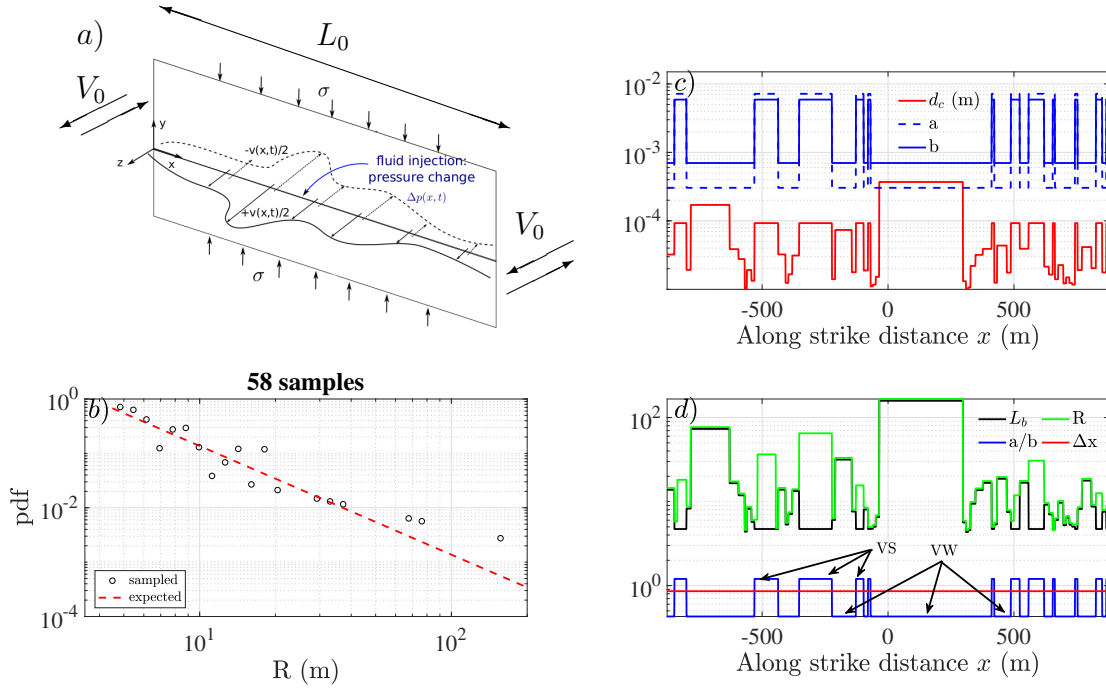


Figure 2.1 – Fault model: (a) Fault system (Mode III): Geometry, slip rate V , length of the fault L_0 (≈ 1.75 km, from Table 2.1), and boundary conditions (far-field normal stress σ and constant slipping rate V_0 at the edges of the model, values in Table 2.1), modified from [Dublanche \(2018\)](#). (b) Frequency distribution of the half lengths R of the fault patches. (c) Distribution of a and b rate- and state-dependent frictional parameters, as well as the critical slip distance d_c along the fault. (d) Distribution of the patch half size R , $L_b = Gd_c/b\sigma$, the ratio of frictional parameters a/b , and the computational cell size Δx , along the fault.

following a power law with a -2 exponent (see Figure 2.1b). We constrain the size of the patches to always exceed the critical size $L_b = Gd_c/b\sigma$ (G is the shear modulus of the elastic medium, value in Table 2.1), so that the different VW patches are able to rupture seismically ([Rubin and Ampuero, 2005](#)). In this study we choose R to vary in the range $[4.5\text{--}167]$ m. Figure 2.1b represents the distribution of the half length of the patches, showing $R_{\min} \approx 4.84$ m and $R_{\max} \approx 167$ m. The 58 samples are randomly distributed along the fault segment. We then assign for each patch a VW or VS behavior, in order to verify a density of asperity ρ of 0.7 ($\rho = L_a/L_0$, where L_a represents the VW length, that is, the summation of the lengths of the VW asperities). Figure 2.1c represents the distribution of the a and b parameter along the fault, while in Figure 2.1d represents the ratio a/b . These values correspond to values found in the laboratory ([Marone, 1998](#)). The choice of $d_c(x)$ was made as follows: It was observed that fracture energy G_f scales with slip δ ([Ohnaka, 2003](#); [Abercrombie and Rice, 2005](#)), as follows $G_f = a\delta^\gamma$, where a and γ are constants; in the context of rate and state friction, the fracture energy is

approximately proportional to the critical slip distance $G_f \propto d_c$ (Rubin and Ampuero, 2005); on the other hand, from elasticity, the slip δ is proportional to the patch size $2R$ and hence to R : $\delta \propto R$. By substituting these two relations in the fracture energy scaling law, we get a proportional relation between the critical slip distance and the patch size $d_c \propto R^\gamma$. In this study we therefore consider a heterogeneous distribution of d_c along the fault; we assume $\gamma = 1$ and propose a space-depending critical slip distance $d_c(x)$ on the VW patches defined as follows: $d_c(x) = d_{c0}R(x)/R_{\min}$, where d_{c0} is the minimum critical slip distance. The minimum and maximum values of d_c are chosen in a way to ensure that $R_{\min} > \min(L_b) = G(d_{c_{\min}})/b\sigma$, and $R_{\max} > \max(L_b) = G(d_{c_{\max}})/b\sigma$. Thus, d_c varies in the range [0.01–0.37] mm, in agreement with values found in the laboratory (Marone, 1998). On the other hand, d_c on the VS patches is considered constant noted d_{cs} , its value was chosen to ensure a good discretization of the VS patches, which will be discussed later. Figure 2.1c represents the distribution of d_c along strike of the fault, while in Figure 2.1d we can compare the values of R and L_b along strike of the fault. This approach involving a heterogeneous distribution of patch sizes along with scale dependent d_c (on fracture energy) was originally developed by Ide and Aochi (2005) to study dynamic ruptures. One of the advantages of our numerical description is the possibility to model the entire seismic cycle and to take into consideration both the weakening and strengthening behaviors of the fault, so that one segment can be reactivated several times, and complex ruptures of multiple sizes can be generated.

We suppose a punctual injection of liquid water into the center of the fault (Figure 2.1a). We increase the pore pressure at the center ($x = x_c$) linearly with time from the beginning of the injection at $t = t_i$ to $t = t_r$ following a slope β to reach a certain maximum pressure p_{\max} , then maintain it constant until the shut-in of the fluid injection at $t = t_{\text{end}}$. We consider that the pore pressure at the injection point drops with the same injection slope β after shut in.

$$p(x_c, t) = \begin{cases} 0 & \text{if } t < t_i \\ \beta(t - t_i) & \text{if } t_i < t < t_r \\ \beta(t_r - t_i) = p_{\max} & \text{if } t > t_r \\ p_{\max} - \beta(t - t_{\text{end}}) & \text{if } t > t_{\text{end}} \end{cases} \quad (2.6)$$

We allow the fluid to diffuse along the fault segment, following the 1-D diffusion equation:

$$\frac{\partial p(x, t)}{\partial t} = D \frac{\partial^2 p(x, t)}{\partial x^2}, \quad (2.7)$$

where $p(x, t)$ is the pore pressure and D is the homogeneous diffusion coefficient defined as $D = K/(\varphi\mu c)$, where K is the permeability, φ is the porosity, μ is the viscosity and c is the summation of the pore fluid compressibility and the compressibility of pore volume due to pore pressure changes (Jaeger *et al.*, 2007). In this study we use typical values for those parameters giving $D = 0.005 \text{ m}^2/\text{s}$ (value in Table 2.1) (Jaeger *et al.*, 2007). Even though, it was observed that hydromechanical and frictional properties of the fault are coupled (Ikari *et al.*, 2009), for simplicity we neglect this effect and we consider only

the direct changes in pore pressure on the rate and magnitude of induced events. We assume that the simulations are isothermal and there is no chemical interaction between the liquid water and the rocks. At first, we assume Dirichlet boundary conditions and impose zero pressure at the edges of the finite fault segment. Other boundary conditions (Neuman) were tested and are discussed in the following section.

Finally, the far-field stressing and the heterogeneous slip distribution along the fault generate elastic stresses that could be approximated by the quasi-dynamic stress τ_e

$$\tau_e(x, t) = \frac{G}{2\pi} \int_{-\infty}^{+\infty} \frac{\delta'(s, t)}{s - x} ds - \eta v(x, t), \quad (2.8)$$

where G is the shear modulus of the elastic medium, δ' is the slip gradient and η is the damping coefficient ($\eta = G/2c_s$, where c_s is the shear wave velocity; Rice (1993); see Table 2.1 for values of G and η).

We assume that the frictional stress (equation (2.2)) balances the quasi-dynamic elastic stress (equation (2.8)). This balance, along with the state evolution law (equation (2.5)), the injection (equation (2.6)), and the diffusion equation (equation (2.7)) form a set of differential equations for the evolution of V , θ , and p along the fault. The system is solved using a fifth order adaptative time step Runge-Kutta algorithm (Fehlberg, 1969). We use the method proposed by Cochard and Rice (1997) to estimate the Hilbert transform of the slip gradient at each time step and thus solve equation (2.8). The fault is discretized into a set of $n = 2^{11} = 2,048$ equal computational cells of size Δx . To ensure continuity, Δx should be smaller than the characteristic size $L_b = Gd_c/b\sigma$ (Rubin and Ampuero, 2005). Since L_b depends of d_c which in turn is variable along the fault, then Δx should be smaller than the smallest L_b . Here we chose $\Delta x = 0.857$ m, giving $\Delta x / \min(L_b) = 0.2$ in all the computations, which is sufficient to ensure continuity. We also force Δx to be smaller than $L_{bs}/5 = Gd_{cs}/5b_s\sigma$ to ensure a good discretization on the VS patches. To satisfy this condition d_{cs} should be larger than $5\Delta x b_s\sigma/G$. Here we chose $d_{cs} = 1.1 * 5\Delta x b_s\sigma/G = 0.092$ mm. Figure 2.1d represents the distribution of L_b along the fault, along with the chosen Δx . We use the FTCS (forward difference approximation in time and a central difference approximation in space) explicit finite difference scheme to solve the diffusion equation, using the same spatial discretization. A sufficient criterion for the stability of the numerical resolution of the finite difference scheme is expressed as a condition on the time step Δt :

$$\Delta t \leq \frac{\Delta x^2}{2D}. \quad (2.9)$$

At each iteration, the time step estimated by the Runge-Kutta algorithm is checked against the stability condition (equation (2.9)).

For initial conditions, we imposed steady state $V = V_0$ and $\theta = \theta_0 = d_{c0}/V_0$ over the VS areas, and we assumed a random distribution of velocity and state variable for the VW

patches, where $\log_{10} V_0$ and $\log_{10} \theta_0$ are uniformly distributed between $[-19, -8]$ m/s and $[3, 4]$ s $^{-1}$, respectively. We let the fault evolve for several cycles while it loses the memory of the initial conditions, before studying the effect of fluid injection. In all the simulations presented below, injection starts at $t = 10$ years and ends at $t = 20$ years. Features of seismic activity before injection starts will be discussed in the next section. Figure 2.2.a shows an example of the evolution of the pore pressure profile along strike. In this example, the pressure at the edges of the fault segment is assumed to be 0 (Dirichlet boundary conditions). At first a transient state governs, where the pressure at the center increases and then stabilizes, while the pore pressure diffuses along strike. After some time, a steady state is reached. In the following, this time is noted t_s . The pressure distribution has been validated by comparison with an analytical solution (see Appendix A, section 2.7). In this figure, the black dashed line represents the pressure profile for $t = 0.4$ years after injection starts, estimated using equation (2.15). Figure 2.2b shows the effect of the injection parameters β and p_{\max} on the evolution of the pressure at one point ($x = 438$ m $\approx L_0/4$) with time. Different values of p_{\max} are represented by different colors, while two different values of β are presented by different line styles.

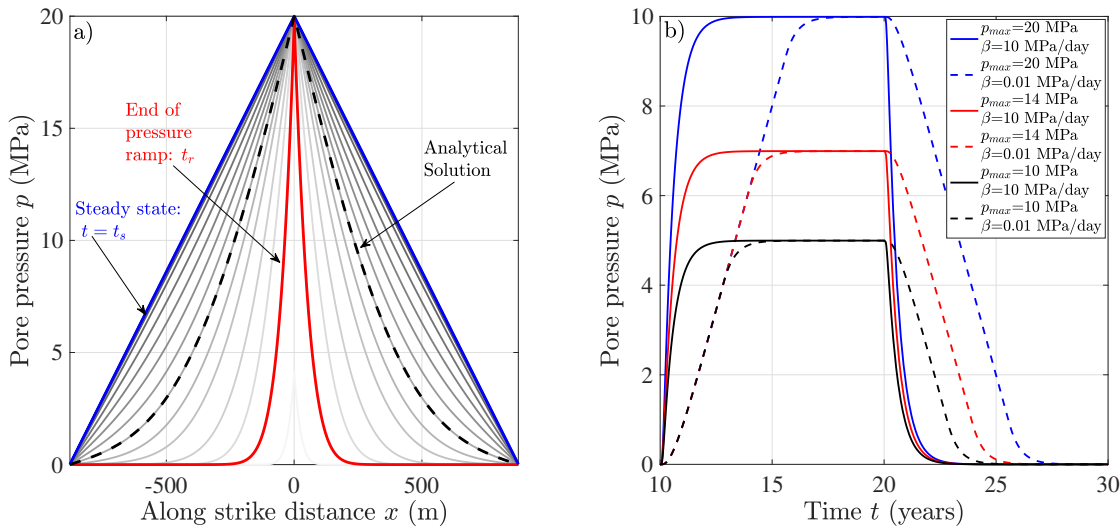


Figure 2.2 – (a) Evolution of the pore pressure profile along strike distance with time for one injection case ($p_{\max} = 20$ MPa and $\beta = 2$ MPa/day). Darker colors correspond to later times. The red and blue curves represent the pore pressure profile at $t = t_r$ and $t = t_s$, respectively. The dashed black line represents the pore pressure profile at $t = 0.4$ years after injection calculated using the analytical solution from Appendix A, section 2.7. (b) Evolution of the pressure at the point ($x = 438$ m $\approx L_0/4$) with time.

When the maximum slip rate exceeds a threshold velocity $v_{\text{dyn}} = a\sigma/\eta$ (Rubin and Ampuero, 2005), the radiation damping term becomes greater than the direct effect of rate- and state-dependent friction. In this case, the elastodynamic effects governs the system. We use this criteria to detect the earthquake onset and thus to create an

earthquake catalog for each simulation. Following each event, we estimate a rupture size L , and we compute the cumulative seismic moment released according to

$$M = GS \langle \delta \rangle, \quad (2.10)$$

where S is the surface of the rupture and $\langle \delta \rangle$ is the average slip. Since the model is 2-D, we use an equivalent rupture surface S defined as $\pi L^2/4$. The average slip is computed as

$$\langle \delta \rangle = \frac{1}{L} \int_{-L/2}^{L/2} (\delta(x, t_2) - \delta(x, t_1)) dx, \quad (2.11)$$

with t_1 and t_2 the onset and the end time of the earthquake. Thus the seismic moment would be

$$M = \frac{\pi GL}{4} \int_{-L/2}^{L/2} (\delta(x, t_2) - \delta(x, t_1)) dx. \quad (2.12)$$

Then, we estimate the moment magnitude M_w using the expression given by [Hanks and Kanamori \(1979\)](#):

$$M_w = \frac{2}{3} \log_{10}(M) - 6.06, \quad (2.13)$$

where M is expressed in Newton meters.

The physical parameters used in the next sections are presented in [Table 2.1](#).

Parameter	Symbol	Value	Comment
Length of the fault	L_0	1,754.5 m	Maximum magnitude expected $M_w \approx 4$
Sliding velocity	V_0	10^{-9} m/s	Typical relative plate motion
Friction coefficient	μ_0	0.6	(Marone, 1998)
Minimum half length of asperity	R_{\min}	≈ 4.84 m	Larger than the nucleation size
Maximum half length of asperity	R_{\max}	≈ 167 m	
Minimum characteristic distance	$d_{c_{\min}}$	0.01 mm	In agreement with values found in the laboratory (Marone, 1998)
Maximum characteristic distance	$d_{c_{\max}}$	≈ 0.37 mm	In agreement with values found in the laboratory (Marone, 1998)
Characteristic distance on VS patches	d_{c_s}	0.092 mm	In agreement with values found in the laboratory (Marone, 1998)
Damping coefficient	η	5 MPa s m^{-1}	(Rice, 1993)
Rate- and State- parameters	a_w	$3 \cdot 10^{-4}$	On VW patches
	a_s	$7.2 \cdot 10^{-3}$	On VS patches
	b_w	$7 \cdot 10^{-4}$	On VW patches
	b_s	$5.9 \cdot 10^{-3}$	On VS patches
Ratio a/b	a_w/b_w	≈ 0.43	On VW patches
	a_s/b_s	1.2	On VS patches
Normal stress	σ	100 MPa	Approximate lithostatic stress at 3 km depth
Shear modulus	G	30 GPa	Typical for a wide range of crustal rocks, sedimentary, metamorphic or igneous (Turcotte and Schubert, 2014)
Dynamic velocity	v_{dyn}	0.006 m/s	$v_{\text{dyn}} = a\sigma/\eta$ (Rubin and Ampuero, 2005)
α coefficient	α	0.23	in the range proposed by Linker and Dietrich (1992)
Diffusivity	D	$0.005 \text{ m}^2/\text{s}$	(Jaeger <i>et al.</i> , 2007)
Injection pressure	p_{\max}	0.5–20 MPa	Refer to section 2.4.3.1
Injection pressure rate	β	0.01– 10 MPa/day	Refer to section 2.4.3.1

¹[Note.]VW = velocity weakening; VS = velocity strengthening.

Table 2.1 – List of physical parameters

2.4 Results

2.4.1 Background Seismicity

Our main objective is to study the effect of fluid injection on the features of seismic activity. The features of seismic activity along the fault during 10 years before fluid injection are presented in Figures 2.3a1, 2.3b1, 2.3c, and 2.3f.

Figure 2.3a1 gives an idea about the time series of the moment magnitude and its mean value estimated using a centered sliding average, with a sliding window of 50 events. The proposed fault model can produce earthquakes of different moment magnitudes M_w in the range [0–3.5]. The cumulative number of earthquakes and the cumulative seismic moment released increase quasi-linearly in time, with an average of 170 earthquakes and $2.3 \cdot 10^{14}$ N m of seismic moment released per year (see Figure 2.3b1). In the following sections, we will note S_0 the seismicity rate before injection (equal to 170 earthquakes per year) and M_0 the moment rate before injection (equal to $2.3 \cdot 10^{14}$ N m/year). Figure 2.3c presents slip profiles for a sequence of 50 successive earthquakes before fluid injection, along with the distribution of the frictional ratio a/b so that we can differentiate VW and VS patches. We can observe a complex pattern of seismic ruptures separated by slow aseismic slip episodes (represented by the area hatched by light cyan in the plot). There exist some small ruptures localized on the smaller VW patches (for instance event A). In this case, the neighboring VS barrier stops the propagation of the rupture along strike. However, along the bigger VW patches, the ruptures are larger and can go beyond the neighboring VS barriers (for instance event B). The proposed fault model can hence generate a complex pattern of ruptures and can bear earthquakes of different magnitudes following a Gutenberg Richter distribution with slope $b \approx 1$ (see Figure 2.3f).

2.4.2 Response to Fluid Injection

Figures 2.3a2, 2.3b2, and 2.3d–2.3f represent the different features of seismic activity after fluid injection started for the case study with the following injection parameters $p_{\max} = 20$ MPa and $\beta = 2$ MPa/day (injection scenario presented in Figure 2.2a). Figure 2.3a2 represents the time series of the moment magnitude M_w after injection starts; we observe clearly that fluid injection changes the distribution of the magnitude of the events. This will be further investigated in Figure 2.3f. After injection starts, the cumulative number of earthquakes along with the cumulative seismic moment experience an enormous increase at the very start of the injection (Figure 2.3b2). During the first year after the injection start, 1,450 earthquakes were detected and around $2 \cdot 10^{15}$ N m of seismic moment was released. Once the pore pressure reaches a permanent state along the fault ($t = t_s$), the cumulative number of earthquakes seems to retake approximately its initial slope; however, the seismic moment appears to be increasing slightly slower than before injection started. At the injection shut in (10 years after the injection started), seismic activity slows down, in terms of number of earthquakes and seismic moment, for around 12 years, before gaining its initial preinjection activity. Figure 2.10 (from

the supporting information) represents the time series of the moment magnitude, while Figure 2.11 represents the cumulative number of earthquakes along with the cumulative seismic moment release, for different injection scenarios, where we can see that the results for the different cases present the same trend as the observations made for the case studied here. Note that the slowing moment increase in Phase III is particularly evident for $p_{\max} > 10$ MPa. This issue will be discussed later. As for the slip distribution along the fault, from Figure 2.3d, we can still observe a complex pattern of seismic ruptures with small localized ruptures on VW patches (event C for instance) and large ones on VW and VS patches (event D for instance). However, we also can observe a large slip concentration at the center of the fault, around the injection point where the pressure perturbation is the largest. The slip at the center of the fault is larger by around 13%.

In order to better quantify the changes in seismic activity in terms of number of earthquakes, we estimated the seismicity rate (gradient of the cumulative number of events with respect to time). Figure 2.3e illustrates the time evolution of the seismicity rate, the mean pore pressure, and the mean pore pressure rate, during fluid injection and after shut in. In order to avoid numerical peaks and oscillations, the seismicity rate was smoothed, using a moving median filter with a nonconstant sliding time window of width the length between 20 consecutive events. We can clearly discern three different phases during fluid injection and two after injection shut in: (I): $t_i < t < t_r$, where the pore pressure increases linearly at the injection point, (II): $t_r < t < t_s$ where the pore pressure at the injection point is maintained constant (equal to p_{\max}) but the pore pressure is not at steady state yet, (III): $t_s < t < t_{\text{end}}$, where t_s is the time needed by the pore pressure profile, along the fault, to reach a permanent state, (IV): $t > t_{\text{end}}$, where the pressure at the injection point drops and (V): when all the pore pressure is diffused outside the fault. During Phase I, the mean pore pressure and the mean pore pressure rate increase along the fault leading to an increase of the seismicity rate; whereas in Phase II, while the mean pore pressure keeps on increasing, the seismicity rate decreases along with the mean pore pressure rate. Finally, in Phase III, the mean pore pressure is constant, the pore pressure rate drops to 0, and the seismicity rate stabilizes around the initial preinjection seismicity rate S_0 , presented by the dashed horizontal line. Additionally, the peak in the seismicity rate approximately coincides with the peak in pore pressure rate, both at $t = t_r$. Phase IV starts at the injection shut in. In this phase, the pore pressure drops, the pore pressure rate takes negative values, and the seismicity rate is lower than S_0 for around 12 years. Finally in Phase V, the pore pressure and the pore pressure rate are 0, and the seismicity rate regains its initial value S_0 one more time. According to these results, the seismicity rate seems to follow the evolution of the pore pressure rate, rather than the pore pressure itself. As illustrated in Figure S3 (supporting information), this correlation is obtained for almost all the injection scenarios tested. For large β and small p_{\max} , the evolution of the seismicity rate is slightly delayed with respect to the pore pressure rate. For the other cases, we observe a direct correlation between the time series of both the seismicity rate and the pore pressure rate.

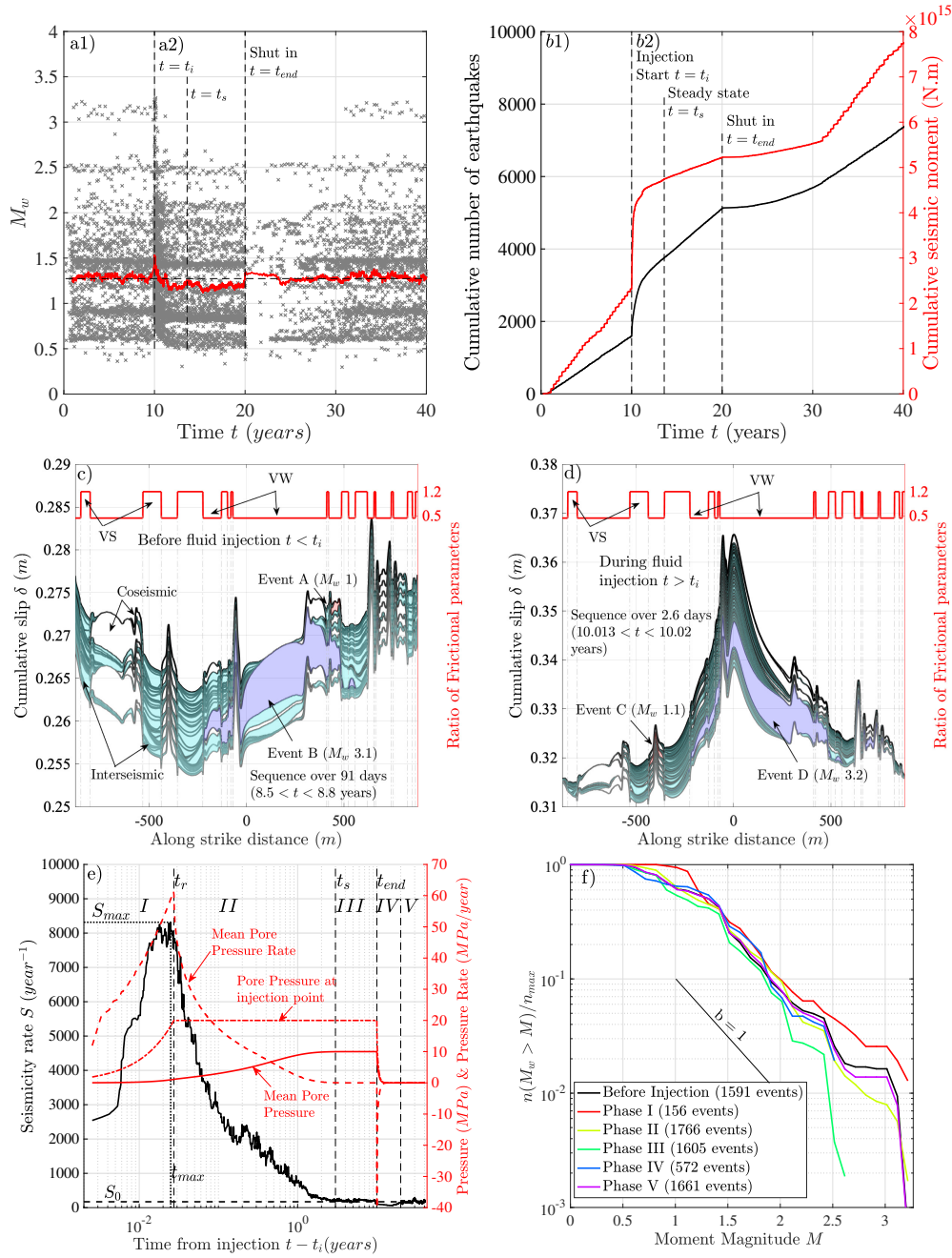


Figure 2.3 – (a) Time series of the moment magnitude M_w . The red curve is a centered sliding average, with a sliding window of 50 events. The horizontal dashed line is the mean value of M_w . (b) Cumulative number of earthquakes (black curve) and seismic moment in Newton meters (red curve). (c, d) Example of the cumulative slip profiles along strike distance for a consecutive 50 earthquakes: One profile is represented before and after each earthquake. (White, blue, and red areas are the coseismic offsets of earthquakes, and light cyan represents the aseismic slip accumulated during the interseismic periods.) Darker colors represent later times. The red curve represents the ratio of frictional parameters a/b along strike distance. (e) Time series of the seismicity rate (black curve), mean pore pressure, pore pressure at injection point, and mean pore pressure rate, on a semilogarithmic scale. The black horizontal dashed line represents the initial seismicity rate S_0 (before injection). Dotted lines represent the point (t_{max}, S_{max}) , where the seismicity rate reaches its maximum. The time axis is normalized from the injection start time t_i . (f) Magnitude frequency distribution of the events before (black curve) and in the different phases (colored curves).

Figure 2.3f represents the evolution of the magnitude-frequency distribution of the events throughout this case study before injection (black curve) and for the different phases (colored curves). Before fluid injection, the magnitudes of the events follow a power law distribution between $M_w = 0.5$ and around $M_w = 3.2$ with a b value close to 1. Due to fluid injection, the magnitude-frequency distribution changes. To start, it appears that Phase I is the most critical: The frequency of intermediate and large magnitudes ($M_w \geq 1.5$) are increased (please note that the used terms intermediate and large are relative to the magnitude range that we have in our results here). This is also observed by the rapid increase of the mean of M_w directly after injection start in Figure 2.3a2. In Phase II, however, we observe a decrease in the frequency of larger magnitudes ($2.2 \leq M_w \leq 3.2$), relative to Phase I. This suggests that the effect of β which only acts in Phase I and p_{\max} which acts in both Phases I and II are not the same. This feature will be further investigated in the next section. In Phase III, the magnitude-frequency distribution is perturbed as well, even though there is no more amplification of the seismicity rate. In this period we observe from Figure 2.3f a deficit of the magnitudes in the range $0.7 \leq M_w \leq 2.6$, absence of very large magnitudes ($M_w \geq 2.6$) and re-appearance of the small magnitudes (better observed in Figure 2.3a2), which explains the slow increase of cumulative seismic moment observed in this phase in Figure 2.3b2. On the other hand, in Phase IV and after the shut in, we observe absence of the large magnitudes $M_w \geq 2.5$. Finally, in Phase V the magnitude-distribution is quasi-similar to the preinjection one. Interestingly, in both Phases III and V, the seismicity rate is the same (equal to S_0) and the pore pressure rate is 0. The only difference between these two phases is in the value of the effective stress. We have that $\sigma_{\text{eff}} = \sigma - p$, if we take the mean pressure along the fault, this would give us an effective stress of 90 MPa in Phase III where $p = 10$ MPa; in Phase V, however $p = 0$, and the effective stress would be 100 MPa. This suggests that the reduction of the effective stress in Phase III may be the cause of the perturbation of the magnitude distribution. We should note that in this case study the maximum magnitude was not exceeded during fluid injection, we will show however in the next section that this may not be the case for different values of β .

2.4.3 Sensitivity Analysis

In the following, we study the effect of the injection parameters on the seismicity rate and the magnitude distribution. We concentrate on the Phases I and II where seismicity increases. We do not investigate further Phase IV because our model is not adapted to study postinjection seismicity, which could be attributed to neighboring faults. This will be discussed later.

2.4.3.1 Choice of Injection Parameters

One hundred sixty-eight injection scenarios were tested by varying independently both the injection pore pressure p_{\max} and the injection pressure rate β , with a constant

diffusivity D and dirichlet diffusive boundary conditions. Twelve different values of p_{\max} are tested in the range $[0.5\text{--}20]$ MPa = $[0.005\text{--}0.2]\sigma_T$. This yields a local reduction of the effective stress between 0.5% and 20% at the injection point, and between 0.25% and 10% globally along the fault (if we assume a mean pressure along the fault). On the other hand, we tested 14 different values of the injection pressure rate β in the range $[0.01\text{--}10]$ MPa/day. This range of values was chosen in order to cover a wide domain of the ratio of injection rate to background rate ($\dot{\tau}_{\text{inj}}/\dot{\tau}_0$). We estimate the injection stressing rate $\dot{\tau}_{\text{inj}}$ during Phase I at the injection point : $\dot{\tau}_{\text{inj}} \approx (\mu_0 - \alpha)\dot{p} = (\mu_0 - \alpha)\beta$, since at the injection point $\dot{p} = \beta$ and because rate- and state- friction coefficient is only a small correction to a constant friction coefficient μ_0 . This yields $\dot{\tau}_{\text{inj}}$ to vary in the following domain $[0.043\text{--}43]$ Pa/s. On the other hand, we estimate an approximate background stressing rate $\dot{\tau}_0 = 0.05$ Pa/s (see appendix B, section 2.8, for details). Thus for the different injection pressure rate chosen ($\dot{\tau}_{\text{inj}}/\dot{\tau}_0$) vary in the range $[0.86\text{--}860]$.

2.4.3.2 Time of Maximum Seismicity Rate and Seismicity Perturbation Duration

We should mention that in this section and for Figure 2.4 we will not present the results of the simulations with $p_{\max} = 0.5$ MPa, the reason will be discussed in the next section. Figure 2.4a shows the correlation between the duration of the injection pressure slope $t_r - t_i$ (i.e., duration of Phase I) and the time delay to reach the maximum seismicity $t(S_{\max}) - t_i = t_{\max} - t_i$ (see Figure 2.3e). t_{\max} depends strongly on the injection pressure rate β . Generally maximum in seismicity is reached when the pore pressure rate reaches its maximum $t_{\max} \approx t_r$. However, for very small values of injection pressure p_{\max} or for the combination large values of β with intermediate values of p_{\max} , Phase I is really short and the seismicity rate can continue to increase for an additional time beyond Phase I: $t_{\max} > t_r$, illustrated in Figures 2.12 and 2.13 as well.

Figure 2.4b shows the correlation between the diffusion duration and the seismicity perturbation duration. The diffusion duration is the duration for the pore pressure to reach a permanent state along the fault $t_s - t_i$, and the seismicity perturbation duration is picked manually for the different simulations as the time when the seismicity rate regains its initial value S_0 . For larger p_{\max} , the time to reach a permanent state is larger, and hence we would expect a larger diffusion duration. From the results, we observe a clear correlation between the duration of the seismicity perturbation and the diffusion duration with a dependence on the injection pressure p_{\max} . However, for low values of p_{\max} , the perturbation duration seems shorter than the diffusion duration, because in this case, the pressure perturbation along strike of the fault near the end of the diffusion is very small relatively to other cases, and thus this may cause the seismicity perturbation to cease. These results suggest that for the different injection scenarios considered, the seismicity perturbation is generally governed by the diffusion of the fluid along the fault segment, thus by the evolution of the pore pressure rate along the fault, once a permanent state for pressure is reached, it will lead to a constant seismicity rate.

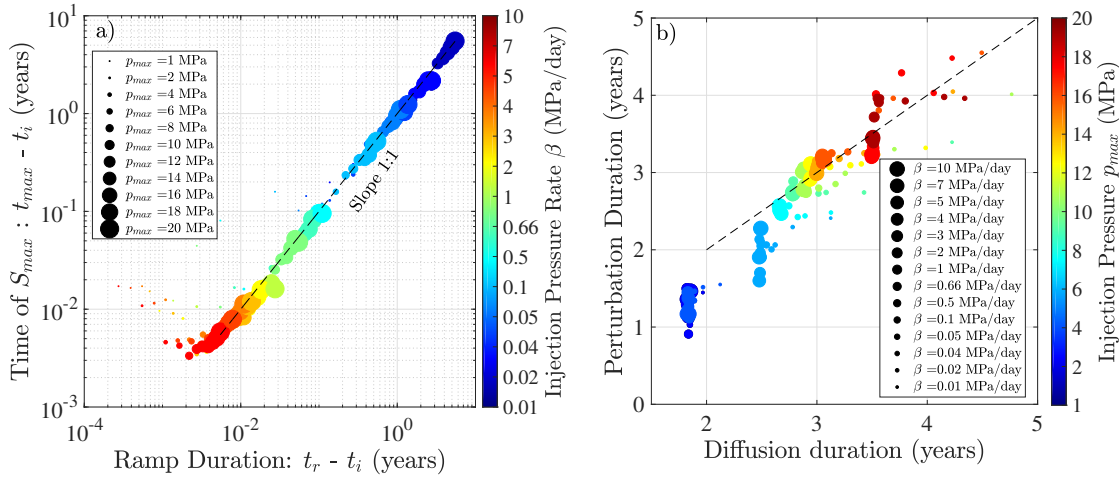


Figure 2.4 – Influence of injection on the induced seismicity parameters: (a) Comparison of the time needed to reach the maximum seismicity rate: t_{\max} and the time needed to reach p_{\max} at the injection point: t_r . The color scale represents different values of the pore pressure rate β at the injection point, and the size of the scattered points is proportional to the maximum pore pressure at the injection point p_{\max} . (b) Comparison of the duration of the induced seismicity sequence with the duration of fluid diffusion. Here, the color scale represents different values of the injection pressure p_{\max} , and the size of the scattered points is proportional to the pore pressure rate at the injection point β .

2.4.3.3 Seismicity Rate Increase

In order to compare the different cases, we quantified the seismicity rate increase due to fluid injection for each case as follows: S_{\max}/S_0 , where S_{\max} is the maximum seismicity rate and S_0 is the initial seismicity rate before injection (see Figure 2.3e). The evolution of the seismicity rate increase with both β and p_{\max} is represented in Figure 2.5a. The small subplot inside the figure is a zoom of the results over the small range of β ($\beta < 1$ MPa/day). First for the lowest value of p_{\max} (0.5 MPa) we do not observe any significant increase in the seismicity rate no matter the value of β . That is why the results of these simulations were not taken into account in the previous section, nor will they be taken for the rest of the study. For $p_{\max} = 1$ MPa, however, we observe a slight increase in the seismicity rate with no dependence on β . For $p_{\max} \geq 2$ MPa, S_{\max}/S_0 increases quasi-linearly with the injection pressure rate β until a certain threshold β^* . Beyond it, the seismicity rate increase shows almost no evolution. This rate threshold β^* however is not the same for the different values of p_{\max} , it appears to be pressure-dependent, and take larger values for larger p_{\max} . For example, we reach a stable S_{\max}/S_0 for $\beta \geq 3, 2,$ and 1 MPa/day for $p_{\max} = 20, 14,$ and 4 MPa, respectively. The seismicity rate increase S_{\max}/S_0 increases also with increasing injection pressure p_{\max} ; however, the dependency on p_{\max} is much less pronounced for very small values of β . The seismicity rate could be

increased up to a factor 80.

[Dietrich \(1994\)](#) proposed an analytical model for the seismicity rate following stress perturbations, with rate- and state-dependent fault properties. He modelled a population of identical asperities as rate and state spring slider systems. Similarly, we can apply Dietrich’s assumptions to our fault configuration, and assume that the fault is made of a collection of independent and non interacting spring slider systems. We can then compute the seismicity rate predicted by Dietrich’s model. Details about the procedure are provided in Appendix C, section 2.9, we should note though that we used the two values of $\dot{\tau}_0$ (0.03 and 0.07 Pa/s) estimated in appendix B (section 2.8). In Dietrich’s model, the different asperities are identical and independent in the sense that no stress transfer is allowed between them. The resulting events would have the same magnitude, that is proportional to the size of the asperity; thus, by choosing the number of asperities, we choose the resulting magnitude of the events as well. In order to cover the M_w range observed in our model, we tested different values of the number of asperities used in the range $[L_0/R_{\max}-L_0/R_{\min}] \approx [10-350]$ asperities, so that in any case we would not have larger or smaller asperities than the ones used in our model. Beyond a certain number of asperities, this model converges and gives the same estimation independently from the number of asperities chosen. We present here the results for a case with 100 asperities, where the size of the different patches is $\approx R_{\max}/10$. The estimations of the seismicity rate increase based on this model for every combination of injection parameters (p_{\max}, β) are presented in Figures 2.5a and 2.5b by the dashed lines (for $\dot{\tau}_0 = 0.03$ and 0.07 Pa/s, respectively). First we observe that the results depends on $\dot{\tau}_0$, where a lower background stressing rate, thus a higher ratio $\dot{\tau}_{\text{inj}}/\dot{\tau}_0$ can lead to a larger seismicity rate increase. Thus, we cannot rely totally on the estimation of the seismicity rate increase that we make from this model, however it can give us a good idea of its quantification with respect to our numerical results. Generally, [Dietrich \(1994\)](#)’s seismicity rate increase presents the same trend as the numerical one: We observe a similar dependency with the injection pressure p_{\max} , and we also observe that the seismicity rate increases with β . For low values of p_{\max} , the seismicity rate increase appears to saturate when β is large. We also observe approximately no amplification on the seismicity rate for the smallest injection pressure ($p_{\max} = 0.5$ MPa). However, this model underestimates the seismicity rate increase generated by our heterogeneous fault, and for $\beta > \beta^*$, the seismicity rate does not saturate, but rather keeps on increasing. In the following, we look into more details into the time series of the seismicity rate. Figures 2.5c and 2.5d represent the comparison for the time series of the seismicity rate generated by our model and the one predicted by Dietrich’s model for two different injection scenarios. We can observe that generally the seismicity rate follows the same trend, it increases at the start until the time $t = t_r$, and then decreases until regaining the initial seismicity rate value. Again, we observe that the analytical approximation underestimates the seismicity rate. Finally we should note that the comparison between the two models remains limited, since Dietrich’s model fails to generate a variation in earthquake magnitude, and neglects the stress transfers between the different asperities. This comparison will be further developed in

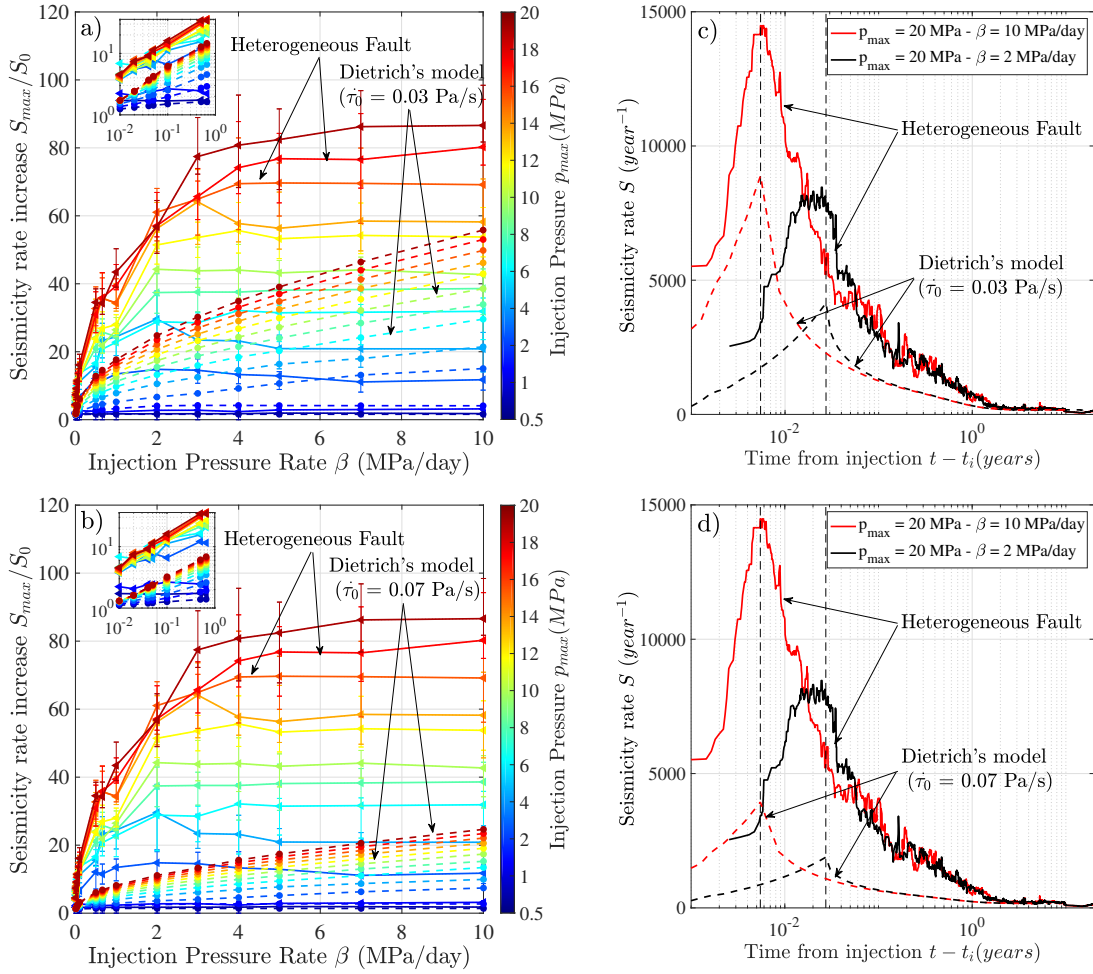


Figure 2.5 – (a, b) Seismicity rate increase S_{\max}/S_0 (ratio of maximum seismicity rate over seismicity rate before injection) as a function of the injection pore pressure rate β . Continuous lines represent the results of the numerical model of the heterogeneous fault, dashed lines represent the seismicity rate increase predicted by analytical approximation based on Dietrich’s 1994 model (for $\tau_0 = 0.03$ in subplot a and 0.07 Pa/s in subplot b). Error bars represent the variability of S_{\max}/S_0 for one simulation. The color scale represents different values of the maximum injection pressure p_{\max} . The small subplot inside the figure is a zoom of the results over the small range of β ($\beta < 1$ MPa/day). (c, d) Time series of the seismicity rate for two different injection scenarios. Continuous lines represent the numerical seismicity rate, and dashed lines represent the one predicted by Dietrich’s model (for $\tau_0 = 0.03$ in subplot c and 0.07 Pa/s in subplot d). The vertical dashed lines represent the time t_r for the different injection scenarios.

the discussion section.

2.4.3.4 Magnitude Content

We are interested to study the effect of the injection parameters on the magnitude frequency distribution when the seismicity rate is the most perturbed, hence in the first and the second phase (see Figure 2.3). Since β only acts in Phase I, we are only interested to study its effect in this phase, we will however study the effect of p_{\max} on both phases I and II. Figure 2.6 illustrates the distribution of the moment magnitude of the events during injection, in comparison with the distribution before fluid injection (black curve, in the different subplots). Figures 2.6a–2.6c emphasize on the dependency of the magnitude distribution on the injection pressure rate β for three different values of p_{\max} in Phase I, whereas Figures 2.6d–2.6f and 2.6g–2.6i emphasize on the effect of the injection pressure p_{\max} , for three different values of injection pressure rate β , in Phases I and II, respectively. First, from Figures 2.6a–2.6c we observe a dependency of the magnitude frequency distribution on the injection pressure rate β , where a larger β can produce more numerous large magnitudes ($M_w > 2$). We can also observe that the maximum magnitude $M_w \approx 3.2$ can be slightly exceeded when β is large enough, with the apparition of M_w 3.4 events (see also Figure 2.10). On the other hand, we do not observe a very clear dependency of the magnitude distribution on p_{\max} in Phase I (Figures 2.6d–2.6f), maybe because in this phase the effect of β dominates. The dependency on p_{\max} is however clear in Phase II (Figures 2.6g–2.6i). For larger pressure perturbations, we observe a more important deficit of large magnitudes ($M_w \geq 2$), whereas for small p_{\max} we do not observe a significant change in the magnitude frequency distribution with respect to the one before injection. This would explain why we observed a slow moment increase in Phase III, particularly for large p_{\max} (see Figure 2.11). We observe nonetheless, a creation of slightly larger magnitudes in Phase II as well.

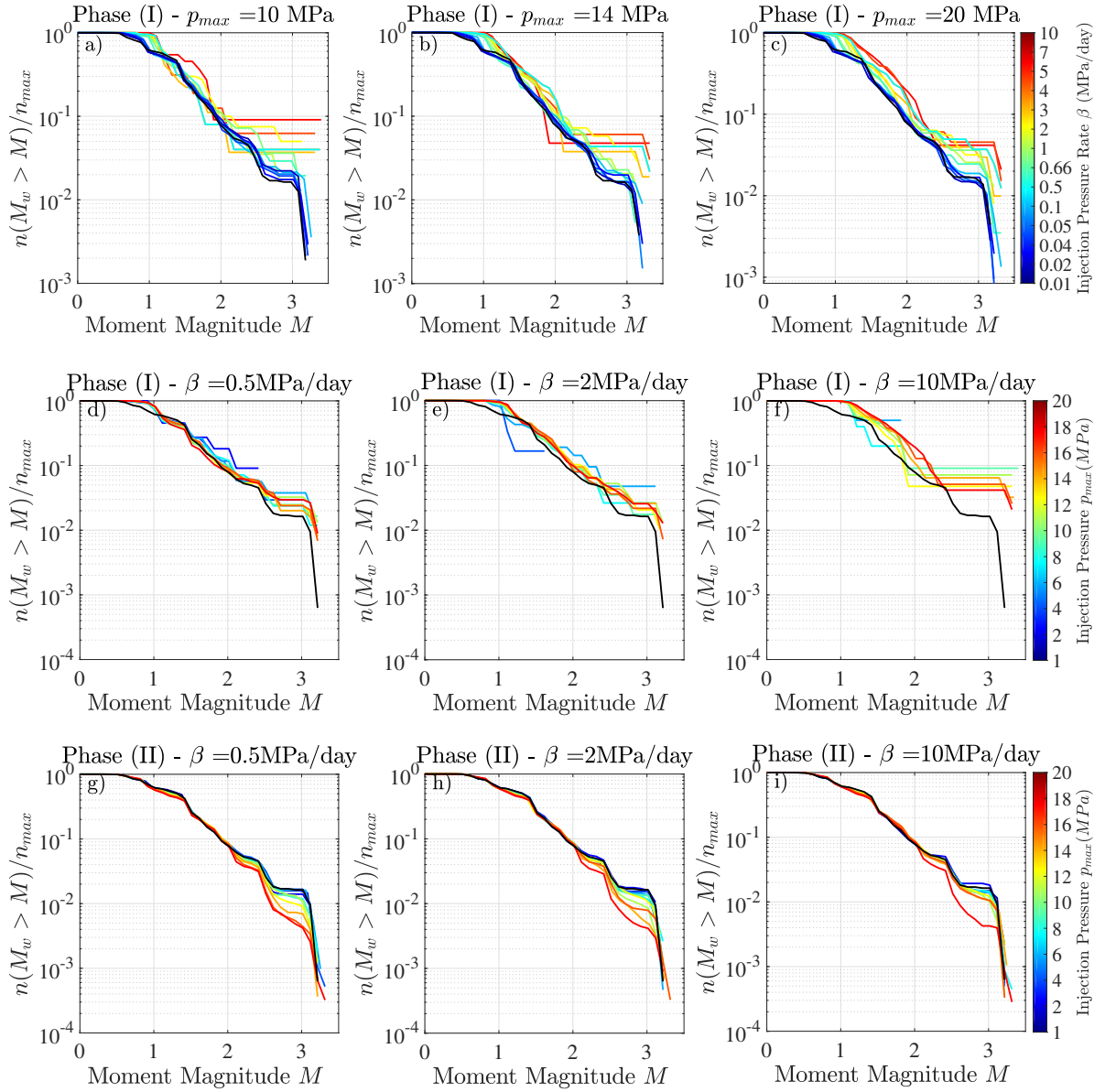


Figure 2.6 – Moment magnitude distribution. Subplots (a)–(c) represent the magnitude distributions during Phase I for three different fixed values of p_{max} , the color scale represents the injection pore pressure rate β . Subplots (d)–(f) and (g)–(i) represent the magnitude distributions for three different fixed values of β , in Phases I and II, respectively. The color scale represents the injection pore pressure p_{max} . In all subplots, the black curve represents the moment magnitude distribution before fluid injection. n_{max} designs the total number of earthquakes in the studied time duration, and M designs the moment magnitude M_w .

To better quantify the magnitude changes, we estimate the b value using the maximum likelihood method (Aki, 1965), in the following range [1–3.2] separately for Phases I and II. $M_w = 1$ is approximately the completeness magnitude of our catalogue (see Figure 2.6). However, for Phase I we only consider the simulations where this phase is large enough in time so the fault has time to generate enough earthquakes (here we chose a minimum of 50 earthquakes to perform the b value computation) in this period to have a good estimate of the b value, otherwise the b value would be biased and its variability would be large. The standard errors were evaluated following Shi and Bolt (1982). Results of the b value are evaluated with respect to changes to the mean effective stress along the fault ($\langle \sigma_{\text{eff}} \rangle \approx \sigma_T - p_{\text{max}}/2$) in Figures 2.7a and 2.7b, and with respect to changes in β in Figures 2.7c and 2.7d. During Phase I, the b value depends especially on the value of β (Figure 2.7c) and does not vary significantly with the effective stress hence with p_{max} (Figure 2.7a). For small values of $\beta \leq 0.05$ MPa/day, the b value increases with increasing β , which could be attributed to an increase in the magnitude of completeness from $M_w = 0.5$ to $M_w = 1$ observed in Figures 2.6a–2.6c. Beyond 0.05 MPa/day, we observe a decrease of the b value with increasing β , which suggests an increase in the proportion of large magnitudes in the studied range. However, for very large β , the uncertainty in the b value is important. This reflects the deviation from a power law decay for large β illustrated in Figures 2.6a–2.6c. On the other hand, in Phase II, from Figures 2.7b and 2.7d we observe that the b value tends to decrease with increasing the mean effective stress, with no clear effect of β in this period, which makes sense because β only acts in Phase I.

2.4.3.5 Seismic Moment Release and number of earthquakes during Phase I, Phase II, and Phase (I–II)

From the previous analysis made on the seismicity rate and magnitude content during Phase I, it appears that there is simultaneous saturation of the maximum seismicity rate, increase of the proportion of large M_w and a decrease of the b value as β increases. Moreover we observed that during Phase II, p_{max} has an important effect on the magnitude distribution and the b value. However, it was hard to make the correlation directly between the seismicity rate increase and the change in the b value. This is because a change in the b value can be interpreted in different ways, for instance in our study we can observe a decrease of the b value by either only increasing the frequency of the largest magnitudes, or by creating new larger magnitudes, or by decreasing the frequency of the smallest magnitudes. Thus, to better understand the link between the seismicity rate and the magnitude distribution for the different injection scenarios, we looked into the changes in the cumulative seismic moment released and the number of earthquakes, due to fluid injection, in Phases I, II and (I–II). In the following, we note n_{inj} the number of earthquakes induced by fluid injection estimated as follows: $n_{\text{inj}} = n_T - n_{\text{tect}} = n_T - S_0 \Delta t$, where n_T is the total number of earthquakes during the period Δt and n_{tect} is an estimation of the number of earthquakes in this period generated by tectonic loading. In the same way we estimate the cumulative seismic moment released due to fluid injection

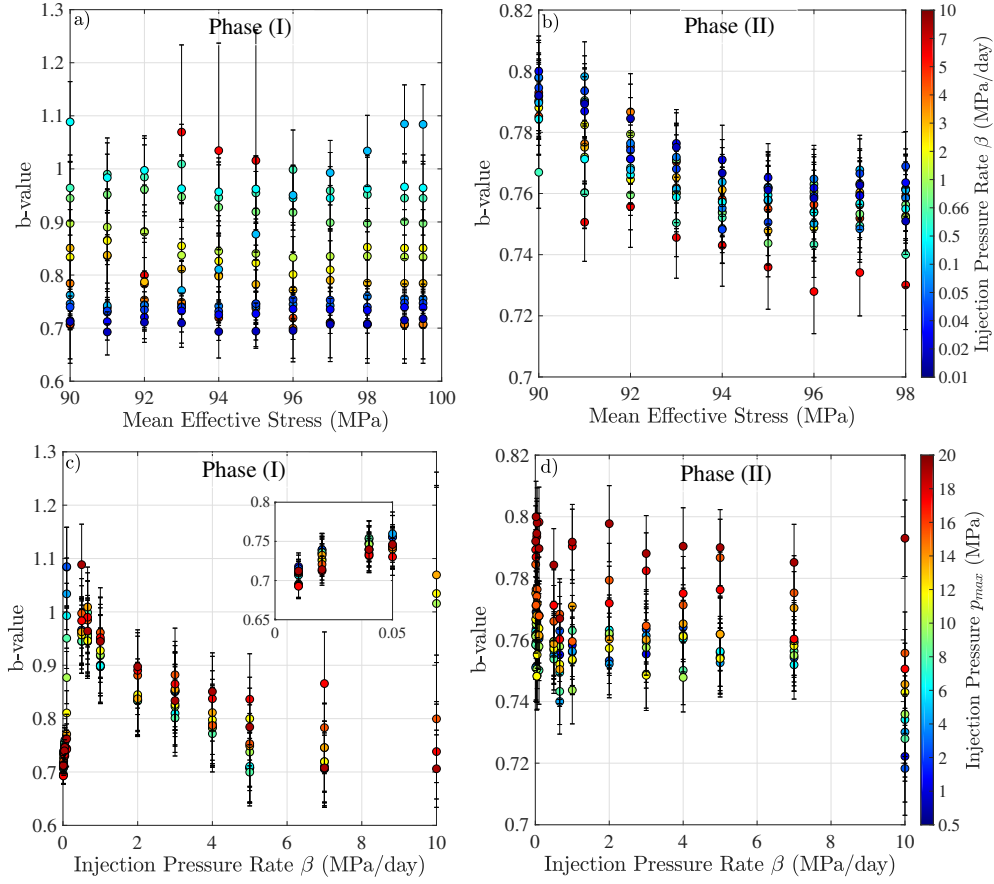


Figure 2.7 – Evolution of the b value, estimated in the M_w range [1–3.2], with the change in effective stress in (a) Phase I and (b) Phase II. The color scale represents different values of injection pressure rate β ; and with β in (c) Phase I and (d) Phase II. The small subplot in (c) is a zoom over the small range of $\beta \leq 0.05$ MPa/day. The color scale represents different values of injection pressure p_{max} . Error bars represent the error on the estimation of the b value for one simulation.

$M_{inj} = M_T - M_{tect} = M_T - M_0 \Delta t$, where M_T is the total seismic moment released during the period Δt and M_{tect} is an estimation of the cumulative seismic moment released during this phase due to tectonic loading. We should note though that the duration of Phase I is controlled by the injection parameters $\Delta t^I = p_{max}/\beta$, the total diffusion duration depends on p_{max} (see Figure 2.4b) : $\Delta t^{I+II} \propto p_{max}$ and the duration of Phase II Δt^{II} is the difference between the two: $\Delta t^{II} = \Delta t^{I+II} - \Delta t^I$ (the subscripts refer to the different phases).

During Phase I (Figure 2.8a1), we observe at first that for a constant injection pressure p_{max} , the number of induced earthquakes and the induced seismic moment released decrease when β increases, as long as β does not exceed the threshold β^* . In this case,

the duration of the Phase I decreases as β increases for the same p_{\max} , which could explain the observed decrease in n_{inj} and M_{inj} . Beyond β^* , for the same injection pressure p_{\max} , as β increases n_{inj} continues to decrease while M_{inj} remains constant. This suggests that the same seismic moment is released through less numerous events as β increases, which would imply that it is liberated through larger earthquakes. Since β represents the instantaneous variation of the imposed perturbation during Phase I, we would expect it to affect the frequency of the earthquakes and the average moment rate. That is why we estimate the average seismicity rate $\dot{n}_{\text{inj}}^I = (n_{\text{inj}}^I)/\Delta t^I$ and the average rate of seismic moment released $\dot{M}_{\text{inj}}^I = (M_{\text{inj}}^I)/\Delta t^I$. From Figure 2.8a2, we observe that in this phase, both the seismicity rate and the moment rate increase at first as β increases. Then, the seismicity rate tends to saturate after the critical threshold β^* (represented by the different stars in this subplot) while the moment rate continues to increase. In this case, larger β can lead to a larger moment rate under a constant seismicity rate increase, suggesting the liberation of the seismic moment through more numerous larger earthquakes, which is coherent with the observations made from Figures 2.6a–2.6c where a larger β can increase the frequency of large magnitudes. Moreover, we observe a general systematic increase of n_{inj} and M_{inj} when p_{\max} increases as well, especially when $\beta > 1$ MPa/day (Figure 2.8a1).

During Phase II (Figure 2.8b), and for small pressure perturbations, we do not observe any clear and significant effect of β on the number of induced earthquakes and the seismic moment released. In this case, n_{inj} and M_{inj} basically depend on the magnitude of the pressure perturbation p_{\max} . They both increase with increasing injection pressure when $p_{\max} < 12$ MPa. Beyond it, the number of induced earthquakes increases faster than the increase of M_{inj} , which could explain why the deficit of large magnitudes observed in Figures 2.6g–2.6i is more important for large p_{\max} . However, for large p_{\max} , we observe a dependency on β when it is small ($\beta < 0.1$ MPa/day): n_{inj} and M_{inj} are relatively small, because in this case Phase I was very long in time and Phase II is very short (during Phase I the fluid had enough time to diffuse towards the boundaries so that the time remaining to reach permanent state, that is, Phase II, is very short).

Figure 2.8c combines the two phases so we can assess the general effect of fluid injection on the induced seismicity. We can thus see that for small injection pressure, the induced seismicity is mainly governed by the injection pressure p_{\max} , while for intermediate to large pressure perturbations it is governed by both β and p_{\max} : in general a larger p_{\max} would induce more numerous events and a higher seismic moment released, a larger β would slightly decrease the number of earthquakes while increasing the seismic moment released, which would lead to the increase in proportion of large magnitudes.

2.4.3.6 Change in Diffusive Boundary Conditions

As mentioned before, for the results presented so far, we used Dirichlet boundary conditions for the diffusion equation (equation (2.7)), where we assume that the pore

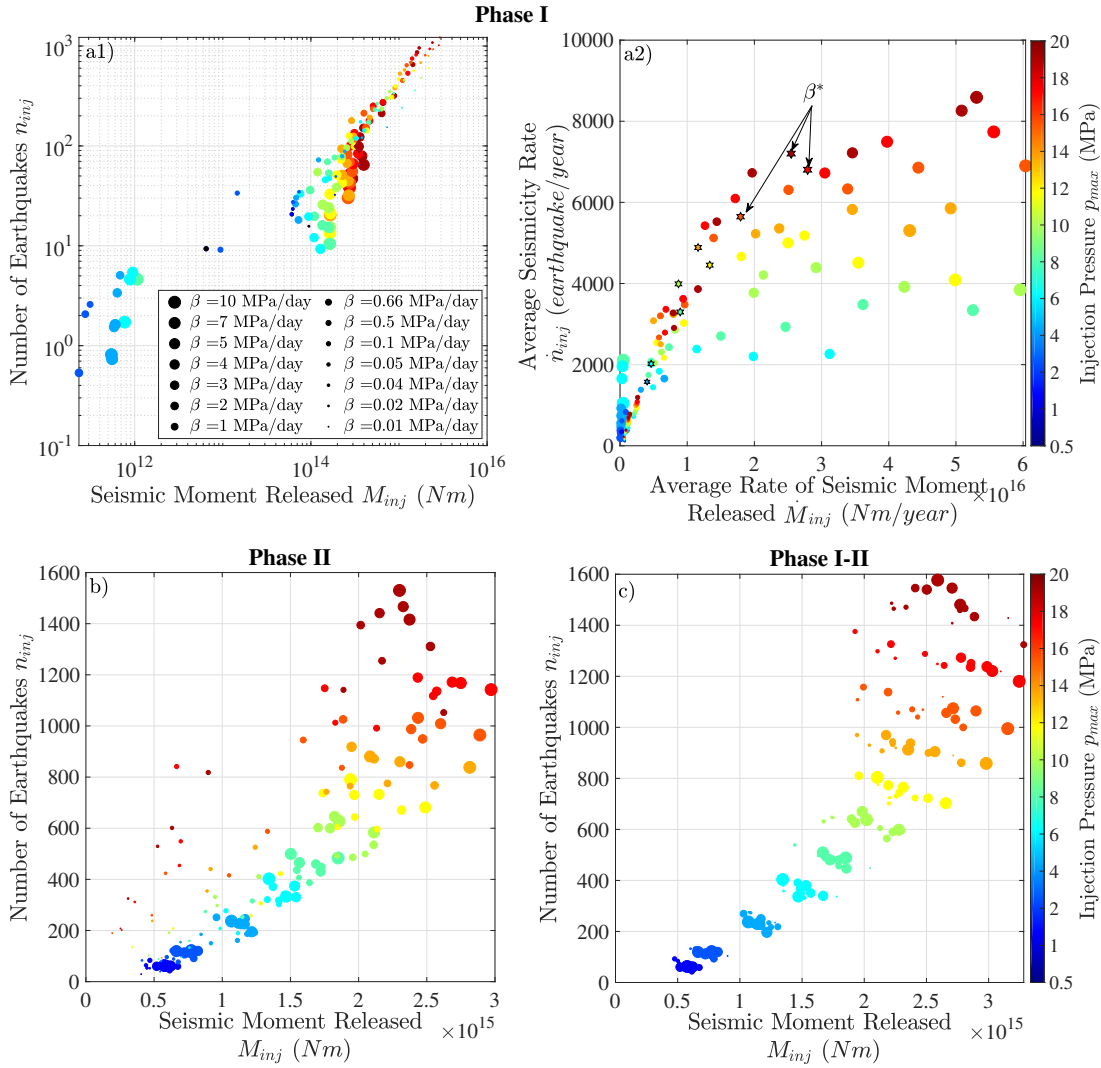


Figure 2.8 – (a1, b, c) Evolution of the number of earthquakes and the seismic moment released with the injection parameters, in Phase I, Phase II and Phase I + II, respectively. (a2) Evolution of the average seismicity rate and the average seismic moment rate with the injection parameters in Phase I. In this subplot, the different stars represent the values of β^* , each color refers to a p_{\max} . In all subplots the color scale represents the injection maximum pressure p_{\max} , and the size of the scattered points represents the injection pressure rate β .

pressure is 0 at the edges of the fault model. We also tested different boundary conditions (Neuman boundary conditions, where we assume that the space derivative of the pore pressure at the fault edge is constant: $\partial p(x, t) / \partial x = k$, in this study $k \approx 10^{-3}$ MPa/m); that is, the flow at the edges is constant. We tested the new boundary conditions for two

values of injection pressure ($p_{\max} = 10$ and 14 MPa), with the 14 different values of β . The changes in boundary conditions will modify the pressure profile at the boundaries of the model, but will induce minor modifications for the pressure profile near the injection point during Phase I and II. Furthermore, we will not observe any changes on the pore pressure profile along strike of the fault until later times (after the pressure reaches the edges of the system). Figure 2.14 in the supporting information represents the comparison for one injection scenario between Dirichlet and Neuman boundary conditions. This change in boundary conditions did not yield any significant change on the seismicity rate which could be related to the observation of Figure 2.3d that the seismicity rate is mainly perturbed near the injection point. Nonetheless, the change in boundary conditions did not yield any significant changes to the dependence of the magnitude frequency distribution in Phases I and II. During Phase III however, the deficit in large M_w is more pronounced for Neuman boundary conditions, because the mean effective stress $\langle \sigma_{\text{eff}} \rangle$ in this case is smaller than the one for Dirichlet boundary conditions.

2.5 Discussion

We presented a coupled numerical model of a heterogeneous planar fault that generates a complex pattern of ruptures of multiple sizes, with a fluid injection-diffusion model. Our model highlights the outcome of fluid flow on the seismicity of the injected fault.

Our results show that the seismicity is immediately disturbed on the onset of fluid injection. This is because in our numerical formulation, the pressure perturbation is directly imposed in the fault. In real cases, a delay would be expected, in order for the pressure perturbation to reach the fault, this delay is generally controlled by the distance separating the injection well from the preexisting faults, as well as by the permeability of the medium surrounding the fault. Since this is not the case in our numerical formulation, the seismicity rate directly exhibits an enormous increase with time correlated with the increase of pore pressure rate. The seismicity rate reaches a peak (Figure 2.3e), that generally coincides with the time of the maximum pore pressure rate perturbation (Figure 2.4a). After this time, even though the pore pressure continues to increase along the fault, the seismicity rate immediately drops because the pressure rate starts to decrease. This is similar to the observed evolution of the seismicity rate in Oklahoma, where the seismicity rate was delayed of several months with respect to changes in injection rate, but correlates with the evolution of the pore pressure rate at 3 km below injection, where the seismicity is detected (Langenbruch *et al.*, 2018). The duration of perturbation is mainly controlled by the fluid diffusion process (Figure 2.4b). As long as the fluid diffuses along the fault, the pore pressure rate evolves and is not at steady state, the perturbation of seismicity carries on.

Our results also suggest that the induced seismicity is controlled by the injection scenario, similar to the results of Aochi *et al.* (2014). In our study, the seismicity rate increase

appears to depend on the injection parameters p_{\max} and β . We found that a larger β can lead to a larger increase of the seismicity rate. For larger β , the pressure rate along the fault is larger and it may drive the fault faster towards failure because it may decrease faster the effective stress along the fault, and hence the frictional strength. However, we observed that β does not seem to have an effect on the seismicity rate increase after a certain threshold β^* . In this case, the increase in stressing rate may be accommodated by changes in the magnitude distribution, with the rate of events staying constant. Hence, for a fixed pressure p_{\max} , large values of β can not produce more numerous events (see Figure 2.5a), however it may produce more frequent large ones. This was observed in Figures 2.6a–2.6c and Figures 2.8a1 and 2.8a2, where we see that when β increases beyond β^* , the seismicity rate stabilizes while the moment rate continues to increase, which would imply the liberation of seismic moment through larger magnitudes. In an attempt to understand the onset of dynamic slip due to fluid injection, Garagash and Germanovich (2012) studied the direct effect of fluid diffusion on the onset of dynamic slip, while Azad *et al.* (2017) modeled the onset of dynamic slip due to fault opening in hydraulic fracturing, where no fluid diffusion is taken into account. Garagash and Germanovich (2012) found also that the injection scenario can affect the transition to dynamic slip. They tested different values of constant injection flow rate, and found that higher values can lead to a decrease in the critical time to dynamic slip, hence a higher risk of dynamic rupture for a higher injection rate. Eventhough, in our work we do not look closely at the onset of dynamic rupture, however both our results emphasize on the effect of the injection rate and show how a rapid pressurization increases the probability of larger rupture.

On the other hand, the pore pressure profile along strike depends on the value of p_{\max} . For the boundary conditions considered, the mean pressure along the fault can reach $p_{\max}/2$. Hence, by increasing the maximum injection pressure p_{\max} , we get a larger pore pressure profile along the fault, and ergo a larger decrease of the effective stress and hence the frictional strength according to equation (2.2). In this case, the stress drop would be lower, and at constant stressing rate $\dot{\tau}$, it will lead to a higher seismicity rate, thus we would expect the fault to reach instability more frequently. This is observed in our results via the dependency of the seismicity rate increase S_{\max}/S_0 on p_{\max} observed in Figure 2.5a, or similarly the dependency of the number of induced earthquakes on p_{\max} observed in Figures 2.8a1, 2.8b and 2.8c. A similar dependency was found by Raleigh *et al.* (1976) during an in-situ fluid injection experiment in the Rangely Oil field Colorado in 1969, where they tested the effect of the bottom hole pressure and found that by increasing/decreasing it, the resulting frequency of earthquakes increases/decreases as well, respectively. In their experiment the initial reservoir pressure was around 17 MPa, injection started with a bottom hole injection pressure of 27.5 MPa and resulted in an average of 28 earthquakes per month, the injection bottom hole pressure was then decreased to 20 MPa leading to a drop in the seismic activity to one earthquake per month. Later on, they re-increased the pressure to 27.5 MPa and recorded an average of 6 earthquakes per month during this increase, then they maintained it at 28 MPa that lead to an average of 26 earthquakes per month. Although in this case, the pore pressure

would not necessarily have reached a steady state, but if we assume that it is the case then the increase in seismicity rate would be in this case $S/S_0 \approx 26/1 \approx 26$, for a pressure perturbation $\Delta p \approx 8$ MPa and $S/S_0 \approx 28/1 \approx 28$ for a pressure perturbation $\Delta p \approx 10$ MPa. This estimate is coherent to what we observe for the seismicity rate increase S_{\max}/S_0 when p_{\max} is between 8 and 10 MPa if we assume an injection pressure rate $\beta > \beta^*$ (in Figure 2.5a). This comparison is however very basic and remains limited, since we do not have all the details about the injection procedure and the pressure history at the injection point.

We used the seismicity rate model proposed by [Dietrich \(1994\)](#) to develop an analytical approximation to our case study, which is presented in Appendix C (section 2.9). The basic assumptions of this analytical model is that there is no interactions between the asperities along the fault, and that it does not allow for variations in earthquake magnitude. This analytical model presents the same general trend for the seismicity rate increase as our numerical results, where it shows that the seismicity rate increase depends on both the injection pressure p_{\max} and pressure rate β . However, since in this model no interactions are allowed between the different asperities, under pressure perturbation each asperity ruptures independently of the others. This will generate events with the same magnitude and will not allow for very small magnitudes as our model does and no cascade of events is allowed. This may be the cause why this model underestimates the seismicity rate increase with respect to our numerical results. On the other hand, since this formulation does not allow for variations in earthquake magnitude as our model does, the seismicity rate does not saturate for $\beta > \beta^*$, but rather keeps on increasing with β . We should note though that in our formulation of this analytical solution, we did not consider the full equation of the seismicity rate proposed by [Dietrich \(1994\)](#), but rather an approximation (details on the assumption and procedure in Appendix C, section 2.9). In conclusion, since the analytical model does not allow for variations in earthquake magnitude, its application remains restricted and the comparison between the two approaches is limited.

Fluid injection does not only influence the seismicity rate, but it can modify the magnitude frequency distribution of the events as well. The results presented in Figures 2.3a, 2.3f, 2.6, and 2.7 suggest that both β and p_{\max} can influence the magnitude distribution. It shows an increase in the frequency of intermediate and large magnitudes during the first phase, which is directly related to β that acts in this phase. This increase is more and more pronounced for larger β as observed in Figures 2.6.a–2.6.c. This effect of β can be more clearly observed in figure 2.7a, where we estimate a lower b value for increasing β . During the second phase however, we observe the effect of p_{\max} on the magnitude distribution, where we see that a higher p_{\max} can lead to less frequent large events. A systematic increase of the b value was observed with increasing p_{\max} in this phase, that is, with decreasing the effective normal stress, and thus decreasing differential stress. A similar relation was observed between the b value and the increasing differential stress with depth, for laboratory experiments ([Scholz, 1968](#)), as well as for earthquake statistics for different continental regions ([Gerstenberger et al., 2001](#); [Spada et al., 2013](#)). [Scholz \(2015\)](#)

proposed the following inverse relation between the b value and the differential stress that can explain the b -depth variability for California, Switzerland, Italy, Greece, Turkey and Japan: $b = 1.23 \pm 0.06 - (0.0012 \pm 0.0003)(\sigma_1 - \sigma_3)$. If we assume an average variation of the b value, we get $b_{\text{numerical}} \approx 0.76 - 0.005(\sigma_1 - \sigma_3)$ ($\sigma_1 - \sigma_3 \approx \mu_0 \sigma_{\text{eff}} = 0.6 \sigma_{\text{eff}}$). The b values obtained here are larger by a factor of around 2 than the one estimated by [Scholz \(2015\)](#). This discrepancy could be due to multiple causes: (1) in our numerical formulation, we model VW patches, the size of which follow a power law distribution with a -2 exponent. This distribution could influence the rupture sizes and thus the b value; (2) in a 2-D formulation, the redistribution of stress following a rupture are generally overestimated with respect to 3-D formulation, which tends to increase the b value. What controls the absolute value of b is not the purpose of this study, and requires more attention. Here we insist on the relative b value changes, which are of the same magnitude ($\approx 10^{-3}(\sigma_1 - \sigma_3)$).

Postinjection seismicity remains nowadays an open subject, for instance the seismicity in Basel ([Deichman and Giardini, 2009](#)) or the seismicity in Youngstown Ohio ([Kim, 2013](#)). In our numerical model, the injection shut in leads to a decrease of the number of earthquakes with respect to the one before injection began, where the pore pressure diffused out of the fault. However, our numerical model is confined in the vicinity of the fault, and we do not explore what happens in the surrounding region. Thus, our model is not capable to predict the seismic activity after shut in, for surrounding fractures or faults, and therefore unable to explain postinjection seismicity as was discussed by [Baisch *et al.* \(2010\)](#), [McClure and Horne \(2011\)](#) and [Dietrich *et al.* \(2015\)](#). For that reason, we did not analyze in details the characteristics of seismicity after shut-in.

Furthermore, it was observed that aseismic slip can in some cases drive postinjection activity ([Bourouis and Bernard, 2007](#)). Eventhough, we observed in our results some slow aseismic slip episodes (Figures 2.3c and 2.3d), the role of aseismic slip in injection induced seismicity and the way it is perturbed by fluid injection were not the purpose of this study. This demands more work and it remains to be investigated in future studies.

Additionally, in our modeling approach, we assumed a constant value of the diffusivity $D = 0.005 \text{ m}^2/\text{s}$. A lower value of diffusivity would induce lower pore pressure rates along the fault, and since in our model the time series of the seismicity rate is correlated to the pore pressure rate, then we would expect to have a lower seismicity rate in this case. We conducted some tests on the same fault model with another diffusivity value $D_2 = 0.1D$ and found that in this case for the same p_{max} , S_{max}/S_0 saturates at lower values. However, a lower diffusivity will lead to a larger diffusion time, and hence a larger Phase II in time. We are not sure how this increase in duration until steady state will affect the number of induced earthquakes and the cumulative seismic moment released. This issue deserves more analysis and we leave it for further studies. Moreover, in our modeling approach the considered diffusivity does not evolve in time. However, the permeability, and consequently the diffusivity, along the fault, can change following

a seismic event and slip accumulation (Zhang and Tullis, 1998; Baghbanan and Jing, 2008), or reduction in vertical effective stress due to fluid injection (Zoback and Byerlee, 1975; Fisher and Zwart, 1996; Ghabezloo *et al.*, 2009; Rutter and Mecklenburgh, 2018). Thus, our model does not allow modeling of shear induced fluid flow for instance, or permeability enhancement. Future works and development of our numerical model would be to include a slip and stress dependent diffusivity.

Finally, we should note that we only tested one fault parametrization. It would be interesting for future work to test different fault configurations and to study how this would affect the resulting induced seismicity.

2.6 Conclusion

We proposed a continuous rate- and state-dependent 2-D model of a heterogeneous fault, that can generate a complex pattern of ruptures with different sizes, coupled with an injection-diffusion model. Our model emphasizes on the consequences of the fluid injection history on seismicity and highlights some key parameters. In particular, we showed that the fluid injection disrupts the state of the fault. It leads to a sharp increase in the seismicity, as well as an increase in the proportion of large magnitudes. Our results suggest that the seismicity rate follows the variation of the pore pressure rate, which was observed recently for the seismicity rate in Oklahoma. The seismicity perturbation stops when the pressure reaches a steady state along the fault. We also pointed out that magnitude frequency distribution of events is sensitive to the evolution of the pore pressure and pore pressure rate along the fault. The injection scenario has a significant effect on the seismicity rate and the magnitudes of the events as well. Larger injection pressure p_{\max} leads to a larger amplification of the seismicity rate, and hence to more numerous events, however it may cause a deficit in the frequency of large magnitudes M_w . On the other hand, the seismicity rate increases with increasing the injection pressure rate β , until a certain threshold β^* . Beyond it, the amplification of the seismicity rate saturates, while the seismic moment is released through larger earthquakes. This suggests that there is a tradeoff between the number of the induced earthquakes and the magnitudes of the events at the scale of a single fault. Finally, we conducted a comparison between our model and the seismicity rate model proposed by Dietrich (1994) and showed that the latter predicts a close dependency of the induced seismicity rate on the injection parameters, however it is not able to model the tradeoff between the magnitudes and the number of the induced earthquakes since it does not allow for variation in the magnitude content.

2.7 Appendix A: Analytical Solution of the Diffusion Equation

In the following, we give the solution of the diffusion equation (equation (2.7)) for half the fault model presented in Figure 2.1a, where $x = 0$ and $x = L = L_0/2$ represent the injection point (center of the fault), and the right edge of the fault, respectively. We solve the two phases ($t_i < t < t_r$) and ($t > t_r$), separately, using Dirichlet boundary conditions: $p(L, t) = 0$.

2.7.1 Injection Phase 1 ($t_i < t < t_r$):

Let $p_1(x, t)$ be the solution of the diffusion equation in Phase 1. In this phase, the boundary conditions are: $p_1(0, t) = \beta t$, $p_1(L, t) = 0$, while the initial conditions are $p_1(x, 0) = 0$. The boundary conditions are nonhomogeneous and time-dependent. We assume that the solution is a summation of a steady state solution $w_1(x, t)$ and a transient state solution $v_1(x, t)$, which is a time-dependent summation of sine functions, as follows:

$$p_1(x, t) = w_1(x, t) + v_1(x, t) = \beta t \left(1 - \frac{x}{L}\right) + \frac{2\beta L^2}{\pi^3 D} \sum_{n=1}^{+\infty} \left(\frac{e^{-D\left(\frac{n\pi}{L}\right)^2 t} - 1}{n^3} \right) \sin\left(\frac{n\pi x}{L}\right). \quad (2.14)$$

2.7.2 Injection Phase 2 ($t_r < t$):

Let $p_2(x, t)$ be the solution of the diffusion equation in Phase 2. In this phase, the boundary conditions are: $p_2(0, t) = p_{\max}$, $p_2(L, t) = 0$, while the initial conditions are $p_2(x, 0) = p_1(x, t_r)$. Similarly, we assume that the solution is a summation of a steady state solution $w_2(x, t)$ and a transient state solution $v_2(x, t)$, which is a time-dependent summation of sine functions, as follows:

$$p_2(x, t) = w_2(x, t) + v_2(x, t) = p_{\max} \left(1 - \frac{x}{L}\right) + \frac{2\beta L^2}{\pi^3 D} \sum_{n=1}^{+\infty} \left(\frac{e^{-D\left(\frac{n\pi}{L}\right)^2 t_r} - 1}{n^3} \right) e^{-D\left(\frac{n\pi}{L}\right)^2 t} \sin\left(\frac{n\pi x}{L}\right). \quad (2.15)$$

2.8 Appendix B: Estimation of the Background Stressing Rate

In order to estimate the background stressing rate $\dot{\tau}_0$ acting on our fault model, we look closely to the evolution of the mean stress τ_m along the fault, along with its time derivative $d(\tau_m)/dt$. We estimate τ_m at each time step using the rate- and state- formulation from equation (2.2). The time series of τ_m and $d(\tau_m)/dt$ are represented in Figures 2.9a and 2.9b over a period of 4.5 years, without fluid injection. We can observe that during the inter-seismic period, the mean stress τ_m increases quasi-linearly following a constant $d(\tau_m)/dt$. However, $d(\tau_m)/dt$ varies in the range [0.03–0.07] Pa/s.

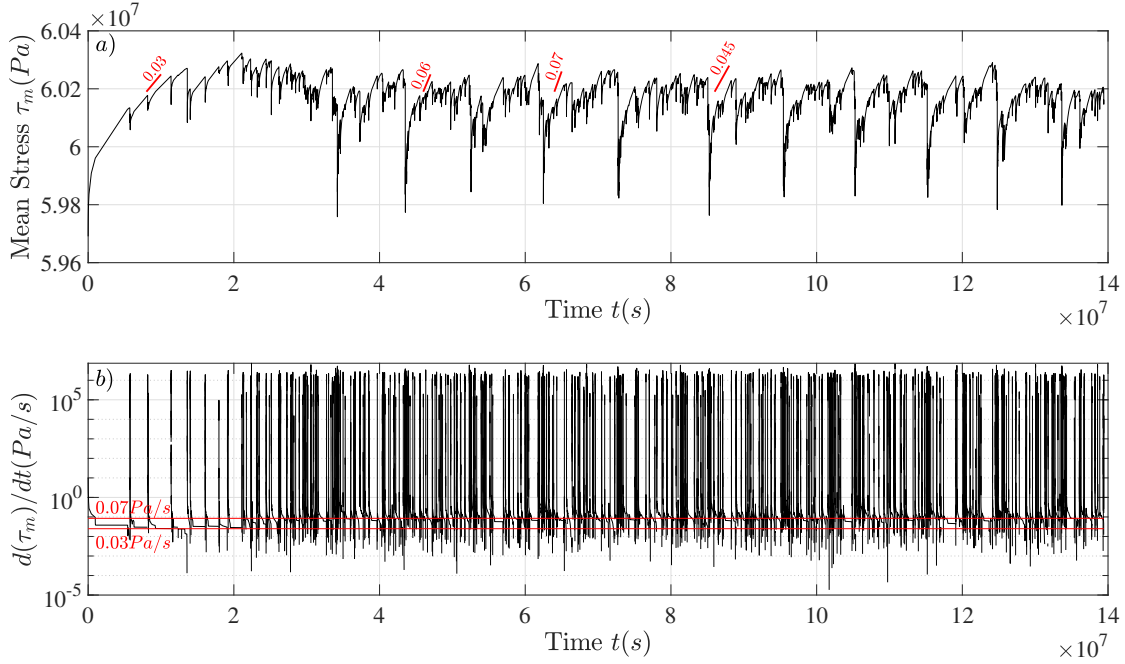


Figure 2.9 – (a) Time series of the mean stress τ_m along the fault. (b) Time derivative of the mean stress $d(\tau_m)/dt$ (only the positive gradient is plotted).

2.9 Appendix C: Analytical Seismicity Rate model following *Dietrich (1994)*

Dietrich (1994) proposed an analytical model for the seismicity rate following stress perturbations, with rate- and state-dependent fault properties. The basic assumptions of this analytical model are that the seismicity originates for a population of identical asperities modelled as rate and state spring slider systems, the faults are close to failure and do not interact (no stress transfer). Thus, it does not allow for variations in earthquake magnitude. In his formulation, the seismicity rate R_D obeys

$$R_D = \frac{r}{\gamma \dot{\tau}}, \quad (2.16)$$

where r is the steady state seismicity rate under constant reference stressing rate $\dot{\tau}$ acting on the faults and γ is a state variable that depends on both time and stressing history, following

$$d\gamma = \frac{1}{a(\sigma - p)} \left(dt - \gamma d\tau + \gamma \left(\frac{\tau}{\sigma - p} - \alpha \right) d(\sigma - p) \right), \quad (2.17)$$

where a is the rate- and state- constitutive parameter, σ is the normal stress, p is the pore pressure, τ is the shear stress and α is a nondimensional constant (*Linker and Dietrich, 1992*). From equation (2.2), we have $\tau/(\sigma - p) = \mu$, and in the following we assume that $\mu \approx \mu_0$ (given the small values of a and b considered). We also assume that $p \ll \sigma$ and

thus $\sigma - p \approx \sigma$, since for the largest injection pressure $p_{\max} = 20$ MPa, the mean pressure along the fault is 10 MPa, and $p - \sigma = 0.9\sigma$. Dividing equation (2.17) by dt , we get:

$$\dot{\gamma} = \frac{1}{a\sigma} - \frac{\gamma}{a\sigma} ((\mu_0 - \alpha)\dot{p} + \dot{\tau}). \quad (2.18)$$

In this study we estimate the seismicity rate from this model using the values of constant background stressing rate $\dot{\tau} = 0.03$ and 0.07 Pa/s (see Appendix B for details). This equation presents two different solutions during injection Phase I and II.

2.9.1 Injection Phase 1 ($t_i < t < t_r$):

$$\gamma_1(x, t) = \frac{1}{\tau_r} e^{-\lambda_1(x, t)} + \frac{1}{a\sigma} e^{-\lambda_1(x, t)} \int_0^t e^{\lambda_1(x, t')} dt' \quad (2.19)$$

where $\lambda_1(x, t) = \frac{\mu_0 - \alpha}{a\sigma} p_1(x, t) + \frac{\dot{\tau}t}{a\sigma}$, and $p_1(x, t)$ is the solution of the pressure diffusion in the Phase I from equation (2.14).

2.9.2 Injection Phase 2 ($t_r < t$):

$$\gamma_2(x, t) = \gamma_1(x, t_r) e^{\lambda_1(x, t_r) - \lambda_2(x, t)} + \frac{1}{a\sigma} e^{-\lambda_2(x, t)} \int_{t_r}^t e^{\lambda_2(x, t')} dt' \quad (2.20)$$

where $\lambda_2(x, t) = \frac{\mu_0 - \alpha}{a\sigma} p_2(x, t) + \frac{\dot{\tau}t}{a\sigma}$, and $p_2(x, t)$ is the solution of the pressure diffusion in the Phase II from equation (2.15).

In order to apply this model, we should choose the number of asperities n (i.e., number of spring slider systems) used. In this case, the background seismicity rate is $S_i = S_0/n$ on each asperity. Then we estimate the time series of the state variable at the center of the asperity i : $\gamma_i(t)$. Then similarly we estimate the seismicity rate $R_{D_i}(t)$ from equation (2.16). Finally, we sum the different seismicity rate $R_{D_i}(t)$ on all the asperities in order to have the general seismicity rate governing the fault $R_D = \sum_{i=1}^n R_{D_i}(t)$.

2.10 Supporting Information

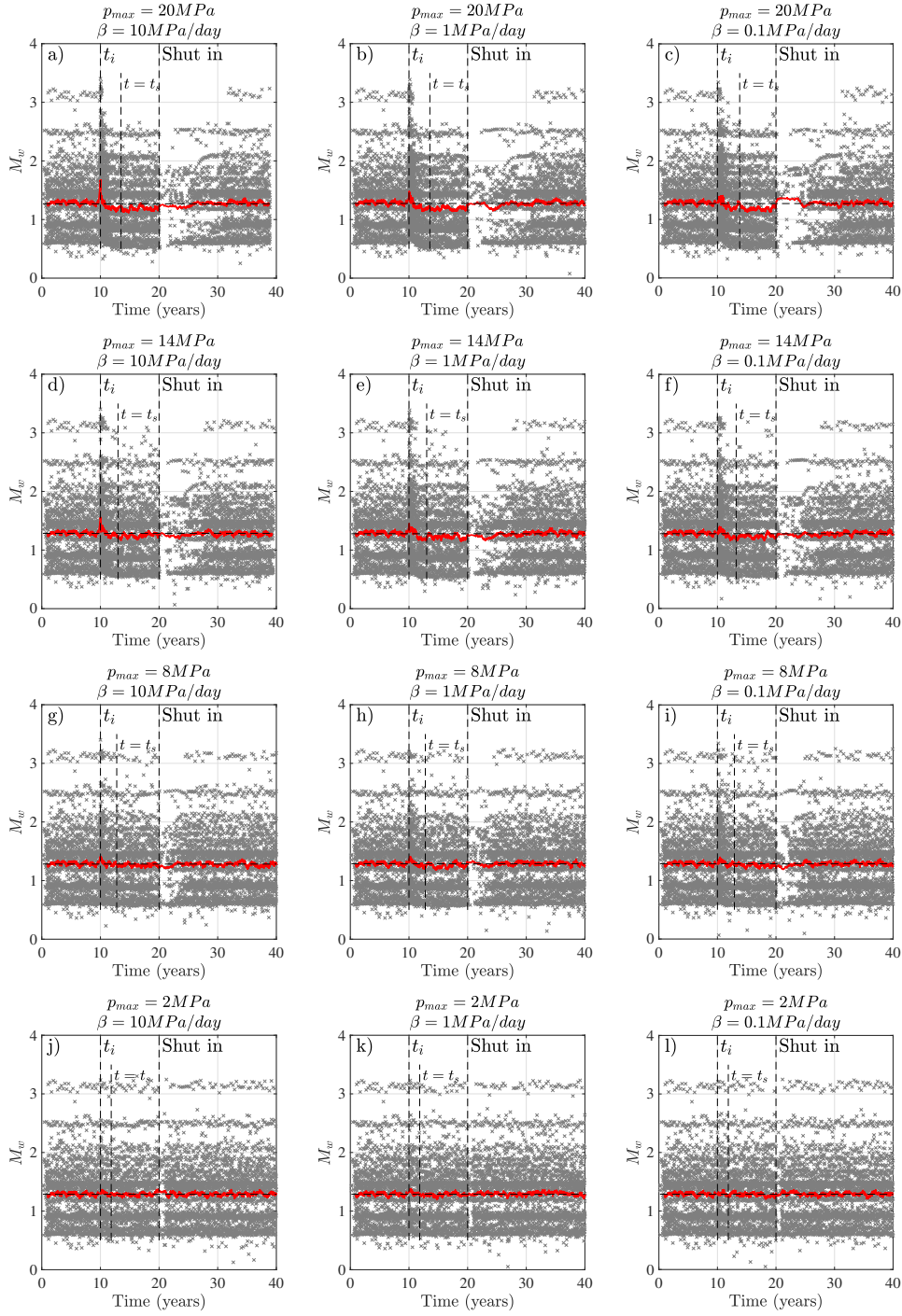


Figure 2.10 – Time series of the moment magnitude M_w for different injection scenarios. The red curve is a centered sliding average, with a sliding window of 50 events. The horizontal dashed line is the mean value of M_w .

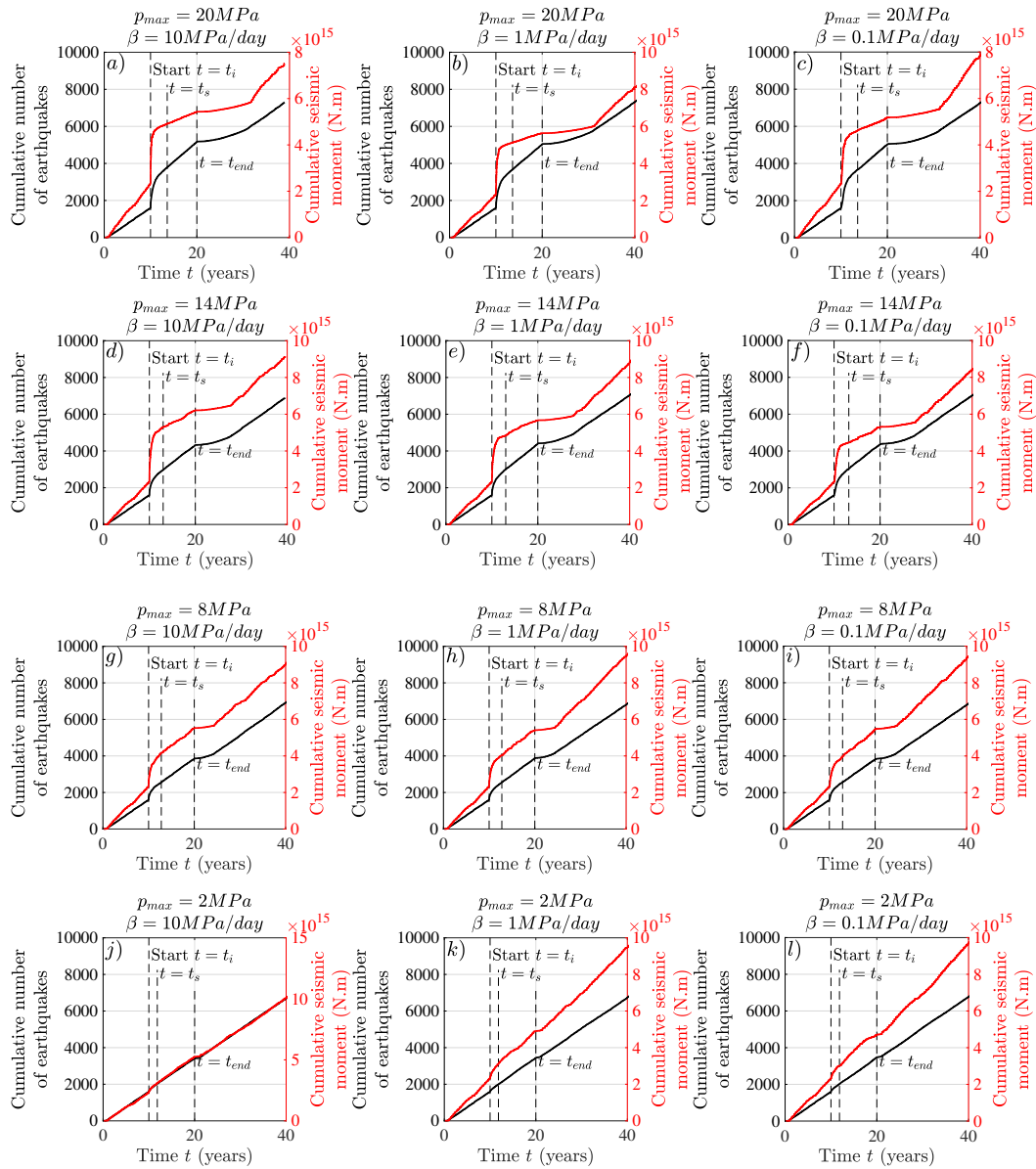


Figure 2.11 – Cumulative number of earthquakes (black curve) and seismic moment in Newton meters (red curve) for different injection scenarios.

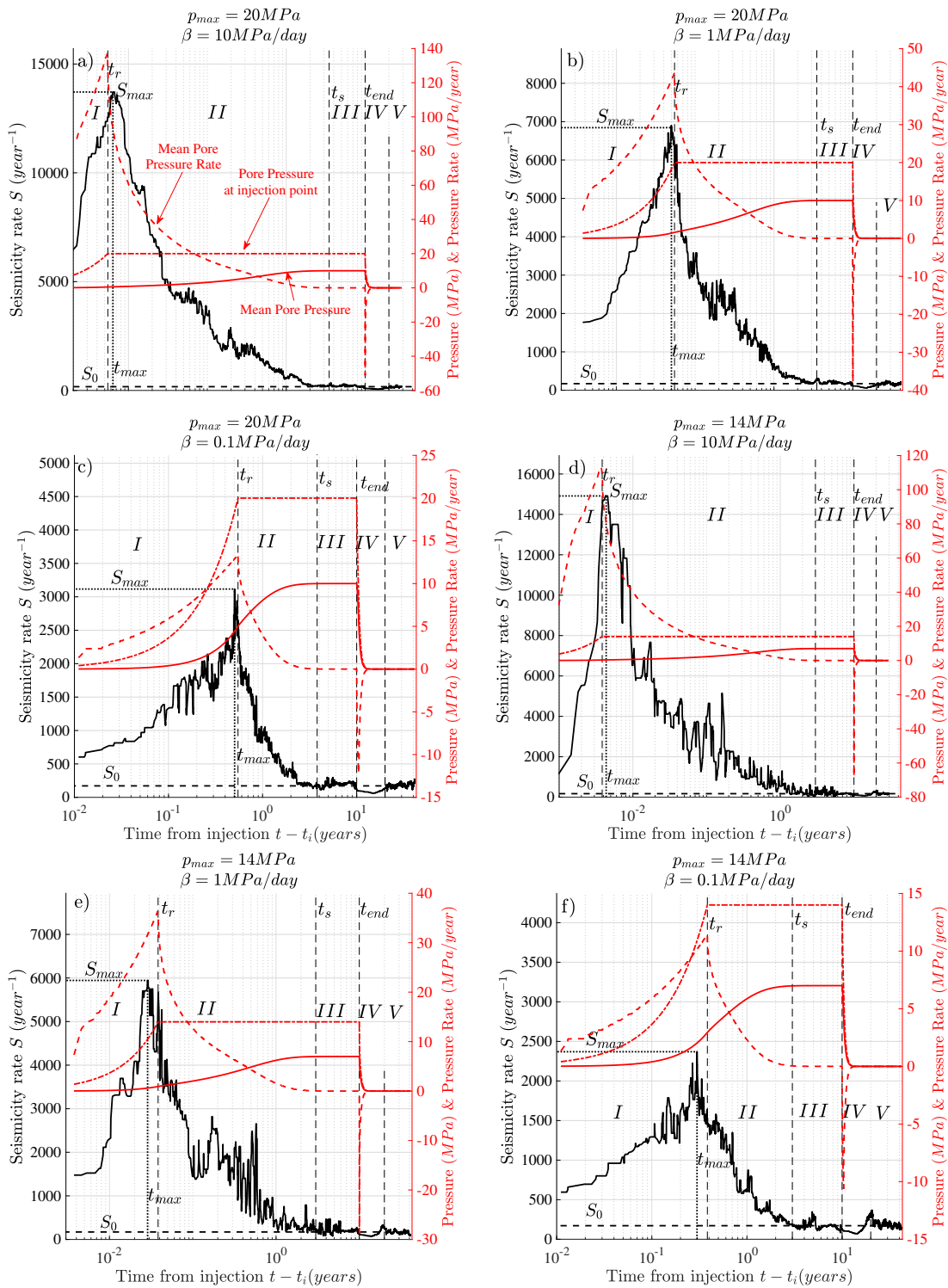


Figure 2.12 – Time series of the seismicity rate, mean pore pressure, mean pore pressure rate and pressure at the injection point, for different injection scenarios.

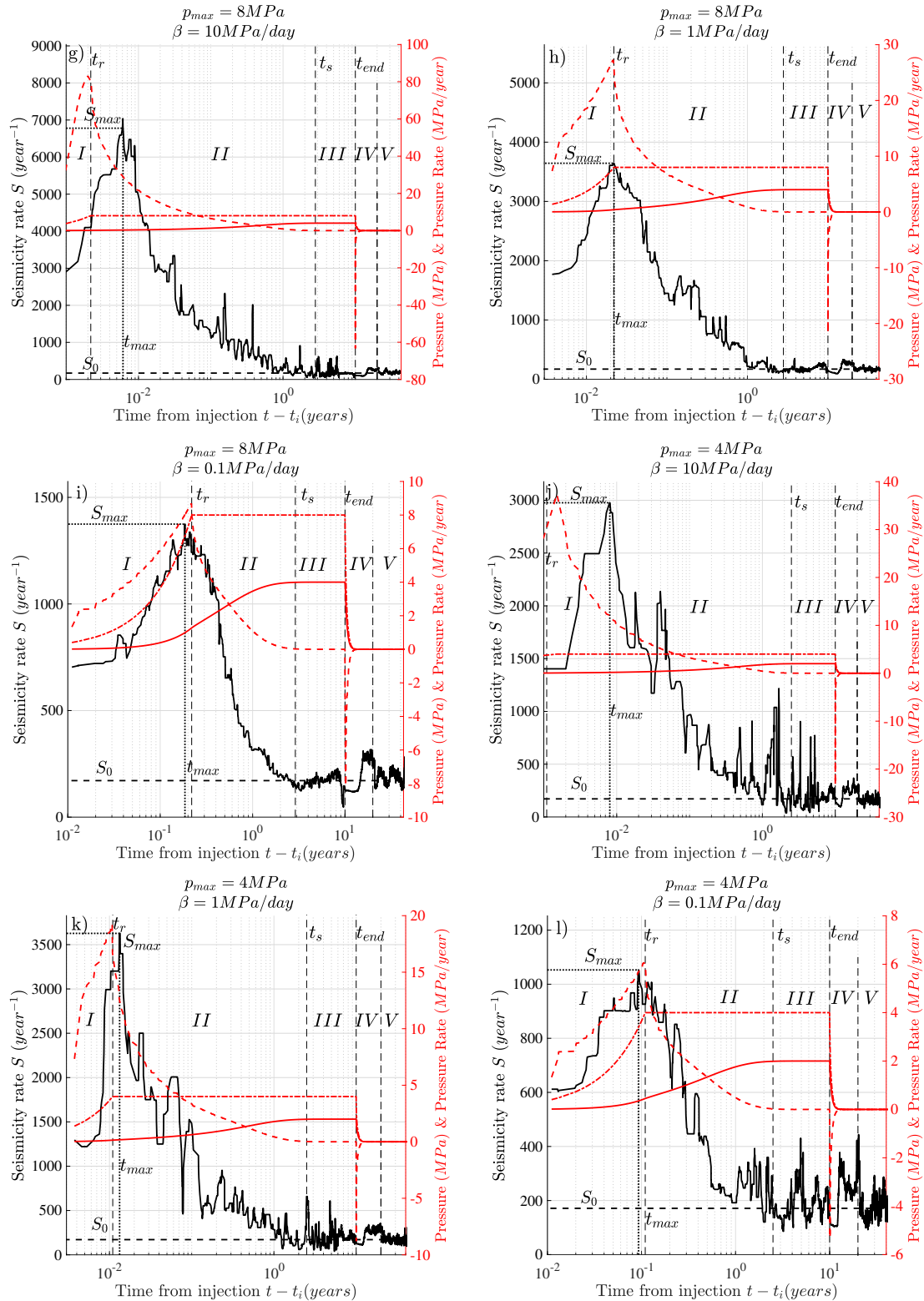


Figure 2.13 – Time series of the seismicity rate, mean pore pressure, mean pore pressure rate and pressure at the injection point, for different injection scenarios.

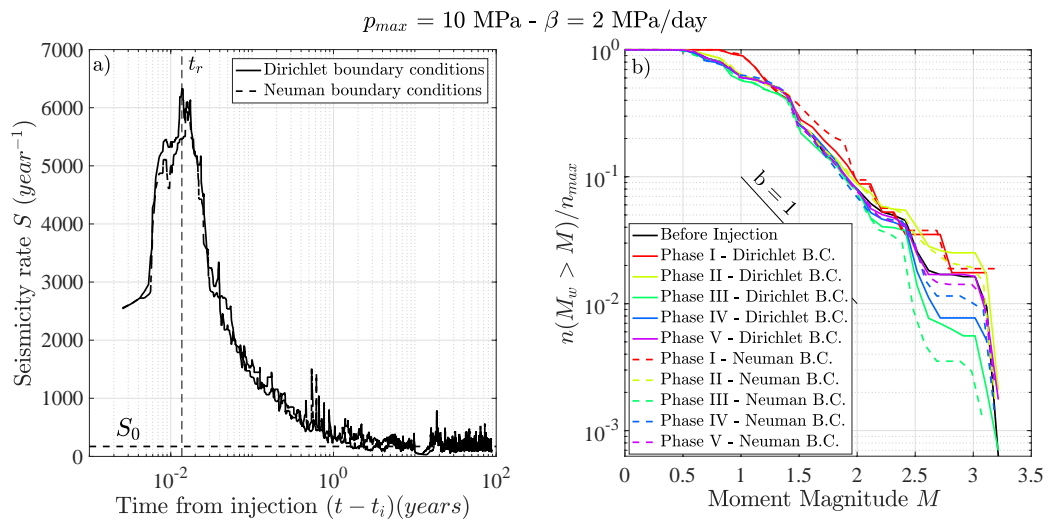


Figure 2.14 – Comparison between Dirichlet boundary conditions (continuous lines) and Neuman boundary conditions (dashed lines). (a) Time series of the seismicity rate. (b) Magnitude frequency distribution.

Chapter 3

Sensitivity of Induced Seismic Activity to Fault Frictional Parameters

Contents

3.1	Introduction	91
3.2	Fault Configurations	93
3.3	Results	94
	3.3.1 Quick Overview of the Background Seismicity	94
	3.3.2 Seismic Response to Fluid Injection	96
3.4	Discussion	101
3.5	Conclusion	103
3.6	Supporting Information	103

Résumé du Chapitre 3 en Français

Ce chapitre est dédié à (1) étendre l'étude qu'on a mené dans le Chapitre 2 pour d'autres configurations de faille hétérogène afin de vérifier que les conclusions qu'on a fait concernant la relation entre les paramètres d'injection d'une part et le taux de sismicité et la distribution des magnitude d'autre part reste valide pour différentes configurations de faille; (2) étudier l'effet des paramètres de frottement de la faille sur sa réponse sismique dans le cas d'injection de fluide, toujours dans le cas d'une faille 2-D hétérogène.

Dans ce chapitre, on génère quatre failles hétérogènes additionnelles, et on utilise les même modèle hydro-mécanique qu'on a présenté et utilisé dans le Chapitre 2.

Dans la première partie du chapitre on montre que la dépendance générale de la sismicité sur les paramètres d'injection qu'on a observé dans le Chapitre 2 reste valide pour les configurations de failles qu'on a testé dans ce chapitre: (1) le taux de sismicité augmente avec l'augmentation de β , jusqu'à ce qu'il se sature; (2) le taux de sismicité aussi augmente avec p_{\max} , (3) pour des valeurs élevées du taux de pression β , la saturation du taux de sismicité se compense par une libération d'un moment sismique plus important (les événements ayant des magnitudes grandes deviennent plus fréquents). Cependant, l'amplitude de la perturbation du taux de sismicité varie d'une configuration de faille à une autre.

Afin d'explorer l'effet des paramètres de frottement sur la sismicité induite, on caractérise les différentes failles en utilisant le rapport a_0/b_0 où a_0 et b_0 sont les moyennes des paramètres de frottement a et b , respectivement, sur la faille. Généralement, plus le rapport a_0/b_0 est élevé, plus la faille présente un comportement stable (Dublanche *et al.*, 2013). Dans ce chapitre on montre que c'est aussi valable dans le contexte d'injection de fluide. En effet, on observe que pour les failles ayant un rapport a_0/b_0 plus élevé, la perturbation de la sismicité est moins amplifiée et le moment sismique libéré est moins important. Nos résultats suggèrent que le taux de sismicité est inversement proportionnel à $(a_0 - b_0)$.

3.1 Introduction

We presented in Chapter 2 a coupled hydro-mechanical model, that allows us to model the diffusion of pore pressure and the associated seismicity along an existing heterogeneous fault governed by rate and state friction (Dietrich, 1992; Ruina, 1983; Linker and Dietrich, 1992). The fault model consists of numerous VS and VW patches characterized by different frictional conditions (rate and state parameters a , b and d_c), respecting different nucleation and continuity conditions (Rubin and Ampuero, 2005), and was able to produce complex seismic ruptures obeying Gutenberg Richter magnitude distribution (Gutenberg and Richter, 1949). Chapter 2 was dedicated to study how the injection parameters (pressure, pressure rate) could influence the features of the induced seismic sequence (rate of earthquakes, magnitude content change). The purpose of this chapter is to extend the previous study onto different fault configurations, in order to: (1) assess whether the obtained results are sensitive to the fault frictional configuration, (2) investigate the effect of the fault frictional parameters on the induced seismicity in such fault configurations.

Indeed, numerous observations of the induced seismic response emphasize on its variability with respect to site and fault properties. For instance, different behavior of seismic sequences was observed for different locations for induced seismicity in Oklahoma and Southern Kansas, where some exhibited strong temporal clustering and the others did not (Schoenball and Ellsworth, 2017). Moreover, following an in-situ experiment, De Barros *et al.* (2016) observed that the number of events may depend on the density of existing fractures. In the context of the EGS project in Soutz-sous-Forêt, 700 seismic events were recorded throughout the hydraulic stimulation of the GPK2 well in Soutz-sous-Forêt in 2000, with a Gutenberg-Richter b value of 1.2, whereas only 250 events were recorded following the hydraulic stimulation of the GPK3 well (only 450 meters away from GPK2) in 2003, having however a Gutenberg-Richter b value close to 0.9, even though the injection pressure and rate were very similar for the two stimulations (Dorbath *et al.*, 2009).

More in particular, McClure and Horne (2014) analyzed the observed induced seismicity due to hydraulic stimulations for six projects (Cooper Basin in Australia, Soutz-sous-Forêt in France, Ogachi in Japan, Rosemanowes in the United Kingdom, Basel in Switzerland and Fjällbacka in Sweden), for which very similar injection scenarios (injection rates and volumes) were used. Among these different projects, McClure and Horne (2014) reported the existence of brittle fault zones for the cases which exhibited higher levels of induced seismicity (Soutz-sous-Forêt, Basel and Cooper Basin). In addition, Shunping *et al.* (2018) correlated the locations of induced seismic events in Oklahoma, including the M_w 5.8 Pawnee earthquake, with geological structures having weak frictional properties.

Beyond observations, mechanical models of fluid induced fault reactivation suggest an important role of the frictional properties. Kroll *et al.* (2017) conducted a numerical study

of fluid injection into a 3-D homogeneous fault governed by rate and state friction, and found that when (b-a) increases (i.e. the rate weakening behavior is more important), the fault produces less earthquakes but with larger magnitudes and therefore have a larger seismic moment release. Beyond seismic ruptures, [Cappa *et al.* \(2018\)](#) reported that the aseismic response may be larger if the fault exhibits significant frictional weakening, while [Dublanche *et al.* \(2019\)](#) showed that the rate and state frictional properties can also affect the dynamics of aseismic crack expansion, in the context of a constant rate fluid injection into a 2-D homogeneous fault.

None of the previous mentioned studies consider frictional heterogeneity along the fault while investigating injection induced fault reactivation. Frictional heterogeneity could however be used to model in a simple way a more general fault zone heterogeneity. Several evidences of fault heterogeneity were reported: (1) [Fagereng and Sibson \(2010\)](#) reported the existence of heterogeneous fault material in subduction zones, (2) observations of seismic repeaters along existing faults ([Nadeau and Johnson, 1998](#); [Lengline and Marsan, 2009](#)) suggest the existence of relatively stable and unstable patches along the faults, (3) and faults generally present geometric heterogeneity.

More in particular [Bourouis and Bernard \(2007\)](#) highlighted the effect of strengthening regions along the faults during the injection experiment in Soutz-sous-Forêt, and showed that the dynamics of microseismicity is strongly dependent on the asperity density along the fault, while according to [Dublanche *et al.* \(2013\)](#) the creeping barriers play an important role in the interactions between the seismic asperities within the fault plane. In addition, in the context of our modeling approach, the use of a heterogeneous fault allows to produce a complex seismic rupture history, which can be compared to real seismicity (see Chapter 2).

For all the reasons mentioned, we are particularly interested in understanding the role of frictional heterogeneity in the slip response to a fluid injection. Here we investigate the role of the frictional properties in the context of the 2-D heterogeneous fault studied in Chapter 2. We generate different fault configurations characterized by different VS conditions, in order to reproduce different stability conditions of the creeping barriers. We use the coupled hydro-mechanical model presented in Chapter 2 along with the different injection scenarios, in order to create seismicity catalogs. As in Chapter 2, we will not look at the detailed dynamics of seismic ruptures, but rather study the general features of induced seismic activity (rate of events and magnitude content).

3.2 Fault Configurations

In this section we present the fault configurations that we investigate. We follow the same procedure and conditions presented in section 2.3 for generating the different fault configurations. We recall some of the main characteristics:

- the fault consists of a combination of velocity-weakening (VW) and velocity-strengthening (VS) patches along the fault, each one being defined by a combination of rate and state parameters (a, b, d_c),
- the patch lengths follow a power law distribution with a -2 exponent,
- each VW patch can nucleate a seismic rupture, independently of the others (Rubin and Ampuero, 2005),
- the critical slip distance of each VW patch is proportional to its size, the one on the VS patches is considered constant and chosen to ensure a good discretization of the VS patches.

To simplify the comparison between the different cases, we generate faults having the same length $L_0 \approx 1.75$ km, similar minimum characteristic slip distance $d_{c_{\min}} = 0.01$ mm, and satisfying an asperity density close to 0.7. These characteristics are similar to the fault studied in Chapter 2 (Figure 2.1, Table 2.1). We also fix the ratio of frictional parameters along the VW patches $a_w/b_w = 0.43$. In order to simulate different stability conditions on the creeping barriers, we vary the ratio a_s/b_s on the VS patches. This results in different ratios a_0/b_0 (a_0 and b_0 being the mean values of the frictional parameters a and b along strike of the fault). According to Dublanchet *et al.* (2013), increasing a_0/b_0 leads to a more stable behavior of the fault. The different ratios a_0/b_0 tested in this study are higher than 1: $a_0/b_0 > 1$.

Here we generate four additional fault configurations. For the rest of this chapter, we will call the fault used in Chapter 2 configuration 1, and we classify the four additional ones with respect to the ratio a_0/b_0 , as configuration 2 to 5. The different characteristics of the new fault configurations are listed in Table 3.1, while Figure 3.1 illustrates the along strike distribution of the characteristic slip distance d_c and the ratio of frictional parameters a/b .

From Figure 3.1a and 3.1b, the spatial distribution of the parameters (a, b, d_c) and the VW and VS patches for the configuration 2 and 3 is quite similar, with different values for the ratio a/b though. This allows us to investigate how the frictional ratio influences the seismic response, regarding of the distribution of the different patches. Configuration 5 (Figure 3.1d) is quite particular, as it contains relatively large VS patches that separate the VW patches.

The different fault configurations are subjected to the same boundary conditions (far-field normal stress σ and constant slipping rate V_0 at the edges of the model), have

Parameter	Symbol	Config. 2	Config. 3	Config. 4	Config. 5
Length of the fault	L_0	1,754.5 m	1,754.5 m	1,754.5 m	1,754.5 m
Number of patches		45	45	42	46
Asperity density	ρ	0.78	0.78	0.79	0.77
Maximum characteristic distance	$d_{c_{\max}}$	≈ 0.29 mm	≈ 0.29 mm	≈ 0.6 mm	≈ 0.6 mm
Characteristic distance on VS patches	d_{c_s}	0.05 mm	0.024 mm	0.023 mm	0.026 mm
Ratio a/b on VW patches	a_w/b_w	≈ 0.43	≈ 0.43	≈ 0.43	≈ 0.43
Ratio a/b on VS patches	a_s/b_s	1.5	2	2	2
Average of the frictional parameter a	a_0	0.001642	0.0019	0.0015	0.0017623
Average of the frictional parameter b	b_0	0.0014426	0.0009648	0.0010617	0.0011672
Ratio of average frictional parameters	a_0/b_0	1.13	1.2	1.41	1.5

¹[Note.]VW = velocity weakening; VS = velocity strengthening; Config. = configuration.

Table 3.1 – Characteristics of the different fault configurations.

the same friction coefficient μ_0 and shear modulus G and hydraulic diffusivity D . Also, for the calculations, we use the same damping coefficient η , dynamic velocity v_{dyn} and [Linker and Dietrich \(1992\)](#)'s coefficient α . We also apply the similar injection scenarios with the same range for the maximum injection pressure p_{max} and the injection pressure rate β . All these values are given in [Table 2.1](#).

3.3 Results

3.3.1 Quick Overview of the Background Seismicity

We follow the same injection procedure as in [Chapter 2](#) and let the fault evolve for 10 years before we start the injection, during which we record the background seismicity. For the different fault configurations, this period is characterized by a quasi-constant number of earthquakes and seismic moment released per year, that we note S_0 and M_0 . The fault can produce a complex pattern of seismic ruptures. The different characteristics of the background seismicity are presented in [Table 3.2](#). In addition, [Figure 3.5](#) in the supporting information ([section 3.6](#)) illustrates the cumulative number of earthquakes, the seismic moment, and the magnitude distribution for these additional fault configurations. We can observe that the seismic moment released per year largely depends on the ratio of average frictional parameters a_0/b_0 . This shows that in the context of this study this ratio can be considered as a proxy to compare the frictional stability of the different fault

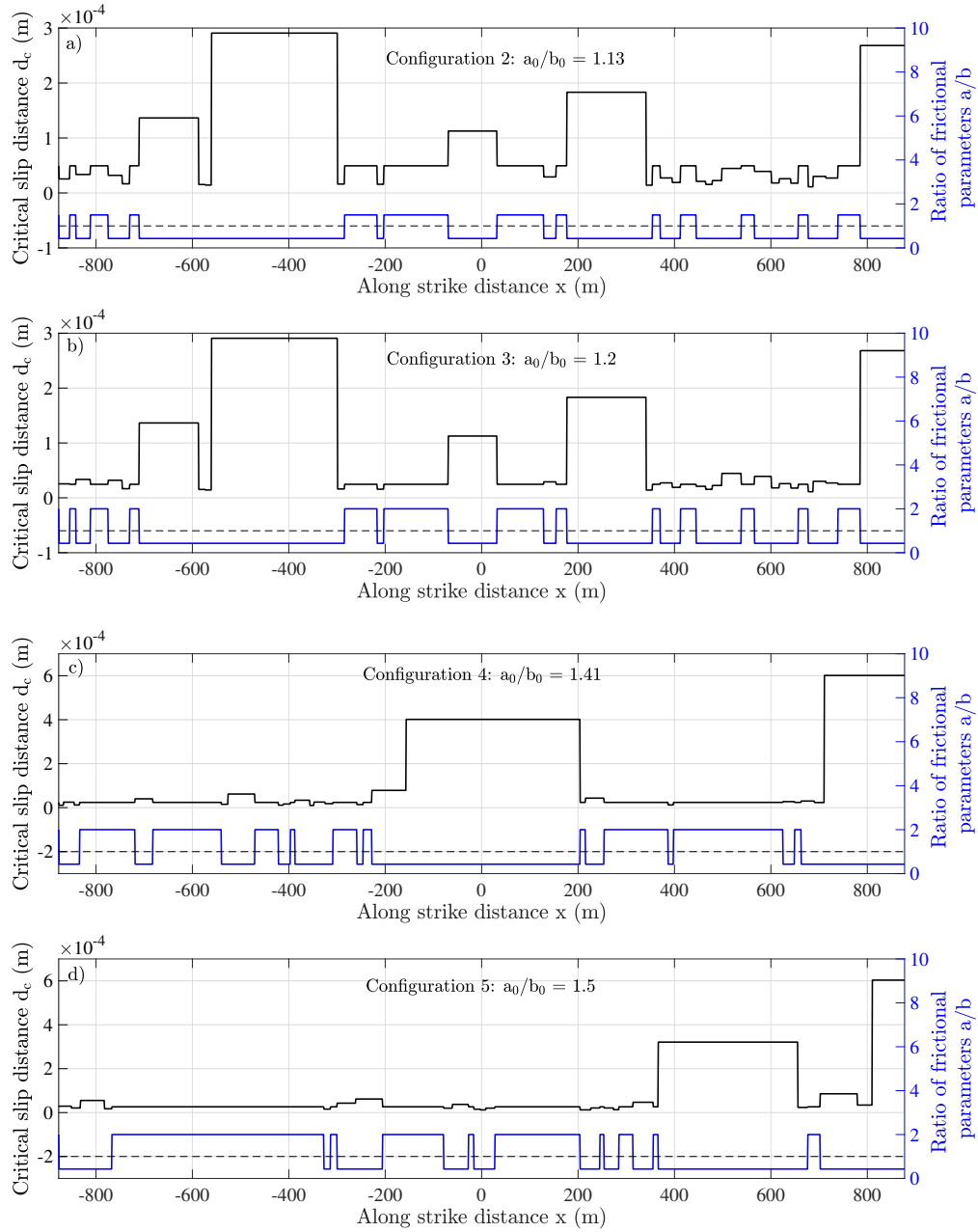


Figure 3.1 – Fault configurations: distribution of the critical slip distance d_c along strike (in black, left axis) and ratio of frictional parameters a/b (in blue, right axis): VW patches are characterized by a ratio $a/b < 1$ and VS patches by a ratio $a/b > 1$. Subplots (a – d) refer to the configurations (2 – 5). Note that the first fault configuration is presented in Figure 2.1 in Chapter 2.

configurations.

Fault	Number of earthquakes per year S_0	Seismic moment released per year M_0	Magnitude range
Configuration 1	170	$2.3 \cdot 10^{14}$ Nm	[0 – 3.5]
Configuration 2	131	$1.7 \cdot 10^{14}$ Nm	[0 – 3]
Configuration 3	125	$1.33 \cdot 10^{14}$ Nm	[0.25 – 3]
Configuration 4	133	$0.08 \cdot 10^{14}$ Nm	[0.3 – 2]
Configuration 5	182	$0.22 \cdot 10^{14}$ Nm	[0.39 – 2.15]

Table 3.2 – Characteristics of the background seismicity for the different fault configurations.

3.3.2 Seismic Response to Fluid Injection

In this section we investigate the seismic response following fluid injection for the different fault configurations. We recall that the injection protocol primarily consists of two phases: (1) linear increase of pressure at the injection point to reach the maximum injection pressure p_{\max} , (2) constant injection pressure equal to p_{\max} . This yields the seismicity rate to increase in Phase I to reach its maximum noted S_{\max} , and then to decrease in Phase II, following the temporal variation of the mean pressure rate along the fault (refer to Figures 2.3e, 2.12 and 2.13). For this reason, we investigate each phase separately. To simplify the comparison between the different cases, we re-plotted the results concerning the configuration 1 (used in Chapter 2) for all the figures presented here. We will first start to evaluate whether the dependency on the injection parameters that we observed in Chapter 2 remains valid for the different fault configurations. Next, we will investigate how the frictional behavior of the fault affects its induced seismic response. As each fault configuration exhibits a particular background seismicity (Table 3.2), we proceed by estimating and comparing the increase in seismicity due to fluid injection, and not the total recorded seismicity.

3.3.2.1 Phase I

To characterize Phase I, we illustrate the increase in seismicity rate S_{\max}/S_0 caused by the imposed pressure history in Figure 3.2, in which the x-axis refers to the injection pressure rate β and the color scale represents the maximum injection pressure p_{\max} . We also estimate an average of the rate of the induced seismic moment released in this phase as follows: $\dot{M}_{\text{inj}} = (M_{\text{inj}})/\Delta t$, where Δt is the time duration of Phase I and M_{inj} is an estimation of the cumulative seismic moment released due to solely fluid injection, determined as follows: $M_{\text{inj}} = M_{\text{T}} - M_{\text{tect}} = M_{\text{T}} - M_0 \Delta t$, where M_{T} is the total seismic moment released during the period Δt and M_{tect} is an estimation of the cumulative seismic

moment released during this phase due to tectonic loading. It is illustrated in Figure 3.3.

Overall, we observe relatively the same dependence with the injection parameters as discussed in Chapter 2. From Figure 3.2, the increase in seismicity rate S_{\max}/S_0 is larger for higher values of maximum injection pressure p_{\max} for the various cases investigated. Moreover, it increases with the injection pressure rate β until it saturates and remains relatively constant. This is the case of the majority of fault configurations, particularly configurations 1 to 4 (Figures 3.2a – 3.2d). Configuration 5 presents an exception, where for the ranges of pressure rate tested here, the seismicity rate increase S_{\max}/S_0 keeps on rising (Figure 3.2e). This behavior is particularly more important for the largest injection pressures p_{\max} .

On the other hand, from Figure 3.3, the average rate of seismic moment released during this phase \dot{M}_{inj} keeps on increasing with the injection pressure rate β , relatively for a wide range of the injection pressure p_{\max} tested. For the smallest values of p_{\max} , the average rate of seismic moment does not vary much with the injection pressure rate β though, for the different fault configurations. For the configurations 2, 3 and 4, for values of pressure rate β above a certain value, the seismicity rate increase S_{\max}/S_0 saturates, while the average rate of seismic moment released \dot{M}_{inj} continues to increase. As the seismic moment is related to the magnitude of the seismic event (Equation 2.13), this implies a shift in the magnitude of the induced seismic events, with larger proportions of higher magnitudes. This is the same tradeoff that was previously observed for Configuration 1 (Figures 3.2a and 3.3a). Figure 3.6 (in the supporting information section 3.6) represents the magnitude distribution for an injection at $p_{\max} = 20$ MPa and for three different values of injection pressure rate ($\beta = 10, 1$ and 0.1 MPa/day). This Figure shows more frequent larger magnitude earthquakes as β increases. This is consistent with the tradeoff that we observe between the seismicity rate and moment rate. We cannot make the same conclusion for configuration 5. Based only on Figures 3.2e and 3.3e, we cannot say whether the continuous increase in \dot{M}_{inj} for the largest β is caused by a change in the magnitude content, or by the continuous increase in the seismicity rate S_{\max}/S_0 observed.

We now examine the effect of the frictional parameters. By comparing Figures 3.2a, 3.2b, 3.2c and 3.2d, we observe that the seismicity rate increase S_{\max}/S_0 takes higher values for fault configurations having a lower ratio of average frictional parameters a_0/b_0 . This is particularly evident for the largest injection pressures ($p_{\max} > 10 - 12$ MPa). For instance, for an injection pressure set to $p_{\max} = 20$ MPa, S_{\max}/S_0 saturates for the values 88, 58, 41 and 37, for the configurations 1 ($a_0/b_0 = 1.01$), 2 ($a_0/b_0 = 1.13$), 3 ($a_0/b_0 = 1.2$) and 4 ($a_0/b_0 = 1.41$), respectively. Similarly at $p_{\max} = 12$ MPa, S_{\max}/S_0 saturates for the values 55, 20, 16 and 15.

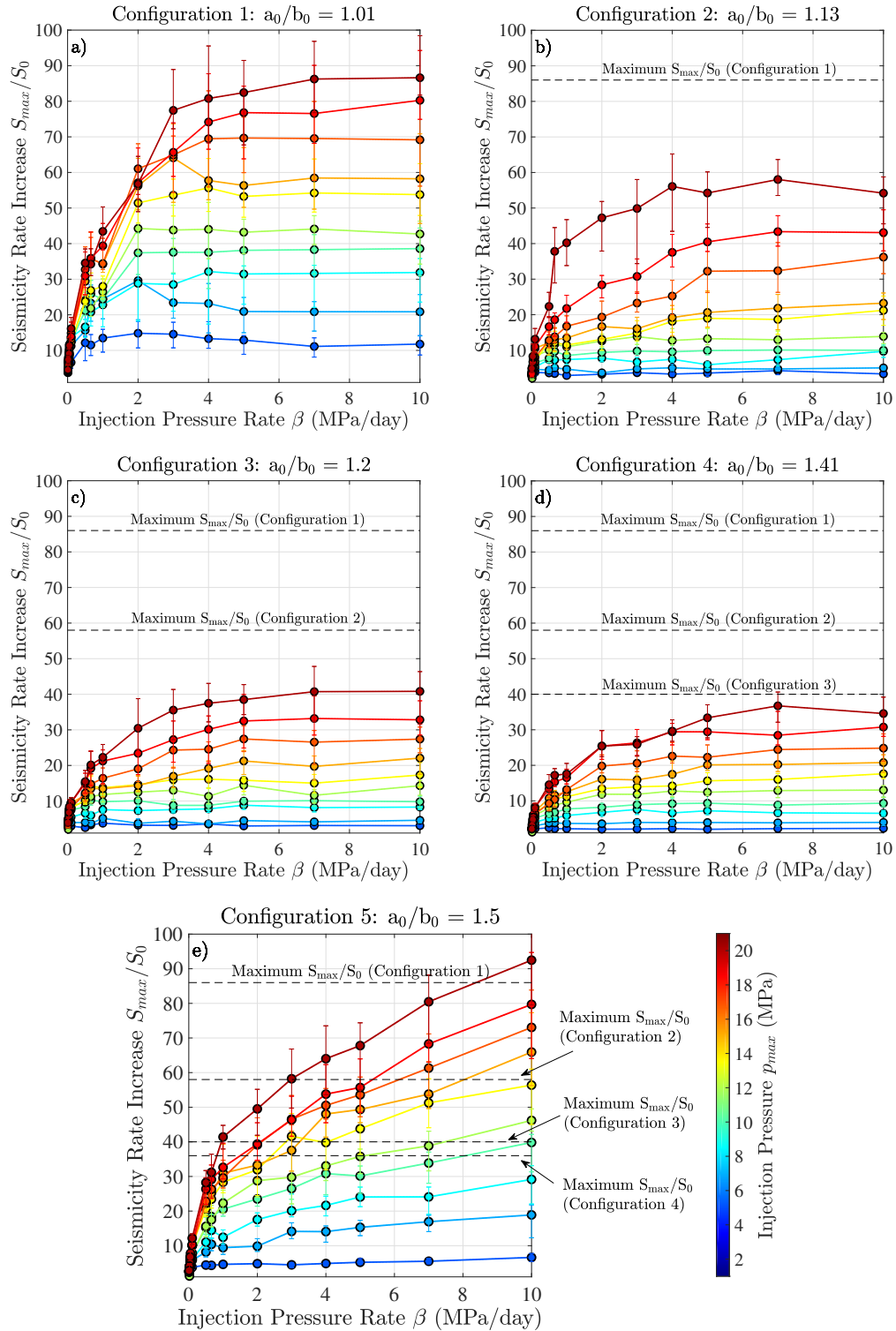


Figure 3.2 – Seismicity rate increase S_{max}/S_0 (ratio of maximum seismicity rate over seismicity rate before injection) as a function of the injection pore pressure rate β , for the different fault configurations: (a) Configuration 1: $a_0/b_0 = 1.01$; (b) Configuration 2: $a_0/b_0 = 1.13$; (c) Configuration 3: $a_0/b_0 = 1.2$; (d) Configuration 4: $a_0/b_0 = 1.41$; (e) Configuration 5: $a_0/b_0 = 1.5$. Error bars represent the uncertainty of S_{max}/S_0 for one simulation. The color scale represents different values of the maximum injection pressure p_{max} . To simplify the comparison, all the subplots have the same y-axis limits, and horizontal dashed lines represent the maximum seismicity rate increase S_{max}/S_0 reached for $p_{max} = 20$ MPa, for the different fault configurations.

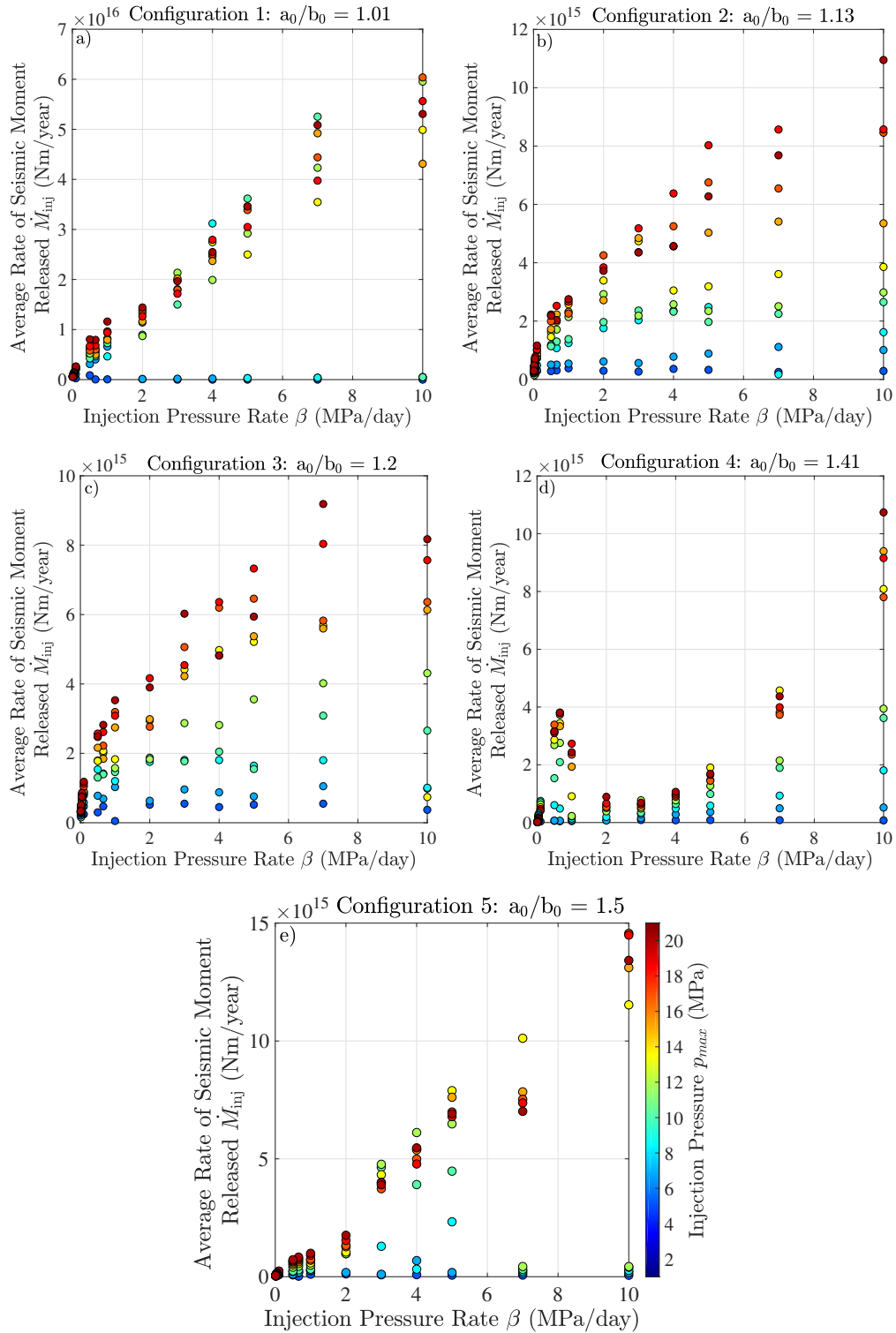


Figure 3.3 – Induced average seismic moment rate \dot{M}_{inj} as a function of the injection pore pressure rate β , for the different fault configurations: (a) Configuration 1: $a_0/b_0 = 1.01$; (b) Configuration 2: $a_0/b_0 = 1.13$; (c) Configuration 3: $a_0/b_0 = 1.2$; (d) Configuration 4: $a_0/b_0 = 1.41$; (e) Configuration 5: $a_0/b_0 = 1.5$. The color scale represents different values of the maximum injection pressure p_{max} . 99

Configuration 5 does not follow the same behavior. For this particular case, the seismicity rate increase S_{\max}/S_0 exceeds the different values reached by the other fault configurations, even though this fault has the higher ratio of frictional parameters $a_0/b_0 = 1.5$ (Figure 3.2e). The behavior of this fault is quite particular with respect to the others, we will discuss this in the next section.

As mentioned in the previous section, the spatial distribution of the asperities along the fault for configurations 2 and 3 is quite the same (Figures 3.1a and 3.1b). They only differ by the values of the frictional parameters. However, the induced seismic response is larger for configuration 2, in terms of seismicity rate increase S_{\max}/S_0 (Figures 3.2b and 3.2c) and also average rate of seismic moment released (Figures 3.3b and 3.3c). This suggests that independently from the asperities distribution along the fault, the ratio of frictional parameters plays an important role.

3.3.2.2 Phase II

To investigate Phase II, we estimate the cumulative seismic moment released due to solely fluid injection in this phase M_{inj} as presented in section 3.3.2. In the same way, we estimate the number of induced earthquakes: $n_{\text{inj}} = n_{\text{T}} - n_{\text{tect}} = n_{\text{T}} - S_0 \Delta t$, where n_{T} is the total seismic number of earthquakes during the period Δt and n_{tect} is an estimation of the number of earthquakes during this phase due to tectonic loading.

As the injection pressure rate β does not play an important role during this phase (refer to section 2.4.3.5), here we plotted directly the number of induced earthquakes with respect to the induced seismic moment released in Figure 3.4. In this Figure, the color scale represents the maximum injection pressure p_{\max} and the shape of the scattered markers refers to the fault configuration. As the behavior of the configuration 5 deviates from the rest of the cases, we only illustrate here the first four fault configurations. From this Figure, we first examine the dependance on the maximum injection pressure p_{\max} .

For the different cases, the number of induced earthquakes and seismic moment released are higher for larger p_{\max} , with no important effect to the pressure rate β . This implies that independently of the fault configuration, the seismic response depends on the pressure diffusion duration, which is proportional to the injection pressure p_{\max} (refer to Figure 2.4 b). This is consistent with the observations made in Chapter 2 (section 2.4.3.5).

We also observe a clear dependence on the ratio of average frictional parameters. Faults with a higher ratio a_0/b_0 exhibit a lower seismic response (lower seismic moment and lesser induced earthquakes) for a specified set of injection parameters. This is particularly evident for configuration 4. In addition, the seismic response of configurations 2 and 3 is not the same, especially for $p_{\max} > 10$: even though the number of induced earthquakes is quite similar for the two faults for a set of injection parameters, the seismic moment released by the configuration 2 ($a_0/b_0 = 1.13$, triangle markers) is slightly

larger than the one released by the configuration 3 ($a_0/b_0 = 1.2$, square markers). This behavior is more pronounced for larger p_{\max} . Having relatively the same number of earthquakes, a higher seismic moment can only be caused by a larger frequency of higher magnitudes. This implies, that for the same asperity distribution, a lower ratio of average of frictional parameters along the fault can produce more frequent large earthquakes.

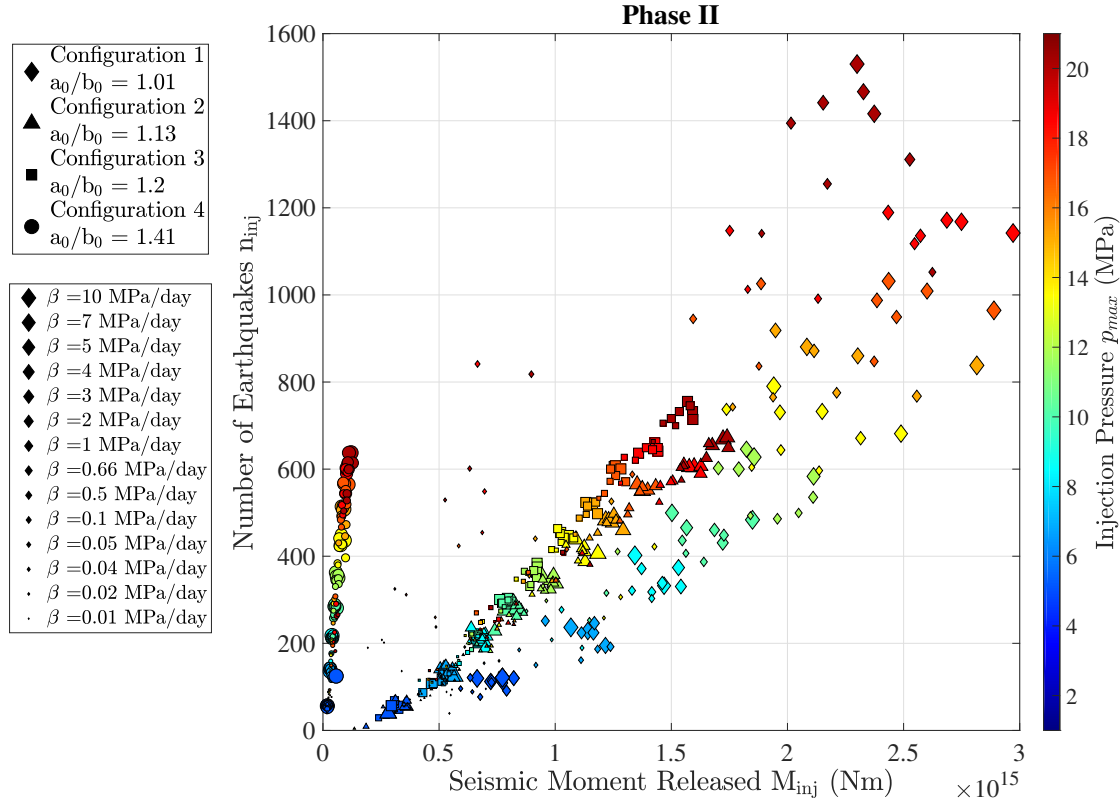


Figure 3.4 – Evolution of the number of earthquakes and the seismic moment released with the injection parameters in Phase II, for the following fault configurations: configuration 1: $a_0/b_0 = 1.01$ (diamond symbol), configuration 2: $a_0/b_0 = 1.13$ (triangle symbol), configuration 3: $a_0/b_0 = 1.2$ (square symbol) and configuration 4: $a_0/b_0 = 1.41$ (circle symbol). The color scale represents the injection maximum pressure p_{\max} , and the size of the scattered points represents the injection pressure rate β .

3.4 Discussion

In this chapter, we perform 560 numerical simulations of fault reactivation due to fluid injection, for four additional different heterogeneous fault configurations. Each fault is characterized by a ratio of average frictional parameters a_0/b_0 , which we use in this study

to evaluate in a general way the frictional stability of the fault.

The seismicity catalogs for the majority of the fault configurations exhibit the same dependence of induced seismic response with respect to the injection parameters. We observe that: (1) the seismicity rate increases with β and then saturates, (2) the seismicity rate also increases with p_{\max} , (3) a trade-off exists between the seismicity rate increase and the magnitude content of the seismic events. This implies that in the context of our numerical approach, the dependence of the induced seismic response on the injection parameters presented in Chapter 2 remains valid for the different fault configurations. The amplitude of the induced seismicity perturbation depends though on the frictional heterogeneity of the fault (ratio a_0/b_0). Configuration 5 presents an exception, for which the seismicity rate increase does not saturate. This behavior is relatively similar to the one estimated by using the simplified analytical model based on the seismicity rate proposed by Dietrich (1994) (refer to section 2.9 and Figure 2.5). This simplified model assumes a population of non-interacting asperities. From Figure 3.1d, the majority of the VW patches are quite small and separated by large VS patches. This particular distribution of the asperities may be considered relatively similar to Dietrich (1994)'s model. As the VW patches are largely separated, it may be hard to overcome the VS patches and generate larger magnitudes. Figure 3.7 in the supporting information (section 3.6) shows that the seismic ruptures for this fault configuration are more or less confined within the VW patches. This may be the reason why the behavior of this particular fault configuration deviates from the rest.

The objective of this chapter is to investigate the effect of the frictional parameters on the induced seismic activity. Following Rubin and Ampuero (2005) and Kroll *et al.* (2017), the stress drop on a single homogeneous asperity is proportional to $(b-a)\sigma_{\text{eff}}$. As the seismicity rate is generally inversely proportional to the stress drop: $S \propto 1/\Delta\tau$, it is also expected to be inversely proportional to the effective stress and the rate and state parameters. The nature of the heterogeneity of the rate and state parameters (a and b) of the faults in study here makes it complicated to choose the appropriate a and b value in order to estimate the stress drop following a seismic event that may rupture several neighbouring patches (VW and neighbouring VS patches). Thus, we cannot make a clear and simple relation between the observed seismicity rate and the rate and state parameters along the fault. Nonetheless, the analysis of the numerical results show that the number of induced earthquakes, as well as the total seismic moment released is sensitive to the ratio a_0/b_0 . Here, the faults with a higher ratio are generally more stable and are less affected by the pore pressure perturbation, and thus exhibit a lower seismicity rate and seismic moment in both Phases I and II (Figures 3.2 and 3.4). These results support the different observations that correlate an increase in the induced seismic response at certain locations with weak frictional parameters (e.g. (Dorbath *et al.*, 2009; McClure and Horne, 2014; Shunping *et al.*, 2018)). In addition, in the context of a constant rate injection into a 2-D homogeneous rate-weakening fault, Kroll *et al.* (2017) showed that the number of induced earthquakes and the events magnitude are highly

dependent on the frictional parameters (b-a).

Finally, for a set of injection parameters (β , p_{\max}), the results show that the seismic moment released is smaller for faults with a higher ratio a_0/b_0 . As the seismic energy is the same (similar injection parameters, injection duration, and hydraulic diffusivity), this implies that for such faults a larger proportion of this energy may be dissipated through aseismic motion. Unfortunately, for the simulations conducted here we did not record the aseismic deformation accumulated along the fault in the catalogs. We thus cannot investigate whether this is really the case, and we leave this for future studies.

3.5 Conclusion

In addition to the numerical simulations presented in Chapter 2, we presented here 560 new simulations that we performed on additional four heterogeneous fault configurations. The different faults exhibit generally the same basic characteristics, and only differ by their frictional parameters. In particular, we characterize each fault with a ratio of average frictional parameters a_0/b_0 which could be used as a proxy to describe the general stability and frictional behavior of such heterogeneous faults.

We first showed that the main tendency that we observed in Chapter 2 regarding the dependence of the injection induced seismic response (seismicity rate and magnitude content) of a heterogeneous fault on the injection parameters (injection maximum pressure p_{\max} and injection pressure rate β) remains valid for the different fault configurations: the rate of events is essentially controlled by the maximum pressure, while the magnitude content depends on both the the maximum pressure and the pressure rate. We then investigated how the frictional parameters affect the induced seismic response, and showed that a more stable fault (higher a_0/b_0) can resist more to fluid injection, and exhibits lower amplification to its seismic activity. These results support numerous real data correlating a larger induced seismic response and weak frictional behavior.

3.6 Supporting Information

In this section we present some additional informations that support our results and discussion, but that are not essential to the conclusions.

Background seismicity for the different fault configurations

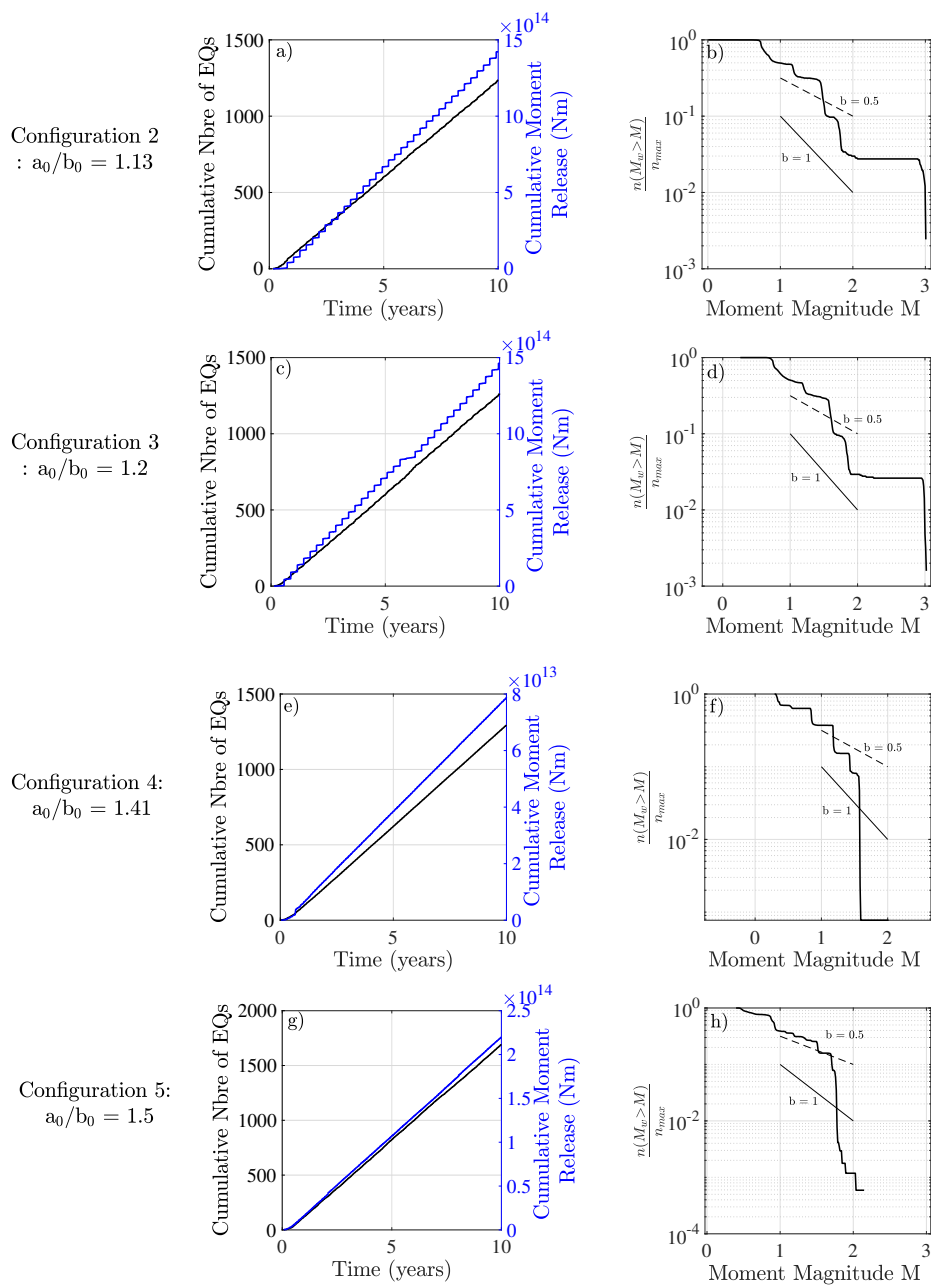


Figure 3.5 – Background seismicity for the different fault configurations: (a, c, e, g) represent the cumulative number of earthquakes (in black, left axis) and the cumulative seismic moment released (in blue, right axis); (b, d, f, h) represent the magnitude frequency distribution; for the fault configurations 2, 3, 4 and 5.

Dependence of the magnitude distribution on the injection parameters during Phase I

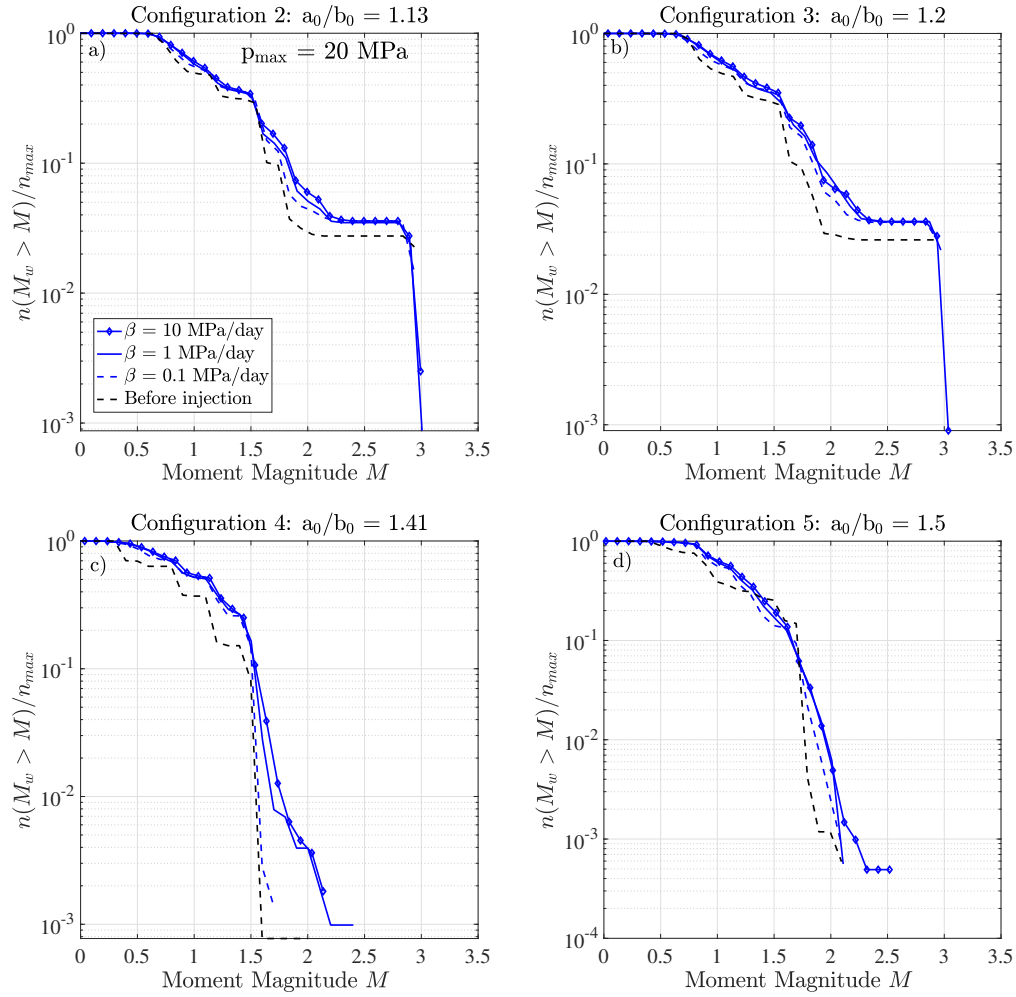


Figure 3.6 – Dependence of the magnitude distribution on the injection parameters: in this example the injection maximum pressure is $p_{max} = 20$ MPa and magnitude distributions are plotted for the following injection pressure rates $\beta = 10$ MPa/day (solid blue line with diamond markers), $\beta = 1$ MPa/day (solid blue line), $\beta = 0.1$ MPa/day (dashed blue line). The dashed black line refers to the magnitude distribution of the events before fluid injection started. (a) Configuration 2: $a_0/b_0 = 1.13$; (b) Configuration 3: $a_0/b_0 = 1.2$; (c) Configuration 4: $a_0/b_0 = 1.41$; (d) Configuration 5: $a_0/b_0 = 1.5$.

Spatial distribution of the seismic rupture for fault configuration 5

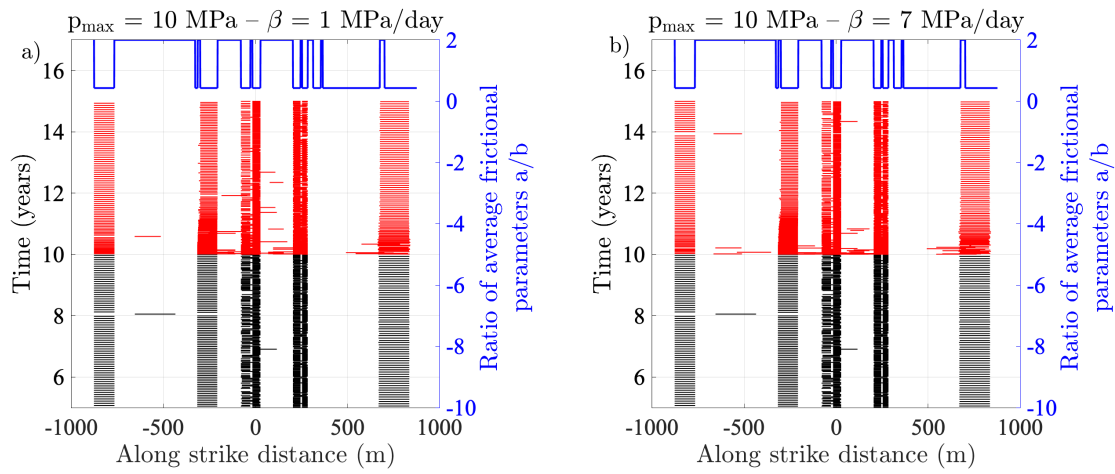


Figure 3.7 – Spatial distribution of the seismic rupture for fault configuration 5: during 5 years before injection (black color) and 5 years during injection (red color). On the left axis is represented the distribution of the ratio a/b along the fault. a) for the injection scenario $p_{\max} = 10$ MPa and $\beta = 7$ MPa/day; b) for the injection scenario $p_{\max} = 10$ MPa and $\beta = 1$ MPa/day.

Chapter 4

Deterministic and Probabilistic Inversions of Pore Pressure Diffusion: Application to Laboratory Injection Experiments

Contents

4.1	Introduction	109
4.2	Experimental Data	111
4.2.1	Experimental Setup	111
4.2.2	Experimental Protocol	113
4.2.3	Experimental Results	113
4.3	Methodology	115
4.3.1	Inverse Problem	115
4.3.2	Deterministic inversion	118
4.3.3	Metropolis Hastings Algorithm	122
4.4	Application to the Experimental Data	125
4.4.1	Estimating the Best Model: Deterministic Approach	125
4.4.2	Estimating the Uncertainties: the MCMC approach	130
4.4.3	Discussion	134
4.5	Diffusivity, Displacement and Effective Stress	135
4.6	Conclusion and Perspectives	140
4.7	Appendix A: Development of the Adjoint State Method	141

The numerical method and the results presented in this chapter are submitted for publication in *Geophysical Journal International*.

Résumé du Chapitre 4 en Français

Ce chapitre est dédié à étudier la variation de la diffusivité hydraulique avec la réduction de la contrainte normale effective et l'accumulation du déplacement sur la faille, associés à la réactivation de faille par injection de fluide. Pour cela, on réalise en collaboration avec François Passelègue (EPFL, Lausanne) des expériences d'injection de fluide à l'échelle du laboratoire, sous chargement triaxial, dans une faille lisse dans un échantillon cylindrique d'Andésite. Pendant les expériences, la pression de pore est enregistrée à deux endroits différents le long de la faille. Les expériences sont réalisées pour différentes valeurs de pression de confinement (30, 60 et 95 MPa).

Afin d'évaluer l'évolution de la diffusivité hydraulique au cours de l'injection, on développe un algorithme d'inversion basée sur l'approche déterministique (en utilisant la méthode d'état adjoint) et on l'applique aux données expérimentales afin d'estimer le meilleur modèle d'une diffusivité hydraulique effective qui peut expliquer les données. Ensuite on développe et on applique un algorithme d'inversion probabilistique (méthode MCMC) afin d'évaluer les incertitudes sur le meilleur modèle.

La méthode numérique était capable de reproduire les données expérimentales pour un large domaine temporel des différentes expériences. Cependant, il était difficile d'ajuster les données pour les derniers temps des expériences, parce que les données expérimentales enregistrées au-delà de ces temps ne sont pas suffisantes pour modéliser proprement le processus de diffusion. Deux solutions pourraient être appliquées: (1) étendre les mesures expérimentales pendant un temps suffisant après que la pression atteint un régime stationnaire sur la faille, (2) application des techniques de régularisation à la solution numérique.

Les résultats d'inversion de la diffusivité hydraulique montrent qu'elle dépend initialement sur la pression de confinement. au cours de l'injection, elle varie avec le déplacement accumulé sur la faille et en particulier avec la réduction de la contrainte normale effective moyenne agissant sur la faille : $D = 0,0015/\sigma^{1.64}$.

L'application d'une telle approche numérique d'inversion pourrait être très avantageuse vue qu'elle permet la reconstruction des profils de pression de pore au cours de l'injection. La comparaison de ces profils avec les données de déformation des jauges et des capteurs acoustiques (sur l'échantillon) permettra de mieux comprendre la relation entre le front diffusif et le front de rupture asismique / sismique.

4.1 Introduction

Understanding how the permeability of a fault evolves during fluid injection activities and through the fault reactivation process is of great interest, for reservoir engineering, enhanced geothermal systems, as well as hydraulic fracturing operations. It can also help better understand the spatio-temporal distribution of induced seismic sequences. However, the interactions between fluids and faults/reservoirs can be complex, as the confining pressure, effective stress and shear slip can affect the hydro-mechanical properties of the fault. On one hand, variation in fault permeability has been observed following changes in effective stress during laboratory experiments (Zoback and Byerlee, 1975; McKee *et al.*, 1988; Ghabezloo *et al.*, 2009; Rutter and Mecklenburgh, 2018) as well as during in-situ permeability measurements (Fisher and Zwart, 1996). On the other hand, seismic events and slip accumulation can also affect the fault permeability (Zhang and Tullis, 1998; Baghbanan and Jing, 2008), as permeability enhancement was observed similarly during laboratory (Chen *et al.*, 2000a; Gutierrez *et al.*, 2000; Wu *et al.*, 2017; Im *et al.*, 2018) and in-situ injection experiments (Guglielmi *et al.*, 2015a,b; Duboeuf *et al.*, 2017; Bhattacharya and Viesca, 2019).

Current permeability measurement methods consist mainly on experimental approaches, in which the permeability is determined via fluid flow analysis, using Darcy's law for instance (Darcy, 1857), either on experimental samples in the laboratory (e.g. Zoback and Byerlee (1975), Zhang and Tullis (1998) and Ghabezloo *et al.* (2009)) or in-situ along a plate-boundary fault (e.g. Fisher and Zwart (1996)). Although quite effective, such classical methods lie on the assumption that the permeability is constant throughout one measurement test. Thus, they do not allow for the characterization of the permeability evolution resulting from slip or changes in effective stress, in the context of a single laboratory injection experiment *per se*.

Beyond permeability enhancement, the relation between the pressure diffusive front and the fault reactivation process is the focus of several research studies. On one hand, the migration of seismic events has been suspected to be driven by the diffusion of pore pressure away from the injection wells (Shapiro *et al.*, 1997). This is proposed for instance for the induced seismic sequences in Denver, Colorado (Healy *et al.*, 1968; Hermann *et al.*, 1981; Hsieh and Bredehoeft, 1981), Soultz-sous-Forêt (Shapiro *et al.*, 2002) and Ohio (Kim, 2013). This mechanism assumes that the reactivation front tracks a particular pressure front. On the other hand, a recent induced seismicity triggering mechanism has been proposed by De Barros *et al.* (2018), where he argues that aseismic deformation could trigger seismic ruptures through stress transfer beyond the pressurized region. A number of numerical and theoretical studies support this theory and predict that the aseismic deformation front can in some cases outpace fluid diffusion (Garagash and Germanovich, 2012; Galis *et al.*, 2017; Bhattacharya and Viesca, 2019; Dublanquet, 2019); however no direct observations have been made so far, as it is difficult to trace the diffusion front for real cases of induced seismicity.

Understanding the relationship between slip (reactivation) front and fluid front requires a better understanding of what controls hydraulic diffusivity in this context. We thus propose a numerical method, in the context of deterministic and probabilistic inversion approaches, that allows to estimate the temporal evolution of the hydraulic diffusivity of an experimental fault throughout an injection test, using the pressure history at two points on the fault. The deterministic approach is a gradient based approach, used to determine the optimal model in a least-squares sense, and the probabilistic one is used to evaluate the associated uncertainties. On one hand, this allows us to characterize the diffusivity enhancement through a single injection experiment and investigate how it varies with slip accumulation and effective stress reduction. On the other hand, the application of such numerical approach could be very advantageous as it potentially allows for reconstruction of the spatio-temporal pore pressure changes, during the injection test and enables us to track the diffusive front. With the use of appropriate acoustic sensors, this can give more insights into the relation between the diffusive front and the aseismic/seismic rupture front.

In this study, we investigate shear induced fluid flow and permeability enhancement during fracture shearing. We used a series of laboratory injection tests on saw cut Andesite rock sample, under triaxial conditions, in which water was injected under constant rate into the experimental fault. The sample was connected to two pressure sensors, at two opposite locations of the fault, and equipped by strain gauges along strike. We then developed and implemented a gradient-based approach (deterministic approach), with the use of the adjoint state technique (Plessix, 2006), and a Markov Chain Monte Carlo algorithm (probabilistic approach) (Robert and Casilla, 2004) in an inversion framework to the experimental data. The objective is to estimate the hydraulic diffusivity enhancement and interpret it with respect to the accumulated shear slip and the reduction in effective stress. In the following, we present the experimental setup and data, then introduce the numerical methods and their application to the data, to finally discuss our numerical findings.

The experimental tests were conducted in collaboration with Dr. François Passelègue from EPFL (Ecole Polytechnique Fédérale de Lausanne) at the Laboratoire de Géologie at Ecole Normale Supérieure in Paris. Such data is not commonly available. In particular, the presence of two boreholes connected to pressure sensors at two different locations along the fault allows for the application of such numerical inversion.

Note: In this chapter we use the following nomenclature: Subscripts indicate the nature of the data point, whether it is the injection (“inj”) or the observation (“obs”) well); Superscripts indicate whether the data is observed experimentally (“E”) or estimated numerically (“N”).

4.2 Experimental Data

4.2.1 Experimental Setup

Triaxial shear experiments were conducted on an Andesite cylindrical rock sample, having a young modulus $E = 64$ GPa and a porosity $\varphi = 2.0\%$ (Li *et al.*, 2019). The cylinder has a length of $H = 8.8$ cm and a radius of $R = 2.0$ cm (values in Table 4.1). Sketches of the front and top view of the experimental setup are represented in Figures 4.1a and 4.1c, while Figures 4.1b and 4.1d show images of the front and top view of the experimental sample placed inside the jacket. A single saw cut fracture represents the experimental fault. It forms a 30-degree angle with respect to the vertical axis of the rock sample, and has an elliptical shape of 8.0 cm length along strike and 4.0 cm wide (values in Table 4.1). Two vertical boreholes were drilled reaching the fault surface, starting from the bottom and top of the rock sample, respectively, at opposing edges of the elliptical fault plane (Figure 4.1a). The boreholes were drilled 5.0 mm away from the edge of the rock sample, and have a 4.0 mm diameter. The bottom borehole was connected to the pump A, where liquid water was injected, and served as the injection borehole; while the top one was connected to the pump B and was sealed during the injection experiment, and served as an observation borehole. The experimental sample was equipped by 8 strain gages that were uniformly distributed along one side of the cylinder, parallel to the fault strike. Additionally, it was equipped by 10 ultrasonic transducers, along the vertical axis of the rock cylinder, 5 from each side; however, the ultrasonic measurements were not exploited during the work presented here.

Parameter	Symbol	Value	Unit
Cylinder Length	H	8.8	cm
Cylinder Radius	R	2	cm
Fault Length	L	8	cm
Fault Width	W	4	cm
Fault Angle w.r.t σ	α	30	($^\circ$)
Young Modulus	E	64	GPa
Porosity	φ	2	%

Table 4.1 – Laboratory Injection Experiment: List of geometrical and mechanical parameters.

The rock sample was subjected to an axial loading σ and radial one P_c (or confining pressure). The normal σ_n and shear stress τ_n (average values on the fault plane) can be estimated by projecting the triaxial stress state onto the fault plane, as follows

$$\sigma_n = \left(\frac{\sigma + P_c}{2} \right) + \left(\frac{\sigma - P_c}{2} \right) \cos \left(2 \left(\frac{\pi}{2} - \alpha \right) \right), \quad (4.1)$$

$$\tau_n = \left(\frac{\sigma - P_c}{2} \right) \sin \left(2 \left(\frac{\pi}{2} - \alpha \right) \right). \quad (4.2)$$

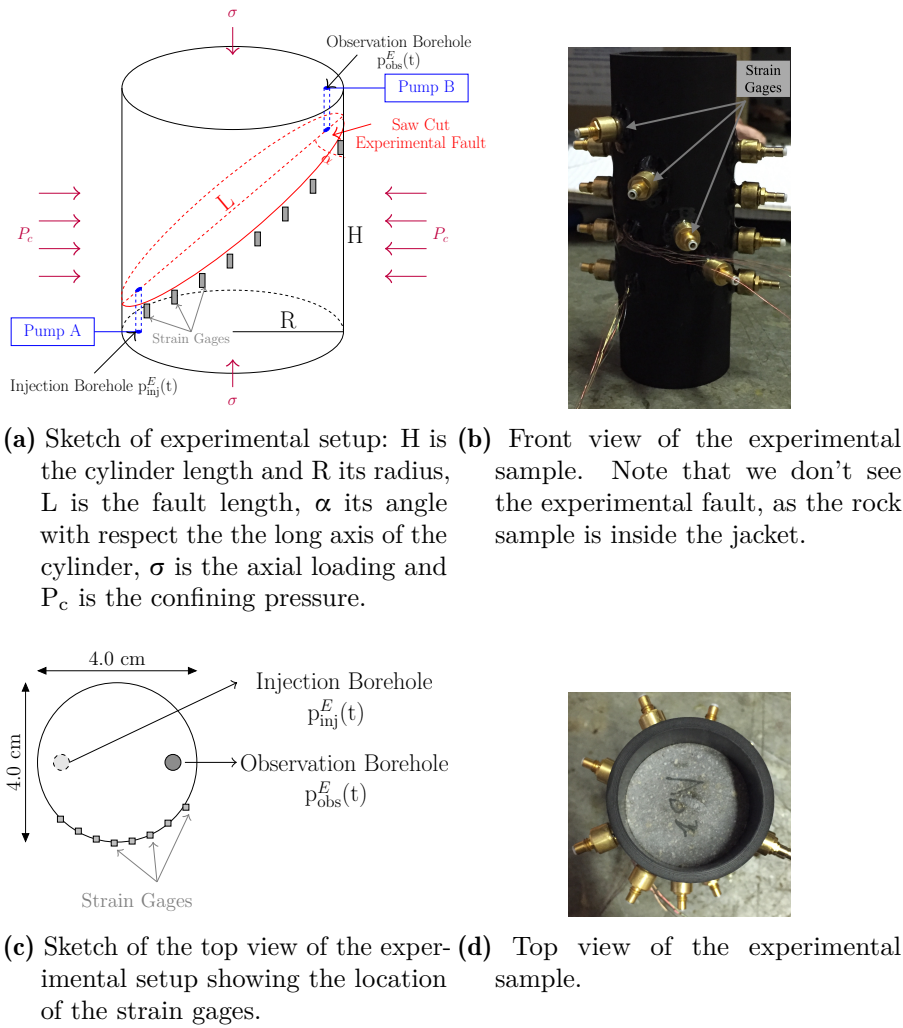


Figure 4.1 – Experimental Setup.

The two boreholes allow us to get a continuous measure of the pressure at two locations along the fault plane (p_{inj}^E and p_{obs}^E) throughout the injection experiment. Average fault slip can also be computed by projecting the axial displacement onto the fault plane. Finally, strain deformations were recorded using the strain gauges. Mechanical measurements (stress, displacement and deformation) were recorded at a frequency of 2,400 Hz, in order to have a good resolution for slip event detection as the rupture and slip velocities can reach 500 m/s and 0.1 m/s, respectively (see section 4.2.3). The fluid flow parameters (pressure, volume and injection rate) were recorded at only 1 Hz, as it is sufficient to track the diffusion process: the diffusion characteristic time is proportional to $t \propto L^2/D$, for hydraulic diffusivity in the range $[10^{-6} - 10^{-5}] \text{ m}^2/\text{s}$, this gives t in the range $[640 - 6400]$ seconds.

4.2.2 Experimental Protocol

We carried out experiments at different confining pressures ($P_c = 30, 60$ and 95 MPa). At the start of the injection experiments, the pore pressure was set to 10 MPa uniformly along the fault plane. At the start of the experiment, a loading phase was conducted: the shear stress was increased to $\sim 90\%$ of the peak shear stress ($\tau_0 = 0.9\tau_p$). For each injection experiment, the peak shear stress was determined by conducting a prior axial loading test. At the end of the loading phase, liquid water was injected throughout the injection borehole, under a constant injection pressure rate of ~ 5 MPa/min, until reaching a pre-set value of maximum pressure (lower than the confining pressure). Injection continued until the pressure equilibrium is reached along the fault plane. As liquid water was injected at ambient temperature, we consider the injection isothermal and neglect any thermo-elastic behavior. Values of the different injection experiment parameters are listed in Table 4.2.

Parameter	Symbol	Exp. 1	Exp. 2	Exp. 3	Unit
Injection Rate		5	5	5	MPa/min
Initial Pore Pressure	p_{init}	10	10	10	MPa
Confining Pressure	P_c	30	60	95	MPa
Maximum Pressure	p_{max}	≈ 29	≈ 59	≈ 89	MPa
Experiment Duration		1063	1877	5548	seconds
Injection Start Time		143	147	670	seconds

Table 4.2 – Laboratory Injection Experiment: List of experimental parameters.

4.2.3 Experimental Results

Figure 4.2 displays the measurements of the pore pressure (at injection and observation boreholes) and the average cumulative displacement throughout the three injection experiments. We should note that the instantaneous decrease then increase in pressure at 1500 seconds for the test at 95 MPa of confining pressure (Figure 4.2c) is caused by a slight imperfection in the experimental protocol: the pump A was emptied and replaced.

Upon the start of injection, instantaneous increases in pressure at the observation borehole are observed, especially for the two injection tests at 30 and 60 MPa of confining pressure. The small subplot inside Figure 4.2b shows the initial pressure increase at the measurement borehole at the start of fluid injection. These increases can not be due to pure diffusion effects and may be due to some direct poro-elastic effects. As in this study we only model the fluid diffusion process, we will not interpret the instantaneous increases for the rest of the study.

From Figure 4.2, we observe that fluid injection and pressure diffusion reactivates the experimental fault. Various slip events are observed during the injection phase for the different tests. We selected in particular a few examples (events A-I) to illustrate

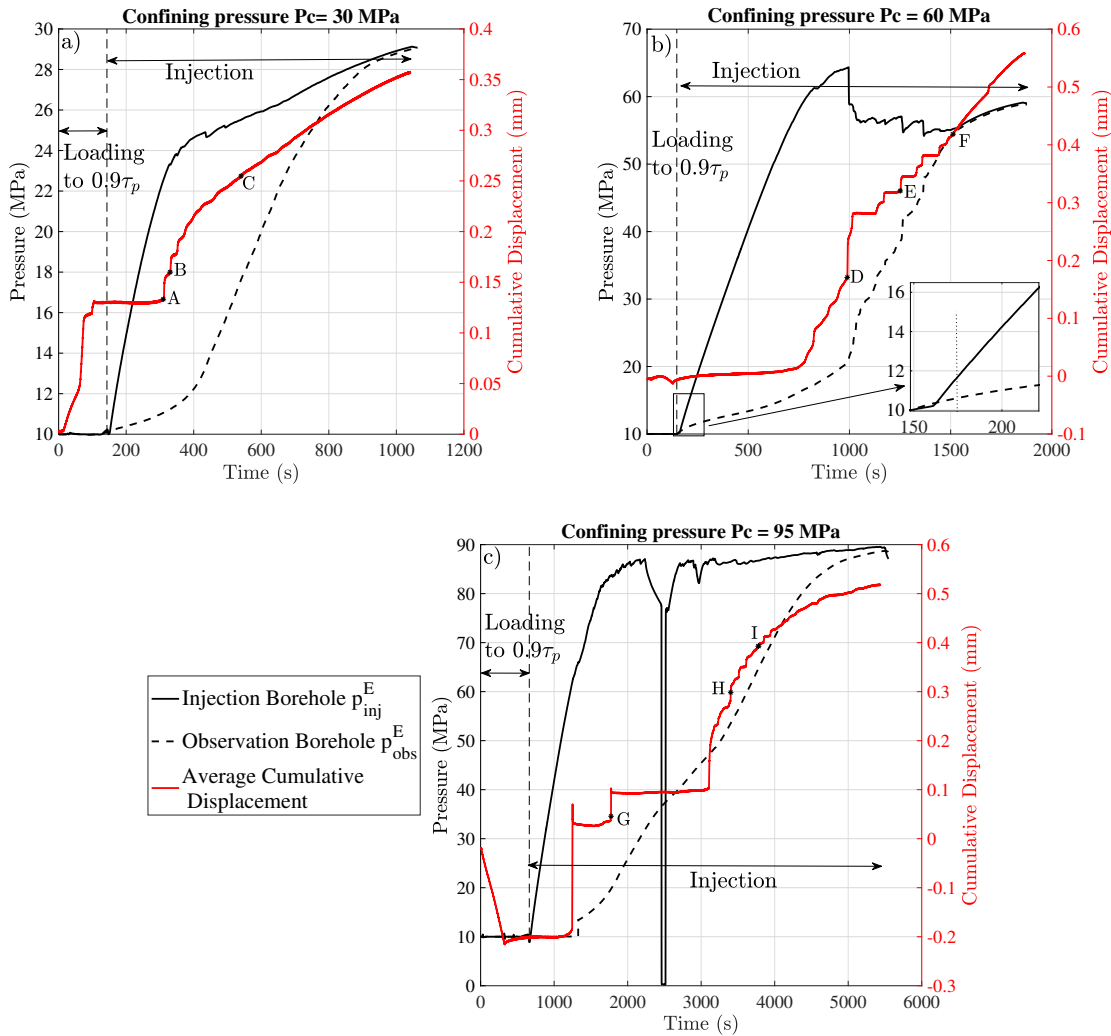


Figure 4.2 – Experimental gross results: Time series of pore pressure (left axis) and average displacement along strike (right axis) for the different injection experiments at the different values of confining pressure P_c : (a) 30 MPa, (b) 60 MPa, here the small subplot is a zoom around the initial time of the injection; and (c) 95 MPa. In all subplots, the vertical dashed line represents the limit between the loading phase and the injection phase. Points A – I represent examples of slip events that will be exposed in Figure 4.3.

the existence of different types of slip events: for instance events A, B, D, E and G are accompanied by a large instantaneous cumulative slip along the fault plane, while the rest does not share this feature. These slip events are characterized by relatively higher

average slip rates with respect to the other events. Note that the average slip rate is estimated as the time derivative of the average cumulative slip measured along the fault. In particular, the average slip rate reaches 0.1 mm/s for event A, 0.69 mm/s for event D and 7.48 mm/s for event G. Figure 4.3 represents the time series of the deformation recorded by the strain gages throughout the injection test, with a special focus around the chosen events. This illustrates the wide range of rupture velocity for different slip events during a single injection test, with ruptures velocities going as high as 29 m/s for event D (Figure 4.3b) and 500 m/s for event G (Figure 4.3c) and as low as 0.06 m/s for event A (Figure 4.3a) and 0.05 m/s for events F and I (Figures 4.3b and 4.3c). We should note though that the various slip events were detected and their rupture velocity estimated by `passelegue_preparation_2019`.

From Figure 4.2, the slip events are associated with instantaneous pressure drops in the injection borehole, and strong increases of pressure in the observation borehole. These changes are particularly significant during events A and B, D and E, and G and H at 30, 60 and 95 MPa of confining pressure, respectively. These instantaneous pressure changes could be interpreted by an enhanced pressure diffusion, that is an increase in the hydraulic diffusivity.

To summarize, the results show that the experimental fault can be reactivated due to fluid injection: (1) through fast/dynamic and slow slip events, (2) it can induce shear induced fluid flow, (3) and it may be accompanied by an enhancement of hydraulic diffusivity. The latter is the main focus of this study. In order to better understand the role of the different parameters at play, we aim to characterize the diffusivity history throughout the injection experiment, as it is suspected to vary with the effective stress reduction, as well as following the different slip events recorded on the fault. We perform numerical inversion on the experimental data in a deterministic and probabilistic frameworks. In the next two sections, we present the development of the numerical method and its application to the experimental data.

4.3 Methodology

4.3.1 Inverse Problem

By definition, the direct problem corresponds to the resolution of the forward problem (modeling equation) that estimates the observations (Data) from a set of model parameters (Model parameters). The inverse problem is the process of estimating the causal factors (Model) from a set of observational data (Data).

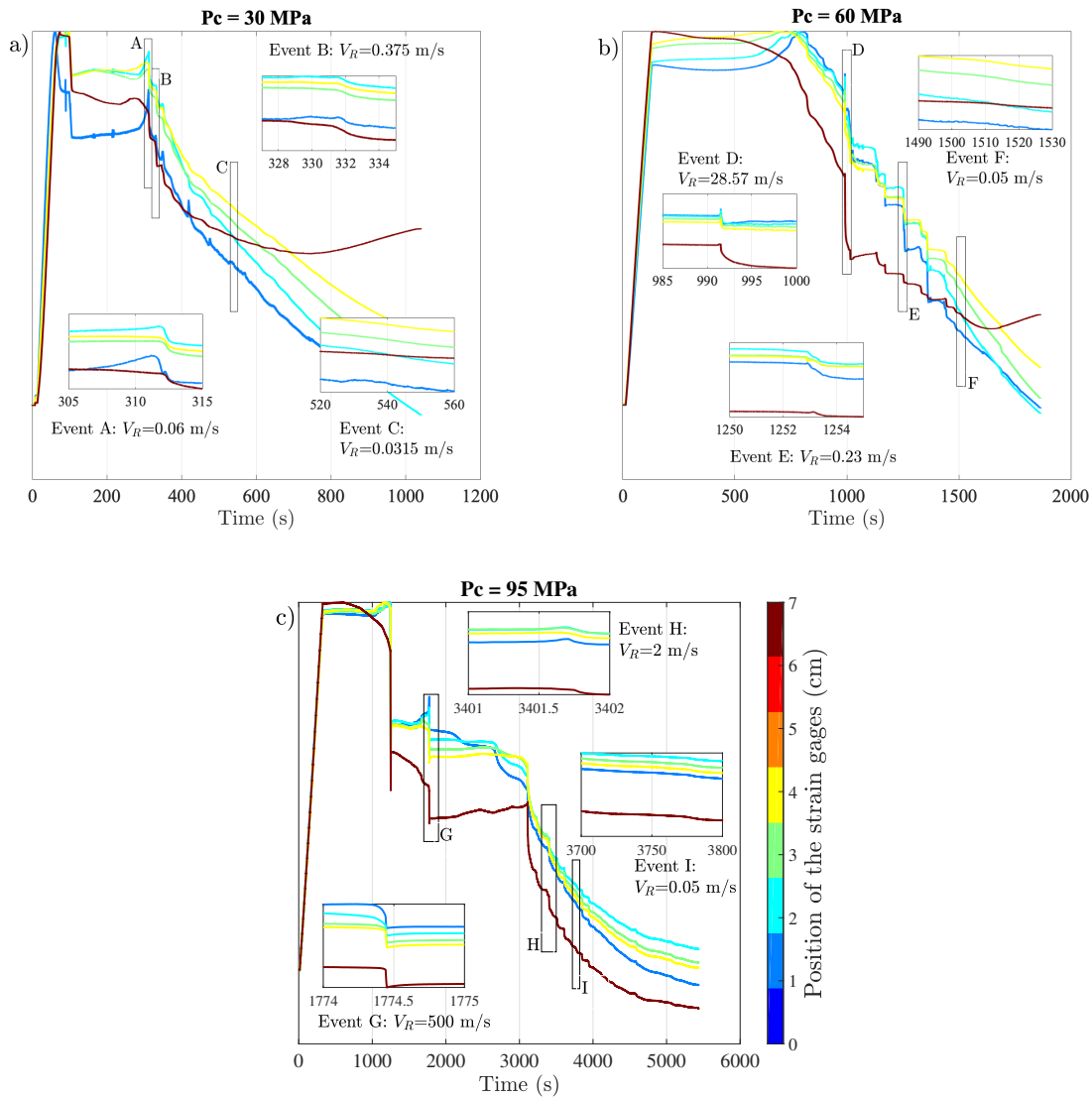
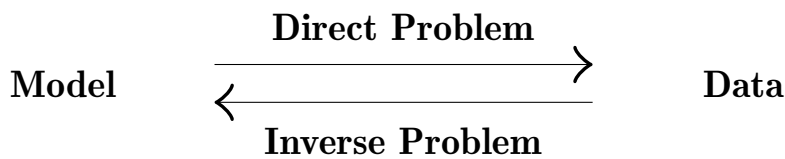


Figure 4.3 – Experimental gross results: Deformation recorded by the strain gages for the different injection experiments at different values of confining pressure P_c : (a) 30 MPa, (b) 60 MPa and (c) 95 MPa. In all subplots, the color scale represents the position of the strain gage with respect to the closest edge of the fault to the injection borehole (refer to Figure 4.1c). In each subplot: the small figures represent a zoom of the subplot for the corresponding slip event and V_R refers to the rupture velocity of the slip event.



In the context of this work, the direct problem consists of solving the diffusion equation along the fault plane:

$$\frac{\partial p}{\partial t} = \nabla \cdot D \nabla p, \quad (4.3)$$

where $p = p(x,y,t)$ is the pore pressure, t is the time and $D = D(x,y,t)$ is the hydraulic diffusivity (assuming that the total compressibility, the fluid viscosity and the porosity are constant), here the model parameter. Knowing the time series of the injected pressure $p_{inj}^E(t)$ and the diffusivity $D(x,y,t)$ (*represents the Model here*), we can estimate the pore pressure at the observation borehole $p_{obs}^N(t)$ (*represents the Data here*). We recall that the super-scripts E and N here stand for experimental and numerical, respectively. The inverse problem consists therefore of minimizing the differences between $p_{obs}^N(t)$ and $p_{obs}^E(t)$, in order to estimate the spatio-temporal evolution of the diffusivity $D(x,y,t)$ along the fault throughout the injection experiment. As we have only one measurement of observations, it would be highly under-determined to inverse for the spatio-temporal history of the diffusivity. Thus, we choose to inverse for an effective diffusivity $D(t)$ that only depends on time in order to reduce the number of parameters to be determined.

$$\left. \begin{array}{l} p_{inj}^E(t) \\ p_{obs}^E(t) \end{array} \right\} \rightarrow D(t)$$

The pressure is initially uniformly set at 10 MPa along the fault plane, and the pressure history $p_{inj}^E(t)$ is imposed at the injection borehole, As no fluid flow is allowed outside the experimental sample, Neuman boundary conditions for the pore pressure variable are assumed at the boundaries of the elliptical fault plane ($\partial p / \partial n = 0$, where n represents the normal direction at the fault boundaries). In this case, Equation 4.3, along with it's initial and boundary conditions, becomes:

$$\frac{\partial p}{\partial t} = D(t) \Delta p, \quad (4.4)$$

$$p(x,y,t=0) = 10 \text{ MPa}, \quad p(x=x_{inj}, y=y_{inj}, t) = p_{inj}^E(t),$$

$$\frac{\partial p}{\partial n} = 0 \text{ at the fault boundaries,}$$

where x_{inj} and y_{inj} are the coordinates of the injection borehole.

The first step of solving the inverse problem consists of solving the direct problem with an initial pre-defined model $D^0(t)$, and of estimating numerically the data at the receiver position, here $p_{obs}^N(t)$. Then the optimal $D(t)$ is estimated in a least-squares sense (between the experimental value of the pore pressure at the observation borehole and the numerical one) (Chavent, 1991; Jarny *et al.*, 1991). It means we assume an additive noise with a Gaussian distribution. The objective functions writes:

$$J[D(t)] = \frac{1}{2} \int \left(p_{obs}^N[D](t) - p_{obs}^E(t) \right)^2 dt. \quad (4.5)$$

4.3.2 Deterministic inversion

The optimal model $D^*(t)$ is the one for which $\partial J / \partial D(t) = 0$. Starting from $D^0(t)$, D is iteratively updated. It assumes for a proper convergence that J is convex. The updated model of the diffusivity would be:

$$D^{n+1}(t) = D^n(t) - \alpha \left. \frac{dJ}{dD(t)} \right|_{D^n}, \quad (4.6)$$

where α is the step length that we will define in the section 4.3.2.3. The gradient $\partial J / \partial D(t)$ is the essential element and represents the correction or the update of the model:

$$\frac{dJ}{dD(t_0)} = \int \left(\delta(t - t_0) \left[\frac{\partial p_{\text{Obs}}^N(t)}{\partial D(t_0)} \right] \cdot [p_{\text{Obs}}^N(t) - p_{\text{Obs}}^E(t)] \right) dt. \quad (4.7)$$

The resolution of Equations 4.4 and 4.6 represents one iteration. A few iterations are needed in order to minimize the objective function. However, one of the main challenges of this method is the estimation of the gradient as the relation between the pressure and the diffusivity is non-linear (Equation 4.4). The jacobian matrix $[\partial p_{\text{Obs}}^N(t) / \partial D(t_0)]$ (in Equation 4.7) is very large and would require a lot of time and memory to be computed (size of model space by data space, typically 30000 x 30000 here). Note that the Jacobian matrix is not strictly needed, as it is multiplied by the data residuals. In order to avoid estimating it, we resort to apply the **Adjoint State Method** which is described in the next section.

4.3.2.1 Adjoint State Method (Gradient method): Theory

The adjoint state method is commonly used to estimate the gradient of a complicated function, in which the variables are solutions of non-linear direct problems, typically a partial differential equation. An extensive review of the method with applications in geophysics is presented by Plessix (2006). The adjoint state method introduces a new variable λ in the estimation of the objective function, which writes in this case:

$$J[D, \lambda, p] = \frac{1}{2} \iiint \left(\delta(x - x_{\text{obs}}) \delta(y - y_{\text{obs}}) (p_{\text{Obs}}^N - p_{\text{Obs}}^E)^2 \right) dx dy dt - \iiint \lambda(x, y, t) \cdot \left[\frac{\partial p}{\partial t} - D \Delta p \right] dx dy dt, \quad (4.8)$$

where x_{obs} and y_{obs} are the coordinates of the observation borehole, and the objective function depends on the diffusivity D , the pore pressure p , and the adjoint state variable λ , which can be seen as a Lagrangian multiplier in a constrained optimization problem. For the sake of simplicity, we did not include the initial and boundary conditions in the previous equation. In the adjoint state method (see Appendix A, section 4.7 for details), the gradient of the objective function is given by:

$$\frac{dJ}{dD} = \iint \lambda \Delta p dx dy, \quad (4.9)$$

where $p = p(x,y,t)$ and $\lambda = \lambda(x,y,t)$ are the solutions of the following partial differential equations:

$$\frac{\partial p}{\partial t} - D(t)\Delta p = 0, \quad (4.10)$$

$p(x,y,t=0) = 10$ MPa, $p(x=x_{inj},y=y_{inj},t) = p_{inj}^E(t)$, and $\frac{\partial p}{\partial n} = 0$ (at the fault boundaries),

$$\frac{\partial \lambda}{\partial t} + D(t) \Delta \lambda = \delta(x - x_{obs})\delta(y - y_{obs}) \left(p_{obs}^N - p_{obs}^E \right), \quad (4.11)$$

$$\lambda(x,y,t=T_{max}) = 0, \text{ and } \frac{\partial \lambda}{\partial n} = 0 \text{ (at the fault boundaries).}$$

For the adjoint state variable λ , we also impose zero flow outside the fault plane ($\partial\lambda/\partial n = 0$) (see Appendix A, section 4.7 for details). In order to simplify the expression of the gradient, we chose zero values at $t=T_{max}$: $\lambda(x,y,T_{max})=0$ (see Appendix A, section 4.7 for details), where T_{max} is the time at the end of the experiment. For this reason, we diffuse the residuals ($p_{obs}^N - p_{obs}^E$) and solve Equation 4.11 from $t=T_{max}$ to $t=0$.

Equation 4.10 represents the diffusion equation, that is by construction the direct problem in this application; while Equation 4.11 represents the additional differential equation that describe the adjoint state variable. These two equations are quite similar, with only a few differences: a source term is present in Equation 4.11 at the receiver position; $-D(t)$ is transformed to $+D(t)$, however Equation 4.11 remains stable as it is solved from T_{max} to 0. Equation 4.6 is then used to estimate the updated model of diffusivity. The process is iterated until the reduction of the objective function become smaller than 10^{-3} .

4.3.2.2 Resolution of the Differential Equations

The two differential Equations (4.10 and 4.11) are solved using an explicit time scheme of the finite volume method. We consider a very simple discretization grid to the fault plane with equal x and y spatial discretization: $\Delta x = \Delta y$. We choose $\Delta x < d_{inj}/2$, where d_{inj} is the distance between the center of the injection borehole and the closest edge of the fault plane along strike. Here $d_{inj} \approx 7$ mm and we chose $\Delta x = \Delta y = 2.5$ mm.

To assure the stability of the numerical resolution, the time step should satisfy the following condition:

$$\Delta t \leq \frac{\Delta x^2}{2 \max(D)}. \quad (4.12)$$

The maximum of the diffusivity could be different through the iteration process, which can result in a variable time step. For the sake of simplicity, we consider for all inversion iterations the same time step, estimated using the largest accepted diffusivity D_{max} :

$$\Delta t \leq \Delta x^2 / 2D_{\max}.$$

4.3.2.3 Numerical Implementation

Figure 4.4 represents the flow chart of the numerical implementation of the deterministic approach in the context of our study. As input for the algorithm, we need the observation measurements, and need to define an initial diffusivity model D^0 , the number of inversion iterations to be conducted and the accepted minimum and maximum boundaries for the model to be inverted D_{\min} and D_{\max} .

Each iteration consists of:

- solving the direct problem (pressure diffusion, Equation 4.10),
- estimating the residuals : $P_{\text{obs}}^N - P_{\text{obs}}^E$,
- diffusion of the residuals from final to initial time (Equation 4.11),
- estimation of the gradient with a simple cross-correlation (Equation 4.9),
- optimizing the gradient step length and updating the diffusivity model (Equation 4.6). In order to optimize the gradient step length, we apply a basic gradient descent algorithm with a semi-fixed α : We assume $\alpha = \alpha_1 \alpha_2$, where we fix the value of α_1 (here = 1) and we estimate the value of α_2 from the first inversion iteration: $\alpha_2 = \delta D / \max(\partial J / \partial D)$, where δD is the accepted increment on the value of the diffusivity update at each iteration. At each iteration we verify that the objective function (estimated using Equation 4.5) is decreasing, if this is not the case, α_1 is divided by two: $\alpha_1 = \alpha_1 / 2$,
- finally bounding the diffusivity model with pre-fixed model boundaries D_{\min} and D_{\max} .

The algorithm stops either when the total number of inversion iterations is reached ($n = N_I$, n being the number of inversion iterations finished and N_I the total one), or when the reduction of the objective function $(J(n) - J(n+1)) / J(n)$ becomes smaller than 10^{-3} .

The adjoint state method is a deterministic approach and its computational cost per iteration is only equivalent to two resolutions of the direct problem. However, it does not allow for sensitivity analysis of the results. This is why, we also apply a Markov-Chain Monte-Carlo algorithm: Metropolis Hastings Method, which will be presented in the next section. On the contrary to the adjoint state method, the Metropolis Hastings algorithm is a stochastic approach and thus requires a large number of model samples. However, it only requires the resolution of the forward modeling and the evaluation of the objective function, without the need of estimating the gradient.

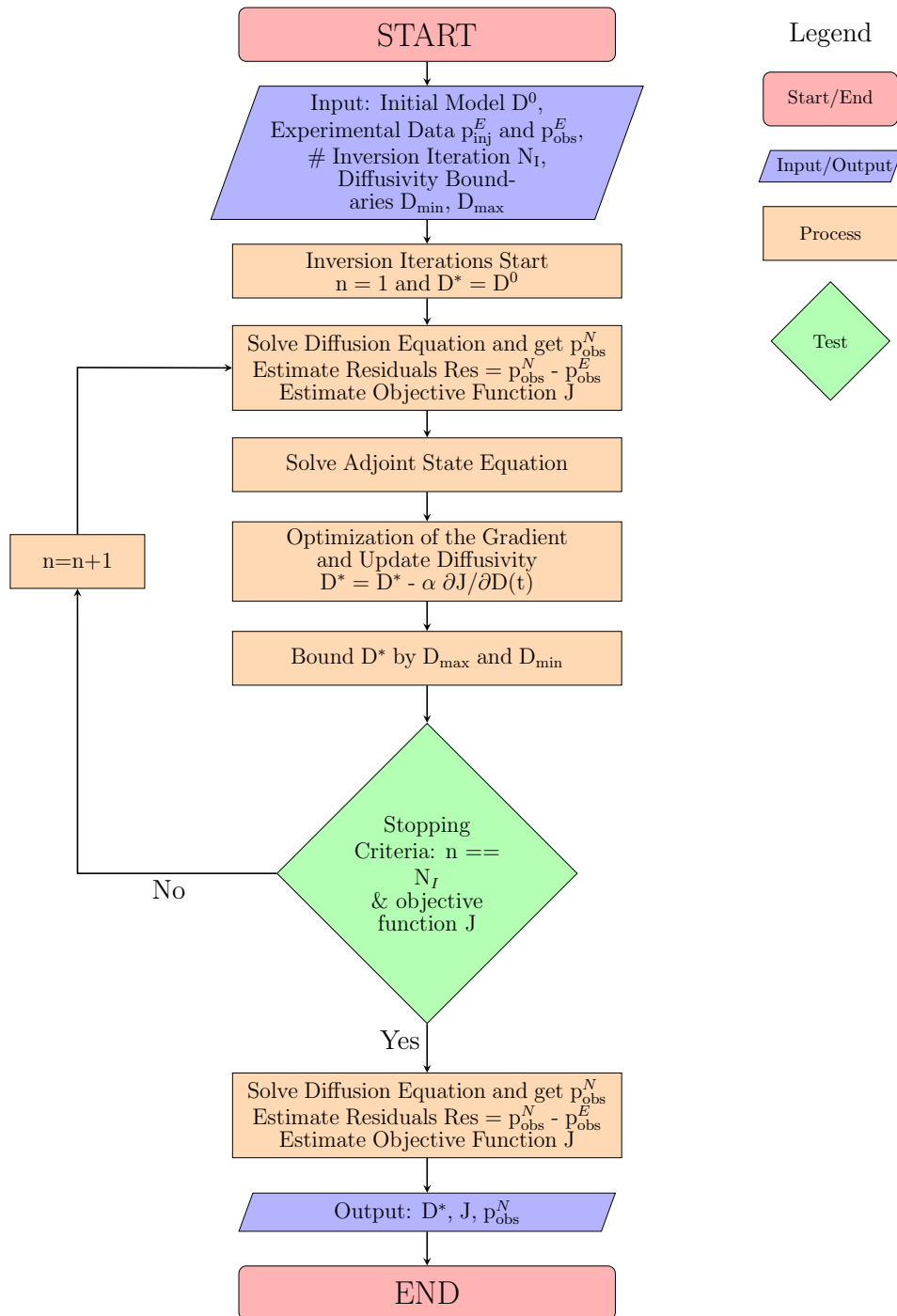


Figure 4.4 – Flow Chart: Application of the deterministic approach to the diffusion equation.

4.3.3 Metropolis Hastings Algorithm

4.3.3.1 Theory and Resolution

The Metropolis Hastings algorithm is one application of the Markov Chain Monte Carlo (MCMC) methods (Metropolis *et al.*, 1953; Hastings, 1970). We apply this method to inverse for the hydraulic diffusivity. The concept of the method relies on conducting a large number of forward computations, with a new model for each computation, in which:

- Each new sample diffusivity model D^{n+1} depends only on the current diffusivity model D^n (Markov Chain),
- Each new sample diffusivity model D^{n+1} corresponds to a random perturbation added to the current diffusivity model D^n (Monte Carlo),

where the superscripts refers to the iteration number of the forward computations. We estimate the acceptance probability for each new diffusivity model D^{n+1} in order to decide whether we accept it or not. The acceptance probability P writes:

$$P = \min \left(\frac{p^{n+1}}{p^n}, 1 \right), \quad (4.13)$$

where p is the probability density function. For the problem studied here:

$$p = \exp \left(-\frac{1}{2} \sum \left(\frac{p_{\text{obs}}^N(t) - p_{\text{obs}}^E(t)}{\sigma^{\text{obs}}} \right)^2 \right), \quad (4.14)$$

where σ^{obs} is the uncertainty on the observational measurements in the laboratory. For this study, the uncertainty of the pressure sensors was $\sigma^{\text{obs}} = 10^{-3}$ MPa. Compared to a Monte Carlo approach, an MCMC is designed to properly sample the a posteriori distribution function, and does not explore all the universe.

As mentioned earlier, this approach requires a large number of forward computations, that is the pressure diffusion process. We solve the pressure differential equation in the same way described for the previous method in section 4.3.2.2: same spatial discretization, time step, initial and boundary conditions. The computation of the diffusion equation requires a rather small time step to assure numerical stability (Equation 4.12) and thus the diffusivity vector is parametrized on a very fine temporal grid. However, it is very complicated to apply the MCMC algorithm to such large number of parameters. For this reason, we apply it on a sparse diffusivity vector (formed by 6 model parameters here), that we later interpolate into the fine grid using a linear interpolation.

From the series of simulations, we can apply statistical analysis for all the accepted models, and display the distribution of each model parameter or the associated momentum and quantiles.

4.3.3.2 Numerical Implementation

Figure 4.5 represents the flow chart of the numerical implementation of the Metropolis Hastings algorithm in the context of our study. Similarly to the adjoint state method, as input parameters, we need the observation measurements, the uncertainty of the observations σ^{obs} , and we need to define an initial diffusivity model D^0 , the number of forward computations to be conducted N_S , the boundaries for the model D_{min} and D_{max} . Each forward computation consists of:

- generating the new model from the current using a random normal distribution, for which we fix the standard deviation $\sigma = 10 \sim 30\% D^0$. This value is chosen to achieve an acceptance rate of 30%,
- interpolating the model from the sparse grid D^n into the fine grid D_i^n (the subscript i refers to the interpolated vector)
- solving the direct problem (pressure diffusion, Equation 4.10),
- estimating the residuals : $p_{\text{obs}}^N - p_{\text{obs}}^E$,
- estimating the objective function (Equation 4.5) and the probability density (Equation 4.14),
- verification that the model satisfies the pre-fixed boundaries (if yes: Total models $n_{\text{Tot}} = n_{\text{Tot}} + 1$)
- estimation of the acceptance probability (Equation 4.13)
- draw a random number β between $[0 - 1]$, and check whether or not the model is accepted (if yes: Selected models $n_{\text{Sel}} = n_{\text{Sel}} + 1$).

The algorithm stops either when the total number of samples to be tested is reached ($n = N_S$) or when mean and standard deviation of the accepted models do not evolve anymore. At the end, the acceptance rate of the algorithm is the ratio between the selected and the total models: $n_{\text{Sel}}/n_{\text{Tot}}$, and should be equal to 30 %.

We expect an initial burn-in phase, in which the objective function decreases rapidly, until the model converges. All the statistics presented in the next section are estimated after this burn-in phase.

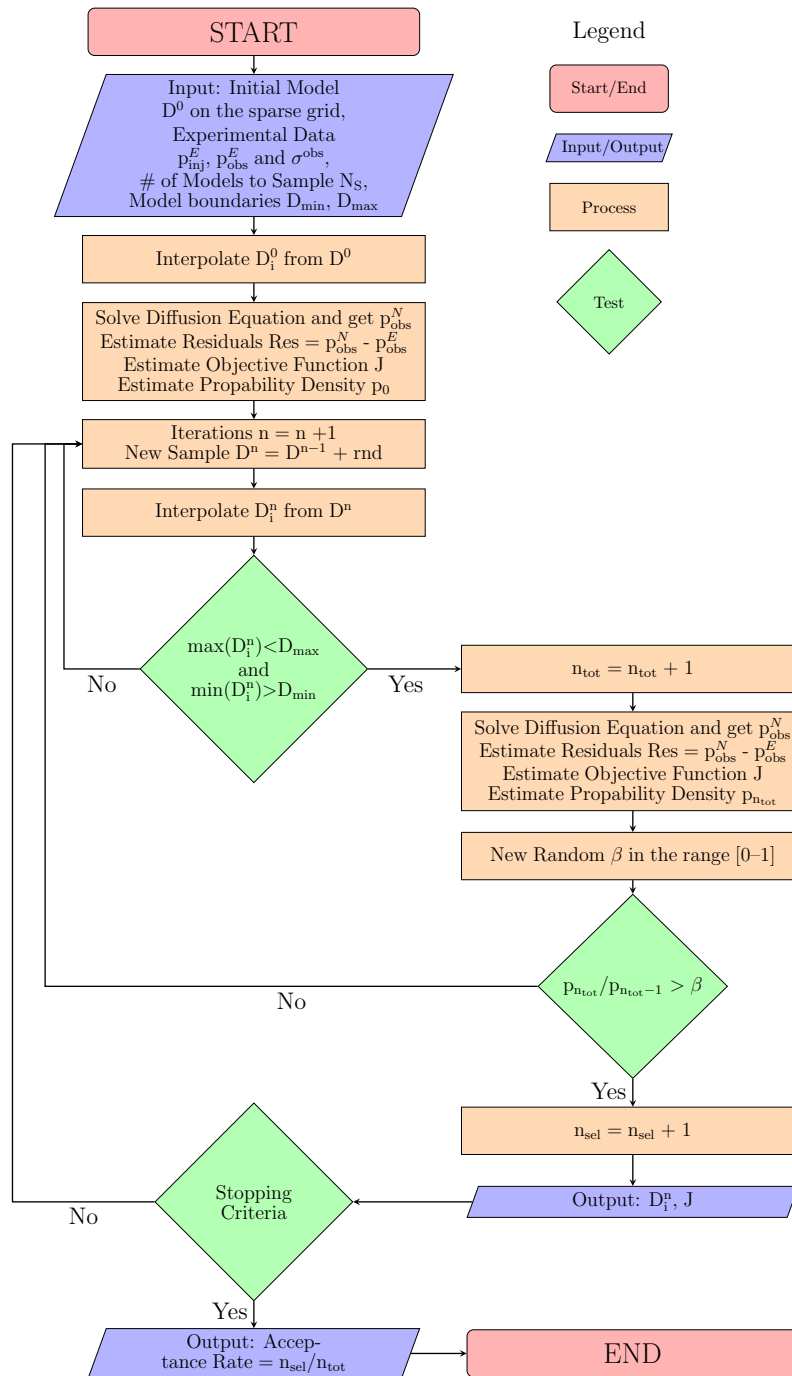


Figure 4.5 – Flow Chart: Application of the Metropolis Hastings Method to the diffusion equation.

4.4 Application to the Experimental Data

We present here the results of the numerical inversion methods on the three experimental injection tests (refer to Table 4.2). We will start by exposing the application of the deterministic approach (adjoint state method) in order to estimate, in the least-squares sense, the best diffusivity model that can explain the experimental data, and then present the probabilistic approach (MCMC) so to estimate the uncertainty and the validity of the best model. The experiment at 60 MPa of confining pressure is the most complicated case as it presents abrupt step-like increases in pressure. For this reason, we will expose and discuss at first the cases at 30 and 95 MPa. We did not apply any specific regularisation for the deterministic approach, for all the results presented here.

We should note, that in this section we will not discuss the physical interpretation of the evolution of the hydraulic diffusivity and leave it to section 4.5.

4.4.1 Estimating the Best Model: Deterministic Approach

- $P_c = 30$ MPa

Figure 4.6 illustrates the application of the deterministic approach to the first injection test at 30 MPa of confining pressure. In this application the number of non-linear iterations was set to 1400 iterations, and we verified at the end of the iterations that the reduction of the objective function was smaller than 10^{-3} (Figure 4.6b). The initial diffusivity model was considered constant $D^0(t) = 4.6 \cdot 10^{-6} \text{ m}^2/\text{s}$ (Figure 4.6c). Several initial models were tested, with no important effects on the inversion results. The modelled pressure at the observation borehole p_{obs}^N (red plot in Figure 4.6a) replicates relatively well the experimental measurement for the majority of the time domain, however some discrepancies are observed. Figure 4.7 is a zoom version of Figure 4.6a over the different rectangle areas. In area number (1) (Figure 4.7b), the measurement and the modeled pressure are quite similar. For area number (2) (Figure 4.7b): $180 < t < 280$ seconds, at this time range, poro-elastic effects are suspected. The model under-estimates the pressure, and we are not able to explain perfectly the experimental data using only pure diffusion. From Figure 4.6c, we observe in this time range a bump in the diffusivity best model, which can not be physically interpreted, as it may be an artificial way for the model to try and replicate the experimental data. The area number (3) (Figure 4.7c) represents the largest times in the experiment $t > 850$ seconds, here also the model under-estimates the measured pressure. It is difficult with our current model to fit the observations as the limited time remaining from the experiment may be not enough to properly model the diffusion process. One way to solve this issue, is to experimentally record the pressure at the observation borehole for a large time after the pressure equilibrium is reached. On the other hand, the use of more advanced gradient optimization approaches (quasi-Newton, pre-conditioning) may help resolve this issue. This will be further explained and discussed in the discussion section. From Figure 4.6c, we observe a plateau in the best model in this time range. We can not perfectly rely on the solution in this domain as the model was not

able to fit perfectly the data here, however the plateau value can give us an estimation about the value of the hydraulic diffusivity in this time range. Figure 4.6b represents the objective function on a semi-logarithmic scale and shows how it decreases with the number of iterations, from ≈ 20 to 4.10^{-2} . For all the reasons mentioned before, we will only focus on the remaining time range $[\approx 300 - 800]$ seconds when physically interpreting the evolution of the hydraulic diffusivity throughout the injection experiment, and we can observe from Figure 4.6c that the hydraulic diffusivity increases throughout the injection experiment, as the pressure diffuses along the fault plane. Finally, Figure 4.6d illustrates the reconstructed pressure profile along a longitudinal section of the fault that intersects the two boreholes: a profile is represented each ~ 42 seconds. In the reconstructed model, the pressure at the injection borehole is by definition imposed, and no fluid flows outside the fault boundaries (gray areas).

- **$P_c = 95$ MPa**

The application of the deterministic approach to the injection test at 95 MPa of confining pressure is presented in Figure 4.8. Similarly to the previous case, a constant initial diffusivity model was used (here $D^0(t) = 6.6.10^{-7}$ m²/s, Figure 4.8c), and several initial values were tested. For this case 1500 iterations were performed, in which the objective function decreased from 400 to 2.10^{-1} (Figure 4.8b). The modeled pressure at the observation borehole p_{obs}^N (red plot in Figure 4.8a) can explain quite well the experimental measurement for the majority of the time domain. We observe at $t \approx 1050$ seconds an abrupt increase in the pressure at the observation borehole p_{obs}^E , following a large slip event (refer to Figure 4.2c). It is quite hard to model such an abrupt change in pressure by considering only pure diffusion process. For this reason, the algorithm try to fit the data the best way possible and produce a smoothed version of the pressure history in this time range. This creates an artificial increase in the hydraulic diffusivity in this time range as seen in Figure 4.8c. Moreover, as mentioned before, in this injection test, the pump A was emptied at $t \approx 2500$ seconds, causing the pressure at the injection borehole to suddenly drop to 0, then re-increase again when the pump was replaced (Figure 4.8a). For this reason, we observe small artificial abrupt changes in the diffusivity observed around 2500 seconds (Figure 4.8c), this can also be observed along the pressure profiles plotted each 175 seconds in Figure 4.8d. Here we chose to take into consideration the emptying of the pump so not to affect the diffusivity history. However, we could apply a mask over this time range to remove this part of the data, or apply regularization to the modeling parameters. Finally, at the largest times $t > 4500$ seconds, the numerical model under-estimates the experimental data. This issue is similar to the one discussed in the previous injection test at largest times (refer to Figure 4.7c). We observe a plateau in the diffusivity history in this time range (Figure 4.8c), and we will only consider the solution in this domain so to get an estimation on the maximum diffusivity value reached during the injection test. For the rest of the study, the diffusivity model in the range $[2000 - 4200]$ seconds will be considered.

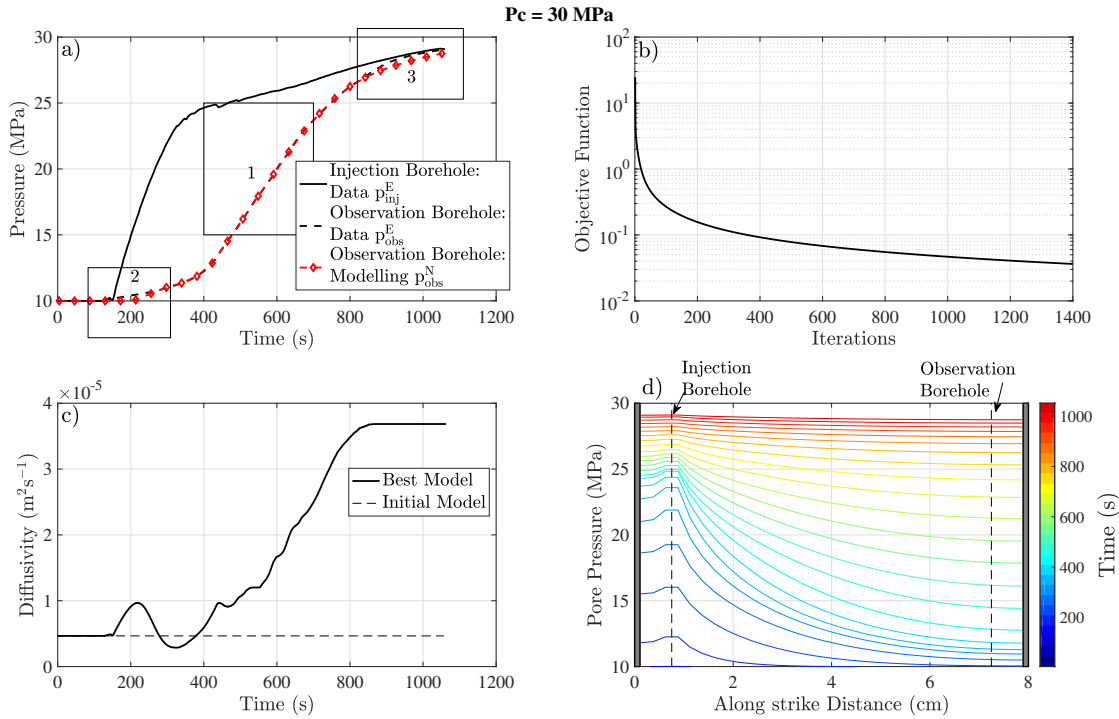


Figure 4.6 – Results of the deterministic approach for the experiment at $P_c = 30$ MPa: (a) Numerical and experimental pressures at the injection and observation boreholes: black color refers to the the experimental data, red color to the numerical results, solid line represents the injection borehole and dashed ones represent the observation borehole. Areas 1,2 and 3 are zoomed and represented in Figure 4.7; (b) Objective function on a semi-logarithmic scale. Stopping criteria: 1400 iterations and the verification that the reduction of the objective function $(J(n) - J(n+1))/J(n)$ becomes smaller than 10^{-3} ; (c) Time series of the diffusivity model: the black line represents the best model, and the black dashed line represents the initial model (Inversion result); (d) Pore pressure profiles along strike of the fault in the reconstructed model: the color scale refers to the time, a profile is plotted each ~ 42 seconds. The vertical dashed lines represent the locations of the injection and observation borehole, and the gray areas are the boundaries of the fault plane where no fluid flow is imposed.

- $P_c = 60$ MPa

Figure 4.9 illustrates the application of the deterministic approach to the injection test at 60 MPa of confining pressure. The initial diffusivity model was considered constant $D^0(t) = 1.6 \cdot 10^{-6} m^2/s$ (Figure 4.9c) and similarly to the previous two cases, several initial models were tested. As mentioned before, the experiment at 60 MPa exhibits different step-like increases in pressure (refer to Figure 4.2b). We were not able to reproduce such a behavior via modeling only a pure pressure diffusion processes. For this inversion, we show results after 200, 1000, 3000 and 5000 iterations. From Figure 4.9a, we can see that

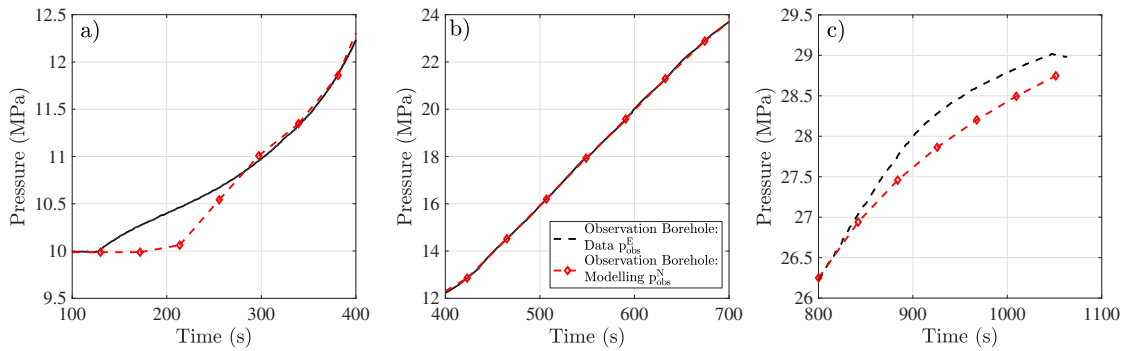


Figure 4.7 – Zoom of Figure 4.6a for only the pressures at the observation borehole, in the following time ranges: (a) $100 < t < 400$ seconds; (b) $400 < t < 700$ seconds; (c) $800 < t < 1100$ seconds.

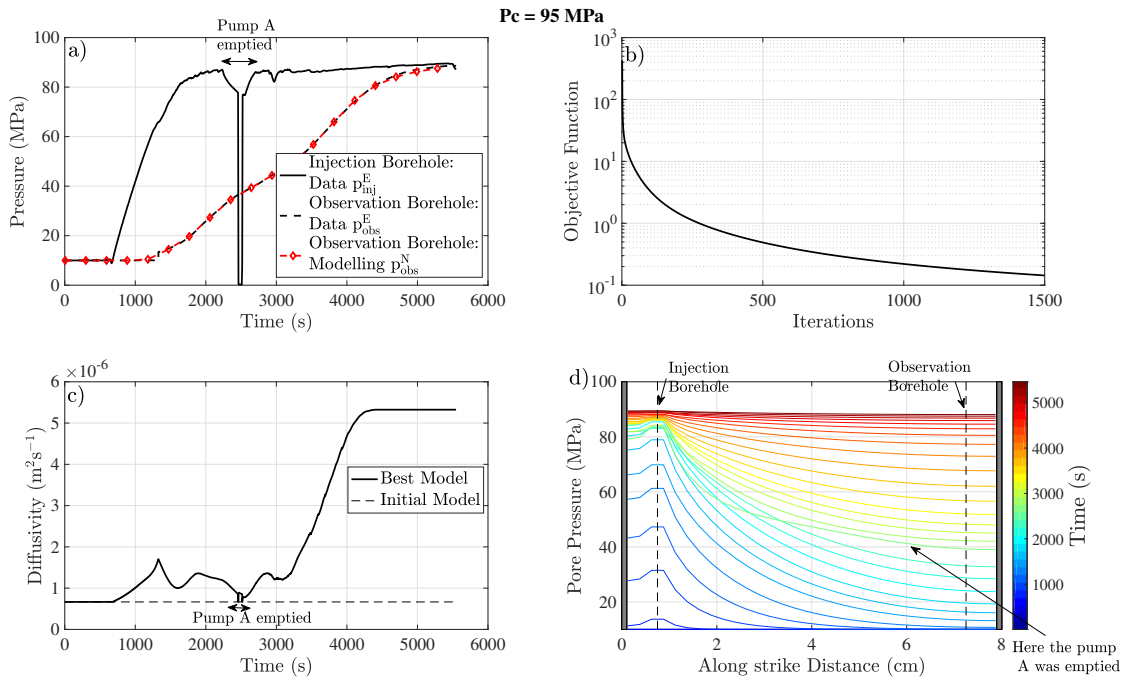


Figure 4.8 – Same as for Figure 4.6, except in (b) Stopping criteria: 1500 iterations and the verification that the objective function becomes smaller than 10^{-3} ; (d) a profile is plotted each ~ 175 seconds.

the numerical model can estimate a very close pressure vector to the one measured at the observation borehole for the majority of the experiment time, and yet it fails to replicate the pressure steps, for instance at $t \approx 1250$ and 1370 seconds (see Figure 4.10b), no matter the number of inversion iterations conducted. On the other hand, from Figure 4.9c, we can notice that the diffusivity model after 200 iterations is rather smooth, whereas various

peaks in the diffusivity model appear at the different locations of the pressure steps. The amplitudes of the peaks can be more important as the number of inversion iterations increases. We are not sure whether these peaks have a physical meaning and to what extent we can be confident as to their amplitude. We recall that no regularization of the diffusivity model has been applied. For these reasons, we choose to stop the inversion at 1000 iterations, even though the objective function is not at its minimum (Figure 4.9b), so as to keep a relative smooth solution. From Figures 4.10a and 4.10c, we can observe the same issues previously discussed for the two first injection tests, where the model under-estimates the experimental data: (1) at small times between 200 and 500 seconds, where pore-elastic effects are suspected, and we observe correspondingly in Figure 4.9c an artificial bump in the diffusivity model in this time range; (2) at the largest times $t > 1450$ seconds, where due to the limited remaining time of the experiment we can not properly model the diffusion process, giving a plateau in the hydraulic diffusivity model (Figure 4.9c). Finally, Figure 4.9d shows the reconstructed pressure profile, after 1000 inversion iterations, for the same longitudinal section as in Figures 4.6d and 4.8d, with a profile plotted each 49 seconds.

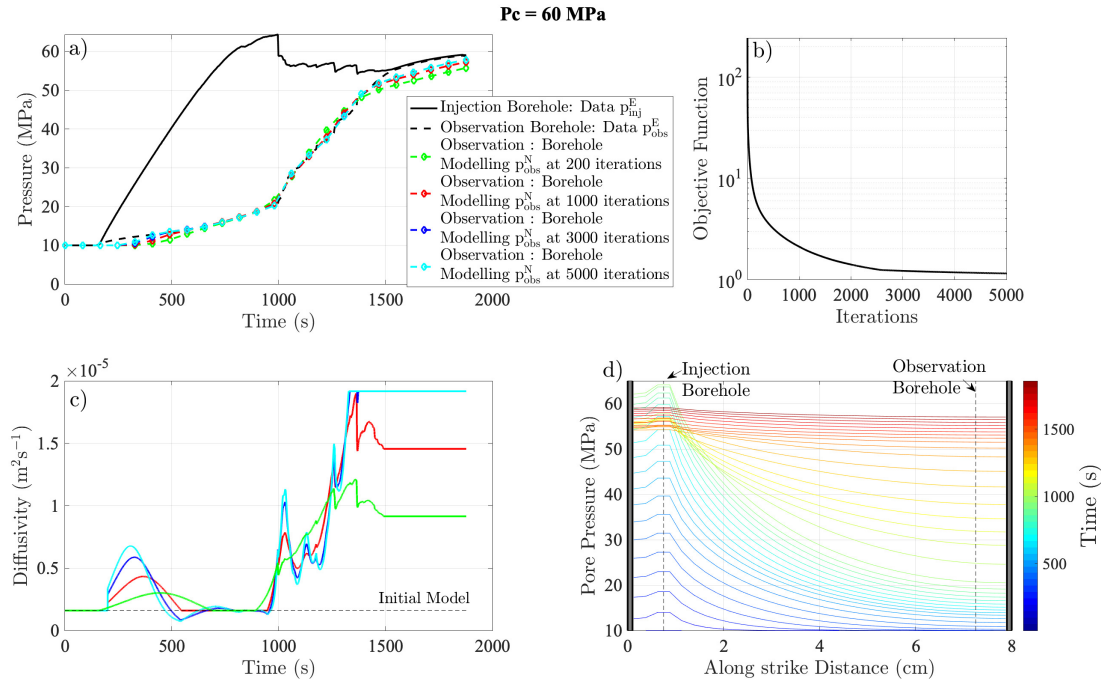


Figure 4.9 – Same as for Figure 4.6, except in (a & c) the colored plots refer to the numerical results: with green, red, dark blue and light blue for 200, 1000, 3000 and 5000 inversion iterations, respectively; (b) Here the stopping criteria is the number of inversion iterations and the verification that the objective function becomes smaller than 10^{-3} ; (d) a profile is plotted each ~ 49 seconds.

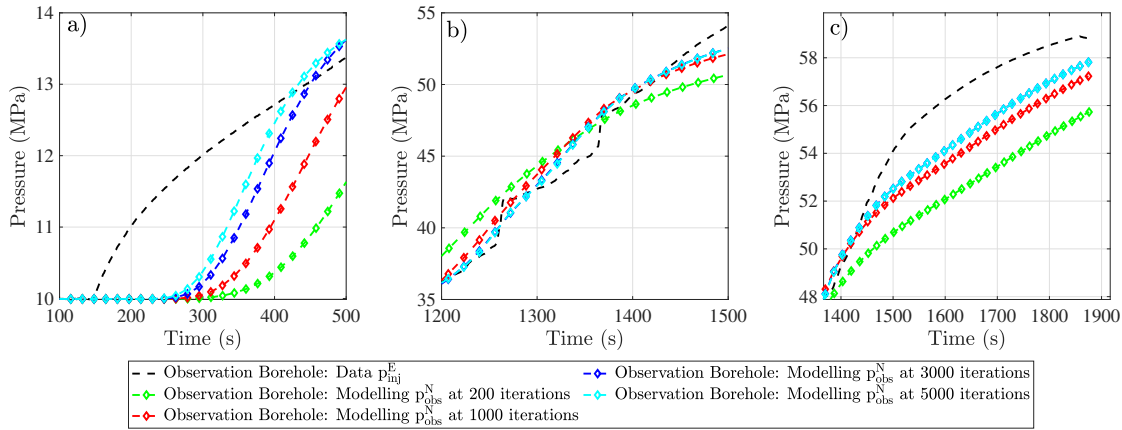


Figure 4.10 – Zoom of Figure 4.9a for only the pressures at the observation borehole, in the following time ranges: (a) $100 < t < 500$ seconds; (b) $1200 < t < 1500$ seconds; (c) $1400 < t < 1900$ seconds.

4.4.2 Estimating the Uncertainties: the MCMC approach

The application of the MCMC method allows us to estimate to what extent the best model (issued from the deterministic approach) is valid and to explore the range of uncertainty for diffusivity history. For the different injection tests, we chose 6 model parameters to describe $D(t)$, evenly spaced in time, and we started the parametrization in the time range where the diffusivity solution, issued from the deterministic approach, is not constant. For instance, the first model parameter is at $t = 280$ seconds for the test at 30 MPa (see Figure 4.11a). We fix the initial model D_{init} to the constant diffusivity value found before injection started by the deterministic and we allow the algorithm to generate new models in the range $[0.01 - 15]D_{init}$. For the different injection tests, we applied the MCMC method for 40,000 iterations, after which we verified that the average and the standard deviations, over the accepted models, of the 6 model parameters have reached stabilization.

Figures 4.11, 4.12 and 4.13 illustrate the results of the MCMC method for the three injection tests at 30, 60 and 95 MPa, where subplot (a) is a statistical representation the accepted models: we show the average $\bar{D}(\text{MCMC})$ in gray, the standard deviations in dashed black lines and quantiles at 68% in green and 95% in pink; we also represent the probability density of the accepted models using the color scale, which represents the distribution of the accepted models over the time history. The probability density can indicate whether the variability of the solution is small (high probability density) or large (small probability density). As mentioned in section 4.3.3.2, the statistics are conducted for the accepted models when the objective function stabilizes after the burn-in phase, in which the objective function decreases drastically (subplot (b)). For the different injection tests, the burn-in phase was fixed at 100 accepted models. Subplots (c) and (d) show how the average and the standard deviation, estimated for the different inversion

points on the sparse grid, stabilise after a certain number of iterations. As mentioned before, this was an important condition in the stopping criteria for the algorithm.

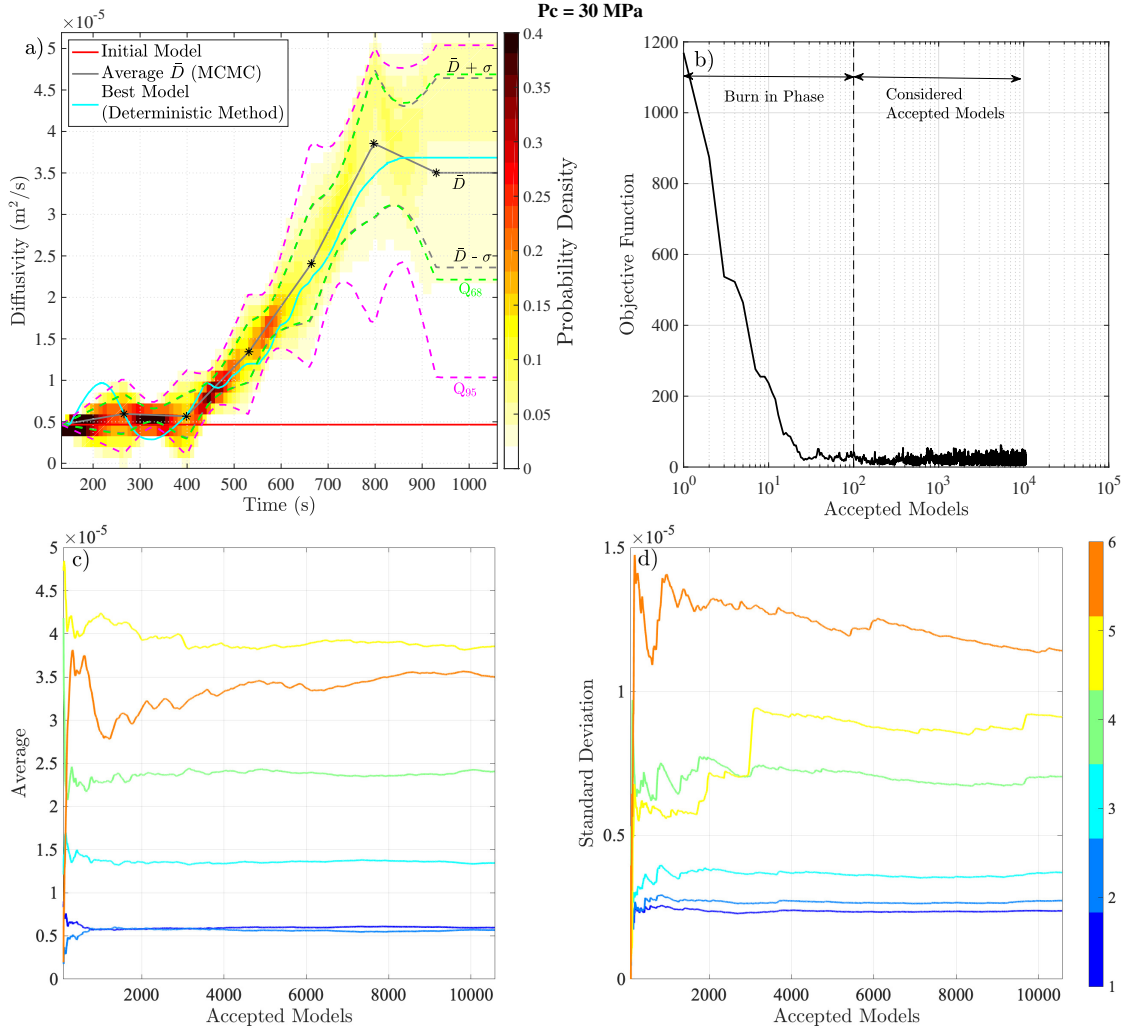


Figure 4.11 – Results of the MCMC Method for the experiment at $P_c = 30$ MPa: (a) Diffusivity Model: Initial model (in red), average of the considered accepted models (in gray) where the scattered stars represent the inverted points on the sparse grid, standard deviation of the accepted models (dashed gray lines), quantiles at 68 (dashed green lines) and 95% (dashed pink lines) and the best model obtained with the deterministic method (in light blue). The color scale illustrates the probability density of the accepted models; (b) Objective function on a semi-logarithmic scale. (c - d) Evolution of the average and the standard deviation of accepted models for the different points on the sparse grid: the color scale refers to the ID of the inverted point, 1 being the first temporal point and 6 the last.

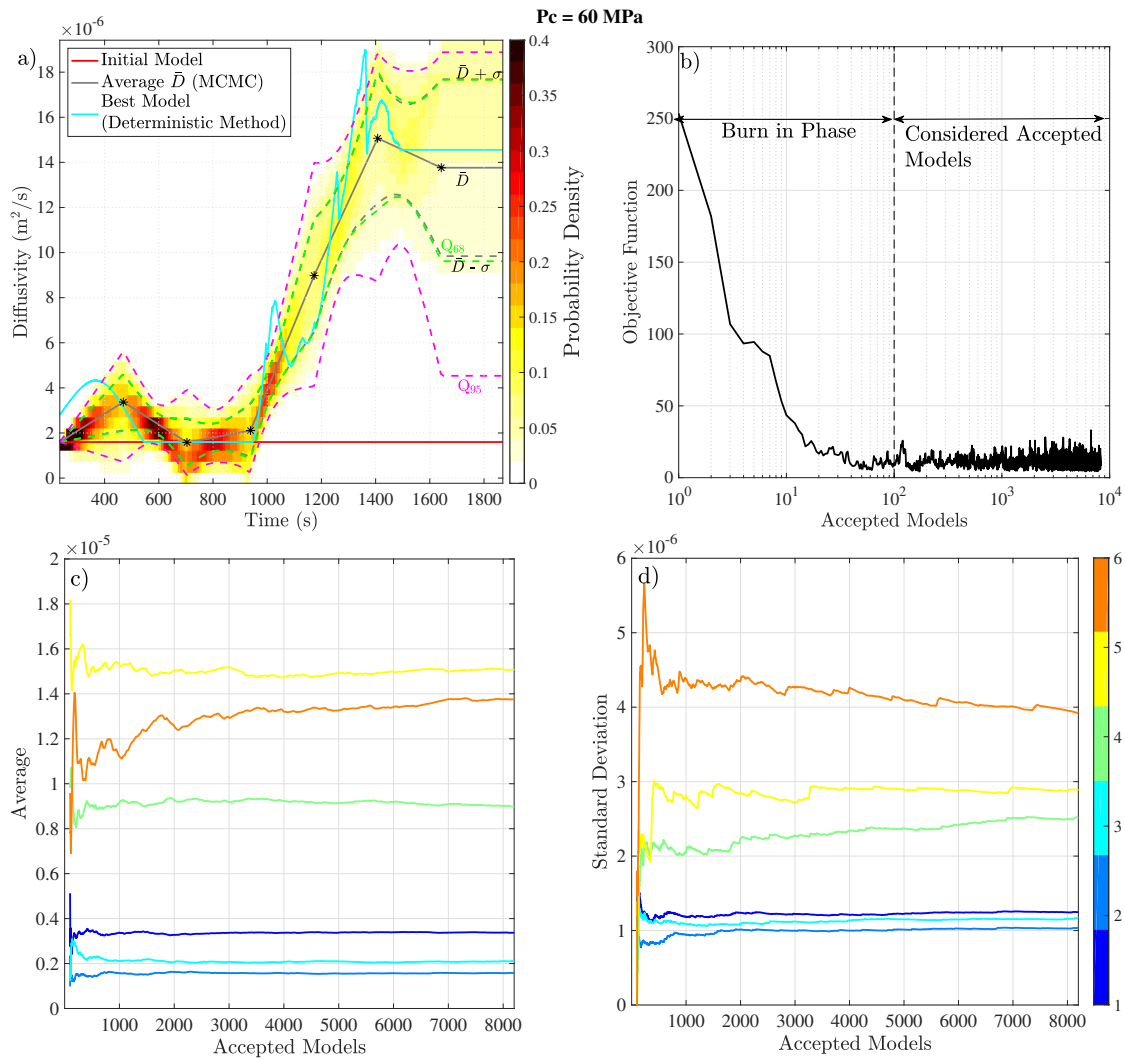


Figure 4.12 – Results of the MCMC Method for the experiment at $P_c = 60$ MPa: Same as Figure 4.11

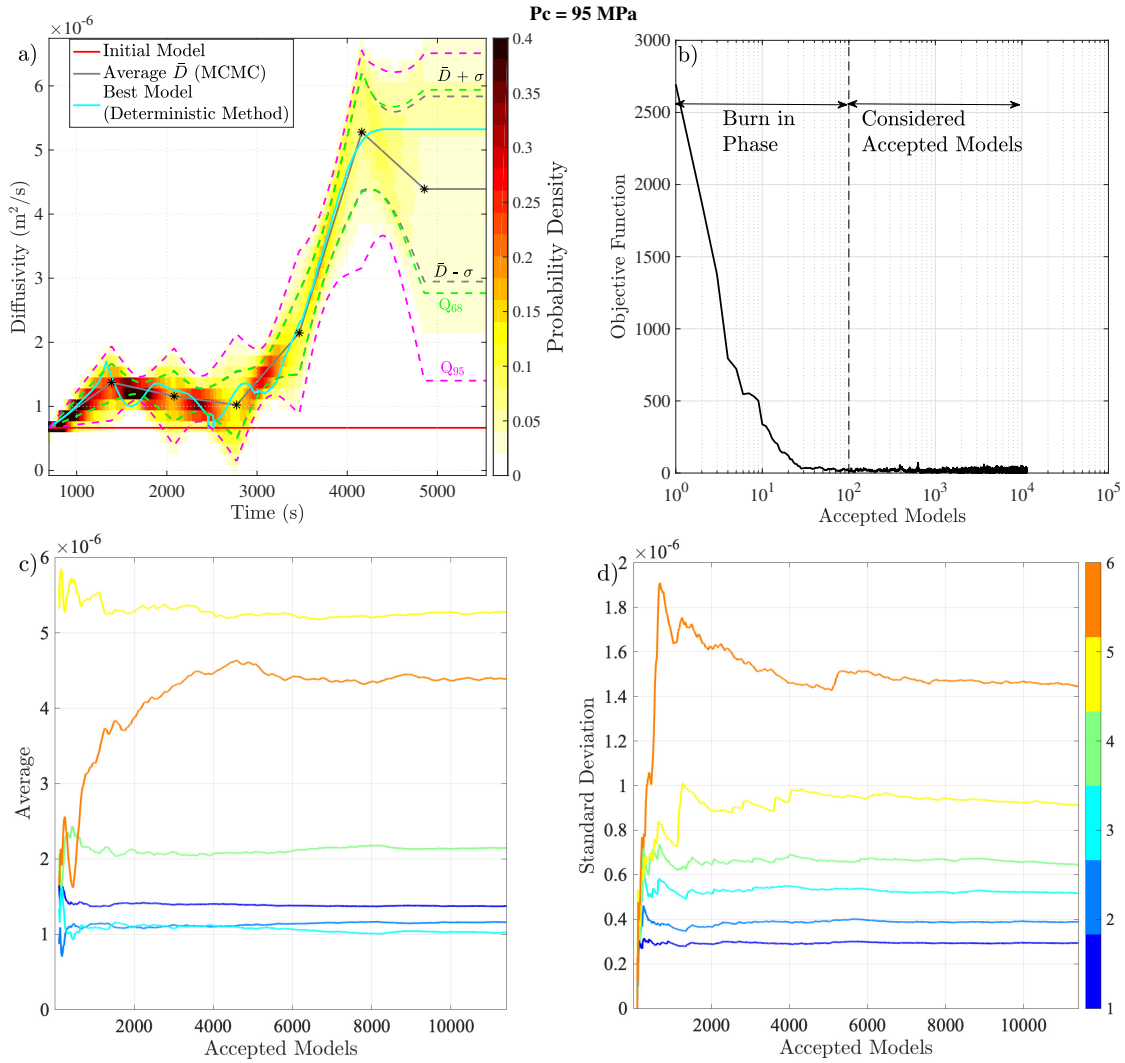


Figure 4.13 – Results of the MCMC Method for the experiment at $P_c = 95$ MPa: Same as Figure 4.11

For the different injection tests, the deterministic best model is close the average \bar{D} (MCMC) for the majority of the time range, exceptions are observed at 60 MPa. We can also notice that the standard deviations are relatively small, and the quantiles are narrow, in the time range that interests us: [400 – 800] seconds at 30 MPa, [700 – 1400] seconds at 60 MPa and [2000 – 4200] seconds at 95 MPa. As expected, the range of accepted models is wider for the largest time of the different tests, as the model is not constrained in this range, because the limited time of the experiment is not enough to model the diffusion process in this time range. We should also note that we do not expect to find the peaks and oscillations in the diffusivity model for the case at 60 MPa, due to the linear interpolation considered and as we did not impose inversion points at

these locations.

4.4.3 Discussion

We presented a deterministic inversion using the simple steepest descent algorithm to minimize the objective function, in which around 1000 – 1500 iterations were needed to converge and estimate the best model of diffusivity history. Other approaches exist and may be more efficient, in which only a few dozens iterations would be needed, for instance: the conjugate gradient method (Shewchuk, 1994) and quasi-Newton approaches (Kelley, 1999). Another way to reduce the number of iterations needed and to reach convergence faster is the application of a preconditioner, in which the concept lies on giving different weights to the different model parameters. This approach is still in the research area, however Brossier (2011) and Metivier *et al.* (2013) showed how it can improve the convergence. This approach in particular could help improve the convergence of the algorithm specially at the largest times where our current method struggles to fit the experimental data.

We should also note that, in the context of this study, we did not introduce any regularisation to the deterministic inversion algorithm. Regularisation techniques rely on additional information, in order to stabilise the solution, for instance if the solution is supposed to be bound between some limits, smooth, have non zero elements, etc. Different regularisation techniques have been proposed (Thikonov and Arsenin, 1977; Engl *et al.*, 2000; Kaltenbacher *et al.*, 2008; Whitney, 2009), and it would be interesting for future developments to be taken into consideration. For instance with the use of such methods, we can avoid the numerical oscillations observed in the diffusivity history for the injection at 60 MPa of confining pressure (Figure 4.9c).

Furthermore, we consider here a spatial homogeneous hydraulic diffusivity along the fault plane, since we only have one point of observation. As the adjoint state method can be applied to multiple observation points, if the experimental protocol can be modified to include multiple boreholes drilled on different locations along the fault plane, we would be able to reconstruct a 3-D (2-D space and time) diffusivity matrix. In this case, the residuals would be: $R = \sum_{i=1}^{N_p} r_i$, where N_p is the number of measurements boreholes, and r_i the residual at the measurement borehole i . The gradient of the objective function becomes: $\partial J / \partial D = \nabla \lambda \cdot \nabla p$. Equation 4.3 is used instead of Equation 4.4, and Equation 4.11 becomes:

$$\frac{\partial \lambda}{\partial t} + \nabla \cdot D \nabla \lambda = \sum_{i=1}^{N_p} \delta(x - x_{\text{obs},i}) \delta(y - y_{\text{obs},i}) (p_{\text{obs},i}^N - p_{\text{obs},i}^E), \quad (4.15)$$

where $D = D(x,y,t)$. Nonetheless, in order to have meaningful results, we should have enough measurements borehole.

We also presented the application of a probabilistic inversion (MCMC method) to our physical problem, in which we explored the uncertainties with respect to the best model of the diffusivity history. For this study we used only 6 model parameters that are evenly spaced in time. However, as showed in Figures 4.6a, 4.8a, and 4.9a, the variation of the hydraulic diffusivity coefficient is not the same throughout the injection experiment. For this reason, a new parametrization with a variable spacing (fine parametrization over the regions where the diffusivity vary a lot, and a sparse one over the regions where the diffusivity is relatively constant) would probably reflect better the uncertainties relative to the diffusivity variation. Moreover, in our approach we chose a simple linear interpolation of the updated diffusivity vector from the sparse grid into the fine one before solving the diffusion process. This implies that the diffusivity vary linearly between the model parameters, which may not be the case in reality. It would thus be interesting to implement a quadratic or lagrangian interpolation between the model parameters.

For the next section, we will use as the diffusivity time history the best model issued from the deterministic approach, and not the average from the MCMC method as it is only defined for 6 model parameters with linear interpolation in between. We also consider the standard deviations calculated from the MCMC method as an estimation of the errors in the deterministic model. Moreover, we will only study the time ranges mentioned above, as they are the easiest to be physically interpreted, as well as having lower uncertainties.

4.5 Diffusivity, Displacement and Effective Stress

The estimated hydraulic diffusivity varies in the ranges $[4.6 \cdot 10^{-6} - 3.7 \cdot 10^{-5}]$, $[1.6 \cdot 10^{-6} - 1.9 \cdot 10^{-5}]$ and $[5.3 \cdot 10^{-6} - 6.6 \cdot 10^{-6}]$ m²/s, at 30, 60 and 95 MPa of confining pressure, respectively. A dependence on confining pressure emerges, as we observe systematically lower values at greater confining pressures. This was previously observed in different studies (e.g., [Zoback and Byerlee, 1975](#); [Wibberley and Shimamoto, 2003](#)).

Throughout the injection experiment, the hydraulic diffusivity increases by one order of magnitude approximately, as shear displacement accumulates on the fault and effective stress decreases following pressure diffusion. This observation shows that diffusivity enhancement can also take place, even at high confining pressures, reaching 95 MPa. Following [Jaeger *et al.* \(2007\)](#), such diffusivity changes could be interpreted as permeability enhancement. Various observations associate permeability enhancement with effective stress reduction (e.g., [Zoback and Byerlee, 1975](#); [McKee *et al.*, 1988](#); [Fisher and Zwart, 1996](#); [Ghabezloo *et al.*, 2009](#)), or with slip accumulation (e.g., [Baghbanan and Jing, 2008](#); [Guglielmi *et al.*, 2015a](#); [Bhattacharya and Viesca, 2019](#)). As well, following shear slip experiments to a fracture in a granite sample, [Esaki *et al.* \(1999\)](#) reported an increase in the hydraulic diffusivity of the rock sample with shear displacement. Here we raise the question on how these two parameters could influence diffusivity enhancement in the same context.

To do so, we consider the best model (deterministic approach) as the numerical estimated diffusivity vector, and use the standard deviations estimated using the MCMC approach as its error-bars. Figure 4.14 illustrates the relation between the mean effective stress and the hydraulic diffusivity variation. The mean effective stress is estimated as $\sigma_{\text{eff}} = \sigma_n - p_m$, where σ_n is the average normal stress along the fault plane estimated using Equation 4.1 and p_m is the mean pressure along the fault plane, estimated from the reconstructed pressure profile, using the best model issued from the deterministic method (refer to Figures 4.6d, 4.8d and 4.9d).

Overall, the results from the three injection tests present the same dependence and tendency: a decrease of the hydraulic diffusivity with the effective normal stress. At 30 and 95 MPa of confining pressure, the results collapse relatively on the same curve, while the ones at 60 MPa present a small difference. A similar dependence between the rock's permeability and the effective normal stress was previously reported by Zoback and Byerlee (1975) and Ghabezloo *et al.* (2009) following permeability test experiments on sandstone and limestone rock samples, respectively. This dependence of the hydraulic properties of the rock to the effective stress may be affected by the opening/closure of the joints along the fracture plane. According to (Bandis *et al.*, 1983), the effective normal

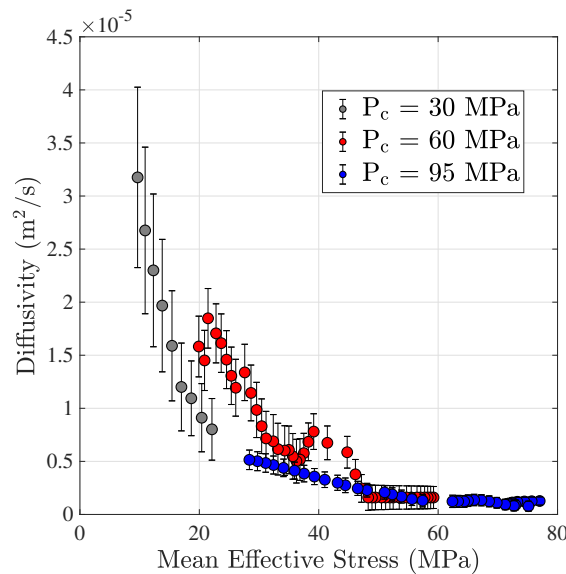


Figure 4.14 – Relationship between hydraulic diffusivity and mean effective stress: at 30 MPa in the range [300 – 700] seconds, 60 MPa in the range [700 – 1400] seconds and 95 MPa in the range [2000 – 4200] seconds. The effective stress is computed as the difference between the normal stress and the mean pore pressure along the fault which is numerically estimated using the inverted diffusivity history. Different colors refer to the different confining pressure values. Diffusivity values are issued from the deterministic method, and the error-bars represented here are the standard deviations estimated using the MCMC method.

stress and the joint closure are related as follows

$$\ln \frac{\sigma}{\sigma_0} = J\delta, \quad (4.16)$$

where σ_0 represents the initial normal stress, J is a constant with dimensions of inverse length and δ is the joint closure. If we (1) assume that $\delta = h - h_0$, where h is the hydraulic aperture, and h_0 is the initial aperture, (2) consider the cubic law where $K = h^2/12$ (K being the permeability) (Snow, 1965; Witherspoon *et al.*, 1980; Bradley, 1987), and (3) consider the following relation between the permeability and the hydraulic diffusivity $D = k/(\varphi\mu c)$, where φ is the porosity, μ is the viscosity and c is the total compressibility (Jaeger *et al.*, 2007), we get the following relation between the hydraulic diffusivity and the effective stress

$$\frac{D}{D_0} = \left(1 - \frac{1}{Jh_0} \ln \frac{\sigma}{\sigma_0}\right)^2, \quad (4.17)$$

where D_0 represents the initial diffusivity value, before the injection test started. Figure 4.15 represents the relation between the square-root of D/D_0 and the logarithm of the ratio σ/σ_0 . Hence, the dependence between the hydraulic diffusivity and the effective normal stress appears to follow the previous relation (Equation 4.17). At 30 and 95 MPa of confining pressure, the results reflect more or less the same behavior ($1/Jh_0 \approx 1.5$). A clear difference is however observed at 60 MPa ($1/Jh_0 \approx 2.1$). This observation suggests that not only the effective stress can affect the hydraulic diffusivity, an additional factor might have an impact as well.

According to Chen *et al.* (2000b), the hydraulic aperture depends on the shear displacement and the confining pressure. For this reason, we investigate the effect of the shear displacement on the hydraulic diffusivity. Figure 4.16 illustrates the evolution of the hydraulic diffusivity with respect to the cumulative slip accumulated along the fault (only in the injection phase: the slip recorded during the loading phase was not considered). For the injection tests at 30 and 95 MPa, the hydraulic diffusivity increases systematically with shear slip. However, this is not the case for the test at 60 MPa, as this experiment exhibits various stick-slip events as well as time periods of negligible displacement (refer to Figure 4.2b). During the latter, the diffusivity continues to increase independently of the shear slip, thus this increase is probably mainly caused by the reduction of the effective stress. Nonetheless, during the stick slip events, our results suggest an acceleration in the diffusivity enhancement, that is later re-compensated by a smaller decrease. We are however not sure to what extent we can rely on the quantitative abrupt increase in the hydraulic diffusivity, as discussed in the previous section. Our results thus suggest that shear displacement can affect the hydraulic diffusivity evolution, as it increases following slip accumulation. This increase may as well depend on the nature of the slip events, as it appears to be a long term increase following slip events with small slip velocities, whereas it presents a short term reversible (hysteresis-like) behavior following stick slip events. In the context of a decametric scale injection test in the underground LSBB laboratory in the South France, Guglielmi *et al.* (2015b) also reported a difference in the permeability enhancement, where linear permeability enhancement was associated with aseismic shear slip, and a very small increase accompanied the seismic phase of

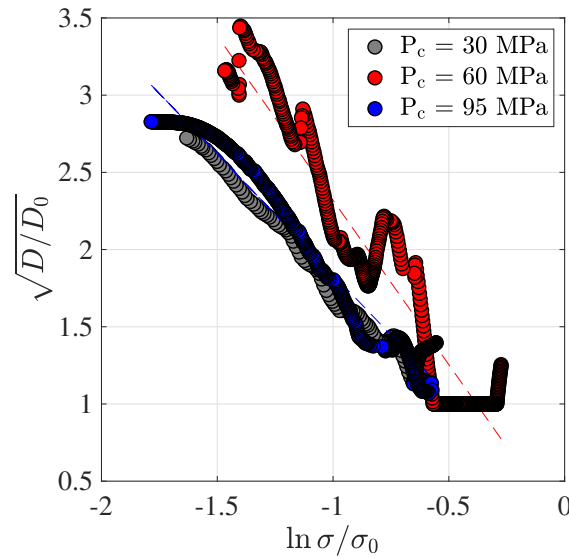


Figure 4.15 – Relationship between the square of the ratio of the hydraulic diffusivity to the initial diffusivity and the logarithm of the ratio of the mean effective stress to the initial effective stress: at 30 MPa in the range [300 – 700] seconds, 60 MPa in the range [700 – 1400] seconds and 95 MPa in the range [2000 – 4200] seconds. Different colors refer to the different confining pressure values. Diffusivity values are issued from the deterministic method.

slip. Nonetheless, we cannot really compare these results to ours: (1) due to the different experiment scale, (2) during this experiment the maximum injection pressure reached 3 MPa which is relatively very small compared to the injection pressure ranges used here, (3) different ranges of loading (around $5 \text{ MPa}\cdot\text{min}^{-1}$ during this experiment).

Our investigation of the relation between the shear slip and diffusivity enhancement remains however limited, as we can only estimate an average shear slip along the fault plane and we can only invert for an effective diffusivity as we only have two measures of pressure. This may especially be true following stick slip events, where localized shear slip along the fault plane might be expected. Permeability anisotropy has been in fact observed to be induced by shear displacement (Zhang and Tullis, 1998; Auradou *et al.*, 2005). For this reason, we strongly recommend for future laboratory experiments to equip the rock sample with multiple pressure and displacement sensors. As the implementation of multiple pressure sources in our numerical inversion is quite easy, such data would allow us to investigate more in details the hydraulic diffusivity enhancement that especially accompanies stick slip events.

The injection tests presented in this study are conducted for a saw-cut fault in a Andesite rock sample. Thus the results presented here correspond to a smooth surface. According to Ye and Ghassemi (2018), shear slip and permeability enhancement are largely dependent on the roughness of the fault. It would certainly be interesting for future studies to conduct such injection tests and hydraulic diffusivity variations analysis

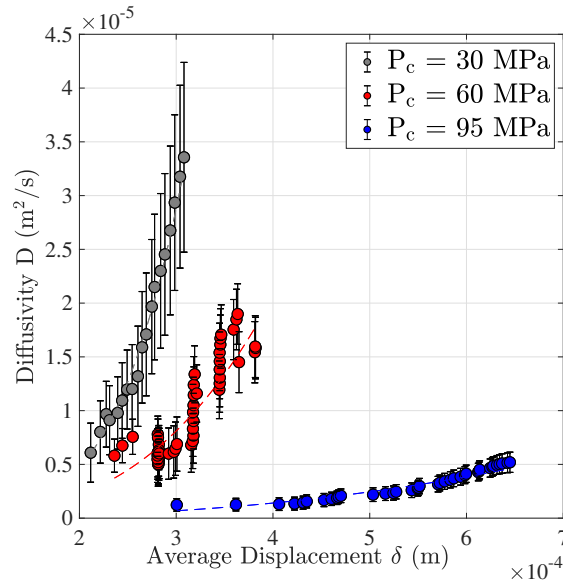


Figure 4.16 – Relationship between hydraulic diffusivity and average cumulative displacement (only recorded in injection phase) for the different injection tests at different confining pressure. Different colors refer to the different confining pressure values. Diffusivity values are issued from the deterministic method, and the error-bars represented here are the standard deviations estimated using the MCMC method. The dashed colored lines represent the numerical fit of the experimental values using a power law relation between the diffusivity and the cumulative slip.

on experimental faults having each a different fault surface roughness.

In a similar context of laboratory injection experiments, [Passelegue *et al.* \(2018\)](#) showed that the injection pressure rate controls the fluid pressures perturbation and thus can affect the fault reactivation. Furthermore [Almakari *et al.* \(2019\)](#) reported the important effect of the injection pressure rate on the seismicity rate and the magnitude content of the seismic events. As in this study fluid was injected into the fault under a constant injection pressure rate, it would also be interesting to test various injection pressure rates and examine whether or not the permeability enhancement may be affected.

Finally, in addition to the characterization of the evolution of the hydraulic diffusivity through a single injection experiment and the investigation of how it varies with slip accumulation and effective stress reduction, the application of such numerical approach could be very advantageous, as it potentially allows for reconstruction of the spatio-temporal pore pressure changes during the injection test, that allows for the track the diffusive front. With the use of appropriate acoustic sensors, this can give more insights into the relation between the diffusive front and the aseismic/seismic rupture front.

4.6 Conclusion and Perspectives

We used in the context of this study laboratory experimental constant-rate injection tests on a saw-cut fault in an Andesite rock sample, under triaxial loading, at different values of confining pressure. This work was a collaboration with François Passelègue, from EPFL, Lausanne. The experimental sample was equipped by two pressure sensors and 8 strain gages, that allow us to measure the pressure history at two locations along the fault plane, and the deformation at 8 points along strike. The fluid injection reactivated the experimental fault, inducing different slip events, that were accompanied by pressure drops in the injection borehole and pressure steps in the observation borehole, which could indicate an enhancement of the hydraulic diffusivity along the fault.

We then developed and performed deterministic and probabilistic inversion to the experimental data, in particular the pore pressure history. This allows us to characterize the time history of an effective hydraulic diffusivity $D(t)$ throughout the injection test. Deterministic inversion, using the adjoint state method, was performed to estimate the best diffusivity model that could explain the experimental data. Then, probabilistic inversion, using an MCMC algorithm, was applied in order to estimate the associated uncertainties.

The numerical method was able to reproduce the experimental data for a wide time range of the different experiments. However, it was difficult to fit the data at the largest times of the experiment, as the remaining data was not sufficient to properly model the diffusion process. Two propositions could be applied: (1) extending the experimental measurement for a sufficient time after the pressure equilibrium is reached along the fault, (2) application of regularization techniques or pre-conditioner to the numerical solution.

Here, we made the choice to invert for an effective diffusivity $D(t)$, as with one observation point the inversion problem would be under-determined to invert for the spatio-temporal variability of the hydraulic diffusivity $D(x,y,t)$. Nonetheless, permeability anisotropy has been observed to be induced by shear displacement (Zhang and Tullis, 1998; Auradou *et al.*, 2005). As the numerical approach that we propose can be applied to multiple observation points very easily, we recommend for future experimental tests, if possible, to include several measurement boreholes connected to pressure sensors. This would allow us to explore the variability of the diffusivity locally near the injection borehole where the pressure gradient is the highest, and along the fault plane following the diffusion front.

In the injection tests presented here, the hydraulic diffusivity was found to largely depend on the confining pressure and to vary throughout the injection experiment with the mean effective stress acting along the fault plane, where an increase by one order of magnitude was observed. The numerical results suggests an effect of the shear slip as well, where we observe different behavior with the respect to the nature of the slip events: long

term hydraulic diffusivity increases accompanied slip events with small slip velocities, whereas a short term reversible increase was observed following stick slip events.

Finally, the experimental sample was equipped by ultrasonic transducers that were not exploited during the work presented here. Using these measurements we can characterize and localize the different rupture sources and investigate the rupture front. Coupling this with the reconstructed pressure profile, from the numerical inversion, we could compare the rupture and diffusive fronts.

4.7 Appendix A: Development of the Adjoint State Method

We present here the development of the adjoint state method applied to the inversion of the hydraulic diffusivity history in the context of a 2-D pressure diffusion inside an elliptical fault plane. We use this method to estimate the gradient of the objective function. In the context of this study, pressure $p_{inj}^E(t)$ is injected in the injection borehole (coordinates x_{inj}, y_{inj}), and measured $p_{obs}^E(t)$ in the observation borehole (coordinates x_{obs}, y_{obs}). We consider an effective diffusivity $D(t)$ along the fault plane. The objective function is:

$$J[D, \lambda, p] = \frac{1}{2} \iiint \left(\delta(x - x_{obs}) \delta(y - y_{obs}) (p_{obs}^N - p_{obs}^E)^2 \right) dx dy dt - \iiint \lambda(x, y, t) \left[\frac{\partial p}{\partial t} - D \Delta p \right] dx dy dt. \quad (4.18)$$

For the sake of simplicity, we did not include the initial and boundary conditions in the previous equation. The total gradient of the objective function is:

$$\frac{dJ}{dD} = \frac{\partial J}{\partial D} + \frac{\partial \lambda}{\partial D} \frac{\partial J}{\partial \lambda} + \frac{\partial p}{\partial D} \frac{\partial J}{\partial p}. \quad (4.19)$$

where $D=D(t)$, $p = p(x,y,t)$ and $\lambda = \lambda(x,y,t)$. We choose p and λ so that $\partial J/\partial p = 0$ and $\partial J/\partial \lambda = 0$, to avoid estimating the Frechet derivatives $\partial p/\partial D$ and $\partial \lambda/\partial D$. Using equation 4.18:

$$\frac{\partial J}{\partial D(t_0)} = \iint \lambda(x, y, t_0) \Delta p(x, y, t_0) dx dy. \quad (4.20)$$

Thus the gradient of the objective function becomes:

$$\frac{dJ}{dD} = \iint \lambda \Delta p dx dy. \quad (4.21)$$

In order to estimate the gradient, we need the pressure p and the adjoint state variable λ . We thus estimate the partial derivatives of the objective function with respect to p and λ using equation 4.18:

$$\frac{\partial J}{\partial \lambda(x_0, y_0, t_0)} = - \left(\frac{\partial p(x_0, y_0, t_0)}{\partial t} - D(t_0) \Delta p(x_0, y_0, t_0) \right). \quad (4.22)$$

As we impose $\partial J/\partial \lambda = 0$, thus equation 4.22 becomes:

$$\frac{\partial p}{\partial t} - D(t)\Delta p = 0, \quad (4.23)$$

which is the pressure diffusion equation, the state equation (by definition). For the derivative with respect to p , we first need to integrate by part. The partial derivative writes:

$$\begin{aligned} \frac{\partial J}{\partial p(x,y,t)} &= \frac{\partial}{\partial p(x,y,t)} \frac{1}{2} \iiint (\delta(x - x_{\text{obs}})\delta(y - y_{\text{obs}}) (p_{\text{obs}}^N - p_{\text{obs}}^E))^2 dx dy dt \\ &\quad - \frac{\partial}{\partial p(x_0,y_0,t_0)} \iiint \lambda(x,y,t) \left[\frac{\partial p}{\partial t} \right] dx dy dt \\ &\quad + \frac{\partial}{\partial p(x_0,y_0,t_0)} \iiint \lambda(x,y,t) D \left(\frac{\partial^2 p}{\partial x^2} + \frac{\partial^2 p}{\partial y^2} \right) dx dy dt. \end{aligned} \quad (4.24)$$

We will now resolve independently each term of the right part of equation 4.24. For the sake of simplicity, we will name the 3 parts A, B and C, that is $\partial J/\partial p(x,y,t) = A - B + C$.

- Part 1

$$A = \delta(x - x_{\text{obs}})\delta(y - y_{\text{obs}}) (p_{\text{obs}}^N - p_{\text{obs}}^E). \quad (4.25)$$

- Part 2: To solve this part we conduct an integration by part with respect to time t .

$$B = \frac{\partial}{\partial p(x_0,y_0,t_0)} \left(\iint [\lambda(x,y,t)p(x,y,t)]_0^{T_{\text{max}}} dx dy - \iiint \frac{\partial \lambda}{\partial t} p(x,y,t) dx dy dt \right), \quad (4.26)$$

where T_{max} is the time at the end of the experiment. The pressure p is 0 at the start of the injection ($p(x,y,t_0) = 0$), and we impose that λ at $t=T_{\text{max}}$ is zero ($\lambda(x,y,T_{\text{max}})=0$), thus the first term of the right part of the previous equation is 0. Thus,

$$B = - \frac{\partial}{\partial p(x_0,y_0,t_0)} \iiint \frac{\partial \lambda}{\partial t} p(x,y,t) dx dy dt = \frac{\partial \lambda(x_0,y_0,t_0)}{\partial t} \quad (4.27)$$

- Part 3: To solve this part we use Green's identities. We know that:

$$\frac{\partial}{\partial x} \left(\lambda \frac{\partial p}{\partial x} \right) = \frac{\partial \lambda}{\partial x} \frac{\partial p}{\partial x} + \lambda \frac{\partial^2 p}{\partial x^2}, \quad (4.28)$$

$$\frac{\partial}{\partial y} \left(\lambda \frac{\partial p}{\partial y} \right) = \frac{\partial \lambda}{\partial y} \frac{\partial p}{\partial y} + \lambda \frac{\partial^2 p}{\partial y^2}. \quad (4.29)$$

By integrating Equations 4.28 and 4.29 over the domain Ω , we get:

$$\int_{\Omega} \nabla \cdot (\lambda \nabla p) dS = \int_{\Omega} \nabla \lambda \cdot \nabla p dS + \int_{\Omega} \lambda \Delta p dS, \quad (4.30)$$

where $dS = dx dy$. This gives:

$$\int_{d\Omega} \lambda \bar{\nabla} p \cdot \bar{n} du = \int_{\Omega} \bar{\nabla} \lambda \cdot \bar{\nabla} p dS + \int_{\Omega} \lambda \Delta p dS, \quad (4.31)$$

where \bar{n} represents the normal vector with respect to the contour $d\Omega$, and du is the distance along the contour $d\Omega$. As no liquid is allowed to flow outside of the fault plane, the flow at the boundaries of the fault is 0 and Neuman boundary conditions are imposed: $\bar{\nabla} p \cdot \bar{n} = 0$ along $d\Omega$, giving:

$$\int_{\Omega} \bar{\nabla} \lambda \cdot \bar{\nabla} p dS + \int_{\Omega} \lambda \Delta p dS = 0. \quad (4.32)$$

Using Green's identities to the adjoint state variable λ and applying the same reasoning, we get:

$$\int_{d\Omega} p \bar{\nabla} \lambda \cdot \bar{n} du = \int_{\Omega} \bar{\nabla} p \cdot \bar{\nabla} \lambda dS + \int_{\Omega} p \Delta \lambda dS, \quad (4.33)$$

We impose no flow for the adjoint state variable λ at the boundaries of the fault plane, thus $\bar{\nabla} \lambda \cdot \bar{n} = 0$ along $d\Omega$, giving:

$$\int_{\Omega} \bar{\nabla} p \cdot \bar{\nabla} \lambda dS + \int_{\Omega} p \Delta \lambda dS = 0. \quad (4.34)$$

By subtracting Equation 4.32 from Equation 4.34, we get:

$$\int_{\Omega} \lambda \Delta p dS = \int_{\Omega} p \Delta \lambda dS. \quad (4.35)$$

If we substitute Equation 4.35 into term C, we get:

$$\begin{aligned} C &= \frac{\partial}{\partial p(x_0, y_0, t_0)} \left(\iiint \left(\frac{\partial^2 \lambda}{\partial x^2} + \frac{\partial^2 \lambda}{\partial y^2} \right) D(t) p(x, y, t) dx dy dt \right) \\ &= \left(\frac{\partial^2 \lambda}{\partial x^2} + \frac{\partial^2 \lambda}{\partial y^2} \right) D(t) \\ &= \Delta \lambda D(t). \end{aligned} \quad (4.36)$$

Therefore, assuming $\partial J / \partial p = 0$, equation 4.24 becomes:

$$\frac{\partial \lambda}{\partial t} + D(t) \Delta \lambda = \delta(x - x_{\text{obs}}) \delta(y - y_{\text{obs}}) \left(p_{\text{obs}}^N - p_{\text{obs}}^E \right) \quad (4.37)$$

Equations 4.23 and 4.37 form a set of differential equations for the pressure p and the adjoint state variable λ . Once resolved, their solutions can be implemented in equation 4.21 to estimate the gradient of the objective function.

Validation of the Gradient Estimation

The final step is to validate this method for the gradient estimation. We first need to verify the key parameters, that are the initial and boundary conditions as well as the source terms for the pressure p and the adjoint state variable λ . Then we estimate the gradient using the finite difference method, as follows:

$$\frac{\partial J}{\partial D(t)} = \frac{J(D(t) + \delta D(t)) - J(D(t) - \delta D(t))}{2\delta D(t)}. \quad (4.38)$$

To do so, we need to impose a local perturbation $\delta D(t)$ at each time step t_0 , and then solve Equation 4.23 once with the diffusivity model $D(t)+\delta D(t)$ and then $D(t)-\delta D(t)$. We estimate for each the residuals and the objective function using Equation 4.5 and then implement the values in Equation 4.38.

This method is very long as it requires the resolution of the forward problem twice for each time step, for each inversion iteration. This is why we only use it for one inversion iteration, and for a few time steps in order to validate the gradient estimation by the adjoint state method. Figure 4.17 illustrates a validation test that we conducted for a synthetic test: the gradient estimated using the adjoint state formulation and the finite difference method for a synthetic test are similar.

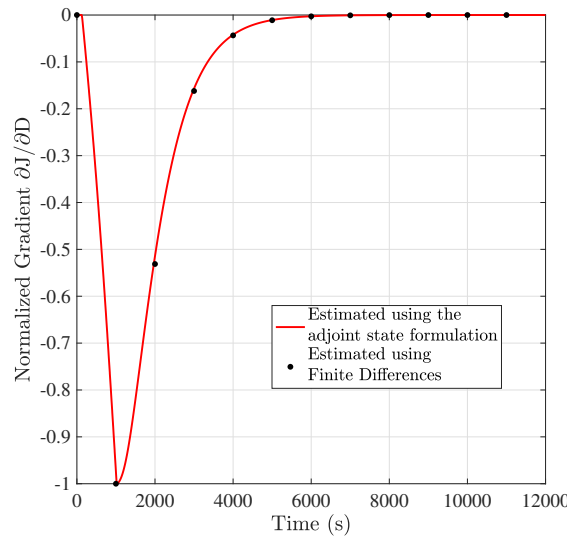


Figure 4.17 – Validation of the Gradient Estimation for a synthetic test. In red: the normalized gradient estimated using the adjoint state formulation; Black circles: the normalized gradient estimated using the finite difference method. These values are for one inversion iteration.

Chapter 5

Conclusions and Perspectives

Contents

5.1	General Conclusion	147
5.2	Perspectives	148
5.2.1	Post Shut-in Seismicity	148
5.2.2	Modeling Induced Aseismic Motion and Second Order Triggering of Seismic Failure	149
5.2.3	Hydro-Mechanical Modeling of Laboratory Injection Tests	149

Résumé du Chapitre 5 en Français

Au cours de cette thèse, je me suis intéressée à étudier la réactivation hydro-mécanique d'une faille pré-existante. En effet, nombreuses observations associent une forte augmentation du risque sismique à des activités d'injection (la géothermie par exemple), dans des régions actives sismiquement (comme en Californie), comme dans des régions de faible sismicité (par exemple à Soultz-sous-Forêt, France).

La réactivation hydro-mécanique des failles était l'objet de nombreuses études d'observations, des études expérimentales ainsi que numériques. Néanmoins, comme nous l'avons montré au chapitre 1, plusieurs aspects de la réactivation hydro-mécanique n'ont pas été complètement explorés ni compris.

Dans cette étude, nous avons en particulier choisi: (1) d'explorer l'effet des paramètres d'injection (notamment la pression et le taux de pression d'injection) sur la réponse sismique (taux de sismicité et distribution de magnitude) pour le cas d'une faille 2-D hétérogène gouvernée par du frottement *rate and state*; (2) d'étudier dans le même contexte de faille le rôle des propriétés de frottement de la faille et voir à quel point ils peuvent affecter la réponse sismique dans le cadre d'injection de fluide; (3) dans la troisième partie, on explore de plus près (à plus petite échelle) la variation de la diffusivité hydraulique au cours de l'injection avec l'accumulation du déplacement sur la faille et la réduction de la contrainte normale effective, lors d'expériences de laboratoire d'injection de fluide sur un échantillon d'Andésite.

J'expose dans ce chapitre les principales conclusions de cette étude:

- observation d'une dépendance de la réponse sismique (taux de sismicité et distribution de magnitude) avec la pression d'injection et le taux de pression,
- pour des taux de pressions assez élevées, le taux de sismicité se sature, et se compense par un moment sismique libéré plus important,
- les failles plus stables résistent mieux à l'injection de fluide: la perturbation du taux de sismicité est dans ce cas moins importante,
- développement de méthodes d'inversion (déterministe et probabiliste) pour estimer l'évolution temporelle de la diffusivité hydraulique au cours d'expériences d'injection.

En outre, je discute dans ce chapitre les possibles pistes afin d'améliorer notre modèle et pouvoir explorer (1) la sismicité après injection, (2) l'interaction glissement sismique/asismique dans le contexte de la sismicité induite, et finalement (3) d'avoir un modèle hydro-mécanique qui tient compte de l'évolution de la diffusivité hydraulique avec le déplacement accumulé sur la faille et la réduction de la contrainte effective.

5.1 General Conclusion

During this thesis, we have taken an interest in further investigating hydro-mechanical fault reactivation. Different seismicity observations indeed associate large increase in the seismic hazard to energy related injection activities (Ellsworth, 2013; Keranen and Weingarten, 2018), whether in tectonically active regions (e.g. California Goebel *et al.* (2016b)) or regions of previously low seismicity (e.g. Western Canada sedimentary basin Atkinson *et al.* (2016), Soultz-sous-Forêt Majer *et al.* (2007)). Induced fault reactivation has been the topic of many observational, experimental and numerical studies. Nonetheless, as we showed in Chapter 1, numerous features and aspects of induced fault reactivation have not been fully explored nor understood. In particular, we chose in this study: (1) to examine to what extent injection operation and fault frictional properties could affect the shear slip reactivation of the fault on a large scale (seismicity rate and magnitude distribution); (2) to investigate on a smaller scale the coupled hydro-mechanical reactivation of the fault (permeability enhancement and slip accumulation).

In this thesis, we coupled a rate and state earthquake simulator (Dublanchet, 2018) with a linear injection and diffusion model. In our numerical approach we consider a Dietrich-Ruina heterogeneous 1-D fault (Dietrich, 1972; Rice and Ruina, 1983; Linker and Dietrich, 1992) embedded in a 2-D elastic medium. In such approach, the fault is able to produce a complex pattern of rupture sequences, with magnitudes obeying a Gutenberg-Richter distribution. We presented this model in Chapter 2, and used it to investigate the effects of injection parameters. In particular, we showed a clear dependency of induced seismic response (seismicity rate and magnitude content) with injection pressure and pressure rate and pointed out an important trade-off existing between seismicity rate perturbations and magnitude content variations of fluid induced seismicity. Understanding how injection parameters could locally influence induced seismicity is of great interest to injection regulators, especially in the context of advanced traffic light systems (ATLS) or when trying to estimate to what extent the induced seismicity contribute to the seismic hazard. We further investigated the effects of fault frictional parameters of heterogeneous faults in Chapter 3. We characterized the frictional behavior of different heterogeneous faults by the ratio of the averages of their frictional parameters, and showed that faults that are more frictionally stable can resist more to fluid injection, as they exhibit lower induced seismicity rates. This leads to a lower amplification of seismic activity and thus a lower seismic energy. We are not sure whether this decrease in seismic energy could be accompanied by a larger aseismic energy dissipation, and we leave this for future studies.

One of the limitations of our modeling approach is the use of a time-independent hydraulic diffusivity. Various correlations have indeed been presented during injection experiments between fault permeability variations on one hand and slip accumulation and effective stress reduction on the other hand, at the laboratory scale (e.g. Zoback and Byerlee (1975), Baghbanan and Jing (2008), Ghabezloo *et al.* (2009) and Rutter

and Mecklenburgh (2018)) and the decametric scale (Guglielmi *et al.* (2015b), Duboeuf *et al.* (2017) and Bhattacharya and Viesca (2019)). Nonetheless, the relation between fault reactivation and permeability enhancement is not as simple, as it is in most of the cases a two-way relationship: permeability evolution could also affect pressure diffusion, one of the principal mechanisms controlling induced seismicity; in the case of a high permeability pore pressure diffuses quickly, whereas in the case of low permeability, pore pressure diffuses slowly and local over-pressures can be expected (Keranen and Weingarten, 2018). For all the reasons mentioned, we were interested in investigating the coupled hydro-mechanical reactivation of a fault. We thus conducted in collaboration with François Passelègue (from EPFL Lausanne) laboratory injection tests on an Andesite rock sample under triaxial loading, during which pore pressure was continuously measured at two locations along the fault plane. In Chapter 4, we developed and applied to the experimental pressure data a deterministic inversion of the 2-D pressure diffusion process, using the adjoint state method (Plessix, 2006), to evaluate hydraulic diffusivity evolution throughout the injection test, and a probabilistic inversion (Metropolis *et al.*, 1953; Hastings, 1970) to estimate the associated uncertainties. The application of such methods in this context can be quite effective. Our results show how the hydraulic diffusivity varies with the effective stress and shear slip accumulation. The ultimate objective is to use such information to improve our numerical approach presented in Chapter 2 by incorporating a hydraulic diffusivity that evolve with the pressure and slip histories $D(t, \sigma, \delta)$ along the fault. We have developed such hydro-mechanical coupling to model the injection experiments and will be further presented in section 5.2.3.

5.2 Perspectives

5.2.1 Post Shut-in Seismicity

As discussed in Chapter 1, numerous cases of post shut-in seismicity have been reported, for instance the seismicity in Basel, Switzerland (Haring *et al.*, 2008; Deichman and Giardini, 2009) and in Ohio (Kim, 2013; Kozłowska *et al.*, 2018). According to Hsieh and Bredehoeft (1981) and Dietrich *et al.* (2015), one of the principal mechanisms driving post shut-in seismicity is pressure diffusion away from the injection well. As in our numerical approach, the diffusion process is confined in the fault and in the vicinity of the injection well without the possibility to diffuse to the surrounding region, our model is not suited to investigate post shut-in seismicity. However, it would be of great interest to expand our results and explore to what extent post shut-in seismicity could be affected by the different aspects that we investigated in this thesis. Recently, Romanet *et al.* (2018) proposed a rate and state mechanical model, similar to ours, that considers a network of neighbouring interacting faults, rather than just one isolated fault. Coupling such model with our injection and diffusion model could help explore how fluid injection into one fault could affect the surrounding faults during the injection activity and after it ceases. In this case, a 3-D diffusion model is needed to compute the pressure history in

the medium and along the faults, however if we are only interested with the state along the fault, we only need a 2-D coupling of the diffusion and the mechanical model.

5.2.2 Modeling Induced Aseismic Motion and Second Order Triggering of Seismic Failure

Beyond micro-seismic activity, injection activities can in some cases initiate some slow aseismic slip episodes. We have presented in Chapter 1 direct and indirect evidence of induced aseismic motion observations (e.g. Wei *et al.* (2015), Guglielmi *et al.* (2015b), Cornet (2016) and Duboeuf *et al.* (2017)). More recently, De Barros *et al.* (2018) argued that in some cases induced seismic failure could be triggered by stress transfer from aseismic slip. Although with our model, we were able to observe some slow aseismic slip episodes (Chapter 2), it only represented a very small fraction of the total slip accumulated along the fault. In our model, the creeping areas (VS patches) are indeed distributed along the fault and cannot interact. We believe this may be the reason why our model cannot produce more aseismic motion, and thus it is not suited to investigate a second order seismic failure driven by aseismic motion. In 2-D fault models embedded in a 3-D elastic medium, like the one presented by Dublanchet *et al.* (2013), the asperities are distributed within a creeping region. As such models can allow for proper modeling of aseismic slip, it would certainly be interesting to couple it with a 2-D pressure diffusion model for future developments and studies.

In addition, Bourouis and Bernard (2007) reported that aseismic slip may have driven post-injection seismic activity in Soultz-sous-Forêt. Thus, extending our modeling approach into 3-D could also be interesting in the perspective of understanding post-injection seismicity.

5.2.3 Hydro-Mechanical Modeling of Laboratory Injection Tests

Finally, we present in this section current works that we started during this thesis, but that are not yet completed. As mentioned before, the eventual objective of Chapter 4 is to characterize the relation between the hydraulic diffusivity history and the shear slip and the effective stress reduction along the fault. This would allow us to investigate the coupled hydro-mechanical reactivation of the fault.

We want to apply such modeling to the laboratory injection tests. For this, we couple the 2-D diffusion model for an elliptical fault that we developed in Chapter 4 (section 4.3.2.2) with the rate and state earthquake simulator that we presented in Chapter 2 (section 2.3). This approach allows to compute both the pressure and shear displacements (and not only pressure). The diffusivity can thus be inverted using both pressure and displacement as observables. Comparing the results of such simulations with the strain data along the fault would allow to provide a better understanding of

the relationship between slip front and pressure front analyzed by [Passelegue *et al.* \(2020\)](#).

We present here a first attempt of the hydro-mechanical modeling of the injection test at 30 MPa of confining pressure (previously illustrated in Figure 4.2a). We consider a frictional homogeneous velocity-strengthening fault using a first set of arbitrary parameters ($a/b = 2.5$, $d_c = 10^{-3}$ m). We present here two cases: (1) using a constant diffusivity throughout the injection; (2) using a time-dependent diffusivity history. For the first test, we consider $D = 4.6 \cdot 10^{-6}$ m²/s, that is the diffusivity value that we estimated during the initial time of the injection experiment using the deterministic approach (Figure 4.6c), whereas for the second test, we use the inverted diffusivity history (Figure 4.6c). From Figures 5.1a and 5.1b, we can see the important effect of using a non-constant diffusivity on both the pressure at the observation borehole (i.e. of the diffusion process) and on the shear displacement accumulated on the fault. With a constant diffusivity the shear displacement accumulated at $t = 1000$ s is 0.025 mm, whereas using the inverted diffusivity history the shear displacement accumulated at $t = 1000$ s is 0.125 mm, that is 5 times larger.

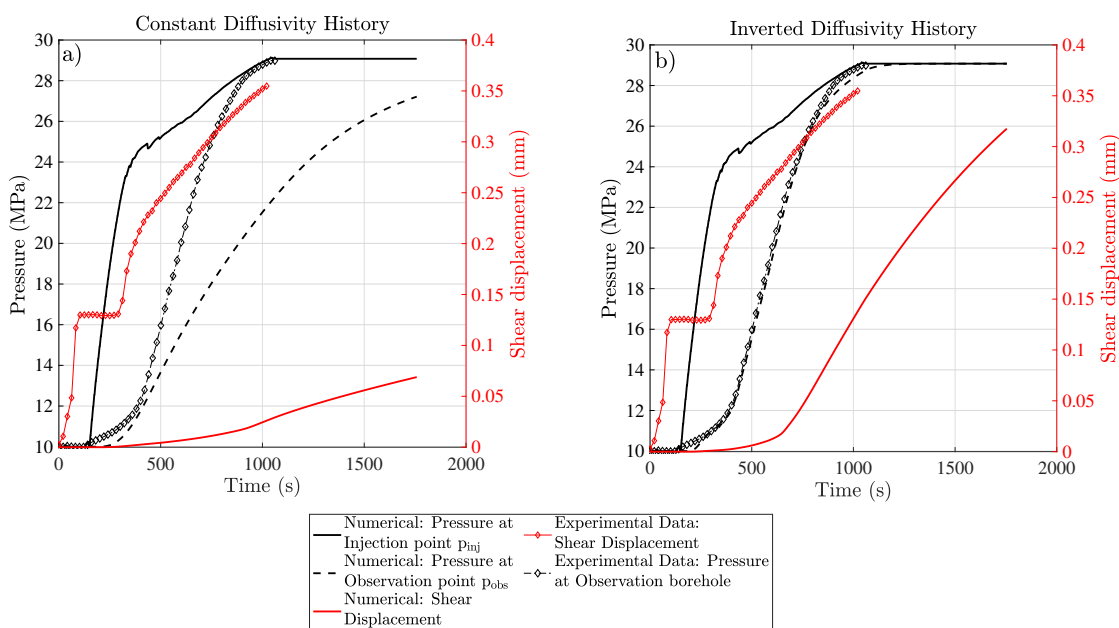


Figure 5.1 – Numerical hydro-mechanical modeling of the laboratory injection test at 30 MPa of confining pressure: (a) with a constant diffusivity history $D = 4.6 \cdot 10^{-6}$ m²/s (diffusivity value found for the beginning time of the injection experiment (Figure 4.6c)); (b) using the inverted diffusivity history (presented in Figure 4.6c). In both subplots pressure is represented in black (left axis) and shear displacement in red (right axis). The plots with diamond markers represent the experimental data: shear displacement (red) and pressure at the observation borehole (black).

However, from Figure 5.1b, the shear displacement measured during the laboratory injection test at $t = 1000$ s is 0.225 mm (if we don't consider the shear displacement accumulating during the loading phase before injection started, i.e. for $t < 143$ s). It is larger than the one we estimate using our numerical model, this discrepancy may be due to the arbitrary frictional parameters that we chose. Finally, this is a continuous work in progress.

Bibliography

- Abercrombie, R. and J. Rice, 2005. Can observations of earthquake scaling constrain slip weakening? *Geophys. J. Int.* **162**, 406–424 (cit. on p. 55).
- Aki, K., 1966. Generation and propagation of G waves from the Niigata earthquake of June 16, 1964. 2. Estimation of earthquake moment, released energy and stress-strain drop from G wave spectrum. *Bulletin of the Earthquake Research Institute*, **44**, 23–88 (cit. on p. 3).
- Aki, K., 1965. Maximum Likelihood Estimate of b in the Formula $\log N = a - bM$ and its Confidence Limits. *Bulletin of the Earthquake Research Institute*, **43**, 237–239 (cit. on p. 71).
- Alden, A., 2018. *The World's Major Earthquake Zones*. ThoughtCo. (Cit. on p. 9).
- Almakari, M., P. Dublanchet, H. Chauris and F. Pellet, 2019. Effect of the Injection-Scenario on the Rate and Magnitude Content of Injection-Induced Seismicity: Case of a Heterogeneous Fault. *Journal of geophysical Research: Solid Earth*, **124** (cit. on pp. 45, 139).
- Aochi, H., B. Poisson, R. Toussaint, X. Rachez and J. Schmittbuhl, 2014. Self-induced seismicity due to fluid circulation along faults. *Geophys. J. Int.* **196**, 1544–1563 (cit. on pp. 41, 52, 75).
- Atkinson, G., D. Eaton, H. Ghofrani, D. Walker, B. Cheadle, R. Schultz, R. Shcherbakov, K. Tiampo, J. Gu, R. Harrington, Y. Liu, M. van der Baan and H. Kao, 2016. Hydraulic Fracturing and Seismicity in the Western Canada Sedimentary Basin. *Seismological Research Letters*, **87**(3) (cit. on pp. 5, 12, 16, 25, 26, 147).
- Auradou, H., G. Drazer, J. Hulin and J. Koplik, 2005. Permeability anisotropy induced by the sheardisplacement of rough fracture walls. *Water Resources Reserach*, **41**, W09423 (cit. on pp. 138, 140).
- Axelsson, G., 2006. Stimulation of geothermal wells in basaltic rock in Iceland (cit. on pp. 4, 12).
- Azad, M., D. Garagash and M Satish, 2017. Nucleation of dynamic slip on a hydraulically fractured fault. *Journal of Geophysical Research: Solid Earth*, **122**, 2812–2830 (cit. on pp. 39, 43, 53, 76).
- Bachmann, C., S. Wiemer, J. Woesnner and S. Hainzl, 2011. Statistical analysis of the induced Basel 2006 earthquake sequence: introducing a probability-based monitoring approach for Enhanced Geothermal Systems. *Geophys. J. Int.* **186**, 793–807 (cit. on p. 51).
- Baghbanan, A. and L. Jing, 2008. Stress effects on permeability in a fractured rock mass with correlated fracture length and aperture. *International Journal of Rock Mechanics and Mining Sciences*, **45**, 1320–1334 (cit. on pp. 35, 44, 79, 109, 135, 147).
- Baisch, S., R. Voros, E. Rothert, H. Stang, R. Jung and R. Schellschmidt, 2010. A numerical model for fluid injection induced seismicity at Soultz-sous-Forets. *International Journal of Rock Mechanics & Mining Sciences*, **47**, 405–413 (cit. on pp. 40, 52, 78).
- Baisch, S., C. Koch and A. Muntendam-Bos, 2019. Traffic Light Systems: To What Extent Can Induced Seismicity Be Controlled? *Seismological Research Letters*, **90**(3), 1145 (cit. on p. 26).
- Bandis, S. C., A. Lumsden and N. R. Barton, 1983. Fundamentals of Rock Joint Deformation. *Int. J. Rock Mech. Min. Sci. & Geomech.* **20**(6), 249–268 (cit. on p. 136).
- Barbour, A., J. Norbeck and J. Rubinstein, 2017. The Effects of Varying Injection Rates in Osage County, Oklahoma, on the 2016 Mw 5.8 Pawnee Earthquake. *Seismological Research Letters*, **88**(4) (cit. on pp. 39, 43, 53).

- Barnhart, W., H. Benz, G. Hayes, J. Rubinstein and E. Bergman, 2014. Seismological and geodetic constraints on the 2011 Mw5.3 Trinidad, Colorado earthquake and induced deformation in the Raton Basin. *J. Geophys. Res. Solid Earth*, **119**, 7923–7933 (cit. on p. 16).
- Bateman, B., 2014. SA earthquake was mine-related. *EWN* (cit. on p. 3).
- Baumgartner, J., 2012. Insheim and Landau: Recent Experiences with Egs Technology in the Urg, (cit. on p. 14).
- BCOGC, 2012. Investigation of Observed Seismicity in the Horn River Basin. Tech. Rep. (Cit. on pp. 12, 16).
- Bhattacharya, P. and R. Viesca, 2019. Fluid induced aseismic fault slip outpaces pore fluid migration. *Science*, **364**, 464–468 (cit. on pp. 31, 44, 109, 135, 148).
- Bjornsson, G., 2004. Reservoir conditions at 3-6 Km depth in the Hellisheidi geothermal field, SW - Iceland, estimated by deep drilling, cold water injection and seismic monitoring (cit. on pp. 4, 12).
- Bommer, J., S. Oates, J. Cepeda, C. Lindholm, J. Bird, R. Torres, G. Marroquin and J. Rivas, 2006. Control of hazard due to seismicity induced by a hot fractured rock geothermal project. *Engineering geology*, **83**, 287–306 (cit. on pp. 24, 25).
- Bonnemann, C., B. Schmidt, J. Ritter, N. Gestermann, T. Plenefisch and U. Wegler, 2010. Das seismische Ereignis bei Landau vom 15. August 2009. Tech. rep. Abschlussbericht der Expertengruppe “Seismisches Risiko bei hydrothermaler Geothermie”. (Cit. on p. 14).
- Bourne, S., S. Oates, T. van Elk and D. Doornhof, 2014. A seismological model for earthquakes induced by fluid extraction from a subsurface reservoir. *J. Geophys. Res.: Solid Earth*, **119**, 8991–9015 (cit. on p. 13).
- Bourouis, S. and P. Bernard, 2007. Evidence for coupled seismic and aseismic fault slip during water injection in the geothermal site of Soultz (France), and implications for seismogenic transients. *Geophys. J. Int.*, **169**, 723–732 (cit. on pp. 3, 22, 78, 92, 149).
- Bradley, H., 1987. *PETroleum engineering handbook* (cit. on p. 137).
- Brossier, R., 2011. Two-dimensional frequency-domain visco-elastic full waveform inversion: Parallel algorithms, optimization and performance. *Computers & Geosciences*, **37**, 444–455 (cit. on p. 134).
- Brown, W. and C. Frohlich, 2013. Investigating the cause of the 17 May 2012 M 4.8 earthquake near Timpson, east Texas. *Seismological Research Letters*, **84**, 374 (cit. on p. 16).
- Burridge, R. and L. Knopoff, 1967. Model and Theoretical Seismicity. *Bulletin of the Seismological Society of America*, **57**(3), 341–371 (cit. on p. 40).
- Byerlee, J., 1978. Friction of Rocks. *Pageoph*, Vol. 116 (cit. on pp. 27, 28, 52).
- Calo, M., C. Dorbath, F. Cornet and N. Cuenot, 2011. Large-scale aseismic motion identified through 4-D P-wave tomography. *Geophys. J. Int.* **186**, 1295–1314 (cit. on p. 22).
- Cappa, F. and J. Rutqvist, 2011a. Impact of CO₂ geological sequestration on the nucleation of earthquakes. *Geophysical Research Letters*, **38**, L17313 (cit. on p. 41).
- 2011b. Modeling of coupled deformation and permeability evolution during fault reactivation induced by deep underground injection of CO₂. *International Journal of Greenhouse Gas Control*, **5**, 336–346 (cit. on p. 41).
- 2012. Seismic rupture and ground accelerations induced by CO₂ injection in the shallow crust. *Geophys. J. Int.* **190**, 1784–1789 (cit. on p. 41).
- Cappa, F., Y. Guglielmi, C. Nussbaum and J. Birkholzer, 2018. On the Relationship Between Fault Permeability Increases, Induced Stress Perturbation, and the Growth of Aseismic Slip During Fluid Injection. *Geophys. Res. Lett.* **45** (cit. on pp. 41, 92).
- Cappa, F., M. Scuderi, C. Collettini, Y. Guglielmi and J.-P. Avouac, 2019. Stabilization of fault slip by fluid injection in the laboratory and in situ. *Science Advances - Geophysics*, **5** (cit. on p. 35).

-
- Chang, K. and P. Segall, 2016. Injection-induced seismicity on basement faults including poroelastic stressing. *J. Geophys. Res.: Solid Earth*, **121**, 2708–2726 (cit. on p. 39).
- Chang, K., H. Yoon and M. J. Martinez, 2018. Seismicity Rate Surge on Faults after Shut-in: Poroelastic Response to Fluid Injection. *Bulletin of the Seismological Society of America*, **108**(No. 4), 1889–1904 (cit. on pp. 39, 53).
- Chavent, G., 1991. On the theory and practice of non-linear least-squares. *Adv. Water Resources*, **14**(2), 55 (cit. on p. 117).
- Chen, Z., S. Narayan, Z. Yang and S. Rahman, 2000a. An experimental investigation of hydraulic behaviour of fractures and joints in granitic rock. *International Journal of Rock Mechanics & Mining Sciences*, **37**, 1061–1071 (cit. on pp. 35, 109).
- Chen, Z., S. P. Narayan, Z. Yang and S. Rahman, 2000b. An experimental investigation of hydraulic behaviour of fractures and joints in granitic rock. *International Journal of Rock Mechanics and Mining Sciences*, **37**, 1061–1071 (cit. on p. 137).
- Choy, G., J. Rubinstein, W. Yeck, D. McNamara, C. Mueller and O. Boyd, 2016. A Rare Moderate-Sized (Mw 4.9) Earthquake in Kansas: Rupture Process of the Milan, Kansas, Earthquake of 12 November 2014 and Its Relationship to Fluid Injection. *Seismological Research Letters*, **87**, 1–9 (cit. on p. 10).
- Clarke, H., L. Eisner, P. Styles and P. Turner, 2014. Felt seismicity associated with shale gas hydraulic fracturing: The first documented example in Europe. *Geophys. Res. Lett.* **41** (cit. on pp. 12, 13).
- Cochard, A. and J. Rice, 1997. A spectral method for numerical elastodynamic fracture analysis without spatial replication of the rupture event. *J. Mech. Phys. Solids*, Vol. 45, No. 8, 1393–1418 (cit. on p. 57).
- Cornet, F., 2016. Seismic and aseismic motions generated by fluid injections. *Geomechanics for Energy and the Environment*, **5**, 42–54 (cit. on pp. 3, 22, 24, 149).
- Cornet, F., J. Helm, H. Poitrenaud and A. Etchecopar, 1997. Seismic and Aseismic Slips Induced by Large-scale Fluid Injections. *Pure and Applied Geophysics*, 563–583 (cit. on pp. 13, 22).
- Darcy, H., 1857. *Recherches experimentales relatives au mouvement de l'eau dans le tuyaux*. Ecole Imperiale Polytechnique. Mallet - Bachelier (cit. on p. 109).
- Davis, S. and C. Frohlich, 1993. Did (or will) fluid injection cause earthquakes? Criteria for a rational assessment. *Seismological Research Letters*, Volume 64, No. 3-4 (cit. on pp. 3, 5, 6, 16, 51).
- Davis, S. and W. Pennington, 1989. Induced seismic deformation in the Cogdell oil field of west Texas. *Bulletin of the Seismological Society of America*, **79**(5), 1477–1495 (cit. on pp. 5, 8, 15).
- De Barros, L., G. Daniel, Y. Guglielmi, D. Rivet, H. Caron, X. Payre, G. Bergery, P. Henry, R. Castilla, P. Dick, E. Barbieri and M. Gourlay, 2016. Fault structure, stress, or pressure control of the seismicity in shale? Insights from a controlled experiment of fluid-induced fault reactivation. *J. Geophys. Res.: Solid Earth*, **121**, 4506–4522 (cit. on p. 91).
- De Barros, L., Y. Guglielmi, D. Rivet, F. Cappa and L. Duboeuf, 2018. Seismicity and fault aseismic deformation caused by fluid injection in decametric in-situ experiments. *Compte Rendus Geoscience - Internal Geophysics (Seismology)* (cit. on pp. 4, 24, 31, 33, 109, 149).
- Deichman, N. and D. Giardini, 2009. Earthquakes Induced by the Stimulation of an Enhanced Geothermal System below Basel (Switzerland). *Seismological Research Letters*, Vol. 80, N. 5, 784–798 (cit. on pp. 4, 14, 16, 17, 25, 26, 51, 78, 148).
- Dempsey, D. and J. Riffault, 2019. Response of Induced Seismicity to Injection Rate Reduction: Models of Delay, Decay, Quiescence, Recovery, and Oklahoma. *Water Resources Research*, **55**, 656–681 (cit. on pp. 40, 43, 52).

- Dempsey, D. and J. Suckale, 2016. Collective properties of injection-induced earthquake sequences: 1. Model description and directivity bias. *J. Geophys. Res.: Solid Earth*, **121**, 3609–3637 (cit. on p. 38).
- Dempsey, D., J. Suckale and Y. Huang, 2016. Collective properties of injection-induced earthquake sequences: 2. Spatiotemporal evolution and magnitude frequency distributions. *J. Geophys. Res.: Solid Earth*, **121**, 3638–3665 (cit. on p. 38).
- Diehl, T., T. Kraft, E. Kissling and S. Wiemer, 2017. The induced earthquake sequence related to the St. Gallen deep geothermal project (Switzerland): Fault reactivation and fluid interactions imaged by microseismicity. *Journal of Geophysical Research: Solid Earth*, **122** (cit. on p. 4).
- Dietrich, J., 1972. Time-Dependent Friction in Rock. *J. Geophys. Res. Vol. 77*(20), 3690–3697 (cit. on pp. 39, 44, 147).
- 1979. Modeling of rock friction. 1. Experimental results and constitutive equations. *Journal of geophysical Research*, **84**(B5), 2161–2168 (cit. on pp. 52–54).
 - 1992. Earthquake nucleation on faults with rate- and state-dependent strength. *Tectonophysics*, **211**, 115–134 (cit. on p. 91).
 - 1994. A constitutive law for rate of earthquake production and its application to earthquake clustering. *Journal of geophysical Research*, Vol. 99, No. B2, 2601–2618 (cit. on pp. v, vii, 36, 39, 43, 46, 50, 53, 67, 77, 79, 81, 102, 168).
- Dietrich, J., K. Richards-Dinger and K. Kroll, 2015. Modeling Injection-Induced Seismicity with the Physics-Based Earthquake Simulator RSQSim. *Seismological Research Letters*, **86**(4) (cit. on pp. 41, 78, 148).
- Dorbath, L., N. Cuenot, A. Genter and M. Frogneux, 2009. Seismic response of the fractured and faulted granite of Soultz-sous-Forets (France) to 5 km deep massive water injection. *Geophys. J. Int.* **177**, 653–675 (cit. on pp. 4, 13, 15, 17, 43, 91, 102).
- Dublanchet, P., 2018. The dynamics of earthquake precursors controlled by effective friction. *Geophys. J. Int.* **212**(2), 853–871 (cit. on pp. 44, 46, 53, 55, 147).
- 2019. Fluid driven shear cracks on a strengthening rate-and-state frictional fault. *Journal of the Mechanics and Physics of Solids*, **132**, 103672 (cit. on pp. 41–43, 92, 109).
- Dublanchet, P., P. Bernard and P. Favreau, 2013. Interactions and triggering in a 3-D rate-and-state asperity model. *J. Geophys. Res.*, Vol. 118, 2225–2245 (cit. on pp. 90, 92, 93, 149).
- Duboeuf, L., L. De Barros, F. Cappa, Y. Guglielmi, A. Deschamps and S. Seguy, 2017. Aseismic Motions Drive a Sparse Seismicity During Fluid Injections Into a Fractured Zone in a Carbonate Reservoir. *J. Geophys. Res.: Solid Earth*, **122** (cit. on pp. 3, 24, 31, 44, 109, 148, 149).
- Edwards, B., T. Kraft, C. Cauzzi, P. Kastli and S. Wiemer, 2015. Seismic monitoring and analysis of deep geothermal projects in St Gallen and Basel, Switzerland. *Geophys. J. Int. - Seismology*, **201**, 1022–1039 (cit. on p. 16).
- Ellsworth, W., 2013. Injection-Induced earthquakes. *Science*, **341**(6142), 1225942 (cit. on pp. 3, 4, 9, 21, 27, 51, 147).
- Engeser, B., 1996. KTB Report 95-3, Dus kontinentale tiej- bohrprogramim der Bundesrepublik Deutschland, Bohrtechnische Dokumentation, Niedersachsisches Landesamt fur Bodenforschung, Hannover. Tech. rep. (cit. on p. 37).
- Engl, H. W., M. Hanke and A. Neubauer, 2000. Regularization of Inverse Problems. Vol. 35. Kluwer Academic Publishers (cit. on p. 134).
- Esaki, T., S. Du, Y. Mitani, K. Ikusuda and L. Jing, 1999. Development of a shear-flow test apparatus and determination of coupled properties for a single rock joint. *International Journal of Rock Mechanics & Mining Sciences*, **36**(5), 641–650 (cit. on p. 135).
- Evans, D., 1966. The Denver Area Earthquakes and The Rocky Mountain Arsenal Disposal Well. *The Mountain Geologist*, **3** (cit. on p. 7).

-
- Evans, K., Z. A., T. Kraft, N. Deichman and F. Moia, 2012. A survey of the induced seismic response to fluid injection in geothermal and CO₂ reservoirs in Europe. *Geothermics*, **41**, 30–54 (cit. on pp. 4, 12, 14).
- Fagereng, A. and R. Sibson, 2010. Melange rheology and seismic style. *Geology*, **38**(8), 751–754 (cit. on pp. 43, 92).
- Farahbod, A., H. Kao, D. Walker and J. Cassidy, 2015. Investigation of regional seismicity before and after hydraulic fracturing in the Horn River Basin, northeast British Columbia. *Canadian Journal of Earth Sciences*, **52**(2) (cit. on pp. 5, 12, 16).
- Fehlberg, E., 1969. Low-order classical Runge-Kutta formulas with step size control and their application to some heat transfer problems. Nasa Technical Report. Nasa (cit. on p. 57).
- Fisher, A. and G. Zwart, 1996. Relation between permeability and effective stress along a plate-boundary fault, Barbados accretionary complex. *Geology*, **24**(4), 307–310 (cit. on pp. 35, 79, 109, 135).
- French, M., W. Zhu and J. Banker, 2016. Fault slip controlled by stress path and fluid pressurization rate. *Geophysical Research Letters*, **43**, 4330–4339 (cit. on p. 33).
- Friberg, P., G. Besana-Ostman and I. Dricker, 2014. Characterization of an earthquake sequence triggered by hydraulic fracturing in Harrison County, Ohio. *Seismological Research Letters*, **85**, 1295–1307 (cit. on p. 11).
- Frohlich, C., 2012. Two-year survey comparing earthquake activity and injection-well locations in the Barnett Shale, Texas (cit. on pp. 9, 38, 52).
- Frohlich, C., C. Hayward, B. Stump and E. Potter, 2011. The Dallas-Fort Worth Earthquake Sequence: October 2008 through May 2009. *Bulletin of the Seismological Society of America*, **101**(No. 1), 327–340 (cit. on pp. 8, 16).
- Frohlich, C., W. Ellsworth, W. Brown, M. Brunt, J. Luetgert, T. MacDonald and S. Walter, 2014. The 17 May 2012 M4.8 earthquake near Timpson, East Texas: An event possibly triggered by fluid injection. *Journal of geophysical Research: Solid Earth*, **119** (cit. on pp. 4, 16, 51).
- Galis, M., J.-P. Ampuero, P. Mai and F. Cappa, 2017. Induced seismicity provides insight into why earthquake ruptures stop. *Science Advances - Geophysics*, **3** (cit. on pp. 38, 43, 109).
- Gan, W. and C. Frohlich, 2013. Gas injection may have triggered earthquakes in the Cogdell oil field, Texas. *PNAS*, **110**(47), 18786–18791 (cit. on pp. 5, 8, 16).
- Garagash, D. and L. Germanovich, 2012. Nucleation and arrest of dynamic slip on a pressurized fault. *Journal of geophysical Research*, **117**(B10310) (cit. on pp. 39, 43, 53, 76, 109).
- Gaucher, E., M. Schoenball, O. Heidbach, A. Zang, P. Fokker, J.-D. van Wees and T. Kohl, 2015a. Induced seismicity in geothermal reservoirs: A review of forecasting approaches. *Renewable and Sustainable Energy Reviews*, **52**, 1473–1490 (cit. on p. 25).
- 2015b. Induced Seismicity in Geothermal Reservoirs: Physical Processes and Key Parameters (cit. on p. 14).
- Gerstenberger, M., S. Wiemer and D. Giardini, 2001. A systematic test of the hypothesis that the b value varies with depth in California. *Geophys. Res. Lett.* **28**(1), 57–60 (cit. on p. 77).
- Ghabezloo, S., J. Sulem, S. Guedon and F. Martineau, 2009. Effective stress law for the permeability of a limestone. *International Journal of Rock Mechanics and Mining Sciences*, **46**, 297–306 (cit. on pp. 35, 44, 79, 109, 135, 136, 147).
- Gibbs, J., J. Healy, C. Raleigh and J. Coakley, 1973. Seismicity in the Rangely, Colorado, area: 1962–1970. *Bulletin of the Seismological Society of America*, **63**, 1557–1570 (cit. on pp. 22, 42).
- Gibowicz, S., 1984. Seismicity induced by surface mining: the Belchatow, Poland, earthquake of 29 November 1980. *International Journal of Rock Mechanics and Mining Sciences & Geomechanics*, **21**(1) (cit. on p. 3).
- 2009. Chapter 1 - Seismicity Induced by Mining: Recent Research, in *Advances in Geophysics*. *Advances in Geophysics*, **51**, 1–53 (cit. on p. 3).

- Goebel, T., J. Haffner and X. Chen, 2016a. Statistical seismicity analysis methods for the detection of fault activation during fluid injection (cit. on pp. 4, 6, 7, 9, 19, 20).
- Goebel, T., S. Hosseini, F. Cappa, E. Hauksson, J.-P. Ampuero, F. Aminzadeh and J. Saleeby, 2016b. Wastewater disposal and earthquake swarm activity at the southern end of the Central Valley, California. *Geophysical Research Letters*, **43**, 1092–1099 (cit. on pp. 5, 11, 16, 19, 20, 147).
- Goodfellow, S., M. Nasser, S. Maxwell and R. Young, 2015. Hydraulic fracture energy budget: Insights from the laboratory. *Geophys. Res. Lett.*, **42**, 3179–3187 (cit. on pp. 33, 34).
- Green, C., P. Styles and B. Baptie, 2012. Preese Hall Shale Gas Fracturing: Review & recommendations for induced seismic mitigation. Tech. rep. (cit. on p. 5).
- Grigoli, F., S. Cesca, E. Priolo, A. Rinaldi, J. Clinton, T. Stabile, B. Dost, M. Fernandez, S. Wiemer and T. Dahm, 2017. Current challenges in monitoring, discrimination, and management of induced seismicity related to underground industrial activities: A European perspective. *Review of Geophysics*, **55**, 310–340 (cit. on pp. 25, 29).
- Grigoli, F., S. Cesca, A. Rinaldi, A. Manconi, J. Lopez-Comino, J. Clinton, R. Westaway, C. Cauzzi, T. Dahm and S. Wiemer, 2018. The November 2017 Mw 5.5 Pohang earthquake: A possible case of induced seismicity in South Korea. *Science*, **360**, 1003–1006 (cit. on pp. 3, 5, 14, 16, 20, 26).
- Guglielmi, Y., D. Elsworth, F. Cappa, P. Henry, C. Gout, P. Dick and J. Durand, 2015a. In situ observations on the coupling between hydraulic diffusivity and displacements during fault reactivation in shales. *J. Geophys. Res.: Solid Earth*, **120**, 7729–7748 (cit. on pp. 31, 109, 135).
- Guglielmi, Y., F. Cappa, J.-P. Avouac, P. Henry and D. Elsworth, 2015b. Seismicity triggered by fluid injection–induced aseismic slip. *Science*, **348**, 1224–1226 (cit. on pp. 3, 24, 31, 32, 34, 44, 109, 137, 148, 149).
- Gupta, H., 2002. A review of recent studies of triggered earthquakes by artificial water reservoirs with special emphasis on earthquakes in Koyna, India. *Earth-Science Reviews*, **58**, 279–310 (cit. on p. 3).
- Gutenberg, B. and C. Richter, 1949. *Seismicity of the earth and associated phenomena*. Princeton University Press, (cit. on p. 91).
- 1954. *Seismicity of the Earth*. 2nd edition. Princeton Univ. Press (cit. on pp. 7, 19).
- Gutierrez, M., L. Øino and R. Nygard, 2000. Stress-dependent permeability of a de-mineralised fracture in shale. *Marine and Petroleum Geology*, **17**, 895–907 (cit. on pp. 35, 109).
- Hanks, T. and H. Kanamori, 1979. A Moment Magnitude Scale. *J. Geophys. Res.* **84**(B5) (cit. on p. 59).
- Haring, M., U. Schanz, F. Ladner and B. Dyer, 2008. Characterisation of the Basel 1 enhanced geothermal system. *Geothermics*, **37**, 469–495 (cit. on pp. 17, 25, 148).
- Hastings, W., 1970. Monte Carlo sampling methods using Markov chains and their applications. *Biometrika*, **57**(1), 97 (cit. on pp. 44, 45, 122, 148).
- Healy, J., W. Rubey, D. Griggs and C. Raleigh, 1968. Disposal of waste fluids by injection into a deep well has triggered earthquakes near Denver, Colorado. *Science*, **161**(3848), 1301–1310 (cit. on pp. 3, 7, 15, 16, 18, 27, 30, 31, 51, 52, 109).
- Hermann, R., S.-K. Park and C.-Y. Wang, 1981. The denver earthquakes of 1967–1968. *Bulletin of the Seismological Society of America*, **71**(3), 731–745 (cit. on pp. 7, 18, 51, 109).
- Hofmann, H., G. Zimmerman, M. Farkas, E. Huenges, A. Zang, M. Leonhardt, G. Kwiatek, P. Martinez-Garzon, M. Bohnhoff, K. Min, P. Fokker, R. Westaway, F. Bethmann, P. Meier, K.-S. Yoon, J.-W. Choi, T.-J. Lee and K.-Y. Kim, 2019. First field application of cyclic soft stimulation at the Pohang Enhanced Geothermal System site in Korea. *Geophys. J. Int. - Seismology*, **217**, 926–949 (cit. on p. 25).

-
- Holland, A., 2011. Examination of Possibly Induced Seismicity from Hydraulic Fracturing in the Eola Field, Garvin County, Oklahoma. Oklahoma Geological Survey Open-File Report OF1-2011 (cit. on pp. 5, 51).
- 2013. Earthquakes Triggered by Hydraulic Fracturing in South Central Oklahoma. Bulletin of the Seismological Society of America, **103**(3), 1784–1792 (cit. on pp. 10, 15).
- Horton, S., 2012. Disposal of Hydrofracking Waste Fluid by Injection into Subsurface Aquifers Triggers Earthquake Swarm in Central Arkansas with Potential for Damaging Earthquake. Seismological Research Letters, Vol. 83, N°2 (cit. on pp. 4, 11, 16, 51).
- Hsieh, P. and J. Bredehoeft, 1981. A reservoir analysis of the Denver earthquakes: A case of induced seismicity. J. Geophys. Res. **86**(No. B2), 903–920 (cit. on pp. 15, 18, 28, 109, 148).
- Hubert, M and W. Rubey, 1959. Mechanics of fluid-filled porous solids and its application to overthrust faulting. Bull. Geol. Soc. Am. **70**, 115–166 (cit. on pp. 27, 52).
- Hummel, N. and T. Muller, 2009. Microseismic signatures of non-linear pore-fluid pressure diffusion. Geophys. J. Int. **179**, 1558–1565 (cit. on p. 38).
- Ide, S. and H. Aochi, 2005. Earthquakes as multiscale dynamic ruptures with heterogeneous fracture surface energy. J. Geophys. Res. **110** (cit. on p. 56).
- Ikari, M., D. Saffer and C. Marone, 2009. Frictional and hydrologic properties of a major splay fault system, Nankai subduction zone. Geophysical Research Letters, **36**, L20313 (cit. on p. 56).
- Im, K., D. Elsworth and Y. Fang, 2018. The influence of Preslip Sealing on the Permeability Evolution of Fractures and Faults. Geophys. Res. Lett. **45**, 166–175 (cit. on pp. 35, 109).
- Jaeger, J., N. Cook and R. Zimmerman, 2007. Fundamentals of Rock Mechanics. Blackwell Publishing (cit. on pp. 56, 60, 135, 137).
- Jarny, Y., M. Ozisik and J. Bardon, 1991. A general optimization method using adjoint equation for solving multidimensional inverse heat conduction. Int. J. Heat Mass Transfer, **134**(11), 2911–2919 (cit. on p. 117).
- Johann, L., S. Shapiro and C. Dinske, 2018. The surge of earthquakes in Central Oklahoma has features of reservoir-induced seismicity. Nature - Scientific Reports (cit. on p. 9).
- Kaltenbacher, B., A. Neubauer and O. Scherzer, 2008. Iterative Resingularization Methods for nonlinear problems. de Gruyter (cit. on p. 134).
- Kanamori, H., 1977. The Energy Release in Great Earthquake. J. Geophys. Res., Vol. 82, No. 20 (cit. on p. 3).
- Kanamori, H. and E. Hauksson, 1992. A slow earthquake in the Santa Maria basin, California. Bulletin of the Seismological Society of America, **85**(2), 2087–2096 (cit. on pp. 5, 51).
- Kelley, C., 1999. Iterative Methods for Optimization. North Carolina State University (cit. on p. 134).
- Keranen, K. and M. Weingarten, 2018. Induced Seismicity. Annu. Rev. Earth Planet. Sci. **46**, 149–174 (cit. on pp. 3, 7, 8, 15, 22, 29, 147, 148).
- Keranen, K., H. Savage, G. ABEYS and E. Cochran, 2013. Potentially induced earthquakes in Oklahoma, USA: Links between wastewater injection and the 2011 Mw 5.7 earthquake sequence. Geology, **41**(6), 699–702 (cit. on pp. 3, 4, 9, 16, 51, 52).
- Keranen, K., M. Weingarten, G. Abers, B. Bekins and S. Ge, 2014. Sharp increase in central Oklahoma seismicity since 2008 induced by massive wastewater injection. Science, **345**, 448–451 (cit. on pp. 4, 9, 18, 22, 28, 42).
- Kim, K.-H., J.-H. Ree, Y. Kim, S. Kim, S.-Y. Kang and W. Seo, 2018. Assessing whether the 2017 Mw 5.4 Pohang earthquake in South Korea was an induced event. Science, **360**, 1007–1009 (cit. on pp. 3, 5, 14–16, 26).
- Kim, W.-Y., 2013. Induced seismicity associated with fluid injection into a deep well in Youngstown, Ohio. J. Geophys. Res: Solid Earth, Vol. 118, 3506–3518 (cit. on pp. 11, 15, 16, 18, 22, 51, 78, 109, 148).

- Kozłowska, M., M. Brudzinski, P. Friberg, R. Skoumal, N. Baxter and B. Currie, 2018. Maturity of nearby faults influences seismic hazard from hydraulic fracturing. *PNAS*, E1720–E1729 (cit. on pp. 11, 15, 17–19, 28, 148).
- Kroll, K., K. Richards-Dinger and J. Dietrich, 2017. Sensitivity of Induced Seismic Sequences to Rate-and-State Frictional Processes. *Journal of Geophysical Research: Solid Earth*, **122**(10), 207–219 (cit. on pp. 41, 43, 53, 91, 102).
- Kwiatek, G., P. Martinez-Garzon, K. Plenkers, M. Leonhardt, A. Zang, S. von Specht, G. Dresen and M. Bohnhoff, 2018. Insights into complex subdecimeter fracturing processes occurring during a water injection experiment at depth in Aspö Hard Rock laboratory, Sweden. *J. Geophys. Res.: Solid Earth*, **123**, 6616–6635 (cit. on p. 32).
- Kwiatek, G., T. Saarno, T. Ader, F. Bluemle, M. Bohnhoff, M. Chendorain, G. Dresen, P. Heikkinen, I. Kukkonen, P. Leary, M. Leonhardt, P. Malin, P. Martinez-Garzon, K. Passmore, P. Passmore, S. Valenzuela and C. Wollin, 2019. Controlling fluid-induced seismicity during a 6.1-km-deep geothermal stimulation in Finland. *Science Advances*, **5** (cit. on pp. 14, 25, 26).
- Langenbruch, C. and S. Shapiro, 2010. Decay rate of fluid-induced seismicity after termination of reservoir stimulations. *Geophysics*, **75**(No. 6), MA53–MA62 (cit. on pp. 17, 38).
- Langenbruch, C. and M. Zoback, 2016. How will induced seismicity in Oklahoma respond to decreased salwater injection rates. *Science Advances - Seismology* (cit. on pp. 9, 22, 23, 42, 52).
- Langenbruch, C., M. Weingarten and M. Zoback, 2018. Physics-based forecasting of man-made earthquake hazards in Oklahoma and Kansas. *Nature Communications* (cit. on pp. 9, 22, 75).
- Lengline, O. and D. Marsan, 2009. Inferring the coseismic and postseismic stress changes caused by the 2004 Mw = 6 Parkfield earthquake from variations of recurrence times of microearthquakes. *J. Geophys. Res.*, **114**, B10303 (cit. on pp. 43, 92).
- Lengline, O., L. Lamourette, L. Vivin, N. Cuenot and J. Schmittbuhl, 2014. Fluid-induced earthquakes with variable stress drop. *J. Geophys. Res. Solid Earth*, **119**, 8900–8913 (cit. on p. 23).
- Lengline, O., M. Boubacar and J. Schmittbuhl, 2017. Seismicity related to the hydraulic stimulation of GRT1, Rittershoffen, France. *Geophys. J. Int.* **208**, 1704–1715 (cit. on pp. 4, 23, 24).
- Li, Z., F. Fortin, A. Nicolas, D. Deldicque and Y. Guéguen, 2019. Physical and Mechanical Properties of Thermally Cracked Andesite Under Pressure. *Rock Mechanics and Rock Engineering* (cit. on p. 111).
- Linker, M. and J. Dietrich, 1992. Effects of variable normal stress on rock friction: Observations and constitutive equations. *Journal of geophysical Research*, Vol. 97, No. B4, 4923–4940 (cit. on pp. 39, 44, 53, 54, 60, 81, 91, 94, 147).
- Llenos, A. and A. Michael, 2013. Modeling Earthquake Rate Changes in Oklahoma and Arkansas: Possible Signatures of Induced Seismicity. *Bulletin of the Seismological Society of America*, **103**(No. 5), 2850–2861 (cit. on p. 6).
- Majer, E., R. Baria, M. Stark, S. Oates, J. Bommer, B. Smith and H. Asanuma, 2007. Induced seismicity associated with Enhanced Geothermal Systems. *Geothermics*, **36**, 185–222 (cit. on pp. 4, 13, 15, 16, 18, 51, 147).
- Marone, C., 1998. Laboratory - derived friction laws and their application to seismic faulting. *Annu. Rev. Earth Planet. Sci.* 643–96 (cit. on pp. 55, 56, 60).
- McClure, M. and R. Horne, 2011. Investigation of injection-induced seismicity using a coupled fluid flow and rate/state friction model. *Geophysics*. Vol. 76, No. 6, WC181–WC198 (cit. on pp. 41, 43, 53, 78).
- 2014. Correlations between formation properties and induced seismicity during high pressure injection into granitic rock. *Engineering geology*, **175**, 74–80 (cit. on pp. 43, 91, 102).
- McGarr, A., 2014. Maximum magnitude earthquakes induced by fluid injection. *J. Geophys. Res.: Solid Earth*, **119**, 1008–1019 (cit. on pp. 3, 12, 19–21, 32, 43, 51).

-
- McGarr, A. and A. Barbour, 2017. Wastewater disposal and the earthquake sequences during 2016 near Fairview, Pawnee, and Cushing, Oklahoma: Induced earthquake sequences during 2016. *Geophys. Res. Lett.* **44** (cit. on pp. [9](#), [16](#)).
- McGarr, A., D. Simpson, L. Seeber and W. Lee, 2002. Case histories of induced and triggered seismicity. *International Geophysics Series*, **81**, 647–664 (cit. on p. [3](#)).
- McGarr, A., B. Bekins, N. Burkhardt, J. Dewey, P. Earle, W. Ellsworth, S. Ge, S. Hickman, A. Holland, E. Majer, J. Rubinstein and A. Sheehan, 2015. Coping with earthquakes induced by fluid injection. Hazard may be reduced by managing fluid injection activities. *Science*, **347**(6224), 830–831 (cit. on pp. [5](#), [9](#), [25](#), [26](#)).
- McKee, C., A. Bumb and R. Koelng, 1988. Stress-dependent permeability and porosity of coal and other geologic formations. *SPE Formation evaluation* (cit. on pp. [109](#), [135](#)).
- Metivier, L., R. Brossier, J. Virieux and S. Operto, 2013. Full Waveform Inversion and the truncated Newton method. *SIAM Journal on Scientific Computing, Society for Industrial and Applied Mathematics*, **35**(2) (cit. on p. [134](#)).
- Metropolis, N., A. Rosenbluth, M. Rosenbluth and A. Telles, 1953. Equation of State Calculations by Fast Computing Machines. *J. Chem. Phys.* **21**, 1087 (cit. on pp. [44](#), [45](#), [122](#), [148](#)).
- Mignan, A., M. Broccardo, S. Wiemer and D. Giardini, 2017. Induced seismicity closed-form traffic light system for actuarial decision-making during deep fluid injections. *Nature - Scientific Reports*, **7**, 13607 (cit. on p. [27](#)).
- Muntendam-Bos, A. and J. Waal, 2013. Reassessment of the probability of higher magnitude earthquakes in the Groningen gas field. Tech. rep. State Supervision of Mines (cit. on p. [13](#)).
- Nadeau, R. and L. Johnson, 1998. Seismological studies at parkfield vi : Moment release rates and estimates of source parameters for small repeating earthquakes. *Bulletin of the Seismological Society of America*, **88**(3), 790–814 (cit. on pp. [43](#), [92](#)).
- Nemoto, K., H. Moriya, H. Niitsuma and N. Tsuchiya, 2008. Mechanical and hydraulic coupling of injection-induced slip along pre-existing fractures. *Geothermics*, **37**, 157–172 (cit. on p. [33](#)).
- Norbeck, J. and J. Rubinstein, 2018. Hydromechanical Earthquake Nucleation Model Forecasts Onset, Peak, and Falling Rates of Induced Seismicity in Oklahoma and Kansas. *Geophys. Res. Lett.* **45**, 2963–2975 (cit. on pp. [9](#), [40](#)).
- Ohnaka, M., 2003. A constitutive scaling law and a unified comprehension for frictional slip failure, shear fracture of intact rock, and earthquake rupture. *J. Geophys. Res.* **108**(NO. B2), 2080 (cit. on p. [55](#)).
- Omori, F., 1894. On the Aftershocks of Earthquakes. *Journal of the College of Science, Imperial University of Tokyo*, **7**, 111–120 (cit. on p. [41](#)).
- Pacheco, P., 1997. Parallel Programming with MPI. Morgan Kaufmann (cit. on p. [46](#)).
- Passelegue, F., N. Brantut and T. Mitchell, 2018. Fault Reactivation by Fluid Injection: Controls From Stress State and Injection Rate. *Geophysical Research Letters*, **45**, 12837–12846 (cit. on pp. [34](#), [139](#)).
- Passelegue, F., M. Almakari, P. Dublanchet, F. Darras and M. Violay, 2020. On the Nature of Fault Slip: From the Field to the Lab. *Nature* (Submitted manuscript) (cit. on p. [150](#)).
- Plessix, R.-E., 2006. A review of the adjoint-state method for computing the gradient of a functional with geophysical applications. *Geophys. J. Int.* **167**, 495–503 (cit. on pp. [44](#), [45](#), [110](#), [118](#), [148](#)).
- Raleigh, C., J. Healy and J. Bredehoeft, 1976. An Experiment in Earthquake Control at Rangely, Colorado. *Science*, **191**, 1230–1237 (cit. on pp. [21](#), [23](#), [30](#), [42](#), [52](#), [76](#)).
- Rice, J., 1993. Spatio-temporal complexity of slip on a fault. *J. geophys. Res.* **98**(B6), 9885–9907 (cit. on pp. [57](#), [60](#)).
- Rice, J. and A. Ruina, 1983. Stability of steady frictional slipping. *Journal of Applied Mechanics*, Vol. 50, 343–349 (cit. on pp. [39](#), [44](#), [54](#), [147](#)).

- Robert, C. and G. Casilla, 2004. Monte Carlo Statistical Methods. Springer (cit. on p. 110).
- Romanet, P., H. Bhat, R. Jolivet and R. Madariaga, 2018. Fast and slow slip events emerge due to fault geometrical complexity. *Geophys. Res. Lett.* **45**, 4809–4819 (cit. on p. 148).
- Rubin, A. and J.-P. Ampuero, 2005. Earthquake nucleation on (aging) rate and state faults. *J. Geophys. Res.*, Vol. 110, B11312 (cit. on pp. 46, 55–58, 60, 91, 93, 102).
- Rubinstein, J. and A. Mahani, 2015. Myths and Facts on Waste Water Injection, Hydraulic Fracturing, Enhanced Oil Recovery, and Induced Seismicity. *Seismological Research Letters*, **86**(4) (cit. on pp. 4, 18).
- Rubinstein, J., W. Ellsworth and A. McGarr, 2012. The 2001 present triggered seismicity sequence in the Raton Basin of southern Colorado/northern New Mexico (cit. on pp. 16, 51).
- Rubinstein, J., W. Ellsworth and S. Dougherty, 2018. The 2013–2016 Induced Earthquakes in Harper and Sumner Counties, Southern Kansas. *Bulletin of the Seismological Society of America*, **108**(No. 2), 674–689 (cit. on pp. 10, 18, 22).
- Rubinstein, L., W. Ellsworth, A. McGarr and H. Benz, 2014. The 2001–Present Induced Earthquake Sequence in the Raton Basin of Northern New Mexico and Southern Colorado. *Bulletin of the Seismological Society of America*, **104**(No. 5) (cit. on p. 4).
- Ruina, A., 1983. Slip instability and state variable friction laws. *J. Geophys. Res.* **88**(B12), 10359–10370 (cit. on pp. 52–54, 91).
- Rutqvist, J., A. Rinaldi, F. Cappa, P. Jeanne, A. Mazzoldi, L. Urpi, Y. Guglielmi and V. Vilarrasa, 2016. Fault activation and induced seismicity in geological carbon storage e Lessons learned from recent modeling studies. *Journal of Rock Mechanics and Geotechnical Engineering*, **8**, 789–804 (cit. on p. 5).
- Rutqvist, J., A. Rinaldi, F. Cappa and G. Moridis, 2013. Modeling of fault reactivation and induced seismicity during hydraulic fracturing of shale-gas reservoirs. *Journal of Petroleum Science and Engineering*, **107**, 31–44 (cit. on p. 53).
- Rutter, E. and A. Hackston, 2017. On the effective stress law for rock-on-rock frictional sliding, and fault slip triggered by means of fluid injection. *Philosophical Transactions of the Royal Society A*, **375** (cit. on p. 33).
- Rutter, E. and J. Mecklenburgh, 2018. Influence of Normal and Shear Stress on the Hydraulic Transmissivity of Thin Cracks in a Tight Quartz Sandstone, a Granite, and a Shale. *Journal of Geophysical Research: Solid Earth*, **123**, 1262–1285 (cit. on pp. 35, 44, 79, 109, 147).
- Schoenball, M. and W. Ellsworth, 2017. A Systematic Assessment of the Spatiotemporal Evolution of Fault Activation Through Induced Seismicity in Oklahoma and Southern Kansas. *J. Geophys. Res.: Solid Earth*, **122**, 10189–10206 (cit. on pp. 9, 18, 38, 91).
- Schoenball, M., T. Muller, B. Muller and O. Heibach, 2010. Fluid-induced microseismicity in pre-stressed rock masses. *Geophys. J. Int.* **180**, 813–819 (cit. on p. 38).
- Schoenball, M., L. Dorbath, E. Gaucher, J. Wellman and T. Kohl, 2014. Change of stress regime during geothermal reservoir stimulation. *Geophys. Res. Lett.* **41**, 1163–1170 (cit. on p. 23).
- Schoenball, M., N. Davatzes and J. Glen, 2015. Differentiating induced and natural seismicity using space-time-magnitude statistics applied to the Coso Geothermal field. *Geophys. Res. Lett.* **42**, 6221–6228 (cit. on pp. 7, 19, 20).
- Schoenball, M., F. Walsh, M. Weingarten and W. Ellsworth, 2018. How faults wake up: The Guthrie-Langston, Oklahoma earthquakes. *The Leading Edge* (cit. on pp. 9, 15).
- Scholz, C., 1968. The Frequency-Magnitude Relation of Microfracturing in Rock and its Relation to Earthquakes. *Bulletin of the Seismological Society of America*, **58**(1), 399–415 (cit. on p. 77).
- 2015. On the stress dependence of the earthquake b value. *Geophys. Res. Lett.* **42**, 1399–1402 (cit. on pp. 77, 78).

-
- Schultz, R., R. Wang, Y. Gu, K. Haug and G. Atkinson, 2017. A seismological overview of the induced earthquakes in the Duvernay play near Fox Creek, Alberta. *J. Geophys. Res.: Solid Earth*, **122**, 492–505 (cit. on pp. 25, 26).
- Scuderi, M., C. Collettini and C. Marone, 2017. Frictional stability and earthquake triggering during fluid pressure stimulation of an experimental fault. *Earth and Planetary Science Letters*, **477**, 84–96 (cit. on p. 33).
- Segall, P., 1989. Earthquakes triggered by fluid extraction. *Geology*, **17**, 942–946 (cit. on p. 28).
- Segall, P. and S. Lu, 2015. Injection-induced seismicity: Poroelastic and earthquake nucleation effects. *J. Geophys. Res. : Solid Earth*, Vol. 120, 5082–5103 (cit. on pp. 39, 53).
- Shapiro, A., J. Kummerow, C. Dinske, G. Asch, E. Rothert, J. Erzinger, H. Kumpel and R. Kind, 2006. Fluid induced seismicity guided by a continental fault: Injection experiment of 2004/2005 at the German Deep Drilling Site (KTB). *Geophys. Res. Lett.* **33**, L01309 (cit. on p. 30).
- Shapiro, S. and C. Dinske, 2009. Fluid-induced seismicity: Pressure diffusion and hydraulic fracturing. *Geophysical Prospecting*, **57**, 301–310 (cit. on pp. 9, 37, 38).
- Shapiro, S., E. Huenges and G. Borm, 1997. Estimating the crust permeability from fluid-injection-induced seismic emission at the KTB site. *Geophys. J. Int.* **131** (cit. on pp. 18, 19, 30, 36, 109).
- Shapiro, S., E. Rothert, V. Rath and J. Rindschwentner, 2002. Characterization of fluid transport properties of reservoirs using induced microseismicity. *Geophysics*, **67**(No. 1), 212–220 (cit. on pp. 18, 37, 109).
- Shapiro, S., C. Dinske and J. Kummerow, 2007. Probability of a given-magnitude earthquake induced by a fluid injection. *Geophys. Res. Lett.* **34**, L22314 (cit. on pp. 19, 21, 43).
- Shapiro, S., C. Dinske and C. Langenbruch, 2010. Seismogenic index and magnitude probability of earthquakes induced during reservoir fluid stimulations. *The Leading Edge* (cit. on pp. 5, 19).
- Shapiro, S., O. Kruger, C. Dinske and C. Langenbruch, 2011. Magnitudes of induced earthquakes and geometric scales of fluid-stimulated rock volumes. *Geophysics*, **76**(6), WC55–WC63 (cit. on p. 19).
- Shewchuk, J., 1994. An Introduction to the Conjugate Gradient Method Without the Agonizing Pain. *School of Computer Science* (cit. on p. 134).
- Shi, Y. and B. Bolt, 1982. The Standard Error of the Magnitude-Frequency b value. *Bulletin of the Seismological Society of America*, **72**(5), 1677–1687 (cit. on p. 71).
- Shunping, P., P. Zhigang and C. Xiaowei, 2018. Locations of Injection-Induced Earthquakes in Oklahoma Controlled by Crustal Structures. *J. Geophys. Res.: Solid Earth*, **123**, 2332–2344 (cit. on pp. 43, 91, 102).
- Simpson, D., 1976. Seismicity changes associated with reservoir loading. *Engineering geology*, **10**(2-4), 123–150 (cit. on p. 3).
- 1986. Triggered Earthquakes. *Annu. Rev. Earth Planet. Sci.* **14**, 21–42 (cit. on p. 51).
- Simpson, D. and W. Leith, 1988. Two types of reservoir-induced seismicity. *Bulletin of the Seismological Society of America*, **78**, 664–683 (cit. on p. 3).
- Skoumal, R., M. Brudzinski, B. Currie and J. Levy, 2014. Optimizing multi-station earthquake template matching through re-examination of the Youngstown, Ohio, sequence. *Earth and Planetary Science Letters* **405**, 274–280 (cit. on pp. 11, 16, 19, 20, 51).
- Skoumal, R., M. Brudzinski and B. Currie, 2015a. Distinguishing induced seismicity from natural seismicity in Ohio: Demonstrating the utility of waveform template matching. *J. Geophys. Res.: Solid Earth*, **120**, 6284–6296 (cit. on p. 11).
- 2015b. Induced earthquakes during hydraulic fracturing in Poland Township. *Bulletin of the Seismological Society of America*, **105**, 189–197 (cit. on p. 11).

- Skoumal, R., M. Brudzinski and B. Currie, 2016. An efficient repeating signal detector to investigate earthquake swarms. *J. Geophys. Res.: Solid Earth*, **121**, 5880–5897 (cit. on p. 11).
- Snow, D., 1965. A parallel plate model of fractures permeable media. PhD thesis. University of California, Berkeley (cit. on p. 137).
- Soma, N., H. Asanuma, H. kaieda, K. Tezuka, D. Wyborn and H. Niitsuma, 2004. On site mapping of microseismicity at Cooper Basin, Australia HDR project by the Japanese team (cit. on pp. 14, 15).
- Spada, M., T. Tormann, S. Wiemer and B. Enescu, 2013. Generic dependence of the frequency-size distribution of earthquakes on depth and its relation to the strength profile of the crust. *Geophys. Res. Lett.* **40**, 709–714 (cit. on p. 77).
- Stabile, T., A. Giocoli, A. Perrone, S. Piscitelli and V. Lapenna, 2014. Fluid injection induced seismicity reveals a NE dipping fault in the southeastern sector of the High Agri Valley (southern Italy). *Geophys. Res. Lett.* **41**, 5874–5884 (cit. on pp. 14, 15).
- Sumy, D., E. Cochran, K. Keranen, M. Wei and G. Abers, 2014. Observations of static Coulomb stress triggering of the November 2011 M5.7 Oklahoma earthquake sequence. *J. Geophys. Res. Solid Earth*, **119**, 1904–1923 (cit. on pp. 3, 16, 51).
- Tang, C., J. Rial and J. Lees, 2008. Seismic imaging of the geothermal field at Krafla, Iceland using shear-wave splitting. *Journal of Volcanology and Geothermal Research*, **176**(2), 315–324 (cit. on pp. 4, 12).
- Thikonov, A. and V. Arsenin, 1977. Solution of ill-posed problems. Winston (cit. on p. 134).
- TNO, 2013. GeoTop modelling. Dutch. TNO rapport R10991 (cit. on p. 13).
- Turcotte, D. and G. Schubert, 2014. *Geodynamics*. Cambridge University Press (cit. on p. 60).
- Turuntaev, S. and V. Riga, 2017. Non-linear effects of pore pressure increase on seismic event generation in multi-degree-of-freedom rate-and-state model of tectonic fault sliding. *Nonlin. Processes Geophys.*, **24**, 215–225 (cit. on pp. 40, 53).
- Valoroso, L., L. Improta, L. Chiaraluce, R. Stefano, L. Ferranti, A. Govoni and C. Chiarabba, 2009. Active faults and induced seismicity in the Val d’Agri area (Southern Apennines, Italy). *Geophys. J. Int.* **178**, 488–502 (cit. on pp. 14, 15).
- Van Thienen-Visser, K. and J. Breunese, 2015. Induced seismicity of the Groningen gas field: History and recent developments. *The Leading Edge* (cit. on pp. 13, 16).
- Van der Elst, N., H. Savage, K. Keranen and G. Abers, 2013. Enhanced Remote Earthquake Triggering at Fluid-Injection Sites in the Midwestern United States. *Science*, **341**(6142), 164–167 (cit. on pp. 3, 51).
- Van der Elst, N., M. Page, D. Weiser, T. Goebel and S. Hosseini, 2016. Induced earthquake magnitudes are as large as (statistically) expected. *J. Geophys. Res.: Solid Earth*, **121**, 4575–4590 (cit. on pp. 20, 21, 43).
- Van Eck, T., F. Goutbeek, H. Haak and B. Dost, 2006. Seismic hazard due to small-magnitude, shallow-source, induced earthquakes in The Netherlands. *Engineering geology*, **87**, 105–121 (cit. on p. 5).
- Verdon, J., B. Baptie and J. Bommer, 2019. An Improved Framework for Discriminating Seismicity Induced by Industrial Activities from Natural Earthquakes. *Seismological Research Letters* (cit. on p. 6).
- Viegas, G., K. Buckingham, A. Baig and T. Urbancic, 2012. Large scale seismicity related to wastewater injection near Trinidad, Colorado, USA (cit. on pp. 16, 51).
- Wei, S., J.-P. Avouac, K. Hudnut, A. Donnellan, J. Parker, R. Graves, D. Helmberger, E. Fielding, Z. Liu, F. Cappa and M. Eneva, 2015. The 2012 Brawley swarm triggered by injection-induced aseismic slip. *Earth and Planetary Science Letters*, **422**, 115–125 (cit. on pp. 3, 22, 24, 149).

-
- Weingarten, M., S. Ge, J. Godt, B. Bekins and J. Rubinstein, 2015. INDUCED SEISMICITY. High-rate injection is associated with the increase in U.S. mid-continent seismicity. *Science*, **348**, 1336–1340 (cit. on pp. 22, 42).
- Whitney, M. L., 2009. Theoretical and Numerical Study of Tikonov’s Regularization and Morozov’s Discrepancy Principle. PhD Thesis. Georgia State University, Department of Mathematics and Statistics (cit. on p. 134).
- Wibberley, C. and T. Shimamoto, 2003. Internal structure and permeability of major strike-slip fault zones: the Median Tectonic Line in Mie Prefecture, Southwest Japan. *Journal of Structural Geology*, **25**, 59–78 (cit. on p. 135).
- Wiemer, S., T. Kraft and D. Landtwing, 2014. Seismic Risk. *Pail Scherrer Inst.* (cit. on p. 27).
- Wilson, M., R. Davies, G. Foulger, B. Julian, P. Styles, J. Gluyas and S. Almond, 2015. Anthropogenic earthquakes in the UK: A national baseline prior to shale exploitation. *Marine and Petroleum Geology*, **68** (cit. on p. 12).
- Witherspoon, P. A., J. S. Y. Wang, K. Iwai and J. E. Gale, 1980. Validity of cubic law for fluid in a deformable rock fracture. *Water Resources Research*, **16**(6), 1016–1024 (cit. on p. 137).
- Wu, W., J. Reece, Y. Gensterblum and M. Zoback, 2017. Permeability Evolution of Slowly Slipping Faults in Shale Reservoirs. *Geophys. Res. Lett.* **44**, 11368–11375 (cit. on pp. 35, 109).
- Ye, Z. and A. Ghassemi, 2018. Injection-Induced Shear Slip and Permeability Enhancement in Granite Fractures. *J. Geophys. Res.: Solid Earth*, **123**, 9009–9032 (cit. on pp. 34, 138).
- Yeck, W., M. Weingarten, H. Benz, D. McNamara, E. Bergman, R. Hermann, J. Rubinstein and P. Earle, 2016. Far field pressurization likely caused one of the largest injection induced earthquakes by reactivating a large preexisting basement fault structure. *Geophys. Res. Lett.* **43**, 10198–10207 (cit. on pp. 4, 9, 16, 52).
- Zhang, S. and T. Tullis, 1998. The effect of fault slip on permeability and permeability anisotropy in quartz gouge. *Tectonophysics*, **295**, 41–52 (cit. on pp. 35, 79, 109, 138, 140).
- Zoback, M. D. and J. D. Byerlee, 1975. Permeability and Effective Stress. *Geologic Notes*, 154–158 (cit. on pp. 35, 44, 79, 109, 135, 136, 147).
- Zobak, M. and S. Gorelick, 2012. Earthquake triggering and large-scale geologic storage of carbon dioxide. *PNAS*, Vol. 29, N. 106, 10164–10168 (cit. on p. 5).

RÉSUMÉ

Cette thèse est dédiée à l'étude de la réactivation de faille par injection de fluide, à l'aide d'un modèle hydro-mécanique de faille rate and state. Bien que les principaux mécanismes à l'origine de la réactivation de faille soient bien connus, différents aspects ne sont pas encore complètement explorés. Dans la première partie de cette thèse, on étudie le rôle du protocole d'injection (pression maximale et taux de pression d'injection), ainsi que le rôle des paramètres de frottement sur le taux de sismicité et la distribution de magnitude, pour des failles 2-D hétérogènes. On souligne d'abord une corrélation temporelle entre le taux de sismicité et le taux de pression de pore gouvernant la faille. On montre ensuite une dépendance du taux de sismicité ainsi que de la distribution des magnitudes sur les paramètres d'injection. Une compensation entre ces deux existe pour de grandes valeurs du taux de pression d'injection. Ce comportement ne peut pas être abordé par le taux de sismicité proposé par [Dietrich \(1994\)](#). En outre, on montre que les failles ayant un comportement de frottement plus stable présente un taux de sismicité et un moment sismique plus faibles. Dans la dernière partie de cette étude, la variation de la diffusivité hydraulique au cours de l'injection de fluide avec l'accumulation du déplacement et la réduction de la contrainte normale effective sur la faille est abordée. On utilise des expériences d'injection (échelle du laboratoire) sur un échantillon d'andésite, où la pression de pore est mesurée à deux endroits sur la faille. En appliquant des méthodes d'inversion, on estime le meilleur modèle de diffusivité et les incertitudes associés, pouvant expliquer les données expérimentales. Avec ces résultats, on peut étendre notre modèle hydro-mécanique, afin de pouvoir calculer la pression de pore, la diffusivité hydraulique et le déplacement accumulé sur la faille.

MOTS CLÉS

Réactivation de Faille, Injection de Fluide, Modèle Numérique de Faille Rate and State, Sismicité induite, Expériences de Laboratoire, Évolution de Perméabilité.

ABSTRACT

This PhD thesis is dedicated to the study of injection induced fault reactivation using a coupled hydro-mechanical rate and state model of a fault. Even though the principal mechanisms behind induced fault reactivation are well known, different aspects are not yet fully explored, nor understood. In the first part of this thesis, we explore successively the role of the injection protocol (in particular, injection maximum pressure and injection pressure rate), and the fault frictional parameters on the rate of induced events and their magnitude content, for different heterogeneous 2-D fault configurations. We first point out a temporal correlation between the seismicity rate and the pore pressure rate governing the fault. We then show a dependence of the rate and magnitude content of the seismic events on the injection parameters, as well as the existence of an important trade-off between them, which could not be addressed using the [Dietrich \(1994\)](#)'s seismicity rate model. Concerning the frictional parameters, we show that for the faults tested in this study, the ones having a more stable frictional behavior exhibit a lower induced seismicity rate and seismic moment released. In the last part of this study, the variation of the hydraulic diffusivity during fluid injection with shear slip and effective stress reduction is addressed. For this, we use laboratory injection experiments on an Andesite rock sample, during which the pore pressure was measured at two locations along the fault plane. In an inversion framework, we estimate the best model and the associated uncertainties of an effective diffusivity history that could explain the experimental data. Using this information, we could extend our hydro-mechanical model, which would allow the computation of pore pressure, diffusivity and slip changes along the experimental fault.

KEYWORDS

Fault Reactivation, Fluid Injection, Rate and State Fault Numerical Model, Induced Seismicity, Laboratory Rock Mechanics Experiments, Permeability Enhancement.